ADDITIVE MANUFACTURING OF AISI D2 TOOL STEEL USING DIRECTED ENERGY DEPOSITION

by

Samer Mohamed Tawfik Abdallah Omar

Submitted in partial fulfilment of the requirements for

the degree of Doctor of Philosophy

at

Dalhousie University
Halifax, Nova Scotia
April 2023

DEDICATION PAGE

I'd like to dedicate this thesis to my lovely family my mother Neama Mohamed, my father Mohamed Tawfik, my wife Dr Omama Ibrahim, my sister Dr Rana Tawfik and my kids Omar, Layan and Dima. I love you and hope to make you proud.

TABLE OF CONTENTS

LIST OF TABLES

LIST OF FIGURES

ABSTRACT

The main objective of the current thesis is to optimise direct energy deposition (DED) process parameters to fabricate parts with good mechanical and geometrical properties and to determine the best of postprocessing heat treatment schedule in order to enhance the the mechanical properties of the as-printed samples.

Firstly, the impact of laser-directed energy deposition (DED) process parameters and post-deposition heat-treatment cycles on the microstructural characteristics and hardness were evaluated for cladding AISI D2 tool steel onto annealed AISI D2 substrates. The influences of powder feed rate, scanning speed and layer height were assessed. After laser deposition, the DED samples were subjected to various tempering heat-treatment cycles. In addition, the wear resistance, indentation, and scratch hardness responses were assessed to evaluate the heat-treatment effect compared to wrought D2. It was demonstrated that the hardness values of the DED fabricated parts were higher than an annealed wrought D2, but lower than the air-cooled D2. Subsequent tempering of the DED printed parts resulted in a final hardness, essentially equivalent to the air-cooled level.

Furthermore, the geometrical characteristics and surface roughness of the DED-processed specimens were assessed. It was concluded that the use of higher laser scanning speeds decreases both the size of single clads and the level of sample over-building. However, there was no clear trend for powder feed rate on either single-clad size or dimensional accuracy. Furthermore, the surface roughness was also assessed using CLSM, to evaluate the influence of the various DED operating conditions. It was demonstrated that the amount of partially un-melted powder particles adhered to the sample surface significantly affects the surface roughness of the DED processed specimens.

The ability to deposit overhang structures using DED was also investigated by depositing inclined thin walls, under various process parameters and angles of inclination. The impact of the process parameters and the angle of inclination on both angle accuracy and side surface roughness were analysed.

These favourable findings contributed to the scientific knowledge of DED of AISI D2 tool steel by optimising the process parameters and reducing the post-processes to obtain high wear resistance, better dimensional accuracy, and improved surface roughness.

LIST OF ABBREVIATIONS USED

A1	Eutectoid temperature
AISI	American Iron and Steel Institute
AM	Additive manufacturing
BCC	Body-centered cubic
BCT	Body-centered tetragonal
BHN	Brinell hardness number
BJ	Binder jetting
CAD	Computer-aided design
CLSM	Confocal laser scanning microscope
CNC	Computer numerical control
d	Spot size
D	Indenter ball diameter
D_{10}	10% of the total particles are smaller than the size reported
D_{50}	50% of the total particles are smaller than the size reported
D_{90}	90% of the total particles are smaller than the size reported
d_{BHN}	Indentation diameter in Brinell hardness test
DED	Direct energy deposition
dT/dt	Cooling rate
d_{VHN}	Average length of diagonals in Vickers hardness test
E	Energy density
EBAM	Electron beam additive manufacturing

EDS	Electron dispersive X-ray spectroscopy
F	Applied force
f	Powder feed rate
FCC	Face-centered cubic
FE-SEM	Field emission scanning electron microscope
f_o	Oscillating frequency
G_r	Real temperature gradient
HAZ	Heat affected zone
HR	Rockwell hardness number
HS_p	Scratch hardness
ICP-OES	Inductively coupled plasma–optical emission spectroscopy
I_e	Beam current
L	Length of wear test stroke
LPBF	Laser powder bed fusion
MEC	Minerals Engineering Centre
Ms	Martensite starting temperature
P	Laser power
PSD	Particle size distribution
S_a	Arithmetical mean height
SDAS	Secondary dendrite arm spacing
SLM	Selective laser melting
SLS	Selective laser sintering
t	Wear test time

TTT	Time-temperature-transformation
U_s	Solidification rate
v	Scanning speed
V_{acc}	Accelerating voltage
VHN	Vickers hardness number
V_{loss}	Wear track volume
w	Scratch width
WR	Wear rate
wt%	Weight percent
XRD	X-ray diffraction
α	Ferrite
γ	Austenite
γ_e	Interfacial free energy
ΔG^*	Critical free energy barrier
ΔG_v	Volume-free energy release
Δy	Shift value (perpendicular to the scanning direction)
Δz	Layer thickness
θ_d	Inclined thin wall design angle
θ_m	Inclined thin wall modified design angle
λ_2	secondary dendrite arm spacing

ACKNOWLEDGEMENTS

First and foremost, I would like to express my deepest gratitude to my supervisor, Dr Kevin Plucknett, for his continuous guidance, patience, and motivation throughout this long journey. I am always humbled by his modesty and sincere advice in my academic and professional choices. Dr Plucknett taught me how to always look at the big picture before tackling problems one at a time. I will always be honoured to be one of his students and to have him as my mentor.

I want to thank my esteemed supervisory committee: Dr Stephen Corbin and Dr Jan Haelssig, for their time and commitment to supervising my thesis.

My appreciation goes to my friends and colleagues who have contributed in diverse ways to my project. I would like to express my gratitude to Dr Mark Amegadzie, Dr Greg Sweet, Dr Addison Rayner, Dr Marciel Gaier, Zhila Russell, Owen Craig, Jon Hierlihy, Paria Siahpour, and Danielle Griffin. Thank you for all the good times, talks, and laughs. I would like to thank Randy Cooke, Patricia Scallion, and Peter Jones for their technical support.

All my heartfelt love and appreciation for my family. I am eternally indebted to my parents for their love and support throughout my life. My sister, Rana, for all the love and memories that we share. My greatest thanks go to the person, who aided me most throughout this journey and most appreciative to the person closest to me, my wife, Omama, for her unremitting encouragement, approvals, acknowledgements and her love.

Finally, my son Omar, and daughters Layan and Dima, I love you and hope to make you proud.

CHAPTER 1 INTRODUCTION

1.1 Research Significance and Aims

The additive manufacturing (AM) market is presently valued at 12.7 billion US dollars, and the AM industry is predicted to grow to reach a value of 15.8 billion US dollars worldwide by the end of 2025 [1]. In terms of the metals AM market value, this covers roughly 20% of the total AM market [1]. As illustrated in Figure 1.1, directed energy deposition (DED) is the second largest metal printing process, with a share of 16% of the metal AM market [2]. This can be attributed to the fact that the DED process can be utilised for fabricating high-level, precision near net shape components. In addition, DED technology is not constrained by a proprietary substrate, so material can be deposited onto an existing surface or to repair a worn part. This benefit arises because of the small heat-affected zone, which leads to low distortion [3].

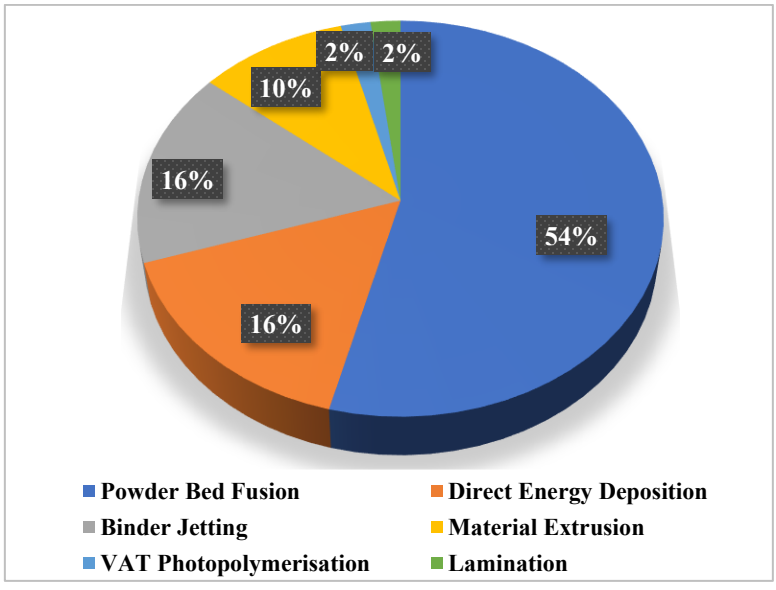

Figure 1.1 Metal AM market [2].

On the other hand, metal AM products can demonstrate a lack of dimensional accuracy after fabrication as a result of variations in material properties, surface roughness, and/or distorted geometry due to either residual stresses or slicing software discrepancies [4-6]. As a consequence, post-processing operations are essential after each print. These operations, such as machining, powder removal, stress relief, surface finishing, support structure removal, etc., were shown to account for 27.9% of an AM part fabrication cost [1,7].

In terms of the proposed material for this research, AISI D2 tool steel is known as a strong example of industrial cold work die steels. This can be attributed to its exceptional wear resistance as a result of the composition including high chromium (~12 wt%) and carbon (~1.5 wt%) contents, which allows the formation of high-hardness carbides through a tempering step. Moreover, the high chromium content also leads to good resistance to both oxidation at high temperatures and surface staining when hardened or polished [8,9].

As a result, each of the aforementioned three aspects (AM market growth, the need for cost reduction, and the industrial applications of AISI D2 tool steel) drive the need to investigate the whole fabrication workflow of DED 'end-to-end'. In addition, the capability of DED to repair worn parts or cracks is highly beneficial for cold work die applications, in which defective parts could be repaired instead of having to replace the whole system. As a consequence, the present investigation was initiated with the DED of AISI D2 tool steel onto substrates of the same material to produce dense parts with good surface and geometrical quality, in order to explore the possibility of reducing the number of post-processes to obtain parts with better mechanical properties.

1.2 Research Objectives

The main objectives of the current thesis is are identify the best DED process parameters to produce parts with good mechanical and geometrical properties, and to assess the effects of postprocessing heat treatments on the possible enhancement of the mechanical properties. This objective can be divided into the following sub-objectives:

1. Generating and characterising additively manufactured structures of D2 tool steel on like substrates using DED.
2. Selection of an optimum processing parameter window, followed by hardness, scratch and wear testing, and microstructural analysis of the as-printed D2 samples.
3. Determining the optimal post-heat treatment schedule to obtain AM parts with desirable mechanical properties (e.g. higher hardness and wear resistance) and surface integrity.
4. Exploring the feasibility of reducing the number of post-processes needed to obtain AM parts with desirable surface finish and dimensional accuracy by optimising the process parameters.
5. Producing design strategies and simple test components with overhung structures by minimizing the discrepancy between designed and actual deposited components. These, in turn, can then facilitate the manufacturing of hollow structures using DED.

1.3 Thesis Outline

This thesis divided into eight chapters, which combine all the goals and objectives of the research.

Chapter 1 provides an outline of the thesis chapter contents and how the overall document is structured. It also includes the objectives, significance, and contributions made by the author to the present research relating to DED-processed D2 tool steel. Furthermore, this chapter illustrates the main contributing information to this field of research which is to provide optimized system parameters using relevant DED equipment and laser technology, in order to print D2 tool steel samples with preferred material properties that provide the utmost usage in the industrial application, such as high hardness and wear-resistant D2 additively manufactured components.

Chapter 2 presents a literature review of relevant background information. The first section of this chapter illustrates the DED process, including a description of the method in addition to the advantages and drawbacks of the DED process in comparison to other metal AM techniques. It demonstrates the impact of the various process parameters on the deposited material, such as physical properties, microstructure, and surface roughness. The second section provides details about evaluating and enhancing different material characteristics (e.g., hardness, wear, surface roughness, residual stresses, etc.). The third section presents a background relating to tool steels, especially for the AISI D2 grade, where the influence of alloying additions and heat treatment on the microstructure and mechanical properties is reviewed.

Chapter 3 demonstrates the main experimental methodologies and types of analysis used in this research. A detailed description for the selected DED process parameters is illustrated. In addition, the methodologies of the pre/post-deposition examinations are presented.

Chapter 4 presents a published journal article addressing the first two objectives through investigating the effects of a wide range of process parameters on the microstructural characteristics of 'as-printed' AISI D2 tool steel. Those characteristics include morphology, chemical composition, and phase formation. The indentation and scratch hardness of these materials was also investigated. Furthermore, the impact of post-deposition heat-treatment cycles on the microstructural characteristics and hardness were evaluated.

Chapter 5 illustrates a submitted journal article that presents a study of the influence of DED process parameters on the geometrical properties and surface roughness of AISI D2 tool steel, with the aim of addressing the third research objective. Within this context, the impacts of laser scanning speed and powder feed rate were evaluated. The geometrical characteristics of the DED processed clad were examined, including the size of single clads, in addition to the dimensional accuracy of the multi-layer specimens. Furthermore, the influence of the various DED operating conditions on surface roughness was also assessed. To address the fourth objective, the ability to deposit overhang structures using DED was investigated, through the deposition of inclined thin walls, conducted under various process parameters and angles of inclination.

Chapter 6 presents a submitted journal article in which an investigation is provided of the effects of varying the targeted layer thickness upon the microstructural, geometrical, hardness, and wear characteristics of the as-processed AISI D2 tool steel. The microstructural characteristics included investigating the morphology of the cross-sections of the DED processed samples, determining the chemical composition and distribution of alloying elements along the cross-section, and exploring the phases formed after DED processing when applying different layer thicknesses. In addition, the Rockwell-C indentation and scratch hardness were examined. The wear resistance of the samples was evaluated. Finally, the surface roughness and dimensional accuracy were assessed. It is worth noting that the effects of layer thickness upon the DED processed characteristics are presented in a single chapter due to the significant impact of layer thickness upon the heating/cooling cycles, which is one of the main parameters in determining the material behaviour.

Chapter 7 demonstrates a comparison between the wear resistance of as-printed AISI D2 tool steel to wrought D2 tool steel subjected to different heat treatment schedules. In order to evaluate the tribological properties, the specific wear rate determined, such that the relationship between the wear rate and the wear test duration could be assessed. In addition, the findings were subsequently explained with respect to the microstructural and microscopic analysis of the wear scars.

Chapter 8 provides a summary of the main research findings and accomplishments from the thesis, as well as recommendations for future work related to this research topic.

The research demonstrated in this thesis was conducted from May 2019 to December 2022. All of the sample preparation, materials characterization, data collection, and draft

manuscript preparation (for journal and conference articles) was completed by the thesis author, unless otherwise stated, operating under the guidance of the PhD supervisor Dr Kevin Plucknett.

Others acknowledged contributions included the construction of the G-code and preparing the DED system, performed by the relevant technicians at Dalhousie University. Inductively coupled plasma optical emission spectroscopy (ICP-OES) analyses were conducted by the Minerals Engineering Centre (MEC) staff at Dalhousie University. Any major metal working was performed by the machinists at Dalhousie University to produce samples (e.g., substrates, cross-sectioned and/or wrought D2 samples).

CHAPTER 2 LITERATURE REVIEW

2.1 General Additive Manufacturing Process Information

Additive manufacturing (AM) is defined as the process where materials are joined, usually layer-by-layer, to form parts from 3D computer models [10]. In AM, the final product is fabricated by adding materials, dissimilar to the traditional manufacturing processes such as stamping and machining in which the final shape is created by subtracting materials from larger sheet metal or stock [11]. AM was also more traditionally known as freeform fabrication and rapid prototyping [12].

AM processes have many advantages, compared to traditional manufacturing techniques. Firstly, AM does not typically require additional resources such as fixtures, jigs, coolants, and cutting tools, which are needed in traditional manufacturing processes. In addition, AM provides high production flexibility, due to the independence of the product quality on labour skills. Furthermore, AM processes have high part flexibility, because a single part can be built with variable mechanical properties; for example, flexible on one side and stiff on the other side. Due to the absence of tooling limitations, complex parts can be fabricated in a single piece. Additionally, there is no need to remove large amounts of material in AM, dissimilar to conventional manufacturing processes, because raw materials are efficiently used in AM processes by creating the part layer upon layer, with the profile of each deposited layer corresponding closely to that ‘slice’ from the computer design file. As a result of the aforementioned advantages, AM demonstrates a positive prospect as a strong candidate for medical, automotive, and aerospace applications. Figure 2.1 illustrates various applications for AM processes [13-15].

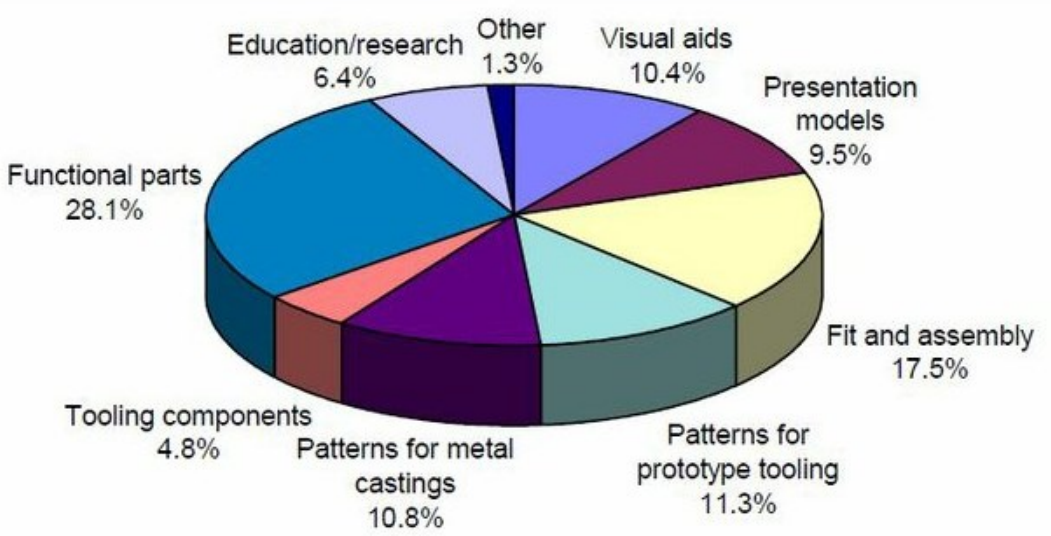

Figure 2.1 Some of the major applications of AM [1].

In contrast, when making comparison to conventional manufacturing processes, AM is not the best candidate for some cases, specifically in the field of mass production due to some clear disadvantages. Firstly, imperfection is one of the primary drawbacks of AM processes because parts fabricated by AM usually have a ribbed and rough surface finish, which is attributed to the large-sized powder particles and plastic beads that are stacked on the surface of the product. In addition, materials used in AM are still limited because a specific material formulation is required for each AM technology; in this respect, a source of carefully formulated feedstocks are needed for each material. Size limitations are also some of the main disadvantages of AM, although this does depend largely on the technique used, as the size of parts produced by AM is still limited because the time needed to finish the construction process can often be very long. Additionally, AM equipment is generally

much more expensive per unit of production than that used for more traditional manufacturing processes [16-18].

2.2 Additive Manufacturing Technologies

Different methods are used to build and combine material layers in various AM processes. Laser or electron beams are used in some methods as a source of thermal energy, to melt or sinter plastic, metal, or even ceramic powders. In other processes, notably binder jet printing, injection printing heads are used in order to spray solvent or binder materials onto powdered polymers or ceramics. Figure 2.2 briefly illustrates the main AM processes [19-21]. In this work, our main focus is on powder-based AM processes, especially DED (referred to in Figure 2.2 as direct metal deposition (DMD)).

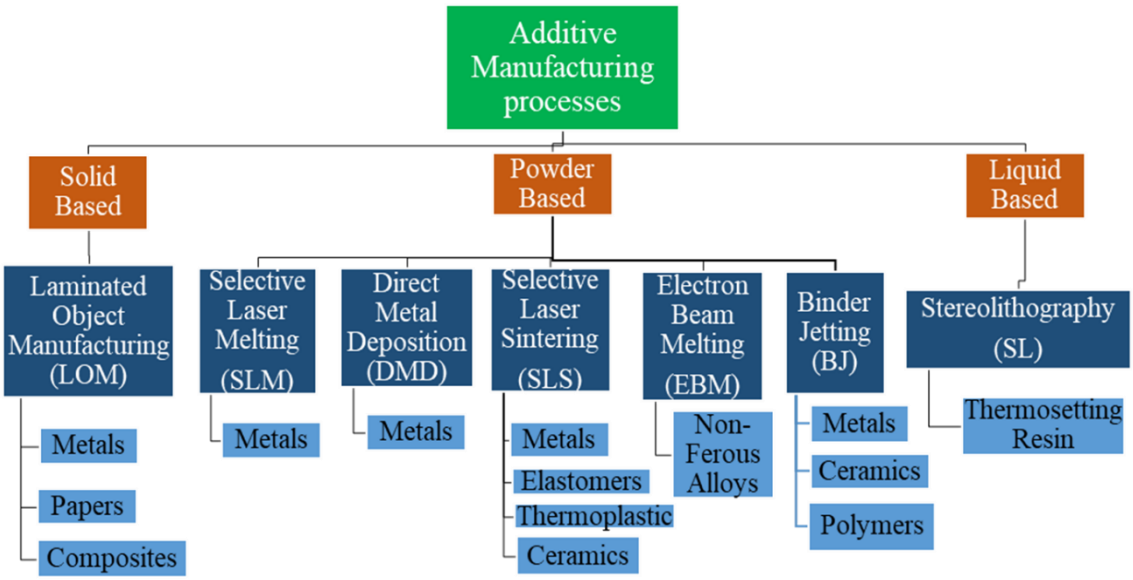

Figure 2.2 A summary of common AM technologies [21].

2.2.1 Laser Powder Bed Fusion

Laser powder bed fusion (LPBF) is one of the powder-based AM techniques where dense metallic parts are produced by selectively scanning a powder bed with a focused laser beam, which melts or sinters the powder. LPBF can be classified into two techniques, based on the level of powder heating. LPBF is called selective laser melting (SLM) when the powder is heated to more than its melting point. While, in the case of heating the powder to just under the melting point (sintering temperature), LPBF is described as selective laser sintering (SLS). A schematic diagram of the LPBF process is presented in Figure 2.3 [22].

One of the main advantages of using LPBF over the other AM techniques is that the un-melted powder from previous layers acts as a support to any overhanging geometry. Furthermore, it can be used with a very wide range of materials. On the other hand, part distortion is a common problem, for LPBF-manufactured components, due to the shrinkage of the build material. In addition, the LPBF process consumes a lot of time to construct the part, while LPBF cannot be used to produce closed-hollow geometries as the loose powder will become entrapped [23].

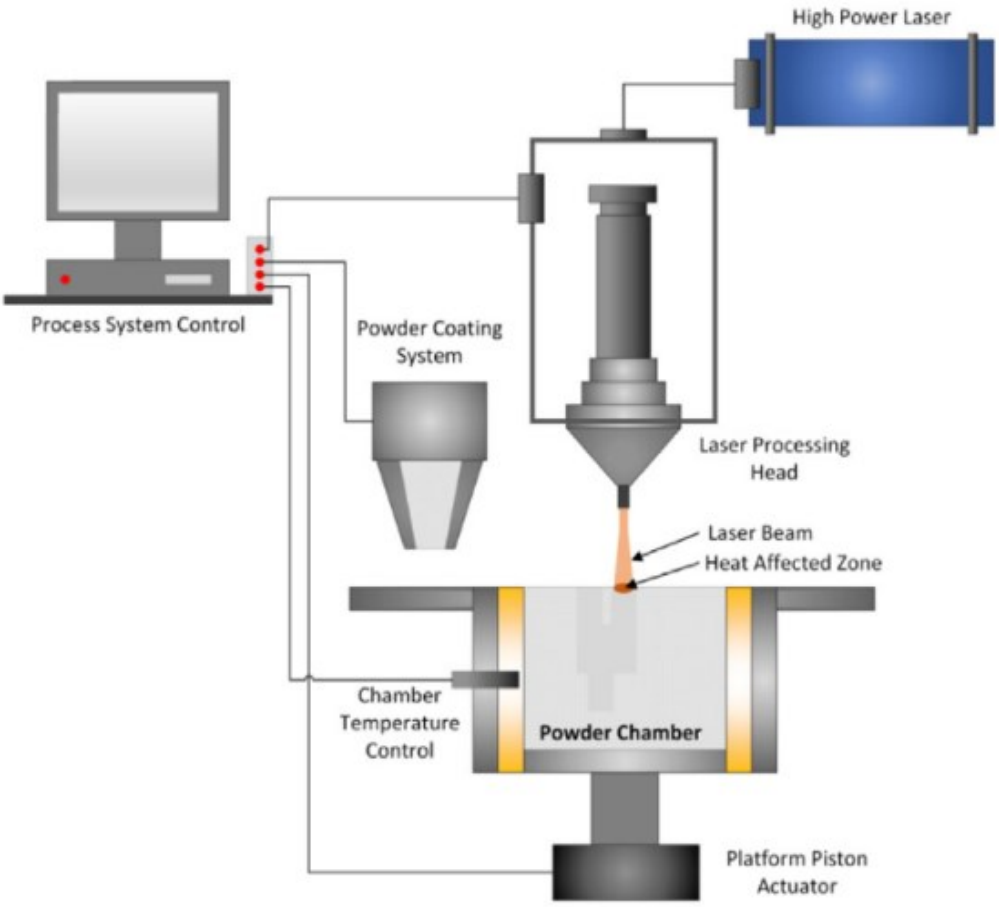

Figure 2.3 Schematic diagram of the LPB process [22].

2.2.2 Electron Beam Additive Manufacturing

Electron beam additive manufacturing (EBAM) can also be classified as a powder-based AM process. In EBAM, the powder bed is scanned and heated layer-by-layer using a focused, high-power beam of electrons. Figure 2.4 shows a schematic diagram for the EBAM process [24]. Although both EBAM and LPBF are powder-bed AM techniques, there are some differences between them. For instance, the heating source for LPBF and EBAM is laser spot and electrostatic charge, respectively. Another difference between

them is that a high vacuum is used in EBAM instead of inert gas in LPBF. Table 2.1 lists some of the main differences between EBAM and LPBF [25].

Table 2.1 Comparison between EBAM and LPBF [25].

Characteristics	**EBAM**	**LPBF**
Thermal source	Electron beam	Laser
Atmosphere	Vacuum	Inert gas
Scanning	Deflection coil	Galvanometer
Energy absorption	Conductivity	Absorptivity
Scan speeds	Magnetically driven, very fast	Limited by galvanometer inertia
Powder heating	Electron beam	Use infrared or resistive heaters
Surface finish	Moderate to poor	Excellent to moderate
Materials	Metals (conductor)	Polymers, metals and ceramics
Powder particle size	Medium	Fine
Energy costs	Moderate	High

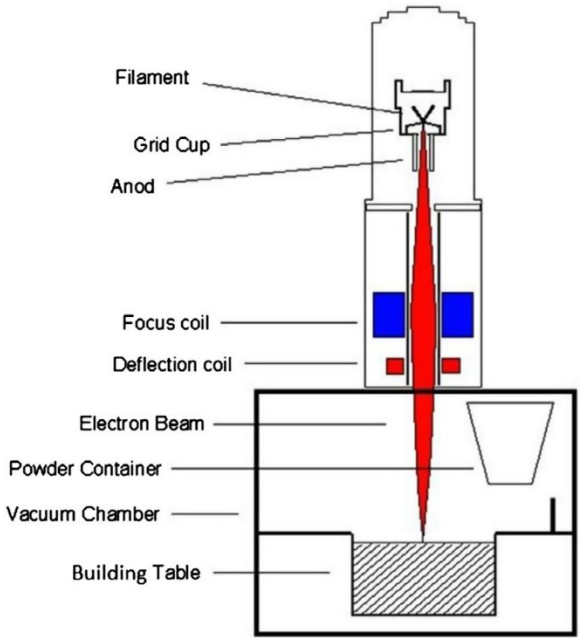

Figure 2.4 Schematic diagram of the EBAM process [24].

EBAM has many advantages compared to other AM techniques. For example, the beam movement is nearly instantaneous. In addition, the vacuum environment helps eliminate impurities such as oxygen. Furthermore, the high energy source is less expensive in EBAM. On the other side, one of the disadvantages of EBAM is that the use of vacuum strips out the alloying agents with low boiling points, such as Mn. Additionally, residual stresses are a problem in EBAM. However, it is much lower than LPBF because of the elevated bed temperatures [26].

2.2.3 Binder Jetting

Binder jetting (BJ) is one of the primary large scale AM techniques that is currently available. BJ is a powder-based process where a liquid binding agent is selectively ink-jetted into a powder bed to fabricate a metal green part. This process is followed by either sintering or melt-infiltration, in order to pyrolyze the binder and obtain final strength and density. While creating the green part, adhesion across the sectional layer can be developed by forming ‘stitching primitives’ as a result of the interaction between the binder droplets and the powder particles. In order to build the next layer, a new powder layer is spread above the previous one, by using a counter-rotating roller. After that, both the new layer and the previous one is stitched together, using the jetted binder. The green part manufacturing is completed by repeating the layer-by-layer process [27]. A schematic drawing of the BJ method is presented in Figure 2.5 [28].

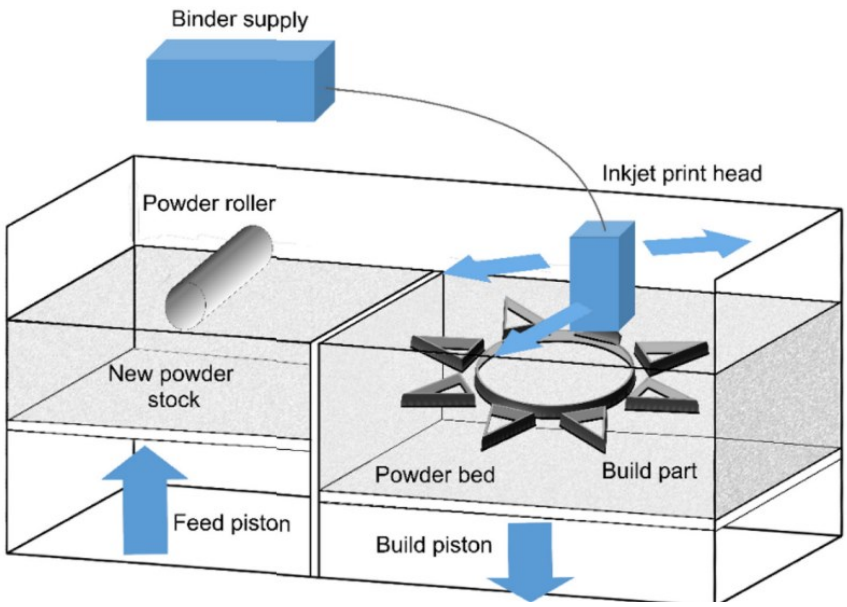

Figure 2.5 Schematic diagram of the BJ process [28].

The BJ technique has many advantages over other AM processes. Firstly, there are no residual stresses in the manufactured part, due to the absence of rapid heating or cooling of a molten pool of material; in BJ processing, the 3D components are shaped in a layer wise manner through the directed application of the binder. In addition, in contrast with laser-heated AM processes, BJ is readily able to process highly reflective materials, such as copper. On the other hand, the required additional post-processing, to improve the mechanical strength of the printed green parts, is one of the main disadvantages of BJ. In addition, BJ is limited to the use of moderately fine packed powders due to the difficulty of spreading ultra-fine powders, where powder agglomeration due to humidity can cause defects in the green part [29], while ultra-fine powders also tend to 'plume' in the BJ system.

2.2.4 Direct Energy Deposition

One AM approach, in which a computer-aided design (CAD) model could be used to directly fabricate fully dense metal parts, is referred to as directed energy deposition, or DED [30-33]. In the 1980s, during the epoch of welding technology based AM, the establishment of the primary theories of DED was fueled by the need for the refurbishing of metallic components [34]. For instance, one of the pioneering techniques was patented by Mehta *et al.* [35] whereby metallic parts could be repaired by a combined system of blown powder, with a laser beam as a heating source. Nowadays, the DED process can be summarised as: a small melt pool of metal being generated as a result of heating a metallic substrate with the aid of a laser beam, while a fine powder stream is deposited into the molten pool, using a powder delivery system. An associated computer numerical control (CNC) is used to drive the laser beam over the desired path to generate a single 2-D layer. Then, the subsequent deposition of layers, one onto another (i.e., layer-by-layer), creates a 3D part [36]. Furthermore, DED is also often known as laser coating [37,38], laser consolidation [39], laser direct casting [40], laser powder deposition [41,42], rapid prototyping [43], solid free-form fabrication [44], etc. Figure 2.6 illustrates a schematic diagram of the DED process [45].

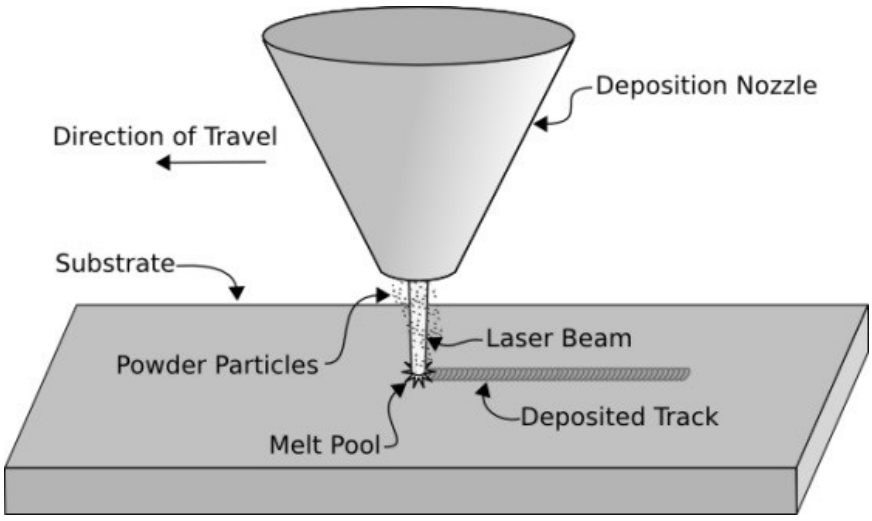

Figure 2.6 Schematic diagram of the DED process [45].

The DED approach possesses several benefits in comparison to other AM techniques. One of the main advantages is that high-value tooling can be conserved instead of having to be substituted with a new part, using DED to repair corroding or critical contacting (i.e., tribological) surfaces [46,47]. Additionally, DED can be utilised to build components with hidden channels, thin walls, or deep cavities, since there are very few restrictions for the geometry of the fabricated parts [16,25]. However, one of the principal drawbacks of DED is that the rapid heating-cooling cycles leads to residual stresses, which can result in cracking or failure of the fabricated component [48-50]. A further disadvantage is that the quality of the manufactured part is inadequately reproducible, due to the extraordinary sensitivity of the deposited material quality to any minor variations or disturbances in the operating process parameters, (e.g., laser power, powder feed rate, scanning speed, etc.) [51].

2.3 DED Process Parameters

Some AM system are pre-programmed by the machine vendors with optimum process parameters for a select range of materials. Typically, in DED, the proper process parameters must be identified by the users for their specific materials and applications, largely because the DED systems are delivered as a flexible platform. The DED process parameters can be classified into three categories: laser scanning, powder, and substrate. The laser scanning parameters include the laser power, laser scanning speed, spot diameter, hatch spacing, and scanning pattern. The powder process parameters include powder feed rate and powder characteristics. Finally, substrate preheating and the method of fixation are examples of substrate process parameters.

2.3.1 Laser Scanning Parameters

- *Laser Power*

Laser power is possibly the most essential parameter in the DED system since the power input determines if the powder particles are fully melted or just sintered. It is worth noting that the indication of laser power value is profoundly dependent on the chemistry of the feedstock. One of the common methods to determine the laser power is referred to as the energy density, as illustrated in Equation 2.1:

$$E = \frac{P}{vd}$$

Equation 2.1: Laser beam energy density [52].

where P refers to the laser power (W), v represents the scan speed (mm/s), and d is the spot size (mm). This equation demonstrates that the energy density is increased by either increasing the laser power or decreasing the laser scanning speed, while the spot size is

usually a fixed value. If the energy density is too high, it leads to excessive dilution of the substrate into the cladding and vice versa. Whereas too low of an energy density results in a lack of fusion [53]. Furthermore, the laser power greatly affects the width of the deposited layer. The use of higher laser power results in a wider depositing layer. This can be attributed to the fusion of more powder during melting [53]. The surface finish of the fabricated part is also profoundly dependent upon the power input. Furthermore, the amount of energy input dominates the cooling with scanning parameters contributing to this as well. It is also essential to consider the laser operational mode (i.e., pulsed or continuous). For the pulsed mode, rapid heating and cooling take place due to the laser being turned on and off which, in turn, results in a more refined microstructure [54]. On the other hand, the use of continuous laser mode causes a minimal increase in hardness [54]. Additionally, it is required to add laser cooling systems when using powers above 4 kW since, at these high temperatures, the optics and the nozzle can be damaged or distorted due to the possibility of powder clogging [55].

- *Scanning Speed*

As previously mentioned, the laser scanning speed affects the energy density, since the increase in speed causes a decrease in energy density. This consequently results in higher cooling rates and melt pool shrinkage [25]. However, from the economical point of view, it is better to use faster scanning speeds in order to reduce the print time; the use of high scanning speeds can lead to molten pool distortion, porosity, and dimensional issues. On the other hand, a slower scanning speed leads to the build-up of heat, which results in tempering of the lower deposited layers [53]. Additionally, the shape of the melt pool is strongly impacted by laser scanning speed. The use of higher scanning speed leads to

alteration in the molten pool shape from an elliptical to a teardrop shape [56]. As a result, large temperature gradients are created which affect the direction of growth. That may lead to higher residual stresses [57].

- *Spot Size*

The spot diameter refers to the area where the laser beam focuses on the substrate at an instant in time, which is invariably indicated by a diameter measurement. The spot size affects the quality of the manufactured part. A larger diameter results in a lowering of the printed resolution of the part and a rougher surface finish. In addition, a smaller spot size results in more localised heating, which could lead to the burning and evaporation of powder [58]. Furthermore, mirrors and lenses are utilised to focus the laser beam onto the substrate. When using higher power, it is necessary to use a cooling system to mitigate the effect of thermal lensing, which causes a change in the beam shape [58].

- *Hatch Spacing*

The deposition path followed by the laser typically covers multiple parallel lines, and the offset between the center of each track is known as the hatch spacing [23]. In order to accomplish bonding and densification, it is required to overlap the lines [25]. Therefore, the hatch spacing is often less than the beam diameter [52]. As illustrated in Figure 2.7, the ideal hatch spacing is determined in the case of having excess powder to fill the gap between the two tracks. That condition is obtained when the overlap area (A2) is equal to the negative space A1. However, any variation in melt pool size or shape could lead to a change in the hatch spacing [57].

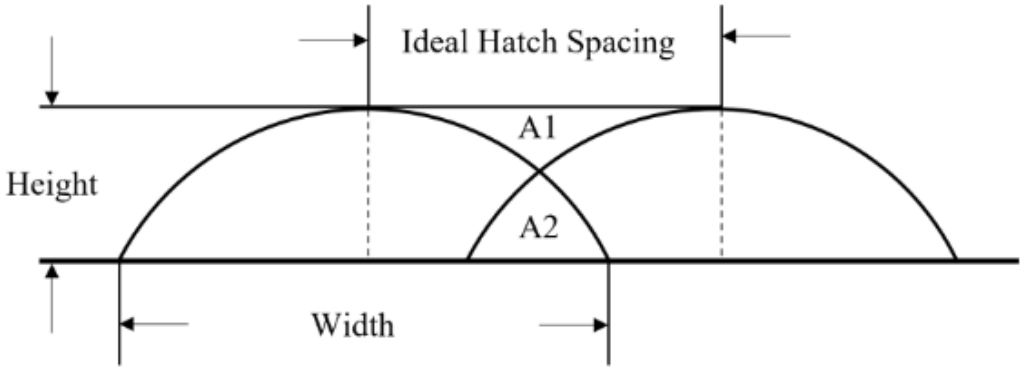

Figure 2.7 Ideal hatch spacing for the DED process, adapted from [59].

- *Scanning Pattern*

The scanning pattern represents the specific beam paths that are followed to deposit the part. The orientation of subsequent layers is changed at 30°, 45°, 90° or randomly to help alleviate the generation of residual stresses in the manufactured part. In addition, the change in successive layer orientation prevents the excess powder from levelling, thus enhancing the surface finish [25].

2.3.2 Powder Parameters

- *Powder Layer Height*

Similar to the majority of the DED operating parameters, the layer height is profoundly impacted by laser power, scanning speed, powder feed rate and spot diameter. For instance, the layer height is increased by increasing either the powder feed rate or laser power [53]. Whereas the use of higher scanning speeds leads to lower layer thickness [58]. Furthermore, the build time, dimensional accuracy and surface finish are influenced by layer height, since a faster build time could be achieved by using higher layer thickness. However, the fabricated part could be under-built. This can arise because the rate of raising

the nozzle is faster than the rate the material is consolidated. On the other hand, setting of thin layer heights results in overbuilt parts due to the deposition of more consolidated material [53].

- *Powder Characteristics*

It is crucial to ensure good flow properties of the powder used in the DED process. In regard to powder flowability, it was reported that spherical powder particles are the most prefered shape [55]. The powder shape significantly affects the layer height and melt pool temperature. Furthermore, the method of powder atomisation impacts the DED process characteristics. For example, due to the irregularity of shape for water-atomised powder, more laser energy is scattered than when a more spherical gas-atomised powder is used, which leads to more melting [60]. Another effect is that, at higher powder feed rates, more powder particles are deposited in the case of using gas-atomised particles than water-atomised ones. This can be attributed to the fact that the shape of the water-atomised particles is irregular, in addition to the fact that the particles are locking together which reduces the flowability, in contrast with gas-atomised powders [60].

2.3.3 Substrate Temperature Parameters

- *Preheating*

Depending on the DED system, the powder and substrate may be preheated, which is invariably beneficial for the properties of the manufactured part. The first advantage is to conserve the energy required for fusion by reducing the amount of laser power needed for melting the powder. A further benefit is that residual stresses and warping could be reduced by preheating [25]. This arises because of the change in cooling rates and temperature

gradients, depending on the extent of the substrate pre-heating [61]. Furthermore, better bonding is more likely to be accomplished by preheating the substrate, in comparison to DED on a cold substrate which results in the formation of cracks [62].

- *Atmosphere and Shielding Gas*

Since oxidation could lead to defects in the DED processed parts and poor bonding between individual layers, especially when depositing reactive material, the enclosure atmosphere is strictly controlled. Therefore, the oxygen level is controlled to be around 100 ppm by using an inert gas purge in a vacuum. Additionally, an inert shielding gas is utilised to deliver the powder. This leads to a higher convection rate and lower solidification time. Argon and helium are the most common inert gases used with a powder feedstock. It is worth noting that the shielding gas flow rate profoundly impacts the level of porosity in the manufacturing part; at higher shielding gas flow rates, the powder could be blown away, or the gases could become entrapped, which results in porosity in either case [25].

2.4 Printing Characteristics

In DED, the deposited material experiences several extreme conditions, because of the interrelated system parameters, in comparison to conventional casting methods. As a result, it is critical to control the molten pool, which can be tailored to achieve preferred final product properties. In addition, the cyclic heating arising in AM, which is a layer-by-layer process, is another printing characteristic required to be analysed. This is due to the fact that cyclic heating of the previously printed layers significantly impacts the microstructure, phases, properties, and surface finish.

2.4.1 Melt Pool Size

In the DED process, the deposition of a precise amount of material onto the substrate, while the laser beam focuses on the same spot, leads to the formation of a small melt pool (with an average diameter and depth of 0.25-1 mm, 0.1-0.5 mm, respectively) [63]. The immediate melt pool volume rapidly solidifies right after the movement of the laser beam past its location; at high scanning speeds, considering material properties and the other DED process parameters, the solidification rate could be as high as 10^3-10^5 °C/s [25]. Consequently, the process can result in the formation of distinctive phases or morphologies in contrast with those found under conventional manufacturing methods [25]. Increasing the energy density leads to slower cooling rates, which in turn causes refining in the microstructure to be similar to the casting case [25]. Therefore, there are innovative DED systems in which new sensing and monitoring equipment is used to control the melt pool size, by controlling the delivery of the feed. This can alleviate the inconsistency between parts, which minimises material wastage and part defects [63].

2.4.2 Thermal History

Due to the layer-by-layer deposition technique, complex thermal cycles are generated during the DED process [25], as the movement of the laser beam results in severe variations in heat build-up and cooling rates. In thin walls, the heat dissipation rate is too slow, which can therefore result in a higher build up in temperature. In addition, the deposition of new layers influences the previously deposited layers by causing their remelting or reheating, potential phase transformations, and/or the formation of complex microstructures [63]. It is also important to note that the aforementioned changes could be occurring together within the same part, which leads to anisotropic properties [25]. In consequence, warping

and crack formation could be caused by the propagated residual stresses due to the complicated thermal history [10]. Therefore, restricted control over the residual stresses, deposited microstructure, and phase transformations is a major problem for DED technology. Hence, the consistency and quality of DED process could be achieved by understanding the propagation of the aforementioned challenges, which results in broader adoption in industrial applications [25].

2.5 DED Product Quality

This section illustrates the desired mechanical characteristics of the parts manufactured by DED. Such characteristics include hardness, wear resistance, surface roughness, and residual stresses.

2.5.1 Hardness

There are plenty of definitions for hardness, depending on the field. For instance, metallurgists define hardness as ‘resistance to penetration’, or sometimes the ‘resistance to permanent deformation’. In contrast, lubrication engineers describe it as ‘resistance to wear’. Moreover, machinists refer to it as a ‘resistance to machining’. All of these properties are correlated to the plastic flow stress of materials [64].

- *Common concept of hardness testing*

Since hardness is generally described as material resistance to permanent indentation, the main concept of hardness testing is to apply a specific load, through an indenter tip of known geometry, onto the surface of the material being examined, with the applied load then held for a specific time. The size or depth of the residual indentation is then measured to determine the material hardness, which is used to indicate the ability to utilise the

material for specific applications. Thanks to the ease of conducting a hardness test, it is considered one of the most common methods for the inspection of metals and alloys.

- *Indentation Tests.*

In indentation tests, the amount of plastic deformation in the material is used to assess the material hardness, which can be determined by measuring the indentation area and/or depth, depending on the test type. Greater penetration depth and projected area are consequently found in softer materials.

  - *Brinell Test*

The Brinell test involves applying a force onto the surface of the examined material using a hardened steel ball. The selection of suitable load and ball diameter is significantly impacted by the hardness of the material being evaluated. For example, a ball with a diameter of 10 mm and a load of 3,000 kgf is used with cast irons. While a 500 kgf load is used for softer materials. Combinations of various loads and ball diameters could be used in Brinell hardness testing while keeping a constant load to square diameter ratio (5 and 30 for soft metals, and steels and cast irons, respectively). The Brinell hardness number (BHN) could then be determined, in kgf/mm^2 by applying Equation 2.2, where F refers to applied force in kgf, D represents the diameter of the indenter ball in mm, and d is the indentation diameter in mm [64].

$$BHN = \frac{F}{\pi D\left[D - \sqrt{D^2 - d_{BHN}^2}\right]}$$

Equation 2.2: Calculation of the Brinell hardness number.

- *Vickers hardness Test*

Similar to the Brinell hardness test, the Vickers hardness test involves application of a specific force onto the surface for a fixed duration. However, a diamond pyramid with a square base is used as the indenter geometry instead of ball (for the Brinell test). This method is valid for numerous metals and alloys, as well as ceramics, with a wide hardness range as a result of the intrinsic hardness and shape of the diamond indenter. A wide range of test loads (i.e., 1-120 kgf, depending on the material hardness) can be used in the Vickers method. In addition, it can be utilised for micro-hardness testing, when keeping the applied loads between 0.005 to 2 kgf on the Vickers scale. Equation 2.3 demonstrates the relation used for obtaining the Vickers hardness number (VHN), in which *F* refers to the applied force, in kgf, and *d* is the average length of diagonals, in mm [65].

$$VHN = \frac{1.8544F}{d_{VHN}^2}$$

Equation 2.3: Calculation of the Vickers hardness number.

- *Rockwell Test*

In the Rockwell test, there are two types of indenters. A diamond cone indenter is used with hard materials. Whereas a hardened steel ball, with sizes of (1/16") or (1/2"), is used in testing the hardness of softer materials. The difference between the Rockwell hardness test and the aforementioned Brinell and Vickers hardness tests is that the Rockwell hardness is determined by measuring the depth of the indentation, instead of the indentation size, as shown schematically in Figure 2.8. Therefore, the accuracy of Rockwell testing is critically dependent upon the sample surface conditions, due to the dependency of the

indentation depth measurements on the surface conditions. In consequence, to minimise the surface condition effect, a minor load of 10 kgf is first applied to establish a reference position. After that, the major load is applied, according to the Rockwell hardness scale, as presented in Table 2.2. Then, the value of the Rockwell hardness number is determined following Equation 2.4, where *HR* is the Rockwell hardness number, *E* is the indentation depth as a result of applying the total load (major plus minor loads), and *e* refers to the indentation depth after releasing the major load. It is worth noting that the Rockwell hardness number is worthless without specifying the scale [64].

$$HR = E - e$$

Equation 2.4: Calculation of the Rockwell hardness number.

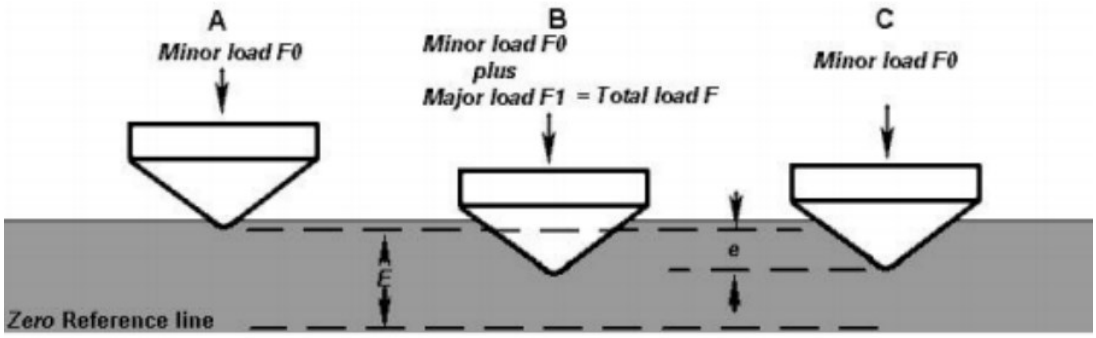

Figure 2.8 Schematic diagram for measuring penetration depth in the Rockwell test [65].

Table 2.2 Commonly used Rockwell hardness scales [65].

	Indenter	Major load F_1 (kgf)	Total Load F (kgf)	Applications
A	Diamond cone	50	60	Cemented carbides, thin steel, shallow case-hardened steel
B	1/16" steel ball	90	100	Copper alloys, soft steels, aluminum alloys, malleable iron
C	Diamond cone	140	150	Steel, hard cast irons, pearlitic malleable iron, titanium, deep case-hardened steels
D	Diamond cone	90	100	Thin steel and medium case-hardened steel, pearlitic malleable iron
E	1/8" steel ball	90	100	Cast iron, aluminum and magnesium alloys, bearing metals
F	1/16" steel ball	50	60	Annealed copper alloys, thin, soft sheet metals
G	1/16" steel ball	140	150	Malleable irons, copper-nickel-zinc and cupro-nickel alloys

2.5.2 Wear Resistance

The study of wear, known as tribology, is a complex process that is constantly being updated. The wear of materials is a problem facing many industries, whether known or unknown. The study of tribology gained greater popularity after the Second World War and is still not fully established compared to other fields of science [66]. Steels are the most common family of materials for tribological applications due to the flexibility of alloying and mechanical properties that can be attained [67]. Generally, there are three stages of wear: (i) a running-in period, (ii) a steady-state period, and (iii) a failure period. During the running-in period, the wear rate depends upon the materials microstructure, mechanical properties, and surface conditions. Next, the wear rate undergoes a steady-state increase and then, finally, the material fails [67]. The type of wear can change depending on several

factors, such as the environment, applied forces, speeds, and the material(s) in contact. Significant changes to the wear mechanism(s) depend on the sliding distance and velocity change, as presented in Figure 2.9. If the sliding time is increased, then the mechanical strength and interfacial adhesion determine the wear mechanisms. If the load is increased, then damage will occur. Further increase of load and sliding will cause heating to decrease the mechanical strength, potentially forming oxide layers, and can lead to phase changes. At very high speeds and distances, there may even be surface melting. This type of wear behavior is similar for all grades of steel [67]. Generally, the worn surface of mild wear can be classified as smooth. Whereas, for severe wear, the worn surface is rough and deeply damaged [67].

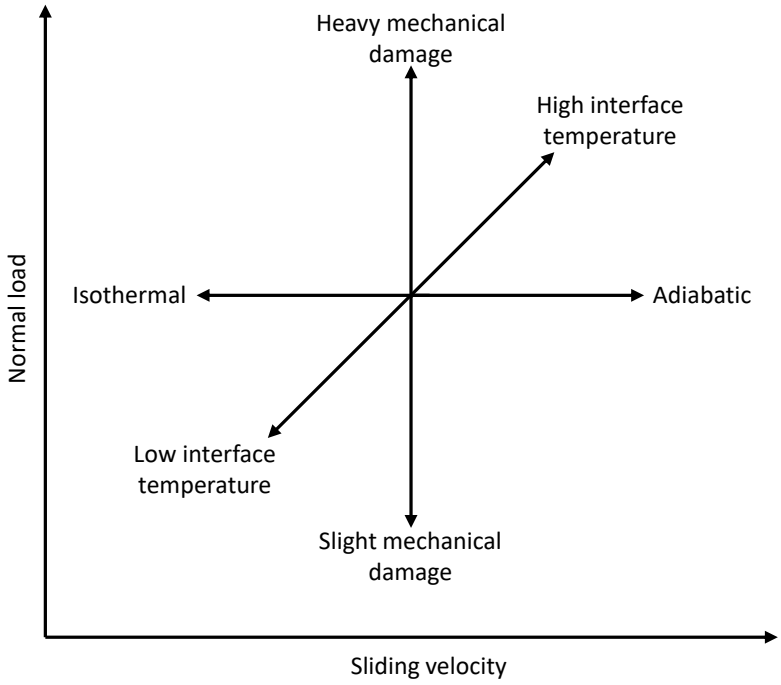

Figure 2.9 Schematic of how sliding velocity and normal load influence wear [67].

- *Types of Wear*

The friction that is generated between the sliding surfaces will result in heat being produced. This heat buildup can be significant, especially at higher sliding speeds, and can influence the wear mechanisms. This heat is mainly removed from the asperities (actual contact areas of the surfaces) and can result in a rapid rise in temperature [66]. This localized heating causes thermal expansion, and a small section of the material elevates and is known as a 'thermal mound'. Since most conditions are difficult to measure during the experiment the worn surface can only be analyzed by the wear particles and worn surface itself [66]. Wear is a complicated form of damage and different conditions produce vastly different types of worn surface. The standard wear experimental set up, regardless of the type of wear mechanism, usually involves a stationary substrate with a moving counter surface. A brief outline of the common types of wear is provided in the following sections.

  - ***Abrasive Wear***

Abrasion is when hard particles are forced into and moved along a surface, which then roughen or scratch the surface [66]. During abrasive wear, material is removed from the surface due to the hard particles moving across under a force. These particles can either be loose or can come from the other surface which is in contact with the abraded surface [68]. Abrasive wear testing follows the ASTM Standard G65, which involves using a stream of dry quartz sand passing between a rotating rubber wheel and the specimen under a specified normal force [68]. Abrasive wear can be categorized by four types of mechanisms: cutting, fracture, fatigue by repeated ploughing, and grain pull-out [66]. Cutting occurs when the particle is harder than the surface. This can be determined easily with microscopy,

especially scanning electron microscopy (SEM). This cutting mechanism is similar to the orthogonal cutting model, but on a much smaller scale, and is referred to as micro-cutting. The shape of the particle will influence the type of cutting mechanism; rough, angular debris particles will have more cutting edges than ones that are rounded [66]. Below the cut surface, significant plastic deformation occurs, leading to strain hardening. Fracture is common in ceramics which are more brittle and lead to cracking. When the surface is ductile, with constant abrasion from rounded particles, cutting is unlikely to occur, rather the surface is deformed which results in fatigue. Grain pull-out is typically associated with ceramics due to the weak boundary between the grains. The removed grain then become pieces of wear debris, and can also cause further damage, being the 'third-body' in a three-body wear scenario (Figure 2.10). Dry sliding is when there is no lubricant or moisture introduced to the contact area. Higher loads will increase the wear rate [69]. There are two modes of abrasive wear, as demonstrated in Figure 2.10. These modes of abrasion wear are reviewed in more detail in prior studies [66,70]. Two-body wear is presented in Figure 2.10(a), in which hard particles are rigidly held and pass over the surface with a more consistent wear pattern on the worn surface. While three-body wear is illustrated in Figure 2.10(b), in which the particles are free to move and slide over the surface, resulting in a more random wear pattern on the worn surface.

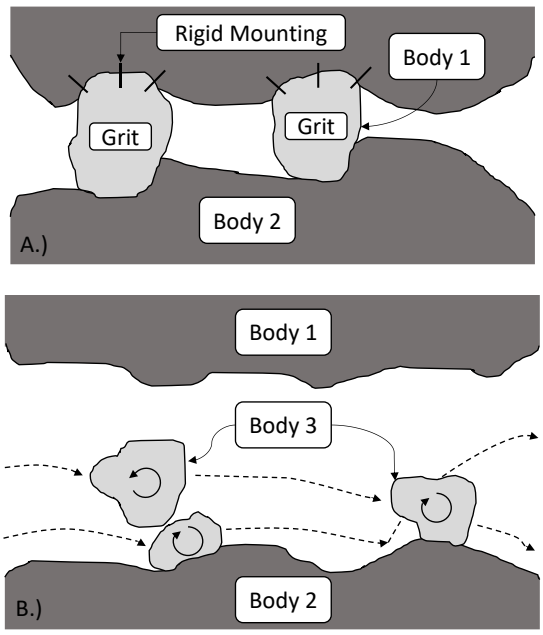

Figure 2.10 Schematic representations of: (a) Two-body, and (b) three-body abrasive wear mechanisms [66].

Abrasive wear resistance is generally recognized as being more common in hard materials but this is not always the case. In steels, the abrasion resistance is determined by the relative proportions of martensite, austenite, bainite, pearlite, ferrite, and carbides [66]. Austenite and bainite have better wear resistance than martensite, when dealing with hard particles, because they have greater ductility and toughness which helps resist micro cutting and fracture. Alloy carbides significantly improve the abrasion resistance of steels and result in their high hardness [66]. There also is evidence that the wear resistance exhibits a linear dependence with the hardness [71]. For steels, it appears that in an abrasive setting, the wear rate is determined by the hardness and toughness of the material [72]. Hard coatings are an attractive choice because they use a small amount of material in a thin surface layer, allowing for more expensive materials to be used. Desired wear properties in sliding wear are not the same as in erosion wear [73]. This is due to:

- In sliding wear, the hard carbides provide a hard-wearing surface that can support the deformation. Whereas, in erosion, there are constant impacts that can damage the unreinforced matrix. As the matrix is damaged further, it has a harder time retaining the reinforcing particles.
- In sliding wear, ceramic materials cause a reduction in the coefficient of friction and help with the surface and further reduce material loss. No such reduction is available for erosion wear.

In softer materials, micro ploughing was observed versus micro cutting [74]. Samples can also work harden, leading to better wear resistance but also stress induced phase changes likely occur from the retained austenite transforming to martensite [74].

- ***Erosion Wear***

Erosion wear is similar to abrasion but the particles impact the surface [66]. ASTM Standard G76 is used for erosion testing, which 34tilizes hard particles suspended in a liquid that impacts the surface of the studied material. This type of wear is commonly seen in gas turbine blades when an aircraft flies through dust or in slurry pump systems on the impeller [66]. Erosion wear encompasses several damage mechanisms, which include: abrasion at low impact angles, surface fatigue during low speed, high impingement angle impact, brittle fracture or multiple plastic deformations during medium speed, large impingement angle impact, surface melting at high impact speeds, and macroscopic erosion with secondary effects [66]. A low angle impact favors a damage mechanism similar to abrasion, because the particle tends to go across the surface at a shallow impingement angle. High angle impacts are more typical of erosion. The speed of the

particle is a critical parameter to consider because if the impact speeds are low, it favors surface fatigue. If the speed of the particle is high, brittle fracture or fragmentation is more common. Depending on whether the evaluated material is ductile or brittle, the impingement angle has a crucial role in the wear rate. Figure 2.11 is a simple schematic that shows the relationship between the impingement angle and wear rate of ductile and brittle material. An impingement angle of zero is negligible because the particle does not impact the surface. At relatively small impingement angles severe wear can occur if the particle is hard and the surface is soft. For brittle materials, severe wear by fragmentation can occur, reaching a maximum at ~90°.

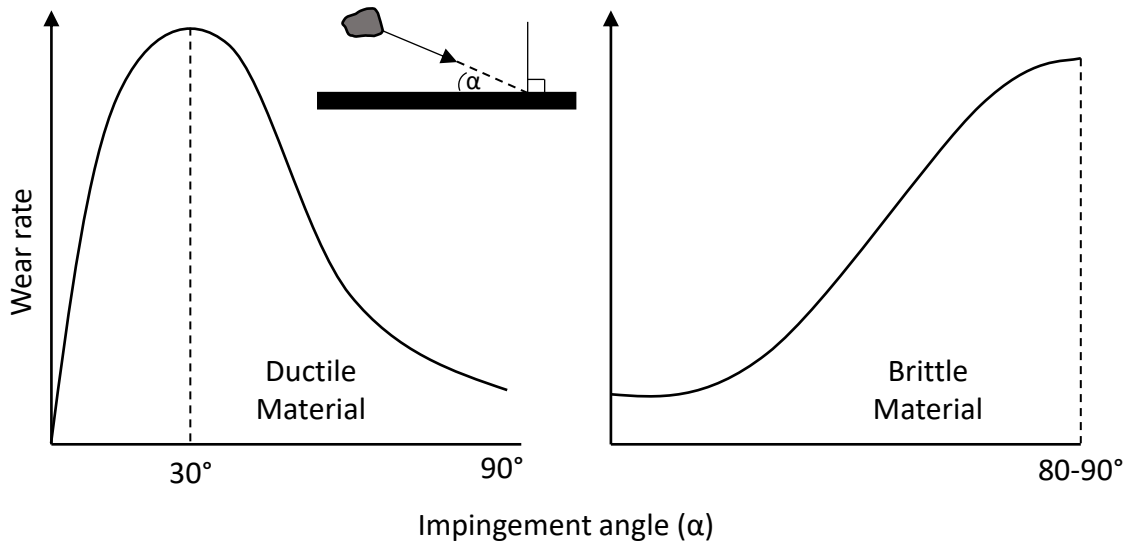

Figure 2.11 Schematic of the wear rate as a function of the impingement angle for both ductile and brittle materials

The size of the particle also determines the erosive wear rate. For steels, if the particle is small it will experience a higher wear rate at lower impingement angles. If the particle is larger, steel has better erosion resistance across all impingement angles [66]. Another

factor to consider about erosion wear is the particle flux. As the particle flux increases, the wear rate increases until a limit is reached because the particles begin to interact with each other [66]. Erosion wear can be influenced by temperature, once it reaches 600°C, which is the softening point of most steels. The best erosion wear resistance for steels differs from abrasion resistance and requires good toughness and hardness. If the steel is experiencing erosion, ductility should be prioritized over the hardness [66].

- ***Adhesive Wear***

Adhesive wear can be very severe and is typically characterized by high wear rates and a large unstable coefficient of friction [66]. This is common when a material of higher hardness encounters a softer material and material transfer occurs. Like materials have a greater tendency to have adhesion. Asperities with sharp slope angles will fail in competition with asperities having small slope angles [66]. The material properties will influence how the asperity breaks. In brittle materials, the break is clean with little deformation and produces fewer wear particles compared to ductile materials [66]. When the material transfers, it is usually smaller than the wear debris but has been significantly work hardened, resulting in ploughing that is inefficient, ultimately leading to cracking from the high tensile stresses [66]. This can be seen by the appearance of coarse grooves on the worn surface of the softer material. To help reduce adhesion, a lubricant may be added. Oxide tribofilms, which readily form on ferrous materials, act as a lubricant and will reform if they are removed. When the oxide layer is damaged, adhesion can occur. When selecting materials for sliding applications, like materials should be avoided. If a poor combination of materials is selected, there is a chance they can become seized together [66].

- ***Oxidative Wear***

This type of wear occurs between dry, unlubricated metals in the presence of oxygen. This usually occurs at elevated temperatures but can also happen if the load and sliding speed are increased, causing the frictional temperature to increase [66]. A general rule is that a thicker oxide film will improve the wear resistance at low temperatures. If the temperature reaches around 500°C, the iron oxide film can reach a thickness between 1 to 10 μm. This type of wear is seen in hot rolling, where the temperatures are elevated [66]. At low temperatures, the oxide is beneficial in reducing adhesive wear, with the oxide layer being supported by the strain-hardened substrate. However, at elevated temperatures, from the environment or frictional heat, the thick oxide film becomes a major contributor to wear [66]. When sliding speeds are above 1 m/s, the oxide film is readily destroyed with a rapid increase in wear and friction. Then the oxide film rebuilds until it reaches a critical thickness where it can no longer support the forces and fails again [66]. Fatigue can also remove the oxide film. When the sliding speeds are below 1 m/s, the slow speeds do not generate enough heat to form an oxide layer. As the temperature increases and there are high stresses, oxidative wear increases. The time for the protective oxide layer to form is reduced, instead it leads to more oxidized wear debris that eventually becomes a ‘glaze’. This glaze is a glassy phase and spreads over the worn surface resulting in mild wear. If the contact pressure is very high, the oxide film can fracture, which is known as ‘peeling’ [66] or spalling. Oxidative wear can transition to adhesive wear depending on the wear conditions. When the loads are lower, oxidative wear is favored. When the load increases, it transitions to adhesive wear II the increased loads break the oxide film. FiIally, it reaches another transition where oxide layers are established and supported by the strain hardened

substrate. In the case of stainless steels, the type of oxide that forms can be more beneficial, which includes Fe_3O_4 and FeCrO. However, severe wear can occur with FeO and Cr_2O_3, which are more brittle [66]. At low speeds and ambient temperatures, the predominant oxide is Fe_2O_3, at intermediate temperatures and speeds Fe_3O_4 is dominant, while at high speeds and temperatures the dominant oxide is FeO [67]. Wear at elevated temperatures becomes more complicated than at room temperature because of thermal softening of materials and oxidation [66,75]. In mild wear, the wear surface is covered by oxide layers generated by the rubbing surfaces, resulting in nanosized wear track debris. During severe wear conditions, the contact is more established and plastic deformation of the surface occurs with debris ranging up to several hundred micrometers [76].

- ***Fretting and Fatigue Wear***

Fretting wear is when there is reciprocating sliding between contacting surfaces, sustained for a long period, with a very small amplitude of sliding. Even if the sliding distance is not that great, a significant drop in fatigue can occur along with severe wear [66]. Since the sliding distance is very small, the wear debris generated stays between the surfaces and can accelerate the wear degradation by abrasion. Like most wear mechanisms, an increase in the hardness does not mean an improved fretting resistance. Rather, the amount of austenite or martensite in the steel has a greater impact on the wear resistance. This type of wear is typically seen where there are vibrations present such as rail wheels or components held together with rivets [66].

Even if the surfaces are well lubricated, wear can still occur. This is caused by repeated contact of the asperities on the surface leading to wear debris being generated from fatigue cracks. As the surface undergoes repeated contact, it begins to become deformed and strain

hardens [66]. As time passes, a weak point in the surface cracks and the crack propagates down into the material. Once this crack connects back to the surface, it will generate wear debris. Iron has a high stacking fault energy, which results in readily forming dislocation cells. The interfaces of these cells are elongated in the direction of sliding and are of high energy. These regions are more likely to exhibit crack formation [66]. Fatigue wear is commonly seen in rolling, where the local contact stresses are high, concentrated, and repetitive. To improve fatigue wear, inclusions (unmelted particles or gas porosity) should be avoided. Fatigue wear can be identified by spalls, which are shallow pits with cracking or flaking at the edges. If there are inclusions in the subsurface, cracks can propagate from these particles. Steels have good fatigue wear resistance but require constant lubrication [66].

- *Microstructural Influences*

Steel has many alloying elements that have different impacts on the microstructure and mechanical properties. Additions of Co, Mo, and Cr are added to help reduce friction, wear and corrosion [77–79]. Carbides have the added benefit of having higher hardness than the matrix but they can inhibit the plastic flow and crack, and then become part of the wear debris [80]. The type of carbide present in the microstructure also provides different wear resistance. For fine abrasive wear, M_6C carbides have better resistance than M_2C. The opposite is true for coarse abrasive wear. The MC carbide has the best wear resistance properties in abrasive conditions [81]. There is conflicting information if the grain size has an impact on wear resistance or if it even has an effect [82]. A smaller grain size leads to less fragmentation which can lead to three-body abrasion. Furthermore, an increase in the hardness, according to the Hall-Petch effect, may have an influence. Wrought steel alloys

have been extensively studied under varying wear conditions, and applying heat treatments can have a positive impact upon wear resistance. When the steel undergoes an austenitisation and quenching process, martensite is produced, leading to a very hard but brittle phase. Martensite has very high wear resistance [67]. After tempering, some of the hardness is lost but the toughness increases, meaning the wear resistance could be improved [83]. Due to the cyclic nature of DED and other AM processes, the quenching effect might be interrupted by a temperature between the martensite start temperature and the martensite finish temperature. This is known as the 'quench and partition' heat treatment [84,85]. This heat treatment, depending on the alloying, will form a microstructure of tempered martensite, bainite, ferrite, pearlite, and retained austenite, leading to excellent wear resistance [86]. Requirements for wear resistance in ferrous alloys are a fine distribution of carbides with fine martensite and retained austenite [87].

- *Wear measurements*

There are several tribological characterization systems that are usually a one-of-a-kind piece of equipment that is constructed in the lab or purchased. They are usually capable of changing the time, load, temperature, environment, and speed of the test. The most common sliding apparatuses include [67,70]:

  - **Pin-on-disc**: in this set up, a pin is held stationary, with a face loading and a disc rotates. The geometry of the pin can change from a non-rotating ball to a flat cylinder. For AM experiments, the disc surface can be directly cladded using the studied material or pins can be directly generated using DED. This test is arguably the most common and follows the ASTM Standard G99.

- **Pin-on-flat**: this is a variation of the pin-on-disc but uses reciprocating motion. The substrate can remain stationary while the pin moves or vice versa. The pin geometry can also change. Fretting wear can also be conducted using this set up. This test follows ASTM Standard G133 for ball on flat.
- **Pin-on-cylinder**: another variation to the pin-on-disc, except the loading on the pin is perpendicular to the axis of rotation.
- **Scratch**: this test uses a diamond indenter to perform a linear scratch on the test material and follows the ASTM Standard G171. Examples of tests can either be a constant load or an increasing load.

Abrasion testing can be set up to do either two-body or three-body testing. For a two-body test, the particle is attached to the moving material. For a three-body test, abrasive particles are introduced into the interface. A list of common testing arrangements includes [67]:

- **Abrasive Belt**: This uses a moving abrasive belt that runs horizontally while the specimen moves transversely. This would be an example of a two-body test, because the particles are rigidly mounted. The sample can also be rotated during the test. These does not appear to be an ASTM standard for this method.
- **Dry Sand Test**: This set up involves loading the sample against a rotating rubber wheel, with the load applied horizontally across the diameter of the wheel while sand particles are fed between the specimen and wheel using gravity. This is a three-body test because the particles can freely move between the two surfaces. This test follows the ASTM standard ASTM G65-16(2021).

- **Wet Sand Test (SAE)**: This test is similar to the previous arrangement, but uses a neoprene wheel with a slurry consisting of deionized water and silica particles from an AFS 50-70 mesh size.

2.5.3 Surface Roughness

As mentioned before, one of the drawbacks of DED is that the manufactured part shows a high surface roughness, which requires post-processing, such as polishing and machining, to accomplish the required surface quality and tolerance. However, there are plenty of causes for high surface roughness in DED processed components. The typical causes of high surface roughness in DED are illustrated as follows:

- **Partially melted powders**: During the DED process, due to heat dissipation from the deposited material to the surroundings, the adjacent powder particles adhere to the high temperature edges of the DED processed part. This results in partial melting and solidification of powder particles along the edges of the sample build [88].
- **Surface pores:** The high scanning speeds and low liquid front rates (i.e. surface tension) in the DED process leads to low densification of the parts. That leads to shrinking and crumpling during the molten pool shrinkage/solidification, which results in the formation of pores [89].
- **Stair-casing:** Stair-casing defects occur as a result of the high laser absorptivity of powders, which leads to dross and spatter formation. In addition, it has been observed that the use of higher layer thickness promotes staircase defects. It is also

known as the stair-stepping effect. It was reported that it is usually found in the Lower layers of DED manufactured parts [90].

Surface roughness significantly influences the geometric and dimensional tolerances of the DED manufactured parts which, in turn, significantly impacts their mechanical properties, especially fatigue resistance. For example, it was reported that the fatigue strength could be decreased by 20-25%, at surface roughness of 200 μm, depending on the AM process [91]. Bayoumi and Abdellatif [92] stated that the surface roughness of DED processed components impacts endurance fatigue limit, fatigue initiation life, and final separation life. As higher surface roughness leads to a higher probability for lower fatigue life and an increased likelihood for crack initiation. In addition, it was found that AM parts have ~60% lower fatigue life in comparison to conventionally manufactured parts. Surface roughness also impacts other mechanical properties, such as tensile strength [93], surface hardness [94], and corrosion strength [95]. Furthermore, surface irregularities result in poor dimensional accuracy [96].

In order to mitigate surface irregularities in DED processed parts, an increase in energy density (i.e., high laser power and low scanning speed) could decrease surface roughness, as long as the heat input is not too high to prevent non-uniform solidification rate and or contribute to high thermal stresses. The use of finer powder particles and a smaller layer thickness could also help to alleviate surface irregularities. Finally, post-processing operations such as machining and chemical/electrochemical polishing can be used.

2.5.4 Residual Stresses

Due to the complex nature of the heating/cooling cycles in DED, the propagation of residual stresses are inevitable in the DED processed parts [97]. This can be explained in relation to the cooling rates in the DED technique, which could be as fast as 10^2-10^4 K/s. In addition, this can result in complicated phase transformations and microstructural changes. The generated residual stresses are profoundly non-uniform along all directions (scanning, in-depth, and transverse directions) [98]. Furthermore, the evolution of distortion and residual stresses in each sample is governed by key physical factors that are largely the same as those observed in fusion welding, such as process parameters, material properties, etc. Finally, residual stresses are categorised into three classifications based on the size of their effect, from macro-stresses (Type I) to atomic-scale stresses (Type III) [99].

Residual stresses play a vital role in determining the final characteristics of the DED processed parts. As residual stresses impact distortion [100], residual-stress driven phase transformations [101], cracking [25], geometric tolerance loss [102], early crack propagation under cyclic loading [103], and delamination at the part/substrate interface, which in turn leads to premature failure of structural components [104].

Measuring residual stresses involves indicating certain measurable quantities, depending on measurement method employed, such as distortion/displacement, sound, or lattice spacing. There are two types of residual stresses measurement techniques, destructive and non-destructive. In destructive techniques, the theory is based on mechanical stress relaxation using hole drilling, ring-core drilling, or serial sectioning [105]. While, in non-destructive methods, residual stresses could be measured by measuring speed of sound

through the specimen [106], Barkhausen noise (the emitted sound by a specimen of ferromagnetic material subjected to an external magnetic field) [107], or measuring lattice spacing using diffraction techniques [108]. Finally, computational models are often utilised to predict the evolution of distortion and stresses as a function of time, in which the equilibrium equations for thermal stresses are solved numerically to predict residual stresses and displacement [102].

There are several means to mitigate residual stresses. Firstly, substrate and/or build chamber preheating is one of the most popular approaches to reduce residual stresses in the fabricated part. As preheating the substrate leads to a reduction in the overall thermal gradients during the DED process which, in turn, decreases the evolution of residual stress. The impact of substrate preheating on distortion accumulation was examined by Corbin et al. [109]. It was observed that the distortion during printing of the first layer could be reduced by 27.4% when preheating the substrate to 400°C. While Lu et al. [100] combined building chamber heating with substrate preheating to investigate the variation in residual stresses and distortion. A reduction in both distortion and residual stresses by up to 90.1% and 80.2%, respectively, were observed after substrate preheating and print chamber heating. The aforementioned studies proved that residual stresses are minimized by substrate and/or build chamber preheating. However, these studies also showed that they could not be completely eliminated by preheating. While additional post-processing is still required.

DED process parameters also influence the evolution of residual stresses in the deposited part. For instance, scanning in smaller islands, shorter deposition length, use of a spiralling-in depositing strategy, thin layer thickness (below the melt pool depth), higher scanning

speeds, and overlap hatch spacing were all noticed to be beneficial for mitigating distortion and residual stresses [110]. In addition, Denlinger et al. [111] studied the impact of interlayer dwell time on residual stresses for both Ti-6Al-4V and IN 625 alloys. It was demonstrated that residual stresses could be affected by increasing the dwell time from 0 to 40 seconds, due to the increased time available for cooling during the deposition, which affects the evolution of temperature gradients. It was observed that, increasing the interlayer dwell time to 40 seconds resulted in a reduction in residual stresses from 710 MPa to 566 MPa for IN 625. In contrast, in terms of Ti-6Al-4V, an increase in residual stresses from 98 MPa to 218 MPa was recorded when increasing the dwell time. Such differences in behaviour between both materials may be arising from differences in the phase transformations occurring during the DED process.

Another way to decrease the residual stresses is to apply a post-print treatment to the surface of the DED part. One approach for surface treatment is magnetic field-assisted finishing which was reported to decrease residual stresses on the surface of the manufactured part from 200 MPa to 70 MPa, in addition to producing a compression stress instead of a tensile stress on the surface of the deposited part [112]. In addition, intermediate rolling of the printed parts, laser shock peening, or mechanical tensioning of the substrate were all explored and found to be good solutions for reducing part distortion and residual stresses [102]. All of the aforementioned post-processing surface treatments were observed to mitigate residual stresses through the introduction of surface compressive stresses, thereby also improving the fatigue life of the DED processed parts.

2.6 Tool Steels

Tool steels can be described as high carbon or alloy steels. AM of tool steels possesses an immense potential for growth due to being a strong candidate in shaping and working basic materials such as metals, wood and plastics. Tool steels have a lot of distinct characteristics such as high hardness and wear resistance, sufficient strength and toughness for working the materials, and resistance to softening at high-elevated temperatures [113]. However, tool steels must be heat-treated in order to get the desired material properties. In additIon, it is typically required to heat-treat tool steel, multiple times, with a complex treatment schedule, in order to gain the desired toughness and hardness [114]. This section presents an overview of the chemical compositions and heat treatment cycles for common tool steel grades.

2.6.1 Classifications of Tool Steels

The classification system of tool steels established by the American Iron and Steel Institute (AISI), is the most commonly used at the present time. In the AISI system, tool steels are classified based on the quenching method applied, the composition, any special characteristics, and the composition. Table 2.3 lists the different classes of tool steels [113]. The present work focuses upon laser DED of the D2 tool steel grade, which is a high carbon, high chromium cold work tool steel.

Table 2.3 A summary of tool steels classifications [113].

Group	Letter symbol
Water-hardening tool steels	W
Shock- resistant tool steels	S
Cold work tool steels	
Oil hardening	O
Medium alloy air-hardening	A
High carbon, high chromium	D
Hot-work tool steels	**H**
Chromium type	H1 to H19
Tungsten type	H20 to H39
Molybdenum type	H40 to H59
High speed tool steels	
Tungsten	T
Molybdenum type	M
Special purpose tool steels	
Low alloy steels	L
Mold tool steels	P

2.6.2 Cold work (high carbon-high chromium) D-type

Although these steels are quite brittle and do not have a sufficient hardness at high speeds, they have high wear resistance and exceptional resistance to deformation. As a consequence of this, they are strong candidates for cold work die steels [113]. The chemical composition of D2 tool steel is presented in Table 2.4.

Table 2.4. The chemical composition of AISI D2 tool steel [113].

Material Type	Composition (wt.%)									
	Fe	**C**	**Si**	**Mn**	**Cr**	**Mo**	**V**	**Co**	**Cu**	**Ni**
AISI D2	**bal.**	1.4-1.6	0.6	0.6	11-13	0.7-1.2	1.1	1.0	0.25	0.3

From Table 2.4, it can be concluded that the reason for having excellent wear resistance is that the carbon and chromium contents are high in the D2 grade, 1.4-1.6 wt.% and 11-13 wt.%, respectively. Furthermore, the high chromium composition in D2 type steel results in good resistance to corrosion, such as staining when polished or hardened, besides high resistance to oxidation at high temperatures [113]. Additionally, the small amount of vanadium (1.1 wt.%) found in the D2 grade refines the grain size. However, it results in a decrease in hardenability. Furthermore, the addition of small amounts of molybdenum enhances toughness and hardenability [114].

2.6.3 Heat Treatment of Wrought Tool Steels and Phases

There are common phases that are formed during and after heat-treating tool steels, including martensite, tempered martensite, ferrite, cementite, retained austenite, and carbides. A general description of the formation of each phase is demonstrated below. Those phases are present in both wrought and AM processed tool steels. However, wrought tool steel has a more homogenous microstructure than an AM manufactured tool steel. This arises because of the severe heating/cooling cycles experienced in laser or electron beam based AM process, which is affected by the number of deposited layers and the chosen system parameters.

For more explanation, as illustrated in Figure 2.12, after heating steel to the austenitising temperature, austenite is formed. The phase transformations that then occur while cooling

steel composition from the austenitizing step can be explained by the time-temperature-transformation (TTT) diagram. From the TTT diagram, it is illustrated that there are various phases to which austenite transforms. Such transformation is profoundly dependent on the cooling rate that is used, which is a function of the undercooling temperature and the time needed to reach the cooling temperature. From Figure 2.12, it can be observed that austenite can be transformed to (coarse or fine) pearlite, (upper and lower) bainite, martensite, or a mixture of these phases, depending on the cooling rate and undercooling temperature step that were used [115].

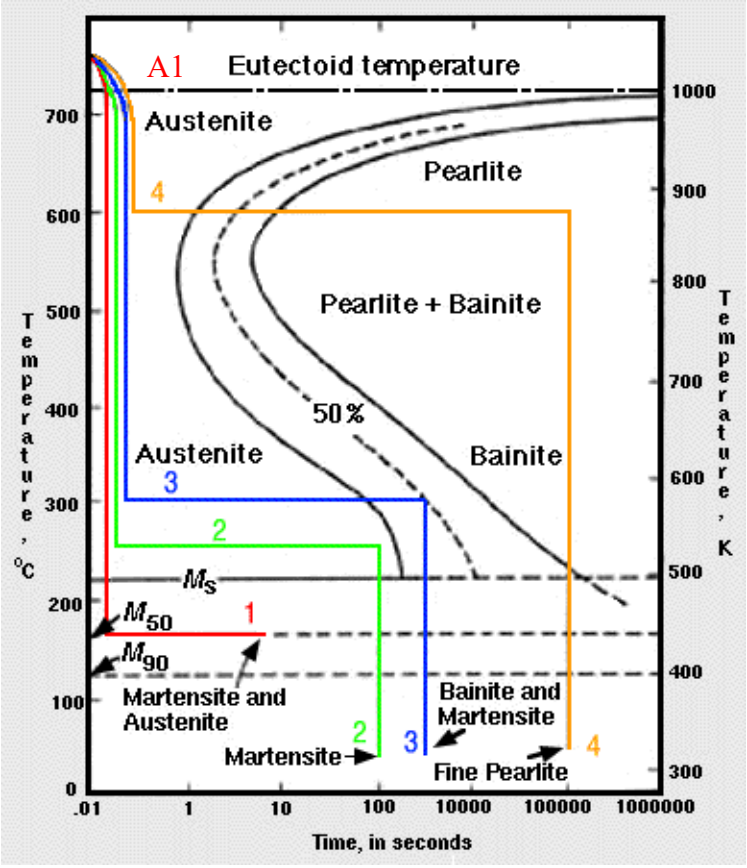

Figure 2.12 Schematic TTT diagram showing relative phase transformations that occur during cooling of eutectoid steel after the austenitising step (i.e., heating above the eutectoid temperature) [115].

- *Formation of Pearlite*

Pearlite is formed from the transformation from austenite (γ) to ferrite (α) and cementite (Fe_3C), while cooling at a temperature roughly higher than 525°C, following:

$$\gamma \rightarrow \alpha + Fe_3C$$

This reaction occurs in the same way as a eutectic transformation upon cooling. However, this transformation is solid to solid, not liquid to solid. In terms of the microstructure of the formed pearlite, it consists of sheets, or lamellae, of cementite embedded in ferrite. As shown in Figure 2.13, the formation of cementite and ferrite is directly in contact with austenite, as the grain boundaries are the location on which nucleation of pearlite starts. Subsequently, pearlite nodules grow at a constant rate into the neighboring austenite grains.

Regarding the effects of undercooling on the formation of pearlite, it was found that, at higher undercooling below the eutectoid temperature (A1), presented in Figure 2.12, site saturation happens due to the high nucleation rate at such temperatures. As a consequence, the pearlite nodules cover all the prior austenite grain boundaries. While, in terms of low undercooling, small nuclei occur. The growth of pearlite nodules as hemispheres or spheres can happen without any interference between each other [56].

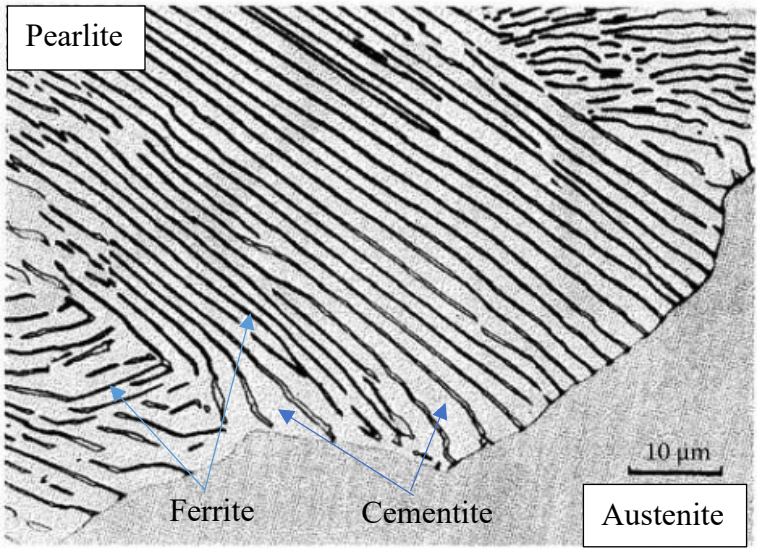

Figure 2.13 Pearlite colony evolving into an austenite grain [56].

- *Bainite Transformation*

The bainite is formed by cooling the austenite to large undercooling below A1 (i.e., below the nose of the pearlite transformation curve). Bainite also consists of ferrite and carbide. However, its microstructure is significantly different from pearlite, as the pearlite contains alternating layers of ferrite and cementite whereas the bainite has a plate-like microstructure. Additionally, the temperature, at which bainite forms has a significant impact on the microstructure of the bainite. At higher temperatures, 'upper bainite' forms which look like needles or laths. While, at lower temperatures, bainite changes from laths to plates, which is called 'lower bainite'.

- Upper Bainite

At high temperatures (350°C-550°C), needles or laths of ferrite with precipitates of cementite between the laths forms upper bainite. Figure 2.14 demonstrates schematically the evolution of this microstructure. The growth of ferrite laths occurs in the austenite in

an analogous way to Widmanstatten side-plates. The nucleation of ferrite takes place on an austenite grain boundary, with a Kurdjumov-Sachs orientation relationship with one of the neighboring austenite grains, (e.g., γ_2 in Figure 2.14). Ferrite laths are formed by the rapid growth of the nucleus into the γ_2 grain, with low energy semi-coherent interfaces. That is attributed to the large degree of undercooling. As this process is repeated at various sites along the boundary of the austenite grains, a group of finely spaced needles evolve. An increase in the carbon content of the austenite takes place, which promotes thickening of the ferrite laths. It is worth mentioning that, at lower temperatures, the bainitic laths are narrower [56].

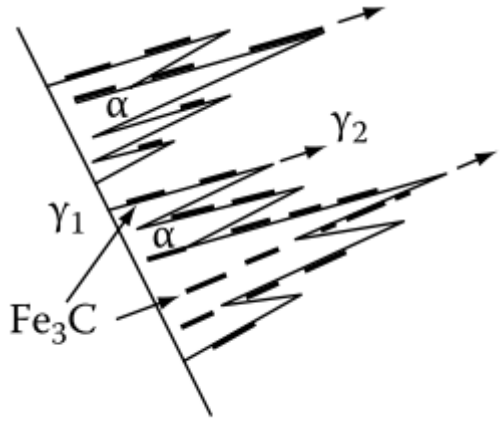

Figure 2.14 Schematic diagram of upper bainite growth [56].

At high temperatures, pearlite and bainite can grow competitively. In such a case, it could be challenging to differentiate between the upper bainite and pearlite colonies. However, both of their crystallographies are different. In the case of bainite, the cementite and ferrite have a specific orientation relationship to the austenite grain in which they are growing, whereas the cementite and ferrite in pearlite do not have a specific orientation relationship to the austenite grain in which they are growing [56].

- Lower Bainite

At adequately low temperatures, variation in the microstructure of bainite takes place, where laths convert into plates and a finer carbide dispersion is formed, similar to the case of tempered martensite. The carbon content affects the temperature at which the transition from austenite to lower bainite occurs, in a somewhat complicated manner, as illustrated in Table 2.5 [56].

Table 2.5. Effect of carbon content on lower bainite transition temperature

Carbon content	**Lower bainite temperature**
Less than 0.5 wt.%C	Increase by increasing carbon
0.5-0.7 wt.%C	Decreases by increasing carbon content
More than 0.7 wt.%C	Constant 350°C

Relatively slow diffusion of carbon happens at the temperatures at which lower bainite develops. The carbides can therefore be either metastable transition carbides (e.g., s-carbide) or cementite. Such carbides are aligned at roughly analogous angles to the plane of the ferrite plane, as demonstrated in Figure 2.15 [56].

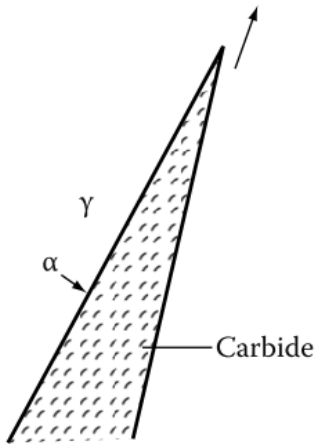

Figure 2.15 A possible growth mechanism, α/β interface advances as fast as carbides precipitate at interface thereby removing the excess carbon in front of the α [56].

- *Formation of Martensite*

At very high cooling rates and a moderately high martensite start temperature, M_S, austenite transforms into martensite. The martensitic transformation is an athermal, diffusionless transformation.

  - Martensite Nucleation

The speed, at which a single plate of martensite can grow to its full size approaches the speed of sound. Therefore, it is extremely challenging to experimentally study the transformation from austenite into martensite. In consequence, many theories were developed in order to predict the nucleation of martensite.

For instance, it was reported that there is an energy barrier that should be overcome to start nucleation. This energy barrier can be estimated using Equation 2.5 [56].

$$\Delta G^* = \frac{512}{3} \cdot \frac{{\gamma_e}^3}{(\Delta G_V)^4} \cdot (s/2)^4 \mu^2 \pi \ \ joules/nucleus$$

Equation 2.5 The energy barrier calculation for martensite nucleation [56].

where ΔG^*refers to the critical free energy barrier, γ_e is the interfacial free energy, ΔG_V represents the volume free energy release, and s is the strain. From Equation 2.5, it was concluded that the energy barrier is sensitive to the values selected for γ, ΔG_V and s.

The presence of dislocations plays a vital role in the formation of martensite, because the transformation from face-centered Cubic (FCC) to body-centered tetragonal (BCT) leads to distortion in the crystal structure. Zener et al. [116] reported that it is required that some atoms jump forward, as illustrated in Figure 2.16. However, it was also found that the new, resulting crystal structure is not fully body-centered cubic (BCC), which is known as Bain

distortion, where an intermediate 3 tetragonal lattice is constructed from the FCC one by choosing the ½ [110]γ, ½ [110]γ and [001]γ directions as new reference frame and by expanding the two first vectors by 12.6%, and reducing the third one by 20.3%, in order to obtain the BCC lattice with appropriate lattice parameters [56].

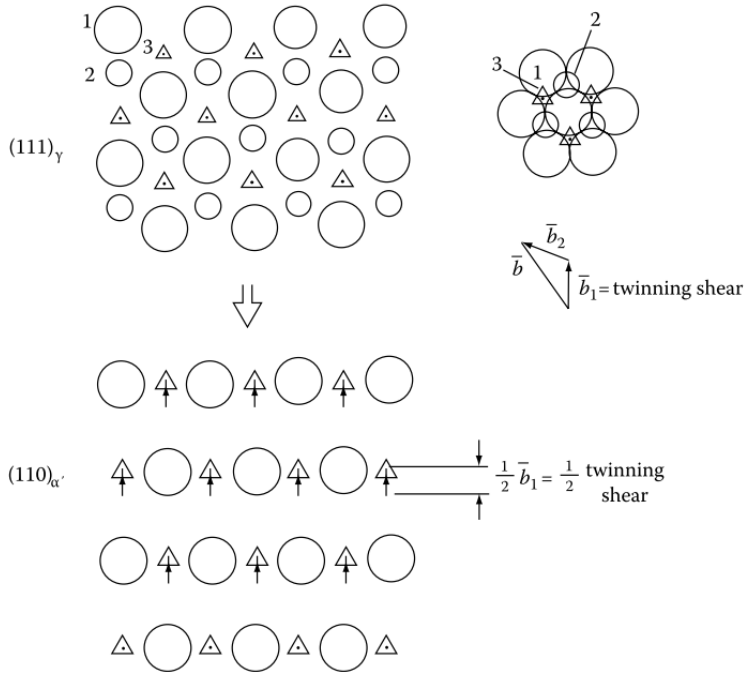

Figure 2.16 Zener's model of the generation of two-atom-thick martensite by a half-twinning [56].

- *Retained Austenite*

Retained austenite is an equilibrium phase that has an FCC crystal structure [113]. The amount of austenite retained after quenching steel is a function of the carbon and alloying contents, with composition influencing the *M*s temperature [117]. Higher alloyed austenite will lower the *M*s temperature resulting in greater concentrations of austenite because of incomplete formation of martensite. The concentration of austenite is increased as the austenitising temperature and time are increased to allow for greater enrichment from the

alloying additions [43]. Retained austenite is unstable under the A1 temperature (725°C) and will decompose into tempered martensite during the tempering process [65].

- *Cooling rate effects*

In terms of the influence of cooling rates on the microstructure evolution in steels, it was found that the equiaxed morphology of ferrite is formed at a slow cooling rate at small undercooling. While the higher cooling rates, at lower temperatures, lead to the development of Widmanstatten ferrite needles.

Another case is that, when the cooling rate is fast enough to avoid the transformation of austenite to ferrite near equilibrium, but sufficiently slow to prevent the formation of martensite (e.g., quenching into brine), the austenite transforms massively to ferrite. The microstructure of the massive ferrite demonstrates irregular grain α/α boundaries, as shown in Figure 2.17. The influence of cooling rate on the transformation temperature of pure iron is illustrated in Figure 2.18 [56].

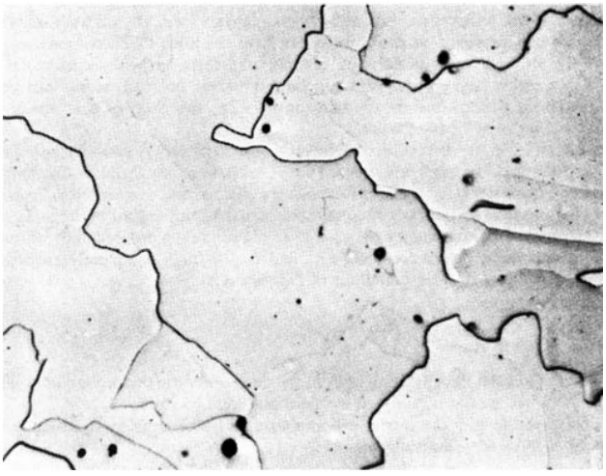

Figure 2.17 Massive ferrite in a Fe–0.002 wt% C steel quenched into iced brine from 1,000°C [56].

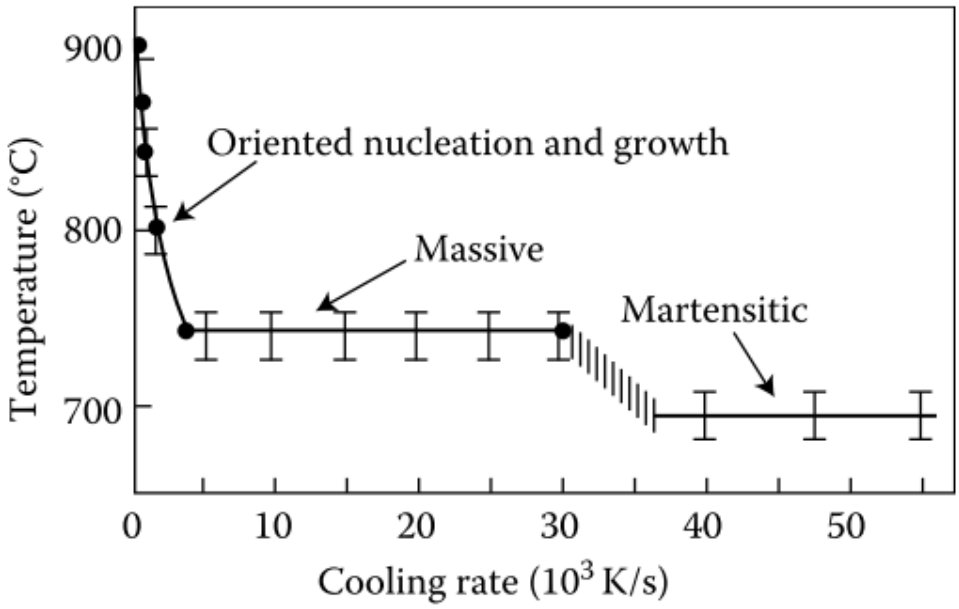

Figure 2.18 The influence of cooling rate on the transformation temperature of pure iron [56].

2.6.4 Hardenability

The enhancement of hardenability is the main purpose of the addition of alloying elements to steels. This can be achieved by increasing the required time for the decomposition of austenite into ferrite and pearlite which, in turn, leads to the production of fully martensitic structures at slower cooling rates. The reduction in the austenite decomposition could be accomplished by decreasing either the nucleation rate or growth rate of ferrite, pearlite, or bainite.

The rate at which pearlite forms at the nose of the C-shaped curve in the TTT diagram (shown previously in Figure 2.12) is the primary factor limiting hardenability. Therefore, there are two different types of elements that affect pearlite growth. The first type are the austenite stabilizers, such as Ni, Mn, Cu, etc., which suppress the A1 temperature. The other type are the ferrite stabilizers (e.g., Mo, Cr, Si), which increase A1 temperature in

order to initiate the formation of ferrite earlier. In addition, all of these elements dissolve substitutionally in austenite and ferrite.

For instance, at equilibrium, any alloy element X will partition between cementite and ferrite. Carbide-forming elements, (e.g., Mo, Cr, Mn) concentrate in the carbides, whereas elements such as Si concentrate in the ferrite. The growth rate of pearlite is dominated by the substitutional diffusion of X because element X is homogeneously distributed within austenite. In terms of the route for substitutional diffusion of elements, it is anticipated that such elements diffuse through γ/cementite and/or γ/α interfaces. Such diffusion is significantly slower than the interstitial diffusion of carbon. Therefore, the pearlite growth rate is reduced.

Regarding ferrite stabilizers, element X will partition even close to the pearlite nose of the TTT curve (large undercooling). For example, Si improves the hardenability by diffusing along the austenite/pearlite interface into the ferrite. In terms of austenite stabilizer (e.g., Ni), pearlite could grow without partitioning, at sufficiently high undercooling. Since the Ni content of the austenite is simply inherited by cementite and ferrite, substitutional diffusion is not needed. Therefore, the growth of pearlite can be as fast as the interstitial diffusion of carbon. However, the non-equilibrium concentration of Ni in the cementite and ferrite results in raising their free energies, which, in turn, reduces the A1 temperature and lowers the total driving force. Thus, the growth rate is kept lower than for the case of binary Fe-C alloys.

When X is a strong carbide-forming element (e.g., Cr or Mo), it was found the rate of growth of pearlite besides the proeutectoid ferrite is decreased; this occurs as a result of the solute drag effect on the moving of γ/α interface. Moreover, the growth rate is not the

only factor that affects the hardenability, as the rate of nucleation of cementite and ferrite could probably be affected by the alloying elements. As the precipitation of X-carbide clusters at the grain boundaries could result in the poisoning of the ferrite nucleation sites [56].

2.6.5 Heat Treatment of D2

D-type tool steel alloys are heat treated uniformly and slowly to the austenitizing temperature in controlled atmosphere furnaces or salt baths in order to be hardened. For D2 tool steels, air is the medium usually used in order to cool the material down from high temperatures, usually in the range of 1,010 to 1,038 °C, after austenitising [114].

In case of austenitising D2 tool steels at too high of a temperature (i.e., over 1,090 °C), it is recommended to temper them with a temperature of more than 450 °C to enhance the material hardness. This is attributed to the fact that more chromium and carbon are dissolved in the austenite after austenitising to 1090 °C, which decreases the *M*s temperature. Therefore, more retained austenite is formed instead of martensite. However, when tempering the material over 500 °C, the retained austenite is transformed into martensite [114].

2.7 Summary

It could be concluded from this chapter that DED is a promising AM technique which is a good candidate for repairing cracked or damaged valuable components. Since AISI D2 tool steel is usually used in fabricating cold forming dies, which are more vulnerable for cracking or damage, in this research, the DED process of D2 tool steel parts on substrates

of the same material was examined, where various process parameters were used to optimise the mechanical and geometrical characteristics of the manufactured parts. Furthermore, the effects of postprocessing heat treatments on the mechanical properties of the DED processed structures was examined and compared the wrought D2 tool steel ones.

CHAPTER 3 EXPERIMENTAL METHODOLOGIES

This chapter demonstrates the experimental methodologies used in this study. This includes the characterisation of raw materials, notably the AISI D2 tool steel powder and wrought material, as well as DED processing conditions and the final properties of the as printed and post heat-treated specimens.

3.1 Raw Material

The feedstock material used in the current DED processing was obtained as a gas atomized powder from TLS Technik Spezialpulver (Bitterfeld-Wolfen, Germany). The powder was provided with a nominal, manufacturer-specified particle size range of 45 to 90 μm. The D2 substrates were provided as plates of dimensions 101.6 x 101.6 x 6.35 mm (4 x 4 x 0.25 inches) from Hudson Tool Steel (Dover, NH, USA). In order to minimise any laser reflection effects in the DED system, the substrates were first sandblasted before DED processing. Furthermore, for comparative purposes, wrought D2 tool steel was supplied as circular rods with a diameter of 19.05 mm (3/4") and a length of 900 mm (36") from Hudson Tool Steel (Dover, NH, USA). These rods were then machined to obtain disc-shaped specimens with a thickness of 10 mm (or 5 mm for wear testing) and the same original diameter (19.05 mm); these samples were then used as a baseline for subsequent tempering heat-treatment evaluation.

3.2 Laser DED Processing

The DED processing stage was conducted using an Optomec MTS-CA system (Albuquerque, NM, USA). This equipment consists of a 1-kW fiber laser with a spot diameter of 0.6 mm, while the feeding system for the powder includes a coaxial powder

nozzle and the option of four discrete powder hoppers. The DED system also has a five-axis machine movement control. In addition to being used as the carrying gas for the injected powder, Ar was also used as the shielding environment within the chamber in order to protect the workpiece from oxidation. The selected DED process parameters are illustrated in Table 3.1. It is worth noting that determination of the evaluated ranges for each of the process parameters was based on the results of previous studies and the equipment design/capabilities.

Table 3.1. A summary of the main DED processing parameters examined.

Parameter	**Value**
Sample dimensions, L x W x H (mm)	25 x 5 x 10
Laser power (W)	400-600
Scanning speed (mm/–in)	400 - 700
Powder feed rate (g/–in)	5.5 - 7.5
Targeted layer thickness (mm)	0.125-0.5
Hatch spacing (mm)	0.381

- *Single Clads, Rectangular and Cubic Specimens*

The laser scanning speed was varied from 400 to 700 mm/min for all experiments. Similarly, powder feed rates were assessed from 5.5 to 7.5 g/min. In addition, 'targeted layer thickness' (i.e., the increment that the laser beam focal point is shifted in the z direction to print the subsequent layer) was also varied from 0.125 to 0.5 mm. The sample identification strategy, noting the full range of parameters studied for the DED processed specimens, will be illustrated in the subsequent chapters. It should be noted that the laser

power and hatch spacing were all kept constant for all of the DED trials, with values of 400 W and 0.381 mm, respectively. A representative example of the actual printed samples is shown in Figure 3.1. As illustrated in Figure 3.1 (a), rectangular geometries with nominal dimensions of 25 x 5 x 10 mm in length, width and height, respectively, were deposited, in addition to twelve initial single track clads. Samples with cubic geometries were also printed, with dimensions of 10 x 10 x 10 mm. Furthermore, specimens with dimensions of 10 x 10 x 5 mm in length, width and height, respectively, were built for analysing the wear resistance of the DED processed components, as illustrated in Figure 3.1 (b).

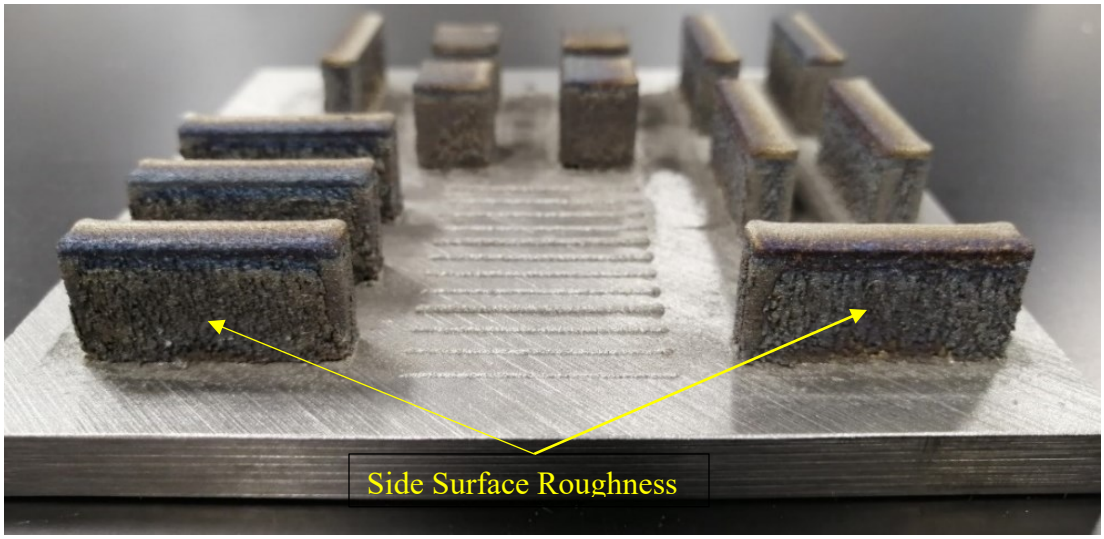

(a)

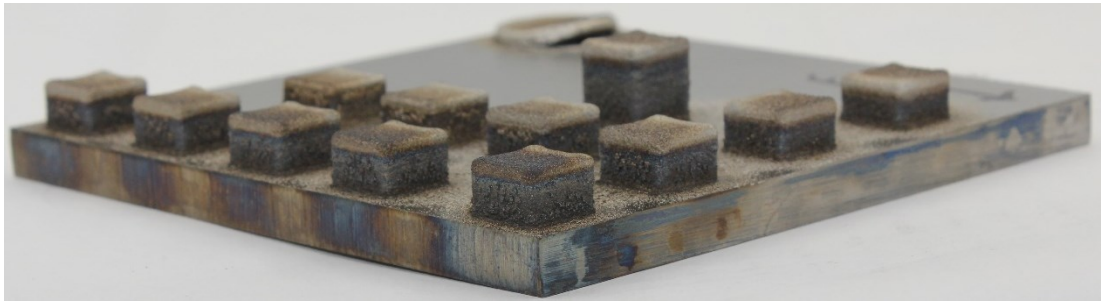

(b)

Figure 3.1. Typical examples of the DED processed D2 tool steel samples.

- *Overhanging Thin Walls*

In addition to the simple geometries already outlined, single track inclined thin walls were also deposited, in order to examine the potential limitations when printing overhanging structures using the DED technique for D2 tool steel. For this segment of the study, two series of thin-walled samples were deposited. The first was fabricated in order to investigate the influence of different process parameters on the discrepancy between the designed angle and the experimentally measured angle, as presented in Figure 3.2(a). For this series, the overhanging thin walls were built with three different angles to the horizontal plane (i.e., 60˚, 70˚, and 80˚). The overhanging walls were 10 x 5 mm in length and height, respectively. As demonstrated in Table 3.1, three different laser powers (400, 500, and 600 W), three powder feed rates (5.5, 6.5, and 7.5 mm/min), and three different laser scanning speeds (400, 600, and 700 mm/min) were used for this portion of the study. The tilt angle for the inclined walls was obtained by shifting the scanning path in the traverse direction (perpendicular to the scanning direction) with a shift value, Δy, calculated using Equation 3.1:

$$\Delta y = \frac{\Delta z}{tan\,\theta_d}$$

Equation 3.1. Calculation of traverse shift value [118].

where Δz is the layer thickness and θ_d represents the design angle (the angle of the DED processed wall with the horizontal plane).

For the second series of inclined samples, the minimum angle to which the overhanging thin wall could be built before failure was investigated. Consequently, three different samples were deposited at three angles (55°, 58°, and 60°), using the following set of DED

parameters (laser power, scanning speed, and powder feed rate of 400 W, 600 mm/min, and 5.5 g/min, respectively); the build plate for these samples is presented in Figure 3.2 (b). It is worth noting that all the DED processed samples in the second batch of inclined walls were deposited using the same physical size as used for the first series.

Furthermore, in order to minimise the error between the actual DED inclined wall sample and the original design angle, based on the process parameters for each specimen, the design angle was modified using the empirical Equation 3.2:

$$\tan\theta_m = \tan\theta_d \cdot \left(0.022\left(\frac{P.f}{v}\right)^4 - 0.341\left(\frac{P.f}{v}\right)^3 + 1.921\left(\frac{P.f}{v}\right)^2 - 4.629\left(\frac{P.f}{v}\right) + 4.932\right)$$

Equation 3.2. Empirical equation for calculating modified design angle.

where, θ_m refers to the modified design angle, θ_d represents the design angle (the exact angle at which the inclined sample needs to be deposited), P is the laser power (in W), f is the powder feed rate (in kg/s), and v is the scanning speed (in m/s); all angles are in degrees. It should be noted that Equation 3.2 was derived following statistical analysis of the results of the first batch of the deposited inclined samples. For the purpose of validating Equation 3.2, eight overhanging thin wall samples were manufactured under a different set of parameters, and two tilt angles of 70° and 60, as shown in Figure 3.2(b). Further details relating to these inclined wall samples are presented in Chapter 5.

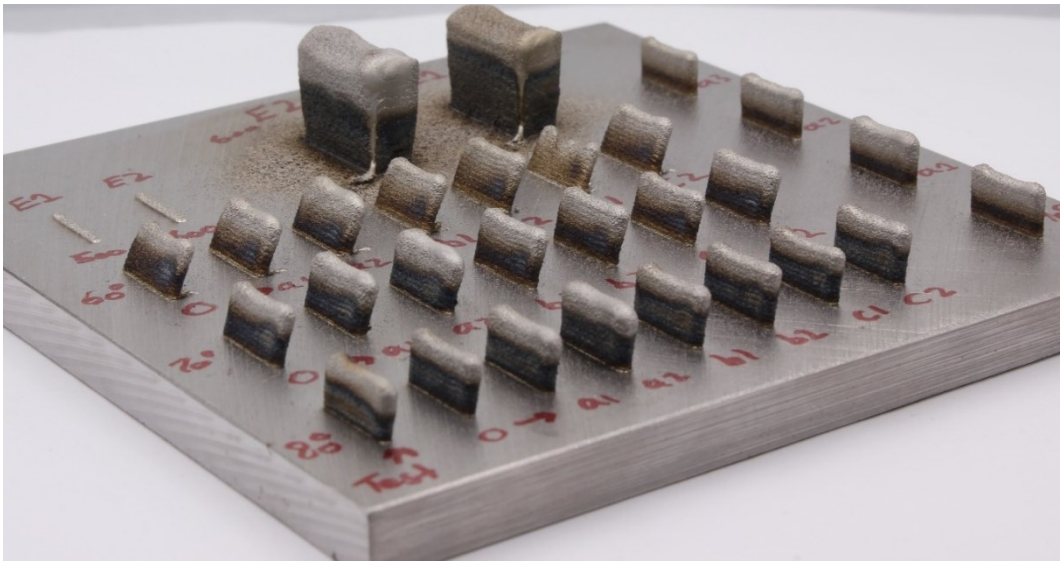

(a)

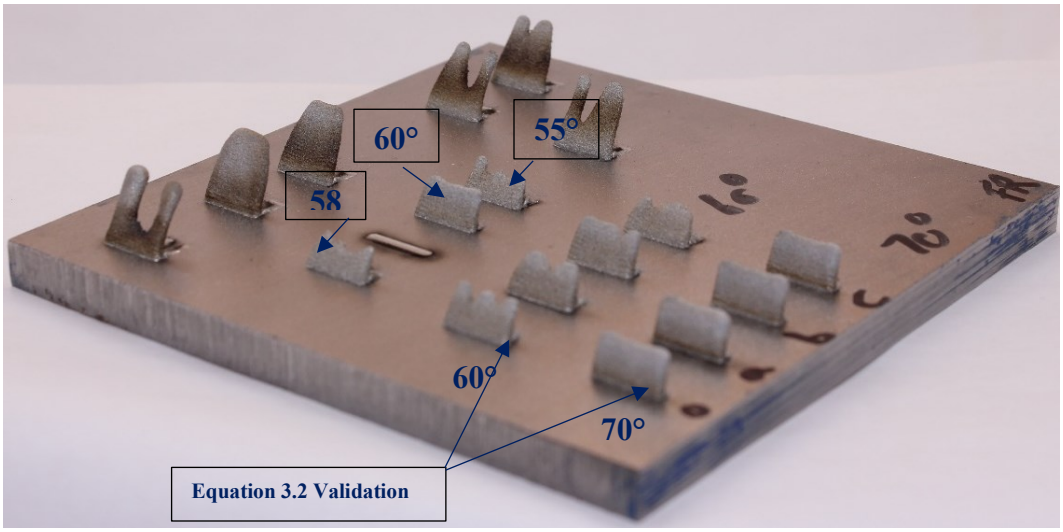

(b)

Figure 3.2. The DED processed plates for inclined thin wall samples: (a) the first series of samples, and (b) the second series of samples.

3.3 Heat-Treatment Cycles

To assess the impact of the use of tempering heat-treatment cycles on hardness for the DED materials, both wrought and DED-processed D2 samples were subjected to a variety of heat-treatments. In this study, all of the heat-treated samples were first austenitized at 1010 °C, for a period of 30 minutes. During heating, the temperature was held at 750 °C (for 30 minutes), as part of the preheating stage, in order to allow the temperature to be uniformly distributed inside the sample before austenitizing. After the austenitizing step, the samples were air-cooled to room temperature.

Subsequently, the first batch of samples (wrought material only) was single-tempered, at various temperatures from 300-700 °C, and held for a total of 120 minutes at temperature. A second batch of the wrought material was initially tempered at the same temperatures as before (i.e., 300-700 °C, again held for 120 minutes at temperature), before then retempering at the same tempering temperature for each sample for an additional 120 minutes. These wrought samples are subsequently referred to as 'double-tempered'. In addition, another heat-treatment scenario was examined in which the material was initially tempered at 400 °C, then retempered at a temperature of 500 °C; this condition was specifically selected for the reasons outlined below. Following these preliminary studies on the wrought material, selected DED-processed samples were then subjected to optimised tempering treatments, based on the data obtained from the initial assessments for the wrought materials. An initial set of DED samples was thus chosen to be heat-treated. Based upon the property analysis of the wrought, heat-treated D2 tool steel (described in Chapter 4), these DED processed samples were subsequently heat-treated under two scenarios. The first involved double tempering at 500 °C (each held for 120 minutes), while

the second involved first tempering at 400˚C before then retempering at 500˚C (again, each held for 120 minutes). The second scenario was chosen by 'combining' the best single-tempering condition for hardness (400˚C) and the best double-tempering scenario for hardness (500˚C) into a two-stage treatment. A schematic representation of a typical heat-treatment schedule, in this instance for a hypothetical double-temper (e.g., both segments at 500 °C), is presented in Figure 3.3.

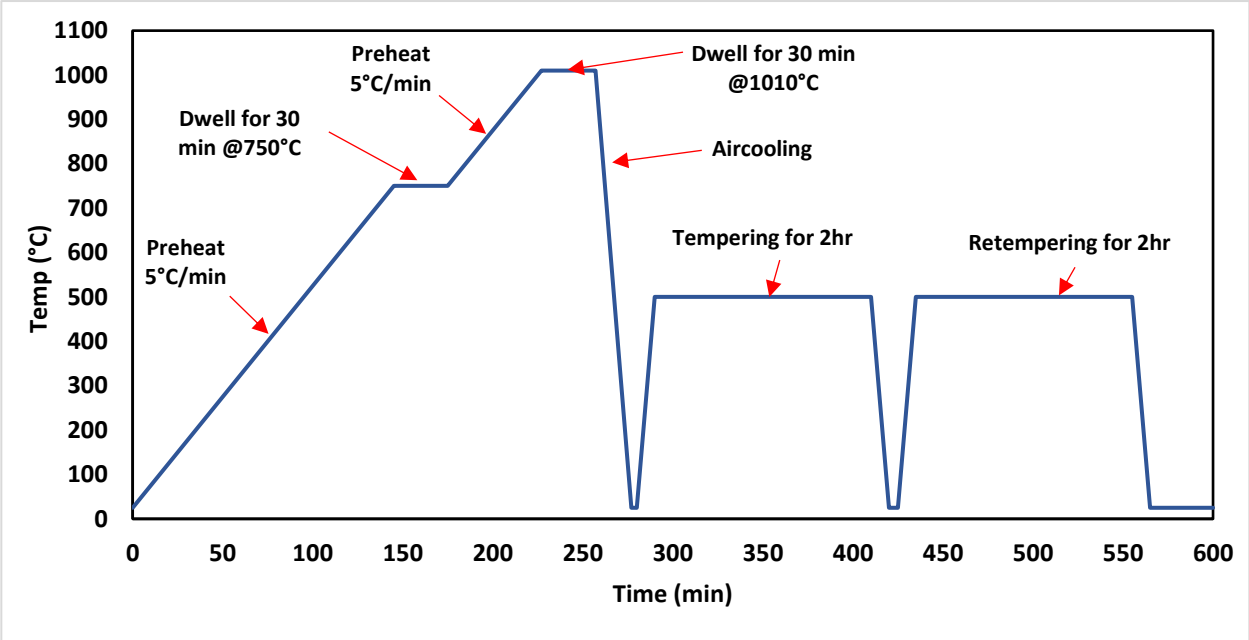

Figure 3.3 Schematic representation of the heat-treatment cycle applied for DED processed samples. In this example, a 'double-temper' is applied, with each temper treatment conducted at 500 °C for two hours.

3.4 Material Characterisation

3.4.1 Characterisation of Raw Materials

- *Chemical Composition*

In order to determine the chemical compositions of the gas atomised feedstock powder and the AISI D2 substrates, inductively coupled plasma optical emission spectroscopy (ICP-OES) analysis was performed. ICP-OES analysis was accomplished using a Varian Vista-PRO system (Varian Inc., Palo Alto, CA, USA), where, before analysis, the material being assessed (either shavings from the substrate plates or the feedstock powder) was subjected to an acid digestion step. The chemical compositions of the AISI D2 feedstock powder and substrates used in this work, which was obtained using ICP-OES analysis, are presented in Table 3.2. In both cases, the compositions were found to be within the normal range expected for D2 tool steel [119].

Table 3.2 AISI D2 tool steel substrates and powder chemical compositions obtained by ICP-OES analysis.

Material Type	**Composition (wt.%)**									
	Fe	**C**	**Si**	**Mn**	**Cr**	**Mo**	**V**	**Co**	**Cu**	**Ni**
AISI D2 Powder	Bal.	1.55	0.41	0.33	11.27	0.64	0.79	0.01	0.01	0.06
AISI D2 Substrate	Bal.	1.50	0.3	0.3	12	0.75	0.9	-	-	-

- *Powder Characteristics*

Powder morphology was examined using a Hitachi S-4700 field emission gun scanning electron microscope (SEM; Hitachi High Technologies Inc., Tokyo, Japan), in order to

examine the microstructures of the D2 raw powder. The SEM operating conditions were set to an accelerating voltage (V_{acc}) of 3 kV and beam current (I_e) of 15 μA, for the purpose of limiting charging artefacts during powder evaluation. A representative SEM image of the feedstock powder is presented in Figure 3.4. It is apparent that the morphology of the powder is generally spherical, as would be anticipated from the gas atomisation process that was used. However, several attached micro-satellites and some irregular-shaped particles can also be observed, which may impact the powder flow response during DED processing.

Figure 3.4. A typical SEM image of the as-received D2 tool steel powder, highlighting a generally spherical morphology with isolated satellite particles.

A Mastersizer 3000 system (Malvern Panalytical, Malvern, UK) was used to assess the particle size distribution of the D2 feedstock powder; for the purpose of assessing the 'intra-batch' variability, three measurements were taken on various samples from the supplied powder batch. Figure 3.5 demonstrates an example for the complete particle size

distribution for the D2 feedstock powder, highlighting that it is monomodal in character. In addition, the flow response of the originally supplied powder was evaluated using a Hall Flowmeter, following ASTM standard *B213-20: Standard Test Methods for Flow Rate of Metal Powders Using the Hall Flowmeter Funnel.* For the powder flow test, the time needed for 50-gram batches of the original powder to pass through the orifice of the Hall Flowmeter was recorded three different times and was then averaged; this examination was done simply to evaluate powder flowability using a known test procedure. However, the validity of using the Hall flow test for DED processing is open to question. Similarly, the feedstock powder apparent density was measured following ASTM standard *B703-17: Standard Test Method for Apparent Density of Metal Powders and Related Compounds Using the Arnold Meter*; in this instance the mean was taken from three separate measurements.

Table 3.3 outlines the measured D2 feedstock powder characteristics (i.e., particle size, flow behaviour, and density). It is apparent that the measured particle size is close to the manufacturer specification (i.e., a D_{50} of ~75 μm), which corresponds to the recommended particle size specified by the manufacturer of the DED system.

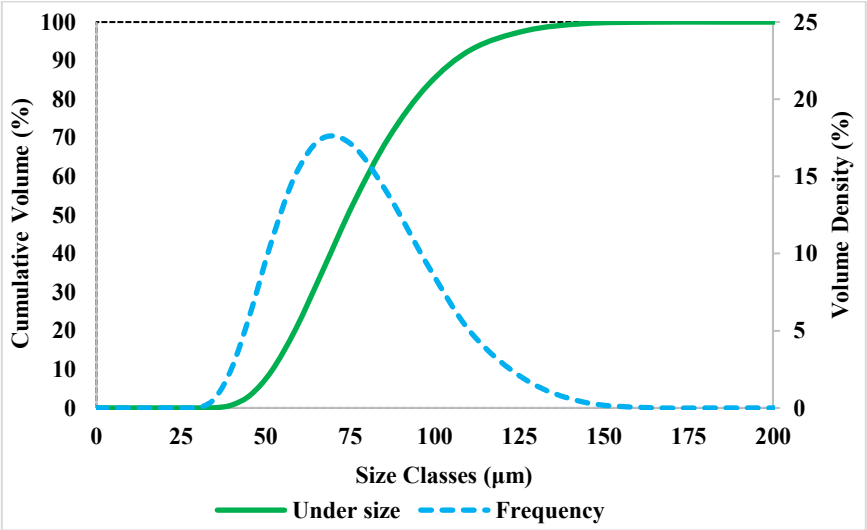

Figure 3.5. Representative particle size distribution for the as-received D2 powder.

Table 3.3. AISI D2 tool steel feed stock powder properties.

Properties (units)		**Value**
Particle Size	D_{10} **(µm)**	51.5
	D_{50} **(µm)**	73.6
	D_{80} **(µm)**	93.9
	D_{90} **(µm)**	106
Flowability (g/s)		3.2 ± 0.06
Density (g/cm^3)		4.20 ± 0.016

3.4.2 Characterisation of DED Processed Specimens

- *Single Clads*

For the DED processed samples, the single clads were assessed in terms of their heights and widths as a function of the DED operating parameters. To achieve this, a confocal laser scanning microscope (CLSM; model VK-X1100, Keyence Corp., Osaka, Japan) was used

to evaluate the cross-sectional profile of the single clads, using a 20x magnification objective lens (with 535.7 nm theoretical resolution). Three measurements were taken in different positions along the length of the single clad, in order to obtain an average value. The CLSM cross-sectional profile data were then analysed using the *Keyence Multifile Analyzer* software.

- *Microstructure analysis*

The same SEM as outlined previously was also used to examine the various wrought, DED processed, and heat-treated D2 samples. For these examples, the SEM was typically operated with V_{acc} and I_e values of 15 kV and 15 μA, respectively. The SEM was also equipped with an energy dispersive X-ray spectroscopy (EDS) system (Inca X-Max 80, Oxford Instruments, Abingdon, UK) for localized chemical analysis of the DED processed and heat-treated materials. For EDS analysis, V_{acc} and I_e values of 5 kV and 20 μA were used, respectively. Although EDS is highly affected by SEM beam contamination, which in turn, affects the accuracy of detecting carbon, in the present work it was used to demonstrate the locations where chromium and carbides precipitate. The different wrought, DED processed, and heat-treated D2 samples that were examined by SEM were mounted in PolyFast (using Citopress-1, Struers, Copenhagen, Denmark). They were then ground and polished to a 1 μm finish (using successively finer SiC paper grades, finishing with Tegramin-20, Struers, Copenhagen, Denmark) and then etched with 5 vol% Nital solution (5 vol% nitric to 95 vol% methanol), by briefly immersing the polished surface into the solution. Each sample was found to require slightly different etching times. Crystallographic phase analysis of the samples was determined using X-ray diffraction (XRD; D8 Advance, Bruker Corp., Billerica, MA, USA), with a Co radiation source,

operating at 35 kV and 27 mA with Co-Kα radiation (Kα = 1.78897 Å) and a Fe filter. A step size and a time per step of 0.02° and 0.5 per second, respectively, were used over a range of 20-130° for 2θ.

- *Indentation Hardness Measurement*

The hardness of the various D2 samples was assessed using both Rockwell indentation and scratch testing. The indentation hardness of the wrought, heat-treated, and DED processed D2 tool steel samples was determined using a Rockwell hardness tester (Wilson-2000, Instron, Norwood, MA, USA). This analysis was conducted using the Rockwell C scale, with a preload of 10 kgf and a final applied load of 150 kgf, using a Rockwell sphero-conical diamond indenter. Each presented Rockwell C value is the average of six individual indentation measurements.

- *Scratch Hardness Measurement*

The scratch hardness was measured on a UMT-1 model universal micro tribometer system (CETR Corp., Campbell, CA, USA), at room temperature (20 ± 2 °C) in an air atmosphere. An applied load of 10 N was used for all scratch tests, with a 5 mm scratch track length. The tip displacement velocity for scratch testing was 10 mm/minute. The scratch hardness was then determined following Equation 3.3.

$$HS_p = \frac{8F}{\pi w^2}$$

Equation 3.3 Calculation of scratch hardness [120].

where HS_p refers to the scratch hardness (in GPa), F is the normal force (in N), and w is the scratch width (in μm). Three individual scratch tracks were conducted on each sample,

to obtain a mean value and standard deviation error. The scratch widths were subsequently measured using CLSM (model VK-X1100, Keyence Corp., Osaka, Japan), with a 10x magnification objective lens. The CLSM scratch image data was evaluated using the Keyence Multifile Analyzer software. A total of nine measurements (i.e., three per scratch, for each of the three scratches) were averaged, to determine the mean scratch width which, in turn, was used to determine the mean scratch hardness following Equation 3.3.

- *Surface Roughness Measurements*

The as-deposited surface roughness of the DED rectangular samples was assessed using the CLSM with the same 20x magnification objective lens. The *Keyence Multifile Analyzer* software was then used to determine the arithmetical mean height (Sa), as a representative parameter for surface roughness evaluation. Based on the outcomes reported by Mazumder and colleagues [121], that the top surface roughness was higher in the width direction than the length, while the side wall roughness was noticed to be higher in the vertical direction than the horizontal direction, for the current study the surface evaluation was conducted along the transverse direction (normal to the laser scanning direction) for the top surface and the height direction (Z-direction) for the side surface. In each measurement, an area slice was recorded to obtain the average Sa for this area slice. The area slice consists of three stitched images, for top surface roughness measurements, and six stitched images, for side surface roughness. While three different area slices at different locations along the surface were selected to get the mean value of the surface roughness along the whole surface. It is worth noting that for the side surface roughness, the X-Z (length-height) plane was normalized to face the CLSM laser beam (i.e., perpendicular to the beam). In addition, the selected areas for evaluation were chosen such that, qualitatively, they exhibited the

highest amount of un-melted powder particles attached to the surface (i.e., the worst case scenario), as highlighted in Figure 3.1. Orientation normalization was not required for the top surface roughness, since it naturally is parallel to the CLSM lens. Additionally, in terms of analysis, the surface resonance was isolated by applying two robust Gaussian filters, as required by ISO standard *11562:1996: Geometrical Product Specifications (GPS) - Surface Texture: Profile Method - Metrological Characteristics of Phase Correct Filters* and ISO standard 16610-21:2011: *Geometrical Product Specifications (GPS) – Filtration – Linear Profile Filters: Gaussian Filters* [122]. Initially, a shortcut filter (S-filter) was applied with a cut-off scale of 2.5 μm, with the aim of removing the small-scale measurement noise [123]. Then, a long-pass filter (L-filter) was used, with a cut-off scale of five times the profile length (in mm)), in order to eliminate undulations and further lateral components [124].

Further investigation of the surface morphology/roughness was conducted using the previously outlined SEM, which was operated with V_{acc} and I_e values of 15 kV and 15 μA, respectively.

- *Cooling Rate Measurements*

In order to clarify the hardness and surface roughness results for the DED processed specimens, in relation to the processing conditions, the DED cooling rates were determined following Equation 3.4:

$$\lambda_2 = B\left(\frac{dT}{dt}\right)^{-n}$$

Equation 3.4 Calculation of cooling rates using the measured SDAS [125].

where λ_2 represents secondary dendrite arm spacing, or SDAS, (in μm), $\frac{dT}{dt}$ refers to the cooling rate (in K/s), and *B* and *n* are experimentally indicated constants, with values of 42.1 μm.s.K^{-1} and 1/3, respectively [126]. The SDAS values were measured using the public domain ImageJ software (National Institutes of Health, Kensington, MD, USA) from digitised SEM pictures of the DED processed specimens; in this instance, 5 measurements per sample were performed, and in each measurement, the spacing along 10 to 15 secondary dendrites was measured and then averaged.

- *Wear Rate Measurement*

The wear resistance of the various D2 samples was evaluated by measuring the wear rate, following ASTM standard *G133-05*: *Standard Test Method for Linearly Reciprocating Ball-on-Flat Sliding Wear*. The wear tracks of the wrought, heat-treated, and DED processed D2 tool steel samples were applied using a UMT-1 model universal micro tribometer system (CETR Corp., Campbell, CA, USA), at room temperature (20 ± 2 °C) in an air atmosphere. The parameters used were not in full compliance with the provisions of Test Method ASTM-G133, Procedure A, because the normal force in these tests was 5 N, instead of 25 N as prescribed by the standard, the stroke length was 5.03 mm, instead of 10.0 mm as prescribed by the standard, and alumina spheres were used for these tests with a diameter of 6.34 mm. All other provisions of Test Method G133 have been followed. The wear tests were taken place at three different test durations (500, 1000, and 2000 s). The surface of the wear samples was ground with sandpaper up to 2000 grit. The sample surfaces were cleaned with ethanol immediately before the tests. In addition, it is worth noting that the wear tracks were applied on the top surface of DED deposited samples.

It is worth mentioning that investigation of the effects of varying DED process parameters and post-heat treatment are to be included in future work, since the wear testing system broke down while completing the presented work in this thesis; a new wear tester is to be installed in May 2023.

The wear rate was determined using Equation 3.5:

$$WR = \frac{V_{loss}}{2.t.L.f_o.F}$$

Equation 3.5 Wear rate calculation [127].

where WR is the wear rate (in mm^3/N.m), V_{loss} refers to the wear track volume (in mm^3), t is the test time (seconds), L represents the length of the stroke (m), f_o is the oscillating frequency (Hz), and F is the applied load (N).

Three individual wear tracks were conducted on each sample, per each set of wear testing parameters, to obtain a mean value and standard deviation error. The wear 'scar' volume losses were measured using CLSM, with a 10x magnification objective lens. The CLSM wear track image data was evaluated using the *Keyence Multifile Analyzer* software, as illustrated in Figure 3.6 (a). In addition, the removed volume from the counter surface of the alumina spheres was also assessed using CLSM, as presented in Figure 3.6 (b). Furthermore, SEM analysis and EDS mapping were used to analyse the wear rate results by determining the wear mechanism and the amount of oxidation developed during the wear test.

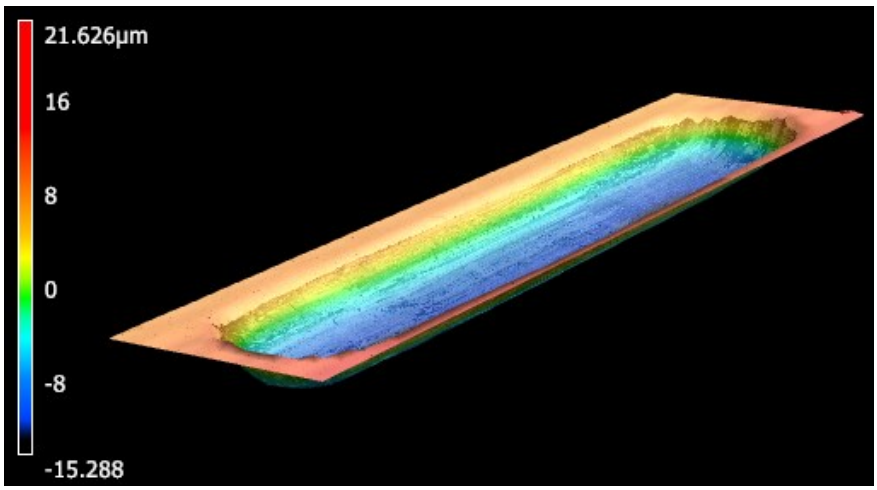

(a)

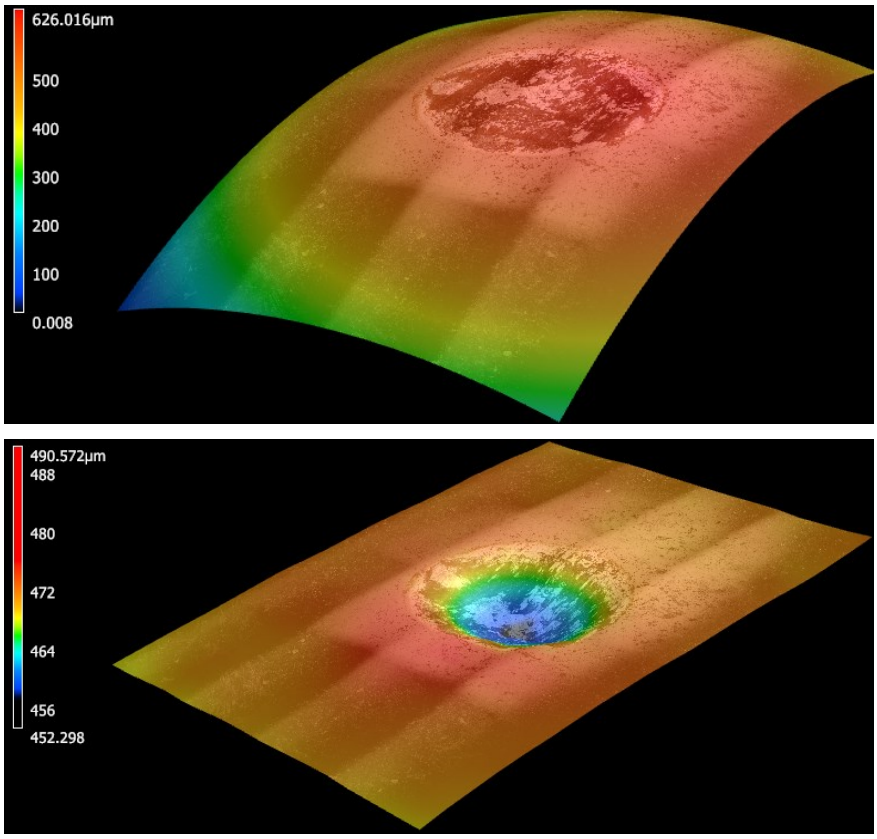

(b)

Figure 3.6 (a) Wear track, and (b) Sphere counter surface using CLSM (both as measured (upper image) and modified to flatten the appearance of the sphere (lower image), and thus calculate the wear volume for the sphere).

- *Overhanging Thin Walls*

In terms of the overhanging thin walls, the CLSM was used to measure the incline angles, while the thin walls were normalized in order to measure the angle in the X-Y plane (i.e., normal to the CLSM beam axis). The images for the thin-wall samples were captured using a 10x magnification objective lens; they were subsequently analysed using the *Keyence Multifile Analyzer* software. The thin-walled samples, with design angles of 70° and 80°, used between 12 and 14 stitched images (2 columns, and 6 or 7 rows), while the overhanging walls with a 60° design angle required 18 stitched images (3 columns and 6 rows). For all samples, the angles between the horizontal line (i.e., the substrate surface), and the outer and inner wall surfaces were measured twice (from both sides), and then averaged to get the mean value. In terms of the surface roughness of the inclined walls, only the outer surface was examined, following the same procedures that were used for determining the surface roughness of the DED processed rectangular specimens. However, the DED processed tilted wall samples were installed in a special mounting 'vice', allowing them to be rotated, for the purpose of aligning the inclined surface perpendicular to the axis of the CLSM laser beam.

CHAPTER 4 The Influence of DED Process Parameters and Heat-Treatment Cycle on the Microstructure and Hardness of AISI D2 Tool Steel

Status: ***Published***: Journal of Manufacturing Processes, 81 (2022): 655-671.

Abstract

The impact of both the laser directed energy deposition (DED) process parameters and post-deposition heat-treatment cycles on the microstructural characteristics and hardness are evaluated for cladding AISI D2 tool steel onto annealed AISI D2 substrates. The influences of powder feed rate, and laser scanning speed were assessed. After laser deposition, the DED samples were subjected to various tempering heat-treatment cycles. The microstructural and compositional characteristics of both the 'as-printed' and heat-treated DED processed samples were investigated using scanning electron microscopy with energy dispersive X-ray spectroscopy, confocal laser scanning microscopy, and X-ray diffraction. The indentation and scratch hardness responses were assessed to evaluate the effects of various heat-treatment schedules, with comparison made to wrought D2. It was demonstrated that the microstructure of the DED processed samples had a dendritic morphology with columnar grains. Moreover, the hardness values of the DED fabricated parts were found to be higher than an annealed wrought D2, but lower than the air-cooled D2. Subsequent tempering of the DED printed parts resulted in a final hardness, essentially equivalent to the as air-cooled level.

Keywords: tool steels; laser direct energy deposition; hardness; microstructure development; tempering; heat-treatment

4.1 Introduction

Laser directed energy deposition (DED) is an additive manufacturing (AM) technology whereby fully dense metal parts can be directly produced from a computer aided design (CAD) model [10,30–33]. This approach also often referred to as laser consolidation [39], laser powder deposition [42], laser coating [37,38], laser direct casting [128], solid free-form fabrication [44], laser powder deposition [41,43],etc. During the process, a metallic substrate is scanned by laser beam in order to create a small molten pool of metal, while a powder delivery system is used to convey a fine powder stream into the melt pool. With the purpose of initially generating a single, nominally 2-D layer, the laser beam is then scanned over a desired path, with the aid of an associated computer numerical control (CNC) system. A 3D object can then be built by depositing layers successively onto one another (i.e., layer by layer) [36]. The initial concepts of DED were established during the era of welding AM in the 1980s, in order to repair metallic parts [129]. For example, a combination system of blown powder and laser heating was patented by Mehta *et al.* [130], for the purpose of component refurbishment.

There are many benefits of using the DED technique instead of other AM methods. Firstly, the geometry of the produced part has essentially no restrictions and can be used to create parts with deep cavities, thin walls, or hidden channels [16,25]. Another advantage is that DED can be employed to repair critical contacting (or corroding) surfaces, which protect high-value tools, instead of being replaced [46,47]. However, the clad quality is drastically sensitive to the disturbances in the process, such as any trivial variation in the operating parameters (e.g., powder feed rate, laser power, scanning speed, etc.) [51]. That leads to

poor reproducibility in the quality of the deposited material. High thermal gradients during the process can typically also result in residual stresses or (in the worst case scenario) cracking, which may eventually lead to failure of the manufactured part [48–50].

AISI D2 tool steel is known as strong candidate for cold work die steels. This can be attributed to its exceptional wear resistance as a result of the composition including high chromium (~12 wt%) and carbon (~1.5 wt%) contents, which allows the formation of high hardness carbides through a tempering step. Moreover, the high chromium content also leads to good resistance to both oxidation at high temperatures and surface staining when hardened or polished [8,9]. However, as-processed D2 tool steel is too brittle and does not have sufficient hardness for many operations. As a consequence, tempering heat-treatments are conventionally required to enhance the hardness of D2 tool steel [113,131,132].

In the DED process, the formed microstructure affects the properties of the manufactured part, such as hardness, tensile strength, toughness, etc. Consequently, some researchers have studied the microstructural development during DED processing of tool steels. Generally, the microstructures of the manufactured parts have one or more of three grain morphologies, namely: columnar, equiaxed, and mixture of columnar and equiaxed [133]. Park et al. [134] used DED to manufacture specimens of both D2 and H13 tool steel on like-composition substrates. The microstructure of the deposited H13 steel contained a mix of the dendritic and cell-type (equiaxed morphology) structures, while the microstructure of the printed D2 steel was mainly dendritic. Furthermore, it was noticed that the grains in the deposited metal were larger at high energy input, due to the relatively low cooling rates leading to grain growth. Similarly, Baek *et al*. [135] deposited M2 and H13 layers onto a substrate of D2 tool steel. It was found that re-melting of the previously deposited layers

resulted in a 'wavy' boundary line between each layer. In terms of deposited H13 layers, there were phases of low carbon martensite, retained austenite, and fine cellular dendrites (containing fine carbides). Regarding the M2 deposited layers, as with the microstructure of the H13 deposited layers, there was fine cellular-dendritic solidification. However, smaller cellular grains were observed in M2 deposited layers than in the H13 deposited layers. Furthermore, Mazumder *et al.* [121] deposited H13 tool steel onto a substrate of mild steel using DED. The microstructure consisted of three different regions. Initially, there was formation of an 'interface' region, in which there was remelting or reheating of the substrate or the previously added materials. Consequently, there was available time for grain growth. Above the interface, since the temperature gradients and cooling rates are high and directional, the grains were more columnar. Above the columnar region, steady state was achieved, resulting in the formation of an equiaxial grain morphology.

Several researchers focused on the indentation hardness of the DED processed tool steel samples, and how it is affected by the post heat-treatment of the manufactured part. For H13 tool steel, Mazumder *et al.* [121] reported that the hardness decreased from the top surface towards the bottom of the sample, which was attributed to the reheating effect of the previously deposited material, effectively annealing the previously added layers. In contrast, Baek *et al.* [136] noted that a small range of variation in hardness at each location resulted, because of the laser power fluctuation and irregular powdered material flow. Comparison has also been made of the hardness of DED processed D2 and H13 tool steel parts to the equivalent wrought material [137]. Post-DED tempering heat-treatments were examined in that work, and it was reported that the deposited D2 steel had lower hardness than the D2 substrate. This was attributed to the fact that, unlike the wrought material, the

microstructure of the DED processed D2 contains a eutectoid structure, including M_7C_3 phases and austenite, as well as dendritic austenite. Conversely, the hardness of the deposited H13 was higher than the H13 substrate, due to the high cooling rate which forms δ-ferrite in the dendritic region in addition to martensite in the inter-dendritic region. Regarding the heat-treatment effects on hardness, it was found that the hardness of the heat-treated DED processed D2 (tempered at 200°C for 4 hours) and H13 (tempered at 600°C for 3 hours) have similar values to those of the heat-treated D2 and H13 substrates [138]. DED of M4 steel and high-wear-resistance steel (HWS) has also been studied, deposited onto a substrate of D2 tool steel. It was observed that the hardness of deposited parts of M4 and HWS, and the heat-treated HWS, are higher than they are for the heat-treated D2 tool steel due to the precipitation of uniform and fine carbides in the DED processed M4 and HWS.

The present work has involved DED of specimens of AISI D2 tool steel powder, deposited onto a substrate of the same material, where different powder feed rates and laser scanning speeds were used during clad deposition. The effects of each individual variable were investigated while fixing the values of the other parameters. After the DED stage, selected samples were also subjected to post-heat-treatment. The DED processed samples were examined in terms of their microstructure, indentation, and scratch hardness of as-deposited and heat-treated parts. Comparison is also made to a wrought equivalent D2.

4.2 Experimental Procedures

4.2.1 Raw Materials

The feed stock material used in the current DED processing was obtained as gas atomized powder from TLS Technik Spezialpulver (Bitterfeld-Wolfen, Germany). The powder was provided with a nominal, manufacturer-specified particle size range of 45 to 90 μm. The D2 substrates were provided as plates of dimensions 101.6 x 101.6 x 6.35 mm (4 x 4 x 0.25 inches) from Hudson Tool Steel (Dover, NH, USA). In order to minimise any laser reflection effects in the DED system, the substrate was first sandblasted before DED processing. Furthermore, for comparative purposes, wrought D2 tool steel was supplied as circular rods with diameter of 19.05 mm and length of 900 mm from Hudson Tool Steel (Dover, NH, USA). These rods were then machined to obtain disc-shaped specimens with a thickness of 10 mm and the same original diameter (19.05 mm); these samples were then used as a baseline for subsequent tempering heat-treatment evaluation.

4.2.2 Laser DED Processing

The DED processing stage was conducted using an Optomec MTS-CA system (Albuquerque, NM, USA). This equipment consists of a 1-kW fiber laser with a spot diameter of 0.6 mm, while the feeding system for the powder includes a coaxial powder nozzle and the option of four discrete powder hoppers. The DED system also has a five-axis machine movement control. In addition to being used as the carrying gas for the injected powder, Ar was also used as the shielding environment within the chamber in order to protect the workpiece from oxidation.

The selected DED process parameters are illustrated in Table 4.1. It is worth noting that determination of evaluated ranges for each of the process parameters was based on the results of previous studies and the equipment design/capabilities. The laser scanning speed was varied from 400 to 700 mm/min. Similarly, powder feed rates were assessed from 5.5 to 7.5 g/min. The sample identification strategy, noting the full range of parameters studied, is summarised in Table 4.2 for the DED samples. It should be noted that the laser power, 'targeted layer thickness'; (i.e., the increment that the laser beam focal point is shifted in the z direction to print the subsequent layer), and hatch spacing were all kept constant for all of the DED trials, with values of 400 W, 0.251 mm and 0.381 mm, respectively. A representative example of the actual printed samples is shown in Figure 4.1.

Table 4.1. A summary of the main DED processing parameters examined.

Parameter	**Value**
Sample dimensions, L x W x H (mm)	25 x 5 x 10
Laser power (W)	400
Scanning speed (mm/min)	400 - 700
Powder feed rate (g/min)	5.5 - 7.5
Targeted layer thickness (mm)	0.251
Hatch spacing (mm)	0.381

Table 4.2. Processing parameters and identification scheme for the rectangular samples.

Sample ID		**Feed rate (g/min)**		
		7.5	**6.5**	**5.5**
Scanning speed (mm/min)	**700**	A1	B1	C1
	600	A2	B2	C2
	400	A4	B4	C4

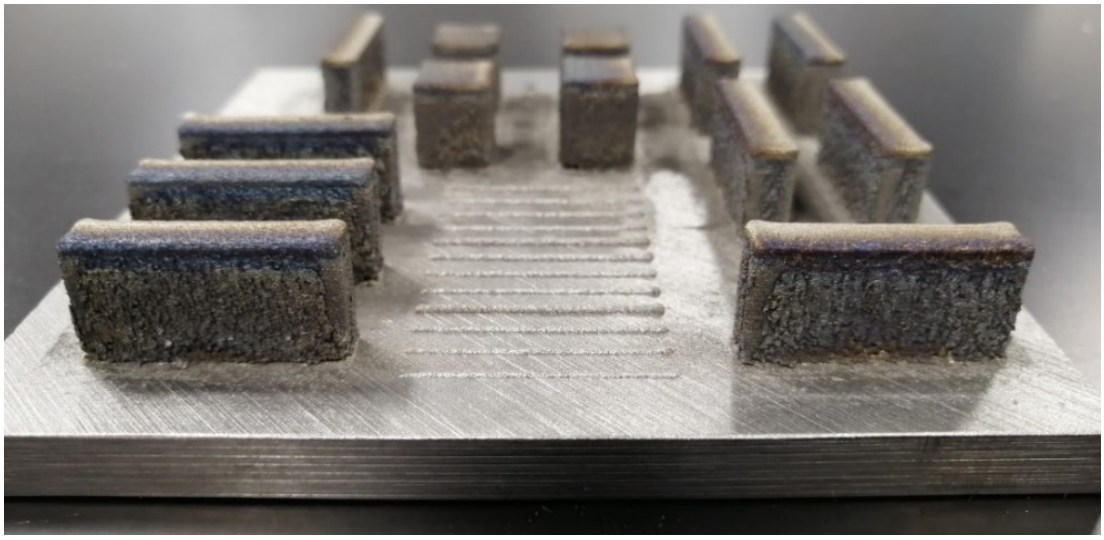

Figure 4.1. Typical examples of the DED processed D2 tool steel samples, showing the rectangular samples (presented in this work). Note that the single-track samples were used for diagnostic purposes and are not discussed in the current paper.

4.2.3 Heat-Treatment Cycles

To assess the impact of the use of tempering heat-treatment cycles on hardness for the DED materials, both wrought and DED-processed D2 samples were subjected to a variety of heat-treatments. In this study, all of the heat-treated samples were first austenitized at 1010 °C, for a period of 30 minutes. During heating, the temperature was held at 750 °C (for 30 minutes), as part of the preheating stage, in order to allow the temperature to be uniformly distributed inside the sample before austenitizing. After the austenitizing step, the samples were air-cooled to room temperature.

Subsequently, the first batch of samples (wrought material only) were single-tempered, at various temperatures from 300-700 °C, held for a total of 120 minutes. A second batch of the wrought material was initially tempered at the same temperatures as before (i.e., 300-700 °C, held for 120 minutes), before retempering at the same tempering temperature for each sample for an additional 120 minutes. These wrought samples are subsequently

referred to as ‘double-tempered’. In addition, another heat-treatment case was examined in which the material is initially tempered at 400 °C, then retempered at temperature of 500 °C; this condition was selected as outlined below. Following these preliminary studies on the wrought material, selected DED-processed samples were then subjected to optimised tempering treatments, based on the data obtained from the initial assessments for the wrought materials. An initial set of five DED samples (A2, B2, C1, C2, C4) was thus chosen to be heat-treated. Based upon the property analysis of the wrought, heat-treated D2 tool steel (described in Sections 3.4 and 3.5), these DED processed samples were heat-treated under two scenarios. The first involved double tempering at 500 °C (each held for 120 minutes), while the second involved first tempering at 400˚C before then retempering at 500˚C (again, each held for 120 minutes). The second scenario was chosen by ‘combining’ the best single-tempering condition for hardness (400˚C) and the best double-tempering scenario for hardness (500˚C) into a two-stage treatment. Table 4.3 illustrates the sample codes and the heat-treatment scenarios used for each of these samples. A schematic representation of a typical heat-treatment schedule, in this instance for a hypothetical double-temper (both segments at 500 °C), is presented in Figure 4.2.

Table 4.3 Sample identification for the heat-treated D2 materials.

Sample ID		Temperature (°C)	
		Tempering	Retempering
Single Tempered	T3	300	-
	T4	400	-
	T5	500	-
	T6	600	-
	T7	700	-
Double Tempered	DT3	300	300
	DT4	400	400
	DT5	500	500
	DT6	600	600
	DT7	700	700
	DT4-5	400	500
Air-cooled	Q	-	
No Heat-treatment	WR	-	

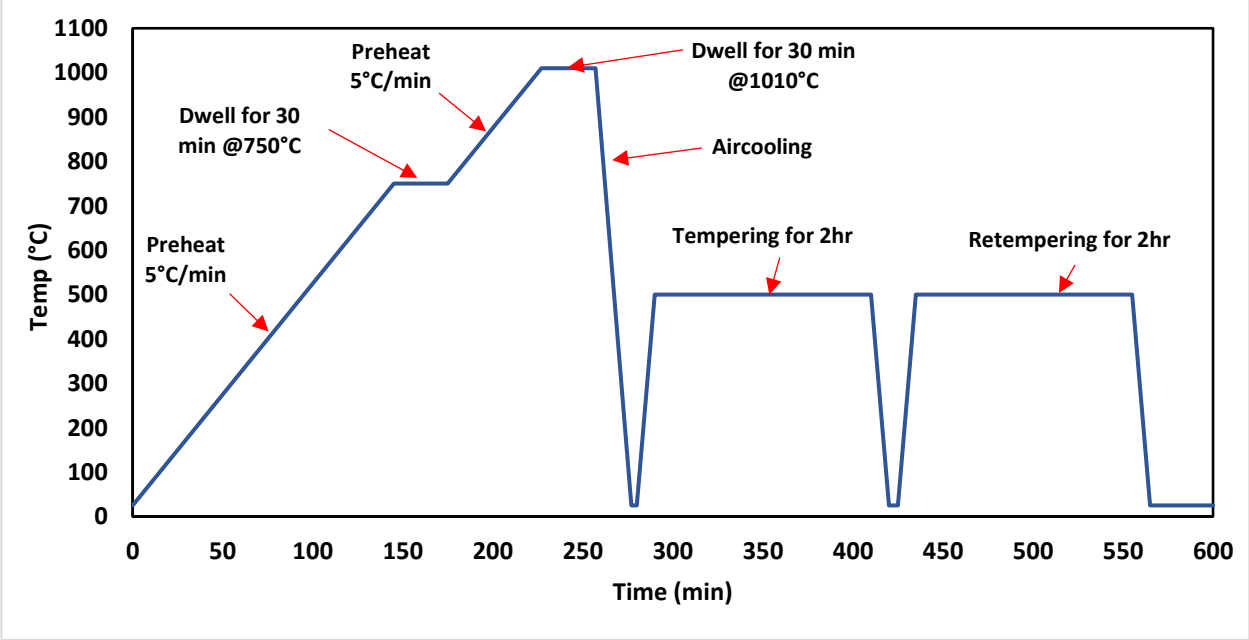

Figure 4.2. Schematic representation of the heat-treatment cycle applied for DED processed samples. In this example, a 'double-temper' is applied, with each temper treatment conducted at 500 °C for two hours.

4.2.4 Materials Characterisation

The chemical compositions of the AISI D2 substrates and the gas atomised feedstock powder were determined using inductively coupled plasma optical emission spectroscopy (ICP-OES) analysis using a Varian Vista-PRO system (Varian Inc., Palo Alto, CA, USA); as the rod-stock wrought material was provided by the same supplier as the substrates, this was not assessed in terms of chemical composition. For ICP-OES, the material being evaluated (either the feedstock powder or shavings from the substrate plates) was subjected to an acid digestion step prior to analysis. The D2 powder particle size was determined using a Mastersizer 3000 system (Malvern Panalytical, Malvern, UK); the 'intra-batch' variability was assessed by undertaking three measurements on different samples from the original supplied powder batch. The feed stock powder was further characterised by measuring its apparent density, following ASTM standard *B703-17: Standard Test Method for Apparent Density of Metal Powders and Related Compounds Using the Arnold Meter*; three repeats were obtained to determine a mean value and standard deviation. Similarly, the powder flow behaviour was assessed using a Hall Flowmeter, following ASTM standard *B213-20: Standard Test Methods for Flow Rate of Metal Powders Using the Hall Flowmeter Funnel*, with the mean taken from three separate measurements for the time required for flow of 50 gram of powder through the Hall Flowmeter orifice; this analysis was simply conducted to assess the flow response using a known test, while it is perhaps questionable whether the Hall flow test holds significant validity for DED processing.

The microstructures of the D2 starting powders were evaluated using a Hitachi S4700 field emission gun scanning electron microscope (SEM; Hitachi High Technologies Inc., Tokyo, Japan). To minimise charging artefacts during raw powder examination, the SEM was

operated with an accelerating voltage (V_{acc}) and beam current (I_e) of 3 kV and 15 μA, respectively. The same SEM was also used to examine the various wrought, DED processed, and heat-treated D2 samples. For these examples, the SEM was typically operated with V_{acc} and I_e values of 15 kV and 15 μA, respectively. The SEM was also equipped with an energy dispersive X-ray spectroscopy (EDS) system (Inca X-Max 80, Oxford Instruments, Abingdon, UK) for localized chemical analysis of the DED processed and heat-treated materials. For EDS analysis, V_{acc} and I_e values of 5 kV and 20 μA were used, respectively. Although EDS is highly affected by SEM beam contamination, which in turn, affects the accuracy of detecting carbon, in the present work it was used to demonstrate the locations where chromium and carbides precipitate. The different wrought, DED processed, and heat-treated D2 samples that were examined by SEM were mounted in PolyFast (using Citopress-1, Struers, Copenhagen, Denmark). They were then ground and polished to a 1 μm finish (using successively finer SiC paper grades, finishing with Tegramin-20, Struers, Copenhagen, Denmark) and then etched with 5 vol% Nital solution (5 vol% nitric to 95 vol% methanol), by briefly immersing the polished surface into the solution. Each sample was found to require slightly different etching times. Crystallographic phase analysis of the samples was determined using X-ray diffraction (XRD; D8 Advance, Bruker Corp., Billerica, MA, USA), with a Co radiation source, operating at 35 kV and 27 mA with Co-Kα radiation (Kα = 1.78897 Å) and a Fe filter. A step size and a time per step of 0.02° and 0.5 per second, respectively, were used over a range of 20-130° for 2θ.

The hardness of the various D2 samples was assessed using both Rockwell indentation and scratch testing. The indentation hardness of the wrought, heat-treated, and DED processed

D2 tool steel samples was determined using a Rockwell hardness tester (Wilson-2000, Instron, Norwood, MA, USA). This analysis was conducted using the Rockwell C scale, with a preload of 10 kgf and a final applied load of 150 kgf, using a Rockwell spheroconical diamond indenter. Each presented Rockwell C value is the average of six individual indentation measurements. Furthermore, the scratch hardness was measured on a UMT-1 model universal micro tribometer system (CETR Corp., Campbell, CA, USA), at room temperature (20 ± 2 °C) in an air atmosphere. An applied load of 10 N was used for all scratch tests, with a 5 mm scratch track length. The tip displacement velocity for scratch testing was 10 mm/minute. The scratch hardness was then determined following equation

$$HS_p = \frac{8F}{\pi w^2}$$

Equation 4.1 Scratch hardness calculation [120].

where HS_p refers to the scratch hardness (in GPa), F is the normal force (in N), and w is the scratch width (in μm). Three individual scratch tracks were conducted on each sample, to obtain a mean value and standard deviation error. The scratch widths were subsequently measured using a confocal laser scanning microscope (CLSM; model VK-X1100, Keyence Corp., Osaka, Japan), with a 10x magnification objective lens. The CLSM scratch image data was evaluated using the Keyence Multifile Analyzer software. A total of nine measurements (i.e., three per scratch, for each of the three scratches) were averaged, to determine the mean scratch width which, in turn, was used to determine the mean scratch hardness following Equation 4.1.

In order to clarify the hardness results of the DED processed specimens in relation to the processing conditions, the DED cooling rates were determined following equation:

$$\lambda_2 = B\left(\frac{dT}{dt}\right)^{-n}$$

Equation 4.2. Calculated cooling rates [125].

where λ_2 represents secondary dendrite arm spacing (SDAS) (in μm), $\frac{dT}{dt}$ refers to the cooling rate (in K/s), and *B* and *n* are experimentally indicated constants, with values of 42.1 μm.s.K^{-1} and 1/3, respectively [126]. The SDAS were measured using the public domain ImageJ software (National Institutes of Health, Kensington, MD, USA) from digitised SEM pictures of the DED processed specimens; in this instance, 5 measurements per sample were performed, and in each measurement, the spacing along 10 to 15 secondary dendrites was measured and then averaged.

4.3 Results & Discussion

4.3.1 Characterisation of Raw Materials

Table 4.4 lists the measured chemical compositions of the AISI D2 substrate and powder used in current study, which were determined using ICP-OES analysis. In both cases the compositions lie within the expected range for D2 tool steel [87,119]. The D2 feedstock powder characteristics, including density, flow behaviour, and particle size are presented in Table 4.5. It can be seen that the powder is close to the manufacturer specifications in terms of particle size (i.e., a D_{50} of ~75 μm), which is the ideal size for the DED system that was used. The overall measured particle size distribution is illustrated in Figure 4.3(a), highlighting that it is monomodal. Figure 4.3(b) shows a representative SEM image of the powder. While the particles exhibit a generally spherical morphology, as might be expected from the atomisation process, there are occasional irregular-shaped particles and also many attached micro-satellites, which may impede flow somewhat in terms of the DED process.

Table 4.4 The raw material chemical compositions determined by ICP-OES analysis.

Material Type	**Composition (wt.%)**									
	Fe	**C**	**Si**	**Mn**	**Cr**	**Mo**	**V**	**Co**	**Cu**	**Ni**
AISI D2 Substrate	Bal.	1.50	0.3	0.3	12	0.75	0.9	-	-	-
AISI D2 Powder	Bal.	1.55	0.41	0.33	11.27	0.64	0.79	0.01	0.01	0.06
AISI D2 Substrate (after DED)	Bal.	1.45	0.61	0.42	7.42	0.70	0.34	0.03	0.16	0.4

Table 4.5 AISI D2 tool steel powder characteristics.

Properties (Units)		**Values**
Density (g/cm^3)		4.205
Flowability (g/s)		3.228
Particle Size	**D_{10} (µm)**	51.5
	D_{50} (µm)	73.6
	D_{80} (µm)	93.9
	D_{90} (µm)	106

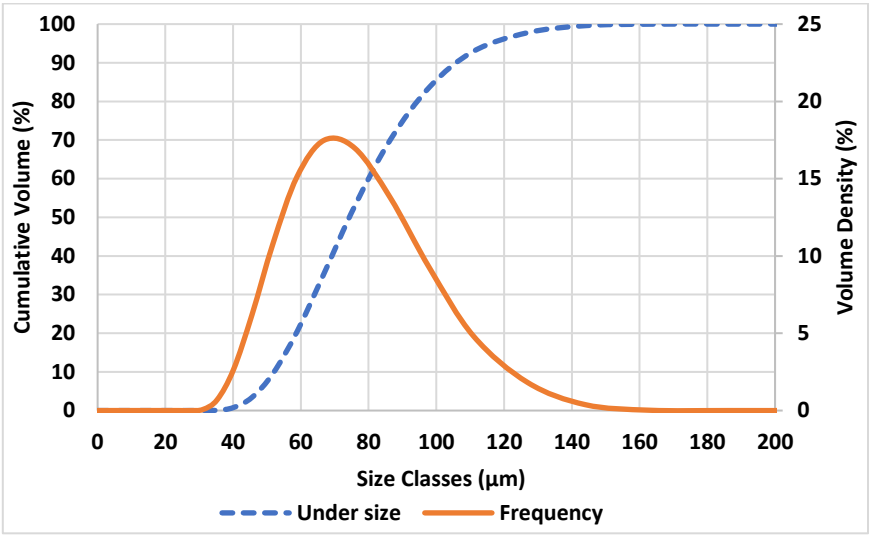

(a)

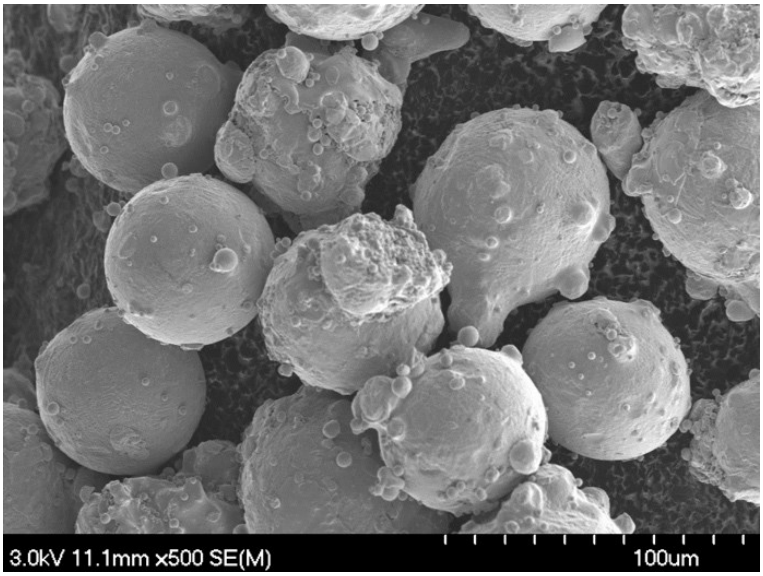

(b)

Figure 4.3. (a) The measured particle size distribution for the as-received D2 powder. (b) A representative SEM image of the as-received D2 tool steel powder.

4.3.2 Microstructural Analysis of As-Deposited DED Samples

The microstructures of the DED manufactured samples were subsequently evaluated using SEM and EDS. As shown in Figures 4.4 and 4.5, it was demonstrated that the grains of the

DED processed D2 samples had a dendritic morphology, with the presence of columnar grains. The direction of the grains changes orientation due to the changing direction of heat flow during the laser transition across the surface. It is apparent that, as shown in Figure 4.4, the lower half of the deposited part prepared under a low scanning speed and low powder feed rate (i.e., sample C4), shows equiaxed grains that are slightly coarser than the grains in samples C1 and A1, respectively. This can be attributed to the increased time available for reheating at low scanning speed. In addition, the lower powder feed rate causes higher temperature gradients and lower cooling rate, because there is less available powder for heat dissipation at any instant in time. Both of the aforementioned reasons can be expected to lead to grain growth in the samples during laser deposition.

The comparison between Figures 4.4 and 4.5 demonstrates that the upper half of the deposited sample shows a more dendritic morphology, with columnar grains, when compared with the lower half of the sample. The formation of dendrites can be attributed to 'constitutional supercooling'. This is due to the fact that, in DED, the real temperature gradient (G_r) in the liquid adjacent to the solid/liquid interface is positive (i.e., heat is dissipated away through the liquid). Therefore, the formation of small protrusions at the solid/liquid interface results in instability in the planar interface, due to the difference in growth rate between such protrusions and the bulk material, which in turn, promotes the formation of dendritic structures [51]. However, the degree of supercooling controls the formation of a cellular or dendritic structure. In conclusion, slow solidification rates (U_s) and high temperature gradients promote a planar growth condition, due to the lowered probability of constitutional supercooling at such a case. Consequently, it could be noticed that the maximum value of (G_r/U_s) is located at the interface between the substrate and the

deposited material. Therefore, at such locations, it is favorable to have a planar solid liquid interface with a cellular structure. However, since (G_r/U_s) decreases towards the surface, the possibility of the formation of a dendritic morphology structure increases from the bottom to the top of the deposited specimen [56]. Furthermore, it was found that the solidification rate is highly dependent upon the scanning speed, as the solidification rate could be determined following Equation 4.3 [51].

$$U_s = v \cos \theta$$

Equation 4.3. The relation between scanning speed and solidification rate [51].

where θ is the angle between the vector representing the direction of the substrate motion, with scanning speed (v), and the vector normal to the solid/liquid surface at a particular point (i.e., the solidification rate). Therefore, it could be concluded that, at higher scanning speed, (G_r/U_s) will be a minimum, so that the possibility of the formation of a dendritic morphology structure increases. While at lower scanning speed, (G_r/U_s) will be a maximum. Consequently, the possibility of the formation of a dendritic morphology structure decreases [51].

While the lower half of the DED processed samples demonstrates more equiaxed morphology. That could be attributed to that the reheating of the previously deposited layers results in tempering of such layers which, in turn, leads to homogenisation. The dendritic morphology is likely present as highly strained grains, which developed as a result of rapid cooling during DED processing. These are subsequently replaced by an equiaxial morphology, potentially in the form of fresh strain-free grains, since there is significant difference in the stored energy between the undeformed and deformed material. Consequently, new small nuclei are formed in the inter-dendritic regions, which grow by

diffusion, until the original dendritic morphology are completely consumed by the new fresh, equiaxial morphology grains [65,139].

The EDS analysis of samples A1, C1 and C4 are presented in Figure 4.6. It was found that chromium carbides are mainly formed along the grain boundaries, as with prior observations for D2 [140]. Furthermore, it is worth noting that analysis of the carbon content via EDS analysis has certain limitations, as a low-Z element. For example, carbon can be over-estimated if there is contamination on the sample surface or within the SEM; for the present work, every effort was made to ensure the samples were thoroughly cleaned before analysis in the SEM. In addition, eutectic coring was observed to be formed at the outer layers of the dendritic structure, as illustrated in Figure 4.6. That arose because the composition of carbon in D2 tool steel (1.5 wt% C) is less than 4.3 wt% (the eutectic composition) but more than 0.5 wt% C (the peritectic composition). Consequently, such an alloy is considered 'off-eutectic'. In such a case, as illustrated in Figure 4.6, solidification usually initiates at the liquidus temperature for 1.5 wt% C, where primary γ dendrites form. As the thickness of the dendrite increases, solute (carbon in this case) is rejected into the remaining liquid until the 4.33 wt% C composition is achieved, at which point the eutectic liquid solidifies [56].

In terms of the formation of crystalline phases following the DED process, Figure 4.7 demonstrates a comparison between the XRD pattern of the baseline (i.e., as-received) annealed D2 tool steel (in wrought form) and the laser DED processed D2 tool. It was found that ferrite was the primary structure for the annealed D2 tool steel. However, austenite was the primary (dendritic) structure for the DED processed sample (sample A1). This arose because, despite the rapid cooling rate during the DED process, the high Cr and

C content in D2 tool steel leads to the formation of a metallic matrix which is mainly austenite and includes an excess of dissolved carbon. In turn, this depresses the martensitic formation temperature [140]. Comparing XRD for the DED processed samples (A1 and C4), as illustrated in Figure 4.7, it was observed that the primary structure for both of the samples was austenite. In addition, it was noted that the specific peak at 60˚ was higher for sample C4 (lower speed and low powder feed rate) than such of sample A1, indicating a greater amount of austenite is present.

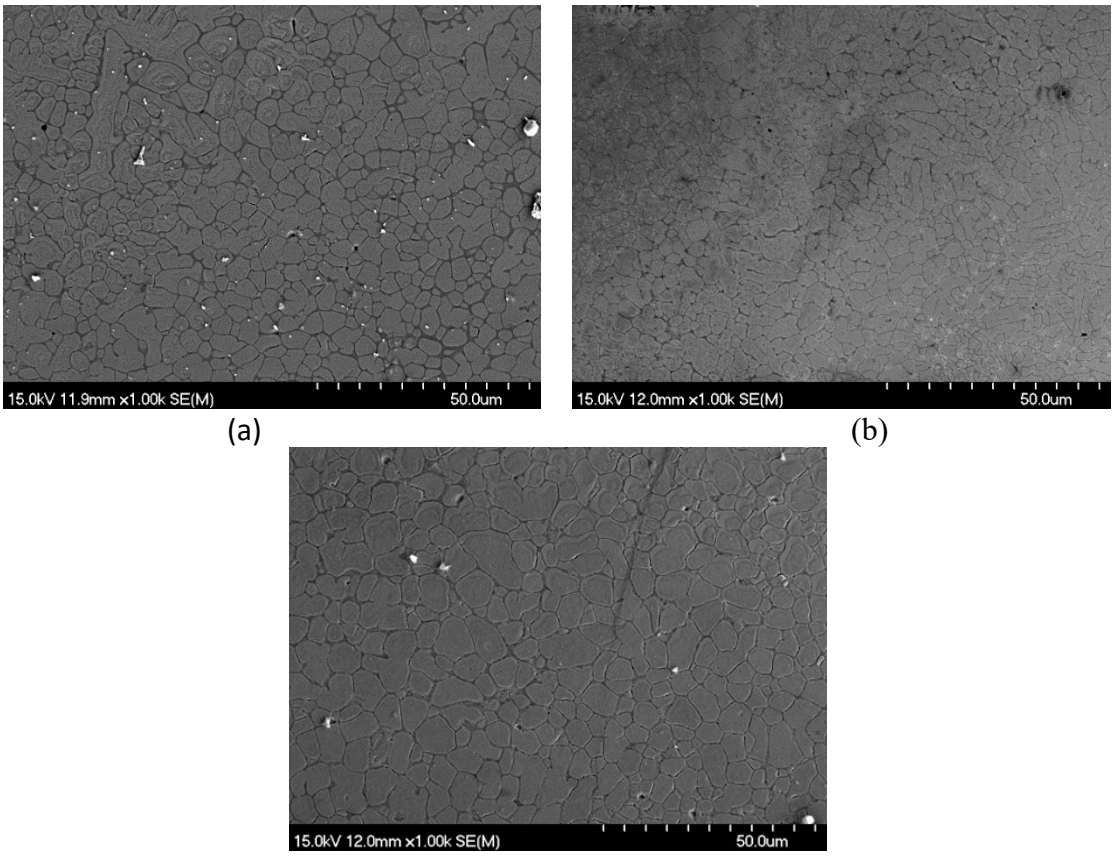

Figure 4.4. Representative SEM images of the lower half of DED processed samples: (a) A1, (b) C1, and (c) C4. Samples were etched with 5 vol% Nital solution.

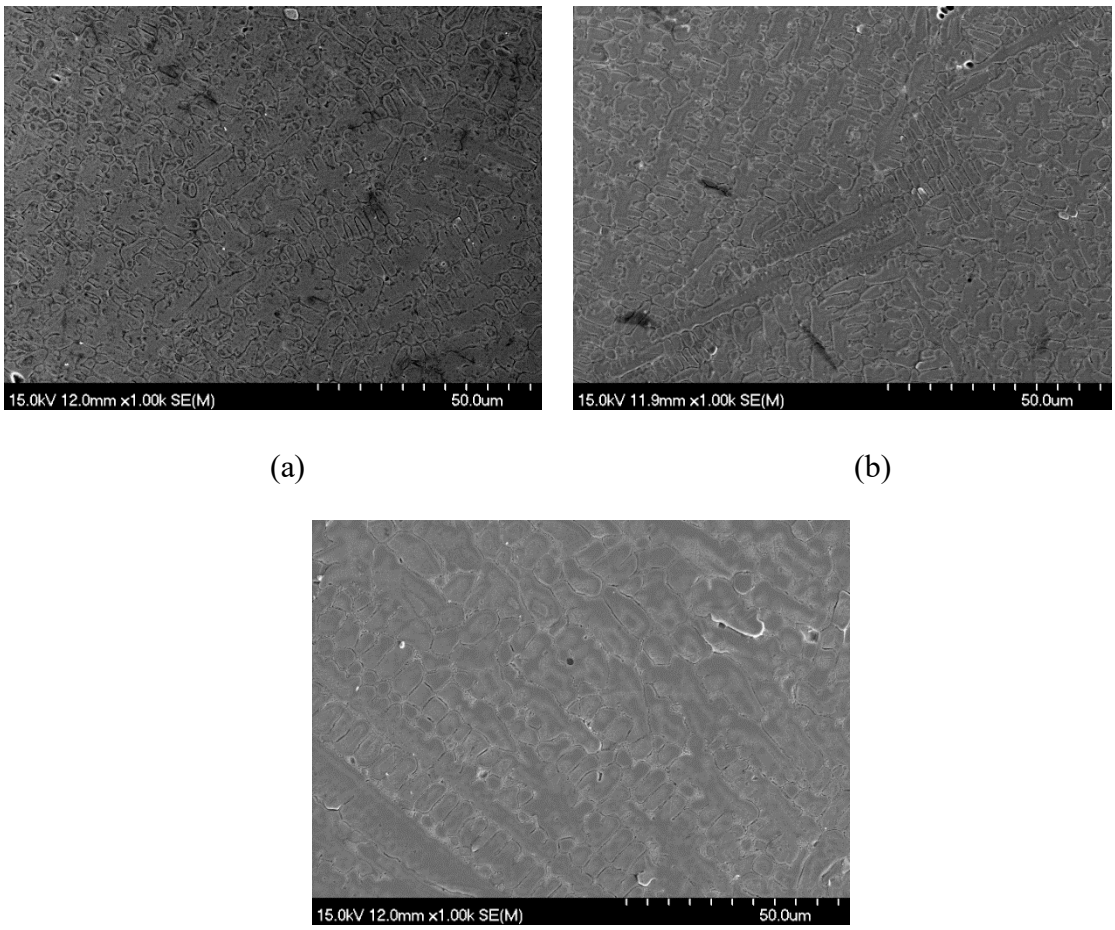

Figure 4.5. Representative SEM images of the upper half of DED processed samples: (a) A1, (b) C1, and (c) C4. Samples were etched with 5 vol% Nital solution.

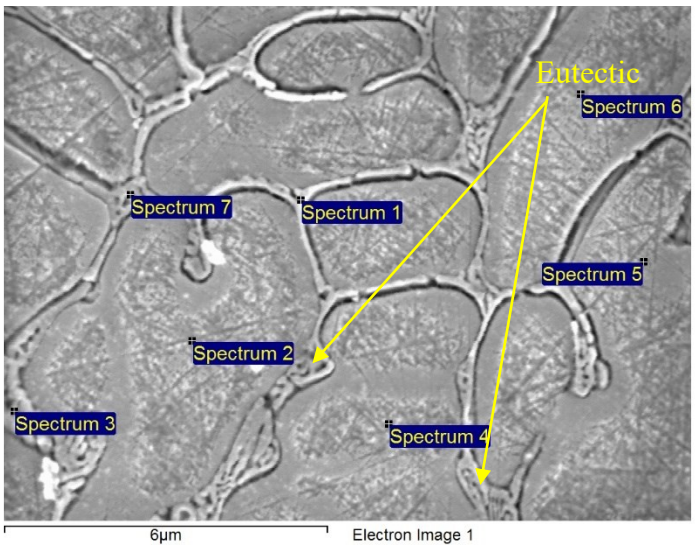

Spectrum	C	V	Cr	Fe
Spectrum 1	6.45	14.51	38.92	40.12
Spectrum 2	2.91	7.11	21.67	68.31
Spectrum 3	12.96	15.18	37.86	33.99
Spectrum 4	3.74	7.16	23.71	65.39
Spectrum 5	4.98	7.69	23.39	63.94
Spectrum 6	4.37	9.31	27.50	58.82
Spectrum 7	7.73	15.70	38.40	38.18

(a)

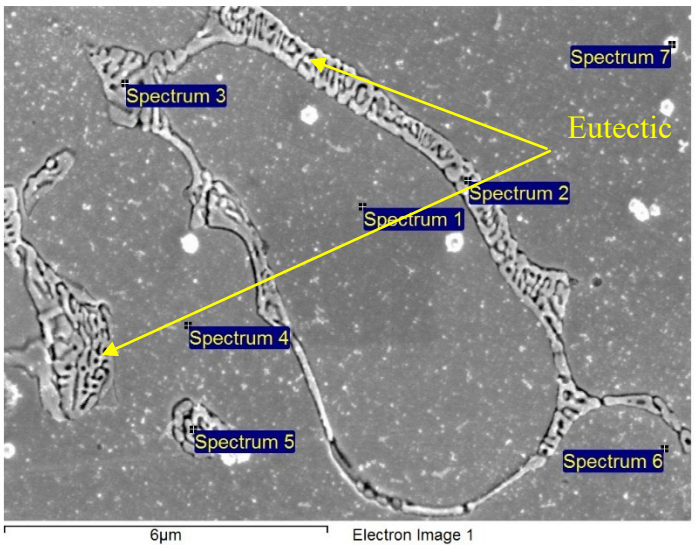

Spectrum	C	V	Cr	Fe
Spectrum 1	1.13	5.49	15.33	78.05
Spectrum 2	5.37	12.37	38.51	43.74
Spectrum 3	4.85	13.66	39.19	42.31
Spectrum 4	1.23	4.01	15.80	78.96
Spectrum 5	5.43	12.82	38.36	43.39
Spectrum 6	1.34	5.26	18.00	75.40
Spectrum 7	1.48	4.90	16.77	76.85

(b)

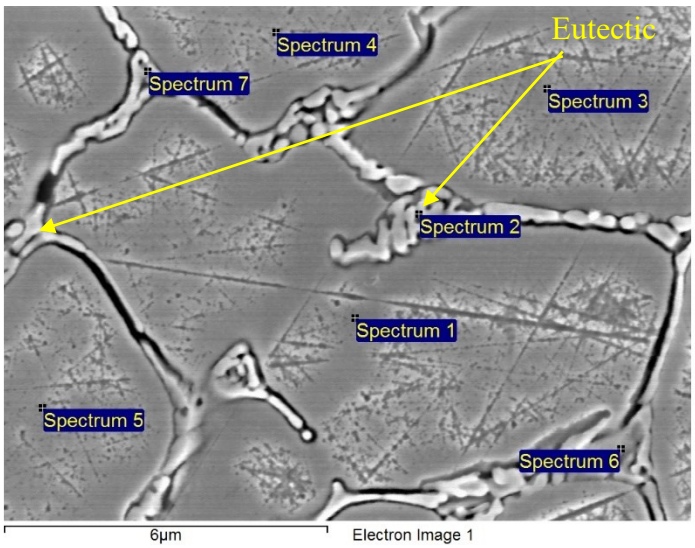

Spectrum	C	V	Cr	Fe
Spectrum 1	1.50	5.11	13.55	79.84
Spectrum 2	6.83	10.38	36.46	46.32
Spectrum 3	1.41	5.81	13.71	79.06
Spectrum 4	1.58	6.08	13.75	78.60
Spectrum 5	1.46	6.65	13.33	78.57
Spectrum 6	5.59	12.43	37.24	44.73
Spectrum 7	1.76	5.24	15.01	77.99

(c)

Figure 4.6. Representative SEM images and the associated EDS analysis data for the middle section of the DED processed samples: (a) A1, (b) C1 and (c) C4. Samples were etched with 5 vol% Nital solution. The presented compositions are wt.%.

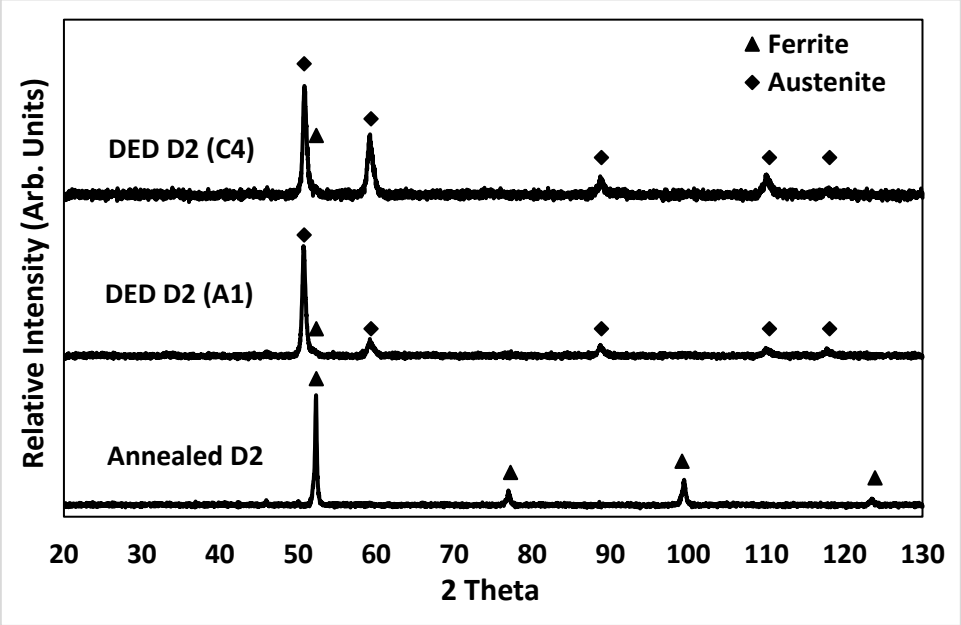

Figure 4.7. Comparison of the XRD patterns recorded for the DED processed D2 samples as-printed (A1 and C4) and annealed D2.

3.3. Microstructural Analysis of Heat-Treated Samples

Figure 4.8 and 4.9 show representative SEM micrographs and the associated EDS analysis for a heat-treated wrought D2 tool steel sample. As demonstrated in Figures 4.8(a) and 4.9(a), it was found that the annealed D2 tool steel contains coarse particles of M_7C_3 carbides, which was precipitated during solidification [132]. Figures 4.8(b) and 4.9(b) illustrate the microstructure of the as air-cooled wrought D2 tool steel. In spite of the dissolution of the smaller carbides during the austenitizing stage, it was observed that the microstructure of the air-cooled specimen contains clearly visible primary and secondary carbides. In addition, the retained austenite and martensitic laths in the matrix could not be resolved due to their fine scale [132].

As illustrated in Figures 4.8(c)-(i), it was observed that the increase in tempering temperature results in an increasing amount of fine secondary carbides, in addition to coarsening of the primary carbides. This arises because tempering of D2 tool steel at

temperatures higher than 300°C leads to decomposition of the retained austenite into the thin grain boundary films of cementite. Since D2 tool steel contains a high chromium content (≈12 wt%), which is a strong carbide-forming element, chromium carbides are formed at the expense of cementite (as carbon is effectively preferentially taken by the chromium). However, the nucleation and growth of chromium carbides occurs through substitutional diffusion, in contrast to the interstitial movement of carbon through the iron lattice, so that the formation of alloy carbides therefore takes place at higher temperatures, which are required to initiate the crucial diffusion of chromium [141].

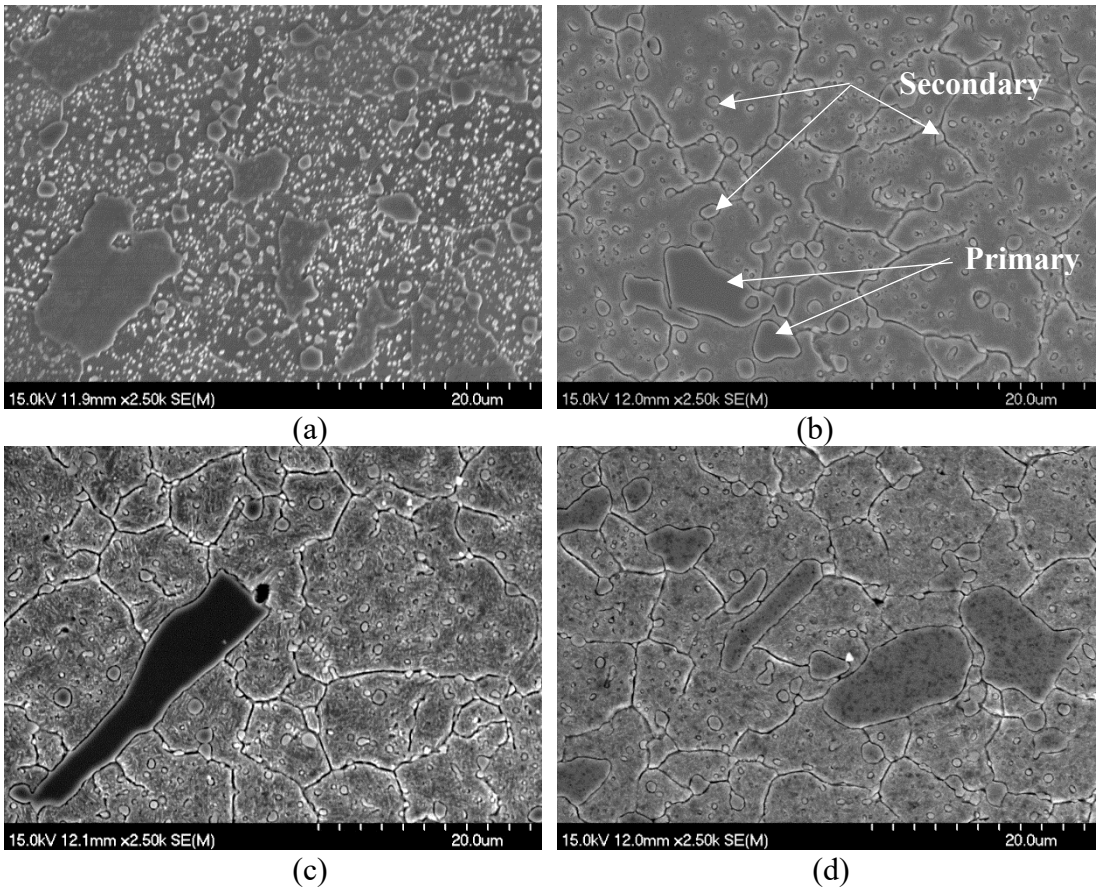

(a) (b)

(c) (d)

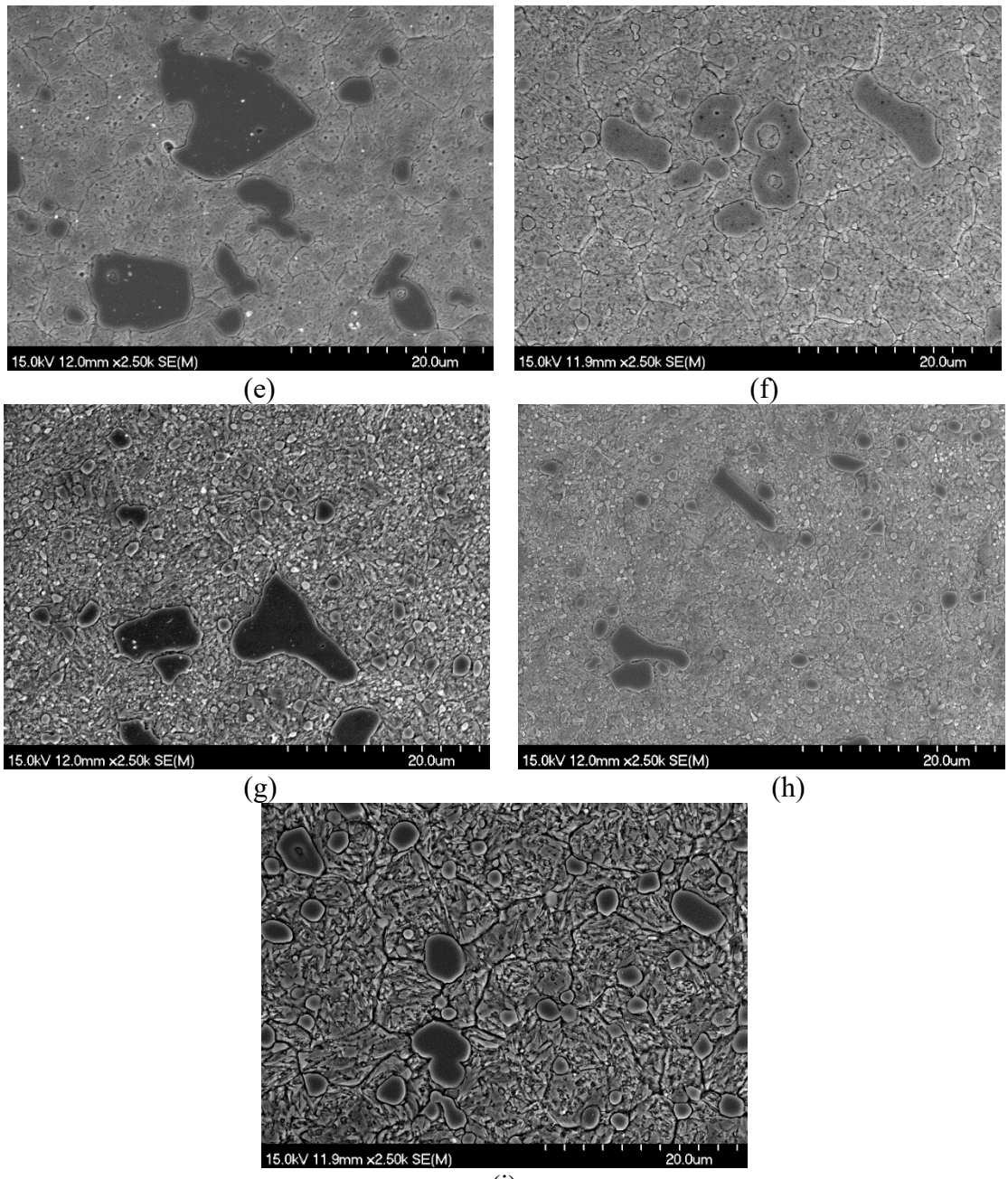

(e) (f)

(g) (h)

(i)

Figure 4.8. Representative SEM images of wrought D2 tool steel for different heat-treatment conditions: (a) as-received, (b) air-cooled , (c) tempered at 400°C, (d) double-tempered at 400°C, (e) tempered at 500°C, (f) double-tempered at 500°C, (g) tempered at 600°C, (h) double-tempered at 600°C, and (i) tempered at 400°C followed by retempering at 500°C (DT4-5). Samples were etched with 5 vol% Nital solution.

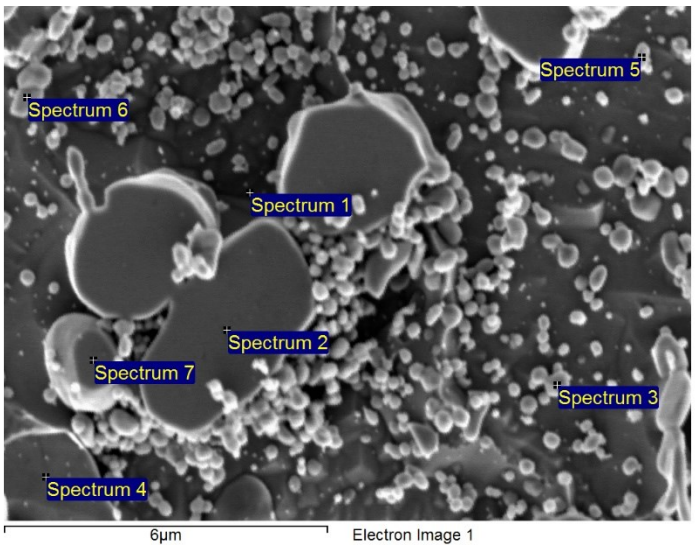

Spectrum	C	V	Cr	Fe
Spectrum 1	1.05	5.61	9.16	84.17
Spectrum 2	6.63	8.82	45.81	38.74
Spectrum 3	6.29	7.00	55.79	30.93
Spectrum 4	0.86	3.83	7.21	88.10
Spectrum 5	6.61	3.97	50.69	38.72
Spectrum 6	3.80	7.05	66.96	22.19
Spectrum 7	6.46	8.66	45.89	38.99

(a)

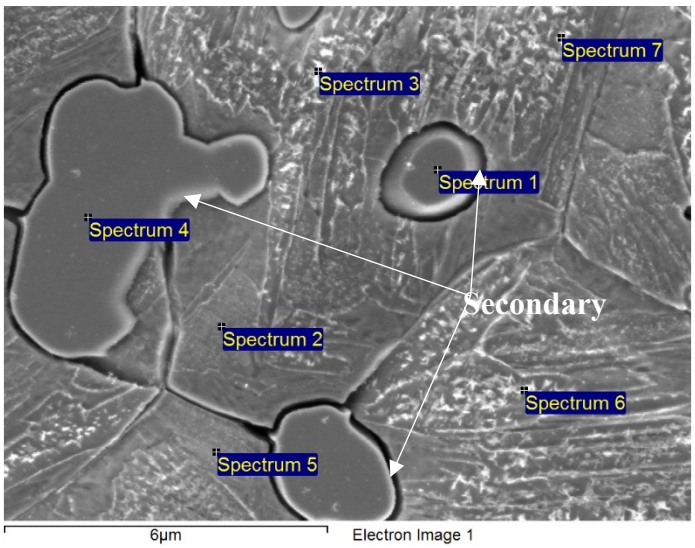

Spectrum	C	V	Cr	Fe
Spectrum 1	6.28	8.70	45.51	39.51
Spectrum 2	0.84	4.42	10.45	84.29
Spectrum 3	1.69	8.35	11.34	78.63
Spectrum 4	6.09	8.79	45.93	39.19
Spectrum 5	1.05	5.79	11.22	81.94
Spectrum 6	1.57	7.78	10.42	80.23
Spectrum 7	0.98	6.03	11.92	81.08

(b)

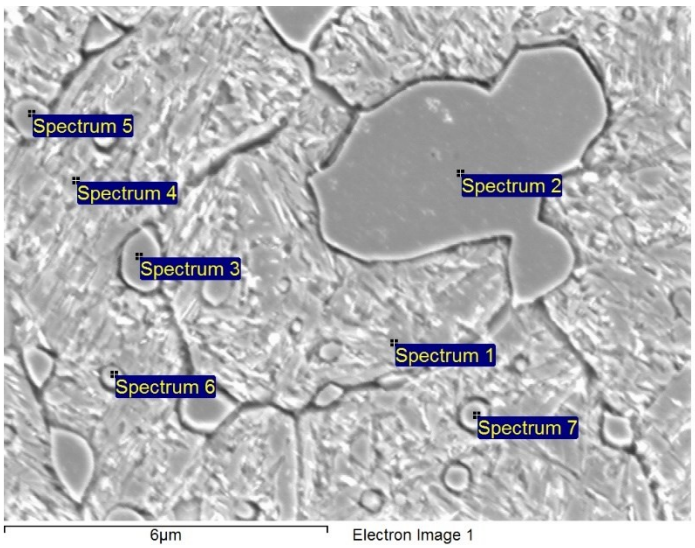

Spectrum	C	V	Cr	Fe
Spectrum 1	1.05	4.96	10.92	83.07
Spectrum 2	7.07	8.36	46.58	37.99
Spectrum 3	6.57	8.38	45.82	39.23
Spectrum 4	1.11	6.61	11.48	80.80
Spectrum 5	6.51	7.29	48.33	37.87
Spectrum 6	4.95	8.71	33.92	52.42
Spectrum 7	5.24	7.60	37.34	49.82

(c)

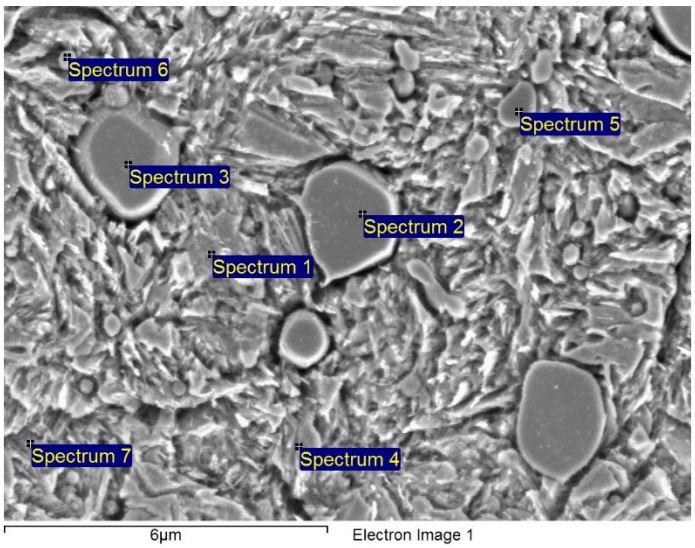

Spectrum	C	V	Cr	Fe
Spectrum 1	1.53	8.62	12.09	77.76
Spectrum 2	6.36	7.84	45.56	40.24
Spectrum 3	6.43	8.57	45.63	39.37
Spectrum 4	0.93	4.68	10.36	84.03
Spectrum 5	6.62	6.52	45.79	41.08
Spectrum 6	4.19	8.38	24.94	62.48
Spectrum 7	1.21	9.00	12.05	77.74

(d)

Figure 4.9. Representative SEM images and the associated EDS data for wrought D2 tool steel for different heat-treatment conditions: (a) as-received, (b) air-cooled , (c) double-tempered at 500°C, and (d) tempered at 400°C followed by retempering at 500°C (DT4-5). Samples were etched with 5 vol% Nital solution. The presented compositions are all in wt.%.

In terms of the effects of the heat-treatment on the microstructures of the DED processed samples, representative SEM images and EDS analyses of sample C1, both before and after heat-treatment are illustrated in Figures. 4.10 and 4.11. It was observed that, after heat-

treatment, fine secondary carbides were precipitated in the matrix (spectrum 3 in Figures 4.11(b)) due to the substitutional diffusion of chromium into the matrix to form chromium carbides at the expense of cementite [142]. . In contrast, chromium carbides were only formed at the grain boundaries in the case of as-processed DED sample. Furthermore, it was found that the grain structure at the upper-half of the as-processed DED sample C1 initially had a dendritic morphology with associated columnar grains, as shown in Figure 4.10(c). Conversely, after initially tempering at 400°C, followed by a second tempering step at 500°C, this grain morphology has converted into a significantly more equiaxed microstructure Figure 4.10(d). This transformation can be viewed as arising as a result of homogenisation during the heat treatment process. In this instance fresh, equiaxial morphology, strain-free grains are formed in place of the deformed grains (i.e., a dendritic morphology which resulted from rapid cooling after DED processing), due to the difference in the stored strain energy between the deformed and undeformed material. As noted earlier, new small nuclei may be generated in the inter-dendritic regions, which then grow by diffusion, consuming the original dendritic morphology [65,139].

In terms of crystallography, Figure 4.12 illustrates the effects of heat-treatment on the XRD pattern of the DED processed sample. It was observed that, as mentioned before, the base dendritic structure in the as-deposited samples was austenite. However, after the heat-treatment sequence (austenitising, air-cooling and tempering), the austenite in the dendritic structure was transformed into tempered-martensite, as confirmed by XRD pattern where the austenite peaks were replaced by ferrite peaks which represents tempered-martensite. This can be attributed to the fact that, at the austenitizing temperature, diffusion of excess carbon within the austenite phase has arisen into the eutectoid structure, forming chromium

carbides. As a consequence, the carbon content in the austenite decreases, which, in turn, increases the martensitic transformation temperature [141].

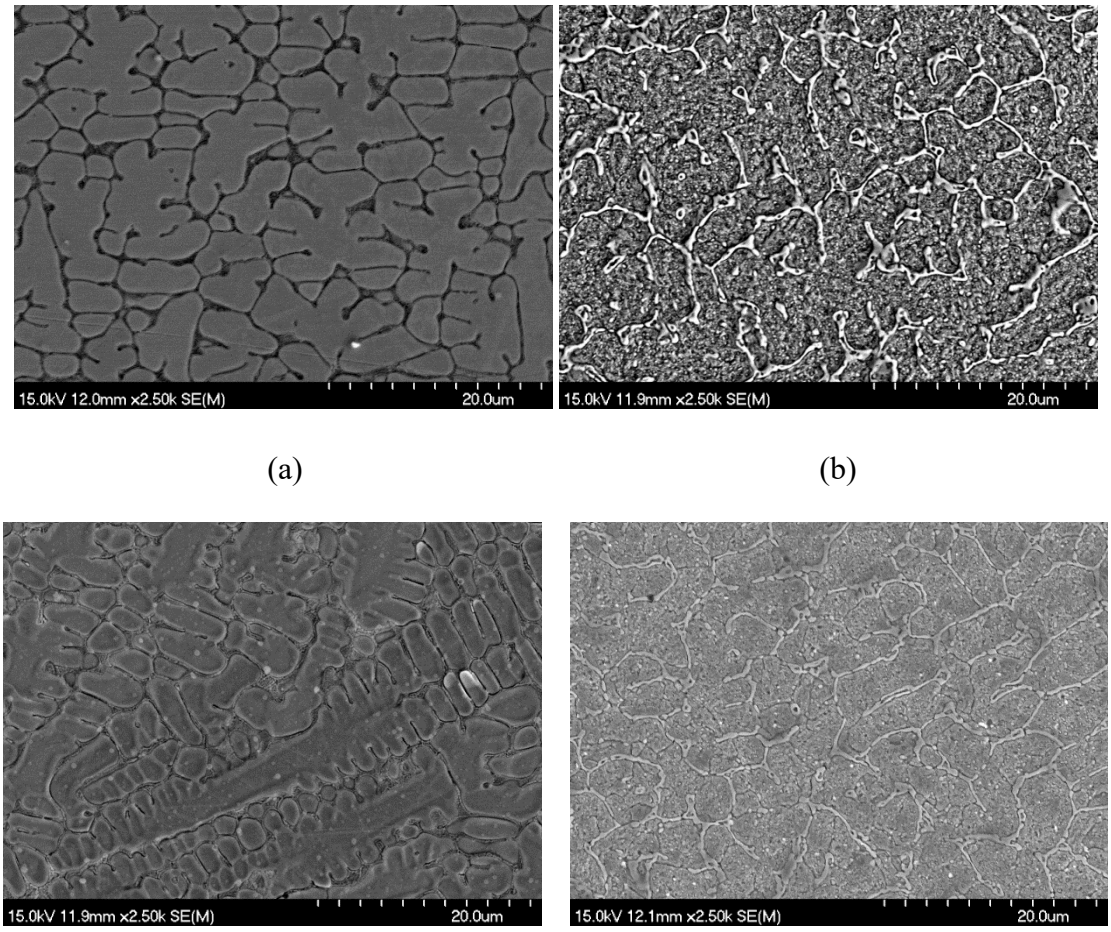

Figure 4.10. Representative SEM images of the lower (a,b) and upper (c,d) halves of the DED sample processed following conditions C1. Images were recorded both before (a,c) and after (b,d) heat-treating with a tempering treatment at 400°C, followed by retempering at 500°C (DT4-5), respectively. Samples were etched with 5 vol% Nital solution.

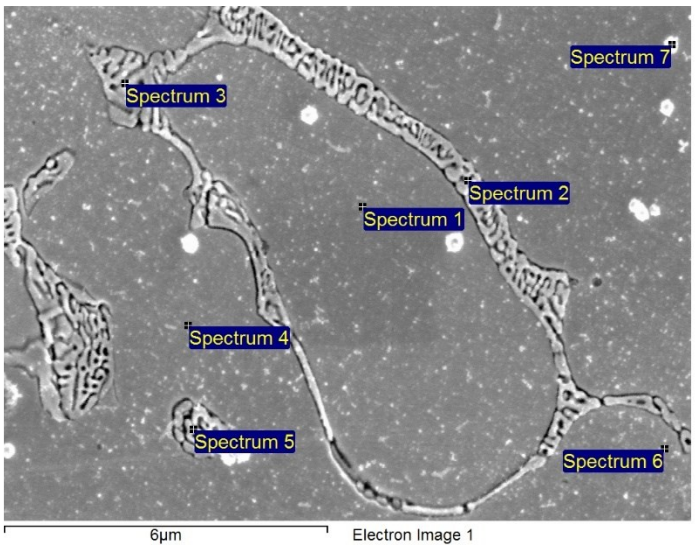

Spectrum	C	V	Cr	Fe
Spectrum 1	1.13	5.49	15.33	78.05
Spectrum 2	5.37	12.37	38.51	43.74
Spectrum 3	4.85	13.66	39.19	42.31
Spectrum 4	1.23	4.01	15.80	78.96
Spectrum 5	5.43	12.82	38.36	43.39
Spectrum 6	1.34	5.26	18.00	75.40
Spectrum 7	1.48	4.90	16.77	76.85

(a)

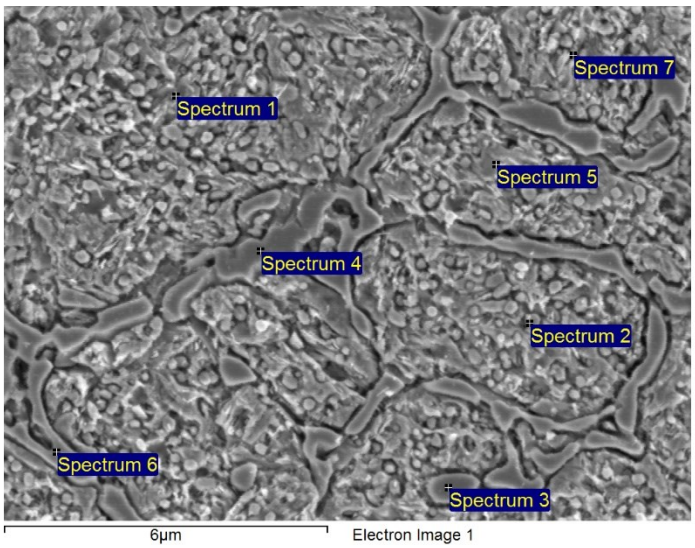

Spectrum	C	V	Cr	Fe
Spectrum 1	1.72	6.16	13.08	79.04
Spectrum 2	2.14	8.81	11.38	77.67
Spectrum 3	4.35	9.56	28.56	57.54
Spectrum 4	6.81	10.13	43.23	39.83
Spectrum 5	1.07	5.45	9.42	84.06
Spectrum 6	1.47	6.40	12.30	79.83
Spectrum 7	2.21	8.58	11.44	77.77

(b)

Figure 4.11. EDS analysis of (a) as-printed sample C1, and (b) heat-treated sample C1 (after heat-treating under tempering at 400°C followed by retempering at 500°C (DT4-5)). Samples were etched with 5 vol% Nital solution. The presented compositions are all in wt.%.

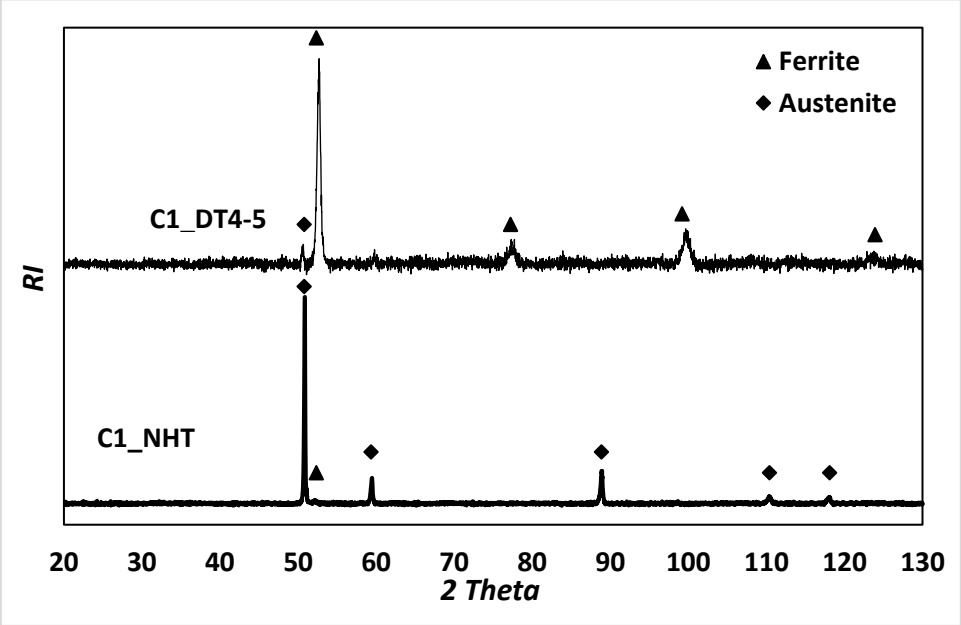

Figure 4.12. Influence of heat-treatment on the measured XRD pattern for the DED processed D2.

4.3.3 Rockwell Hardness Measurements

The indentation hardness values for the wrought, DED as-processed, and heat-treated D2 tool steel samples (both wrought and DED processed) were determined using the Rockwell C scale hardness test. Figure 4.13(a) demonstrates the influence of both the laser scanning speed and powder feed rate on the Rockwell hardness, for samples spatially located at the bottom, middle and top regions of the as-printed DED parts. Generally, it can be readily noted that the hardness at the bottom of the sample, near to the original substrate, is much lower than that measured in either the middle or upper regions after laser deposition. In the initial stage of deposition the cooling rate is relatively higher than in the later stages, due to the lower temperature in the regions adjacent to the deposited material and the heat dissipation through the substrate which acts as a heat sink, in earlier stages of the deposition, in comparison to the more accumulated heat and shallower temperature gradients, at later stages of deposition; the lower hardness at the bottom of the samples

can be attributed to the reheating effect that occurs on the initially deposited layers, which leads to grain growth and consequently a reduced hardness through the Hall-Petch effect [143–145].

Regarding the impact of the laser scanning speed and powder feed rate, as presented in Figure 4.13, some clear variation in mean hardness between the different samples is apparent. It was observed that, for the same powder feed rate, there is a peak recorded for mean hardness at a scanning speed of 600 mm/min. It is thought that this arises because the scanning speed influences the properties of the deposited material in two opposing ways. The first is that a lower scanning speed results in more available time for heat to be absorbed by the deposited layer (and substrate), which leads to a lower temperature gradient. However, the use of a lower scanning speed would also increase the period of time before the same point on the deposited layer is reheated by the next pass of the laser heat source. Consequently, a greater amount of time is available to cool down, which results in a lower rate of temperature build up, and hence a higher temperature gradient. Therefore, the mean hardness results were evaluated by estimating the mean cooling rate (using Equation 4.2), as a function of the process parameters. The calculated cooling rates for selected examples of the processing conditions are presented in Figure 4.14. Comparison of the measured hardness, in Figure 4.13, with the cooling rates estimated in Figure 4.14 (a), demonstrates that the calculated mean cooling rates for the DED processed samples are broadly consistent with the trends observed for the mean hardness. The proportional relationship between the measured hardness and the calculated mean cooling rates is illustrated in Figure 4.14 (b). A higher mean cooling rate was found at a scanning

speed of 600 mm/min, which corresponds with the highest measured mean Rockwell C hardness for the as-printed samples.

In addition, it was observed that the effects of powder feed rate upon the mean hardness are highly dependent on the laser scanning speed. The lowest mean hardness was measured at the lower powder feed rate (5.5 g/min), due to a Hall-Petch related effect. This arises because, at the lower powder feed rate, there is less available powder for heat absorption, which leads to higher temperature gradients. Consequently, this causes grain growth in the deposited material, as shown previously in Figure 4.5(c), leading to a decrease in the mean hardness. Finally, in terms of optimised properties, the highest mean hardness, in the middle of the sample, was recorded at a scanning speed of 600 mm/min and powder feed rate of 7.5g/min for the present materials in the DED as-processed state (sample A2).

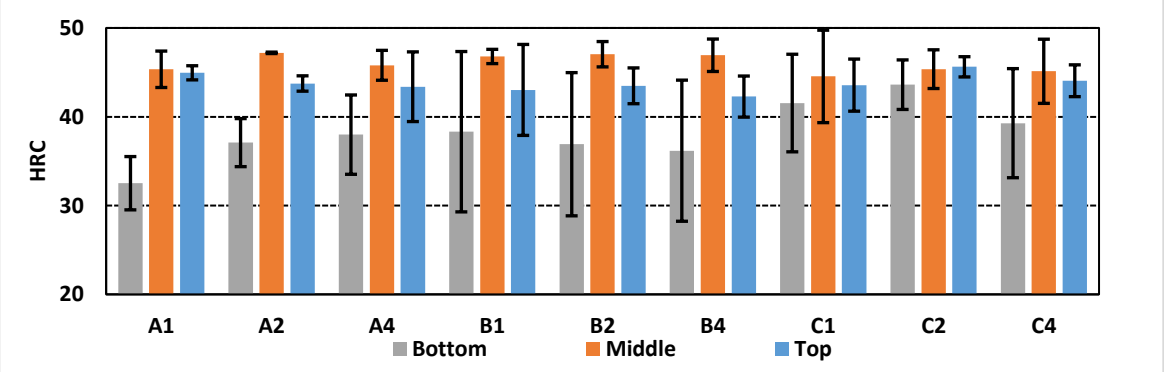

Figure 4.13. Measured Rockwell C indentation hardness of selected 'as-printed' samples as a function of location.

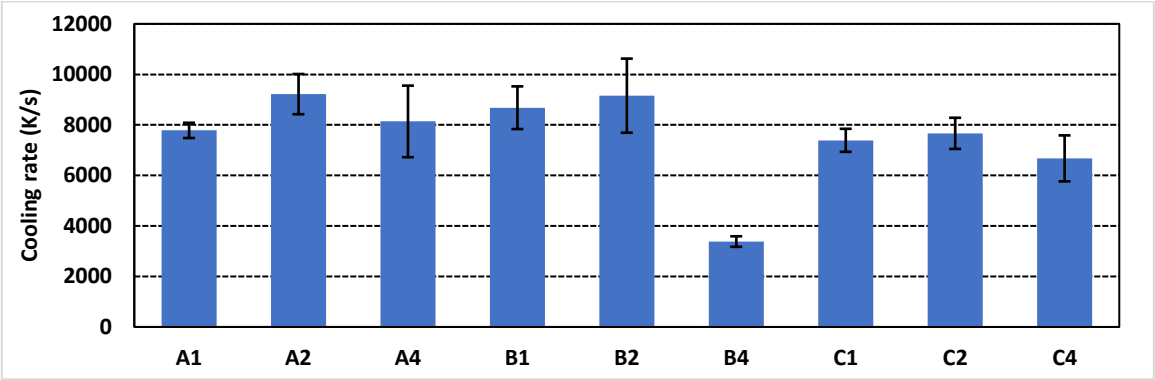

(a)

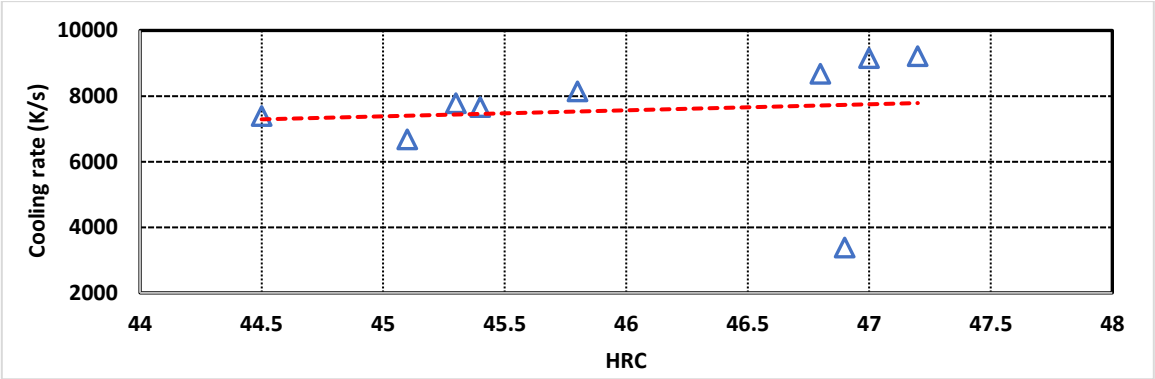

(b)

Figure 4.14. (a) Calculated cooling rate of selected 'as-printed' samples using Equation 4.2, and (b) The relationship between the measured hardness and the calculated mean cooling rates.

The heat-treatment effects on the hardness of wrought D2 tool steel are shown in Figure 4.15, under the heat-treatment scenarios mentioned previously in Table 4.3. It was found that the air-cooled sample has the highest hardness, at 63.4 HRC, in comparison to 20.7 HRC for the wrought D2 tool steel. This significant increase can be attributed to the formation of high hardness martensite in the air-cooled D2 tool steel [132].

It is apparent that the hardness values of the heat-treated samples were lower than air-cooled state, as a result of the decomposition of martensite (formed in the air-cooling step) into ferrite and carbide phases [146]. Additionally, the increase in either single or double tempering temperature from 300°C to 500°C results in only a modest change in hardness

(≈2.5 HRC). This arose because of the secondary hardening phenomenon, which is a form of age-hardening response, where comparatively much finer alloy carbides are formed in preference to coarse cementite [147]. As mentioned before, at higher tempering temperatures than 300°C, decomposition of the retained austenite into thin grain boundary films of cementite occurs. The high content of chromium in the D2 tool steel composition then leads to the formation of chromium carbides, at the expense of cementite, upon tempering. However, high temperatures are needed to initiate the substitutional diffusion of chromium into the cementite matrix, such that greater tempering benefits are observed at the higher temperatures. The critical temperature was previously determined to be around 500°C [141] which corresponds well with present observations. Consequently, there is a plateau in the hardness values, for either single or double tempering, within the temperature range of 300-500°C, with a further slight increase when double tempering at 500°C. Nevertheless, it could be observed that the use of single or double tempering temperature higher than 500°C leads to significant drop in hardness. This is due to the expectation that, at temperatures higher than 500°C, chromium carbide coarsening rapidly occurs, which leads to a decrease in hardness [141].

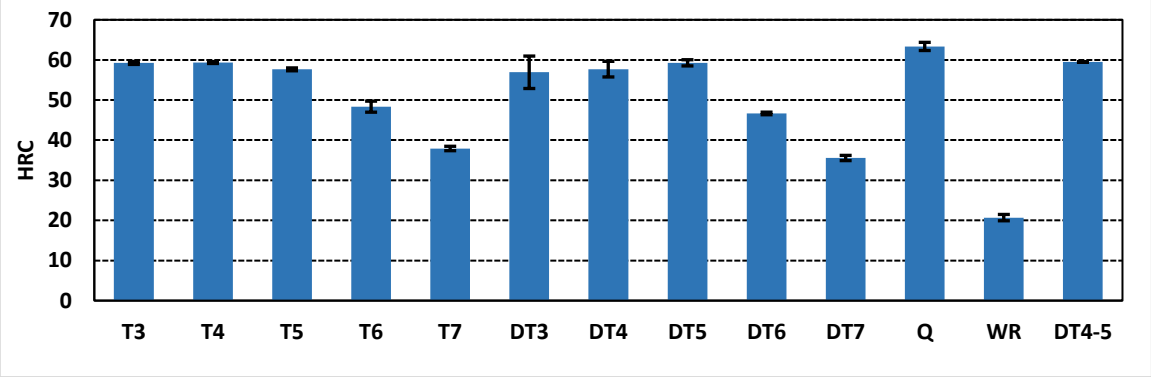

Figure 4.15. The effects of tempering heat-treatment schedules upon the Rockwell C hardness values of wrought D2 tool steel.

Figure 4.16 shows the effects of heat-treatment on the DED fabricated samples; in this instance a sub-set of tempering cycles have been selected from those evaluated for the wrought. It was found that the tempering heat-treatments significantly improve the hardness of the DED processed samples, generating values as high as the air-cooled (wrought) D2 tool steel. This can potentially be explained in terms of the transformation of austenite in the dendritic regions of the DED processed samples, forming martensite during heat treatment [132,146]. Another reason for this high hardness is the formation of extremely fine carbides, as illustrated through the EDS analysis (Figure 4.9). Both of these reasons result in improvement in hardness of the heat-treated samples [148]. Finally, it was observed that the hardness of the heat-treated DED processed sample under the DT4-5 scenario was marginally higher than was achieved after heat-treated by using double tempering at 500˚C. Here a clear nucleation and growth treatment appears to be beneficial for initially forming very fine nuclei, that can then be grown in the secondary stage at the higher temperature. In addition, as illustrated in Figure 4.16 (b), it could be observed that, after heat-treatment, the previously clear differences in hardness between the bottom, middle, and top of the sample has almost disappeared. That could be attributed to homogenisation due to heat treatment, as explained previously in Section 4.3.2.

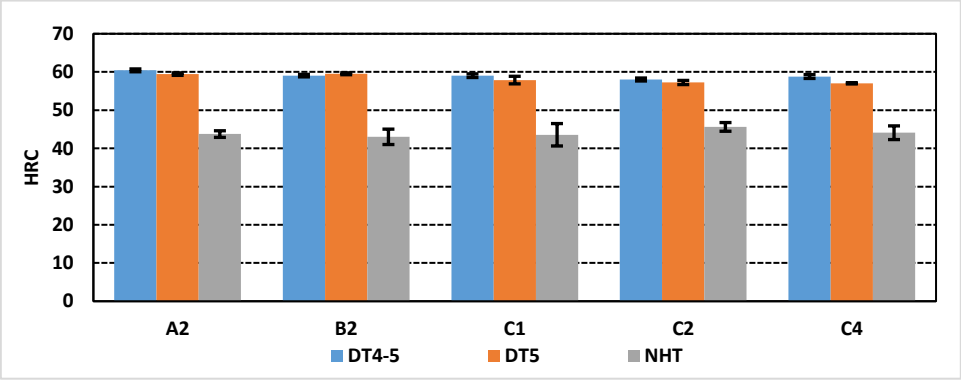

(a)

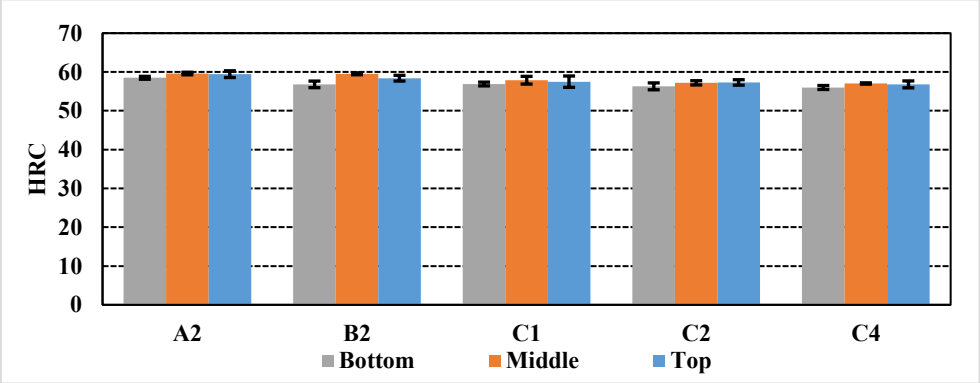

(b)

Figure 4.16. Measured Rockwell C indentation hardness of selected heat-treated DED processed samples: (a) comparison between the different heat-treatment sets, and (b) as function of position along the sample height, for DED heat treated samples, double tempered at 500°C.

4.3.4 Scratch Hardness Evaluation

In order to further examine the effects of both the basic DED process parameters and the heat-treatment schedules upon the mechanical response, the scratch hardness values of the wrought D2, DED as-deposited D2, and both the heat-treated wrought and DED-processed D2 tool steel samples, were assessed. As mentioned previously, the data was evaluated on the CLSM using the Keyence Multifile Analyzer software; the scratch width was measured using the CLSM and applied to Equation 4.1 to indicate the scratch hardness. In terms of the as-processed DED samples, the measured scratch hardness values, as a function of location (bottom, middle and top of the DED fabricated parts), are illustrated in Figure 4.17. It was observed that the mean scratch hardness at the bottom of the sample, near to the original substrate, is slightly lower than in the middle, or the upper regions of the sample. This observation, which is in agreement with the previously shown Rockwell C hardness measurements, can be attributed to the grain size and associated Hall-Petch response, in which the reheating effect on the initially deposited layers leads to higher

temperature gradients and lower cooling rate. In turn, this results in grain growth and, ultimately, a reduced hardness.

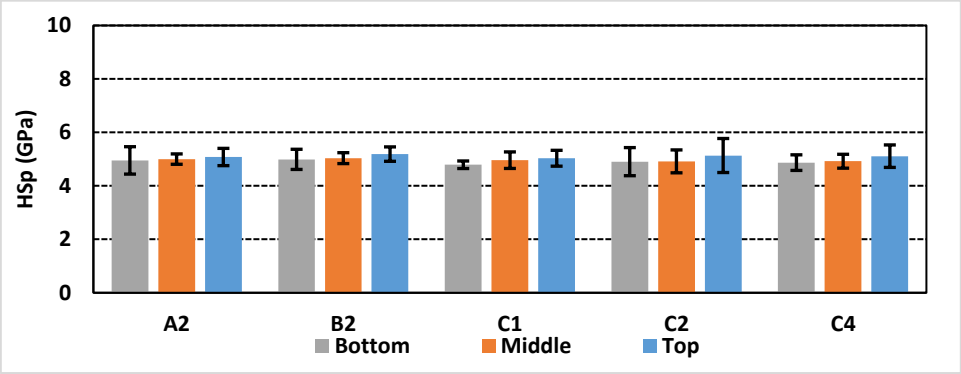

Figure 4.17. Scratch hardness measurements of selected, as-printed DED samples as a function of spatial location in the sample relative to the build orientation.

Figure 4.18(a) presents the impact of the various heat-treatments upon the scratch hardness of the wrought D2 tool steel. It was significant, and largely expected, that the scratch hardness results exhibit the same trends as indentation hardness. It was observed that the maximum scratch hardness values were recorded in the air-cooled samples, due to the presence of formed martensite following air-cooling of the D2 tool steel [132]. Furthermore, after tempering or double-tempering, it was found that decomposition of the martensite developed during the air-cooling stage, into carbides and ferrite after heat treatment, leads to lower scratch hardness in the tempered samples than the air-cooled ones [146].It was found that there was a peak for scratch hardness when single tempering at 500°C, double tempering at 400°C, or tempering at 400°C followed by retempering at 500°C. This could be attributed to the secondary hardening phenomenon outlined earlier; at a single or double tempering temperature higher than 300°C, fine chromium carbides are evolved in the matrix, replacing coarse cementite, which is formed as a result of the decomposition of the retained austenite [147]. Since the evolution of chromium carbides is

profoundly dependent upon temperature, due to the development of these carbides is arising from substitutional diffusion, the amount of the fine chromium carbides increases with increasing tempering temperature [141]. This broadly explains the observed increase in scratch hardness by increasing the single or double tempering temperature. However, as with the Rockwell hardness evaluation, at very high tempering temperatures, the chromium carbides quickly coarsen, which leads to the significant drop in scratch hardness after single or double tempering at higher than 500°C.

In terms of the use of an optimised heat-treatment upon the scratch hardness values for the DED-processed samples (Figure 4.18(b)), it is seen that the scratch hardness is improved after a post-DED tempering heat-treatment. It is again apparent that this arose because of the development of fine secondary carbides in the matrix for the heat-treated DED samples, in comparison to the formed carbides being only present at the grain boundaries for the as-deposited DED samples, as confirmed by the prior EDS analysis presented in Figure 4.9. Furthermore, the evolution of tempered-martensite occurs during heat-treatment in expense of the austenite in the dendritic region, as demonstrated in the XRD analysis in Figure 4.12.

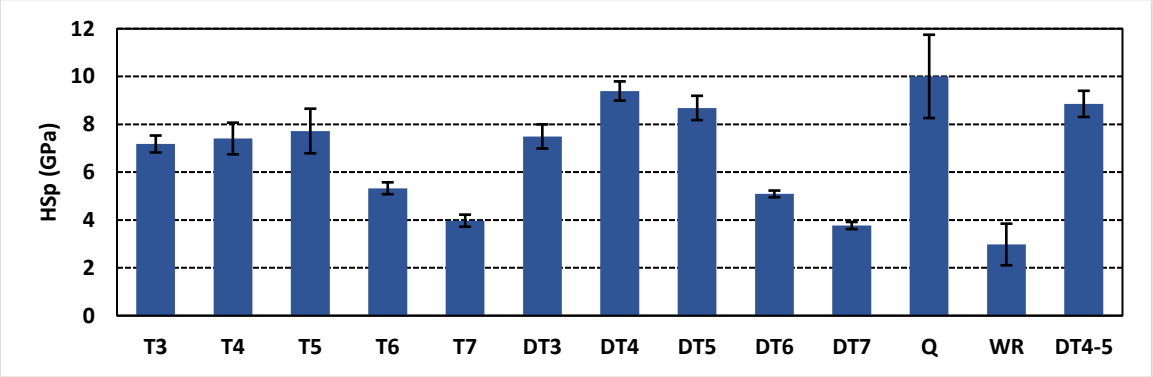

(a)

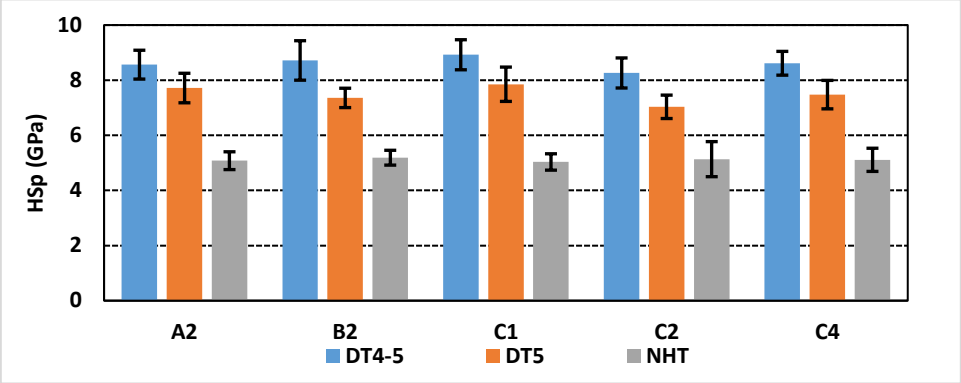

(b)

Figure 4.18. (a) Scratch hardness of wrought and heat-treated D2 tool steel. (b) Scratch hardness measurements of the heat-treated DED samples as a function of temper treatment.

4.4 Conclusions

The present work has focused upon the effects of laser scanning speed and powder feed rate on the microstructure, indentation hardness, and scratch hardness of laser DED-processed D2 tool steel clads. A study has also been conducted into the effects of various tempering scenarios, comparing wrought D2 with the response of heat-treated DED-processed samples.

The following conclusions were obtained from the study:

- In terms of the sample microstructures after DED processing, the middle zone of the DED processed samples showed a dendritic morphology, with the presence of columnar grains, which was attributed to the constitutional cooling as a result of rapid cooling of the DED processed samples. A more equiaxed morphology was observed at the lower half of the DED processed samples.
- After tempering heat-treatment, the dendritic morphology transforms into a significantly more equiaxed microstructure through homogenisation. Additionally, fine secondary carbides were precipitated in the matrix due to substitutional

diffusion of chromium into the matrix to form chromium carbides at the expense of cementite. In contrast, chromium carbides were only formed at the grain boundaries for the as-processed DED samples.

- Austenite was the primary (dendritic) structure for the DED processed sample, despite the rapid cooling rate during the DED process; the high chromium and carbon content in D2 steel leads to the formation of a metallic matrix which is primarily austenite and includes excess dissolved carbon. In turn, this suppresses the martensitic formation temperature.
- After heat-treatment, the austenite in the dendritic structure was transformed into tempered martensite. At the austenitizing temperature, diffusion of excess carbon in the austenite occurs into the eutectoid structure, forming chromium carbides. Consequently, the carbon content in the austenite decreases, increasing the martensitic transformation temperature.
- In terms of the indentation and scratch hardness of the 'as-deposited' DED-processed parts, the initially deposited layers (adjacent to the substrate) were much lower than that measured in either the middle or upper regions after laser deposition. This is attributed to the reheating effect that occurs for the initially deposited layers, which leads to grain growth and consequently a reduced hardness through the Hall-Petch effect.
- Applying tempering to the DED processed samples, it was observed the heat-treatments significantly improve the hardness, to essentially the level of the air-cooled D2 tool steel. This can be explained in terms of the transition from austenite

in the dendritic regions of the DED clads, to a tempered martensite during the heat treatment in combination with the formation fine secondary carbides.

Acknowledgements

The authors would also like to thank the technical assistance of Mr. Randy Cooke and Dr. Greg Sweet (Dalhousie University) with DED printing of the samples. Ms. Patricia Scallion is also gratefully acknowledged for support with both SEM and XRD analyses. This work was financially supported through the NSERC Strategic Project Network Grant Holistic Innovation in Additive Manufacturing (HI-AM) through [Grant No. NETGP 494158-16].

CHAPTER 5 The Influence of DED Process Parameters on the Geometrical Properties and Surface Roughness of AISI D2 Tool Steel

Status: ***Submitted***: Surface & Coatings Technology

Abstract

The influence of laser directed energy deposition (DED) process parameters (laser power, laser scan speed, and powder feed rate) were assessed in terms of the geometrical characteristics and surface roughness when cladding AISI D2 tool steel onto annealed, like-composition substrates. The impacts of laser scanning speed, and powder feed rate were evaluated. The geometrical characteristics of the DED processed clads, including the size of single clads, in addition to dimensional accuracy of the multi-layer specimens, were examined using confocal laser scanning microscopy (CLSM). It was concluded that the use of higher laser scanning speeds decreases both the size of single clads and the level of sample over-building. However, there was no clear trend for powder feed rate on either single clad size or dimensional accuracy. Furthermore, the surface roughness was also assessed using CLSM, to evaluate the influence of the various DED operating conditions. It was demonstrated that the amount of partially un-melted powder particles adhered to the sample surface significantly affects the surface roughness of the DED processed specimens. Moreover, the ability to deposit overhang structures using DED was investigated by depositing inclined thin walls, under various process parameters and angles of inclination. The impact of the process parameters and the angle of inclination on both angle accuracy and side surface roughness were analysed using CLSM.

Keywords: tool steels; laser direct energy deposition; surface roughness; dimensional accuracy; overhang structure; confocal laser scanning microscopy

5.1 Introduction

Additive manufacturing (AM) involves the use a computer aided design (CAD) model to subsequently fabricate complex-shaped parts [10,30–33]. One AM approach for metal components, known as laser directed energy deposition (DED), involves creation of a small melt pool of metal, as a result of heating a metallic substrate with the aid of laser beam, while a fine powder stream is deposited into the molten pool using a powder delivery system [34,36]. The general DED approach has also been referred to as laser coating [37,38], laser consolidation [39], laser direct casting [40], laser powder deposition [41,42], rapid prototyping [43], or solid free-form fabrication [44].

DED has several benefits in comparison to other AM techniques. For example, high-value components can be conserved instead of being replaced outright, by means of employing DED for the purpose of repairing corroding or worn surfaces [46,47]. In contrast, one of the principal drawbacks of DED is that the quality of the manufactured part has limited reproducibility, due to the high sensitivity of the deposited material quality to any minor variations in the operating process parameters, (*e.g.*, laser power, powder feed rate, scanning speed, etc.) [51]. A number of DED studies have examined the effects of process parameters on the quality of the clad structure for a range of materials.

In terms of dimensional accuracy of single clads and manufactured parts, Lee and colleagues [149] concluded that an increase in either laser power or powder feed rate causes an increase in the clad size; it was noted that the higher the scanning speed, the lower the

bead size. The same trend was also reported by Ravi et al. [150]. However, Shim and colleagues [151] reported that there was a particular laser power value, below which the use of higher power increases the clad height. However, above that value, increasing laser power decreases the clad height. In contrast, in another study, it was noted that there was no effect for scanning speed variation on clad width [152]. The effects of the laser stand-off distance on the size of single clads has also been assessed [153]; it was noted that an increase of the laser stand-off distance resulted in greater width as the laser beam became wider due to the gaussian distribution. Bi et al. [154] compared two methods of power control (i.e., constant power and closed loop process control). In the constant power method, the cooling rates and molten pool temperature changed throughout the deposition period. It was observed that the wall thickness was inhomogeneous; the edges were found to be thicker and higher. For the closed loop process control method, the molten pool temperature was maintained at a constant value, while varying laser power. This approach presented a more homogeneous wall thickness and height, as well as less variation in the cooling rates.

In terms of the impact of process parameters on the surface roughness of the deposited part, Choi and Hua [155] studied the effect of specific energy, layer thickness, and overlap width on the surface roughness of DED processed structures. The top surface roughness was essentially unaffected by specific energy and layer thickness. However, using a higher percentage of overlap resulted in a clear roughness reduction in the top surface. In contrast, the side surface roughness was observed to be reduced by decreasing the layer thickness. In another study, it was shown that higher scanning speeds led to convex shaping at both ends of the deposited part, where the size of the convex region was increased by raising

the scanning speed [156]. It was also noted that, at high energy density, the shaping resolution was poor, due to adhered un-melted powder.

Depositing overhanging structures is one of the major challenges in DED processing, unlike laser powder bed techniques, in which the overhanging structure is supported by the surrounding powder [157,158]. Consequently, various techniques have been applied to fabricate overhanging structures using DED. Nassar and Reutzel [159] demonstrated that two physical phenomena dominate the formation of these structures. The first is surface tension, which protects the molten zone from failure and resists gravity effects, when the laser is on an area. The second is rapid solidification of the molten material, initially from the sides and the bottom, when the laser has moved away. Other studies have demonstrated that inclined structures could be produced by tilting or rotating the deposition head or the substrate to minimise the effect of gravity [30,31]. Wang et al. [118] built overhanging thin walls by shifting the laser beam in the width direction by a particular increment; it was observed that using a reciprocating deposition pattern leads to symmetrical and even surfaces. Conversely, use of unidirectional deposition resulted in defects at the ends of the deposition path (i.e., collapse of the ends). It was also observed that the layer thickness dramatically affects the accuracy of the deposited overhanging angle.

In the present work, AISI D2 tool steel powder was deposited onto like-composition substrates, in order to build single clads, and multi-layer, multi-track specimens. Various laser scanning speeds, powder feed rates and layer thicknesses were used during the DED processing. The investigation of the effects of each individual parameter was conducted while the other parameters were kept at constant values. The DED processed single clads were studied in terms of their size and dilution, while the multi-layer, multi-track structures

were examined for their dimensional accuracy in addition to their top and side surfaces roughness. Furthermore, overhanging thin-walls were also built under different DED process conditions (laser power, powder feed rate and laser scanning speed). These samples were assessed for the accuracy of the experimental measured angle in comparison to the designed angles, while the side surface roughness and dimensional accuracy were also examined for these samples. Finally, an empirical equation has been developed, with the aim of decreasing the discrepancy between the designed and the experimentally measured angles.

5.2 Experimental Procedures

5.2.1 Raw Materials

In the present DED process, the AISI D2 feed stock material was provided from TLS Technik Spezialpulver (Bitterfeld-Wolfen, Germany) as gas atomised powder, with a size range of 45 to 90 μm specified by the manufacturer. Similar D2 substrate plates, with dimensions of 101.6 x 101.6 x 6.35 mm (4 x 4 x 0.25 inches), were obtained from Hudson Tool Steel (Dover, NH, USA). The influence laser reflection within the DED system was minimised by sandblasting the top surface of the substrate before DED processing.

5.2.2 Laser DED Processing

For the DED processing stage, an Optomec MTS-CA system (Albuquerque, NM, USA) was used. This equipment has a five-axis machine movement control. In addition, with a controlled atmosphere capability, Ar provides a shielding environment inside the chamber for the purpose of protecting the workpiece from oxidation, in addition to being employed as the conveying gas for the deposited powder. The DED system utilizes a 1-kW fiber laser,

with a 0.6 spot diameter, while the powder delivery system comprises a coaxial powder nozzle; powder can be supplied from up to four separate powder feed units.

The selected range of investigated DED process parameters is summarized in Table 5.1. In order to examine the effects of the different process parameters, one was varied while the other parameters were all fixed for that series of experiments. The assessed ranges for each of the process parameters were determined based on the equipment capabilities/design and the from prior studies presented in the open literature. Specifically, the laser scanning speed, powder feed rates, and laser power were varied from 400 to 700 mm/min, 5.5 to 7.5 g/min, and 400 to 600 W, respectively. The other main process variables, such as layer thickness, hatch spacing and dwell time (the time at which the laser is off before scanning the subsequent layer) were all maintained constant for the outlined experiments, as presented in Table 1; the hatch spacing, layer thickness, and dwell time were maintained at 0.381 mm, 0.251 mm, and 1 s, respectively. Table 5.2 summarises the sample identification strategy, stating the full range of examined parameters.

Table 5.1. A summary of the main DED processing parameters examined in the present work.

Parameter	**Value**
Scanning speed (mm/min)	400 - 700
Powder feed rate (g/min)	5.5 - 7.5
Laser power (W)	400-600
Hatch spacing (mm)	0.381
Layer thickness (mm)	0.251
Dwell time (s)	1

As illustrated in Figure 5.1 and Table 5.2, nine simple rectangular geometries with dimensions of 25 x 5 x 10 mm in length, width and height, respectively, were deposited using three different scanning speeds (400, 600, and 700 mm/min) and three different powder feed rates (5.5, 6.5, and 7.5 g/min). In addition, twelve initial single clads were deposited using four different scanning speeds (400, 500, 600, and 700 mm/min) and three different powder feed rates (5.5, 6.5, and 7.5 g/min). However, for both the rectangular geometries and single clads deposits, the laser power was kept constant at 400 W.

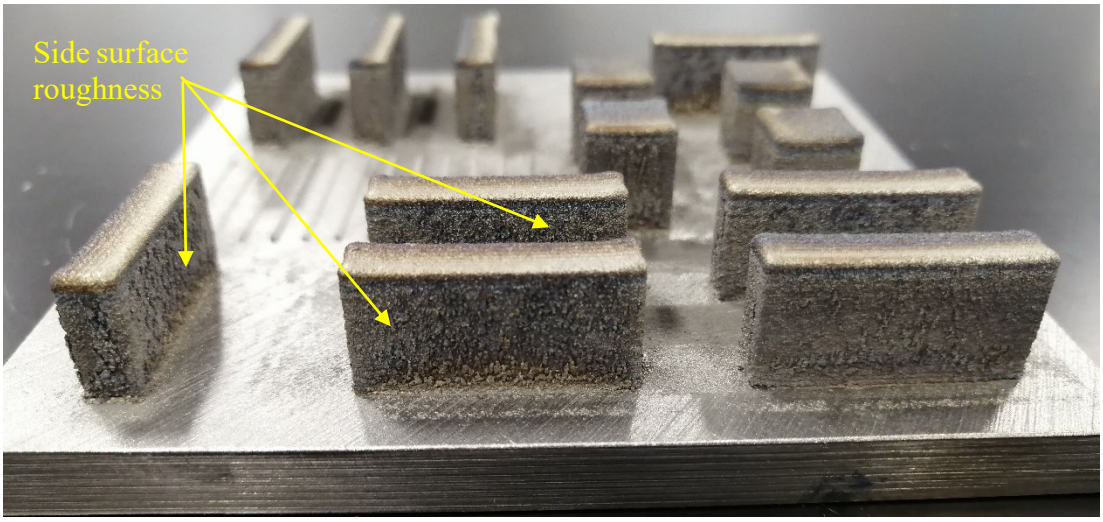

(a)

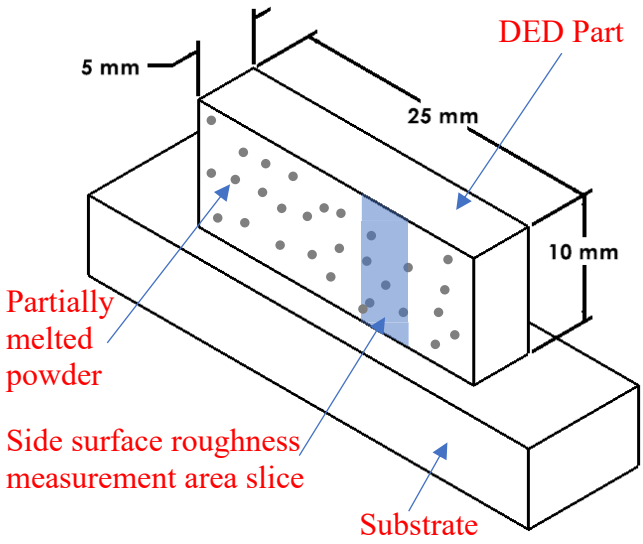

(b)

Figure 5.1. (a) An example of a DED processed D2 tool steel build plate and samples. This particular plate presents the rectangular samples and single-track clads (mid-plate on the left-hand side). Note that the cubic samples shown on the right-hand side are not considered in the current work. (b) Schematic diagram for DED printed sample and how surface roughness is measured.

In addition to the simple geometries already outlined, (single track) inclined thin walls were also deposited in order to examine the potential limitations when printing overhanging D2 structures using the DED technique. For this segment of the study, two series of thin walled samples were deposited. The first was fabricated in order to investigate the influence of different process parameters on the discrepancy between the designed angle and the experimentally measured angle, as presented in Figure 5.2(a). For this series, the overhanging thin walls were built with three different angles to the horizontal plane (i.e., 60˚, 70˚, and 80˚). The overhanging walls were 10 x 5 mm in length and height, respectively. As demonstrated in Table 5.2, Three different laser powers (400, 500, and

600 W), three powder feed rates (5.5, 6.5, and 7.5 mm/min), and three different laser scanning speeds (400, 600, and 700 mm/min) were used for this portion of the study. The tilted angle was obtained by shifting the scanning path in the traverse direction (perpendicular to the scanning direction) with a shift value, Δy, calculated using the following Equation:

$$\Delta y = \frac{\Delta z}{tan\,\theta_d}$$

Equation 5.1. Calculation of the shift value to produce inclined walls [118].

where Δz is the layer thickness and θ_d represents the design angle (the angle of the DED processed wall with the horizontal plane).

For the second series of inclined samples, the minimum angle to which the overhanging thin wall could be built before failure was investigated. Consequently, three different samples were deposited at three angles of (55°, 58°, and 60°), following the set of DED parameters (termed O-6), demonstrated in Table 5.2; the build plate for these samples is presented in Figure 5.2(b). It is worth noting that all the DED processed samples in the second batch of inclined walls were deposited using the same size used for the first series.

Furthermore, in order to minimise the error between the actual DED inclined wall sample and the original design angle, based on the process parameters for each specimen, the design angle was modified using the following empirical equation:

$$\tan\theta_m = \tan\theta_d \cdot \left(0.022\left(\frac{P.f}{v}\right)^4 - 0.341\left(\frac{P.f}{v}\right)^3 + 1.921\left(\frac{P.f}{v}\right)^2 - 4.629\left(\frac{P.f}{v}\right) + 4.932\right)$$

Equation 5.2. Empirical equation for determining the modified design angle.

where, θ_m refers to the modified design angle, θ_d represents the design angle (the exact angle at which the inclined sample needs to be deposited), P is the laser power (in W), f is the powder feed rate (in kg/s), and v is the scanning speed (in m/s); all angles are in degrees. It should be noted that Equation 5.2 was derived following statistical analysis of the results of the first batch of the deposited inclined samples. For the purpose of validating Equation 5.2, eight overhanging thin wall samples were manufactured under four different set of parameters (O-4, O-6, A1-6, B1-6), presented in Table 5.2, and two tilt angles of 70° and 60, as shown in Figure 5.2(b).

Table 5.2. Identification scheme for full range of examined parameters.

Sample ID	Power (W)	Feed rate (g/min)	Speed (mm/min)	Application in experiments				
				Rectangular parts	Single clads	Inclined thin walls		
						Series-1	Series-2	Equation 5.2 validation
O-4	400	5.5	400	✓	✓	✓		✓
O-5	400	5.5	500		✓			
O-6	400	5.5	600	✓	✓	✓	✓	✓
O-7	400	5.5	700	✓	✓	✓		
A1-6	500	5.5	600			✓		✓
A2-6	600	5.5	600			✓		
B1-4	400	6.5	400	✓	✓			
B1-5	400	6.5	500		✓			
B1-6	400	6.5	600	✓	✓	✓		✓
B1-7	400	6.5	700	✓	✓			
B2-4	400	7.5	400	✓	✓			
B2-5	400	7.5	500		✓			
B2-6	400	7.5	600	✓	✓	✓		
B2-7	400	7.5	700	✓	✓			

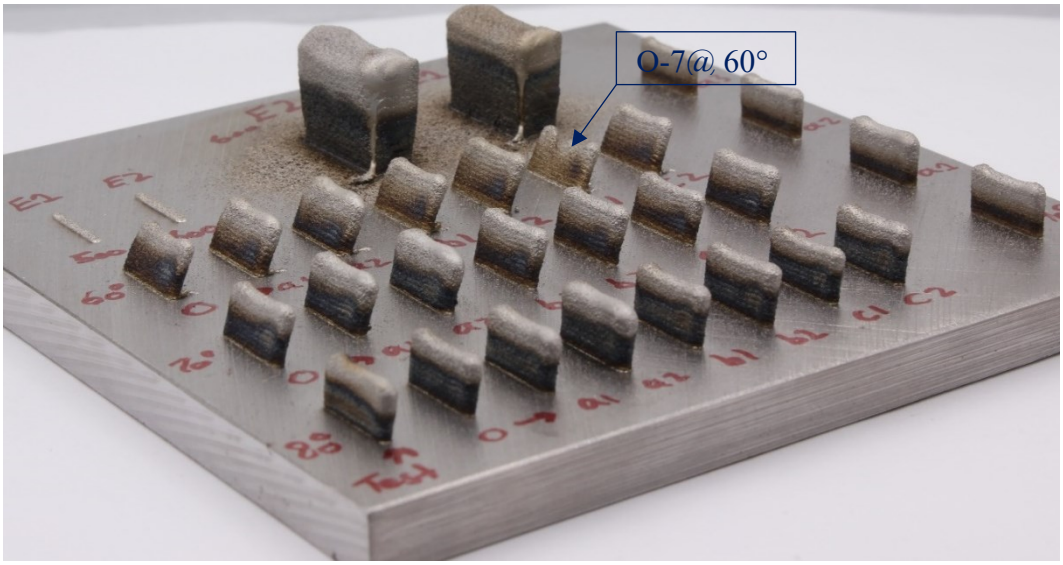

(a)

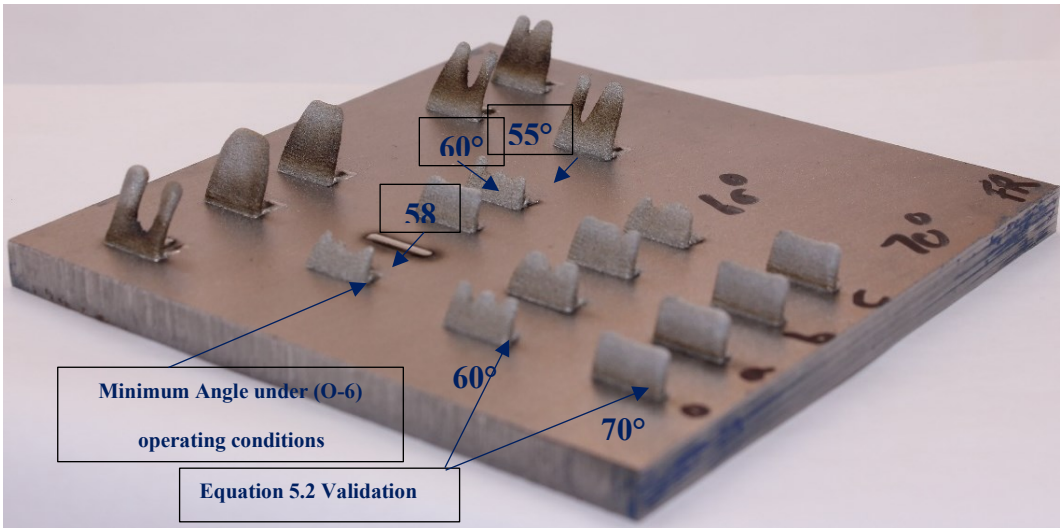

(b)

Figure 5.2. The DED processed plates for inclined thin wall samples: (a) the first series of samples, and (b) the second series of samples. Note that the rectangular specimens in (a), and the higher height samples in (b) are not considered in the current paper. Ignore the sample identification written down on the substrate.

5.2.3 Materials Characterisation Procedures

- *Characterisation of Raw Materials*

In order to determine the chemical compositions of the gas atomised feedstock powder and the AISI D2 substrates, inductively coupled plasma optical emission spectroscopy (ICP-OES) analysis was performed. ICP-OES analysis was accomplished using a Varian Vista-PRO system (Varian Inc., Palo Alto, CA, USA), where, prior to analysis, the material being assessed (either shavings from the substrate plates or the feedstock powder) was subjected to an acid digestion step. Powder morphology was examined using a Hitachi S4700 field emission gun scanning electron microscope (SEM; Hitachi High Technologies Inc., Tokyo, Japan), in order to examine the microstructures of the D2 raw powder. The SEM operating conditions were set to an accelerating voltage (V_{acc}) of 3 kV and beam current (I_e) of 15 μA, for the purpose of limiting charging artefacts during powder evaluation. Furthermore, a Mastersizer 3000 system (Malvern Panalytical, Malvern, UK) was used to assess the particle size distribution of the D2 feedstock powder; for the purpose of assessing the 'intra-batch' variability, three measurements were taken on various samples from the supplied powder batch. In addition, the flow response of the original supplied powder was evaluated using a Hall Flowmeter, following ASTM standard *B213-20: Standard Test Methods for Flow Rate of Metal Powders Using the Hall Flowmeter Funnel.* For the powder flow test, the time needed for 50 gram batches of the original powder to pass though the orifice of the Hall Flowmeter was recorded three different times, and was then averaged; this examination was done simply to evaluate powder flowability using a known test procedure. However, the validity for using the Hall flow test for DED processing is open to question. Similarly, the feed stock powder apparent density was measured

following ASTM standard *B703-17: Standard Test Method for Apparent Density of Metal Powders and Related Compounds Using the Arnold Meter*; in this instance the mean was taken from three separate measurements.

- *Characterisation of the DED Processed Materials*

For the DED processed samples, the single clads were assessed in terms of their heights and widths as a function of the DED operating parameters. To achieve this, a confocal laser scanning microscope (CLSM; model VK-X1100, Keyence Corp., Osaka, Japan) was used to evaluate the cross-sectional profile of the single clads, using a 20x magnification objective lens (with 535.7 nm theoretical resolution). Three measurements were taken in different positions along the length of the single clad, in order to obtain an average value. The CLSM cross-sectional profile data was analysed using the *Keyence Multifile Analyzer software.* For the DED processed rectangular samples, evaluation of the dimensional accuracy was conducted manually using a Vernier caliper, with five measurements performed for each dimension/sample to obtain a mean value. The as-deposited surface roughness of the DED rectangular samples were obtained using the CLSM with the same 20x magnification objective lens. The *Keyence Multifile Analyzer software* was then used to determine the arithmetical mean height (Sa), as a representative parameter for surface roughness evaluation. Based on the outcomes reported by Mazumder and colleagues [121] that the top surface roughness was higher in the width direction than the length, while the side wall roughness was noticed to be higher in the vertical direction than the horizontal direction, the surface evaluation was conducted along the transverse direction (normal to the laser scanning direction) for the top surface and the height direction (Z-direction) for the side surface. In each measurement, an area slice was recorded to obtain the average Sa

for this area slice. The area slice consists of three stitched images, for top surface roughness measurements, and six stitched images, for side surface roughness. While three different area slices at different locations along the surface were selected to get the mean value of the surface roughness along the whole surface. It is worth noting that for the side surface roughness, the X-Z (Length-Height) plane was normalized to face the CLSM laser beam (i.e., perpendicular to the beam). In addition, the selected areas for evaluation were chosen that, qualitatively, exhibited the most amount of un-melted powder particles attached to the surface (the worst case), as demonstrated in Figure 5.1 (b). Orientation normalization was not required for the top surface roughness, since it naturally is parallel to the CLSM lens. Additionally, the surface resonance was isolated by applying two robust Gaussian filters, as required by ISO standard *11562:1996: Geometrical Product Specifications (GPS) - Surface Texture: Profile Method - Metrological Characteristics of Phase Correct Filters* and ISO standard 16610-21:2011: *Geometrical Product Specifications (GPS) – Filtration – Linear Profile Filters: Gaussian Filters* [122,162]. Initially, a shortcut filter (S-filter) was applied with a cut-off scale of 2.5 μm, with the aim of removing the small-scale measurement noise [123]. Then, a long-pass filter (L-filter) was used, with a cut-off scale of five times the profile length (in mm)), in order to eliminate undulations and further lateral components [124].

Further investigation of the surface morphology/roughness was conducted using the previously outlined SEM, which was operated with V_{acc} and I_e of 15 kV and 15 μA, respectively. Similarly, polished cross-sections of the fabricated DED specimens were also analysed using the SEM. They were first mounted in PolyFast (using Citopress-1, Struers, Copenhagen, Denmark), before being ground and polished to a final surface finish of ~1

μm (with sequentially finer SiC paper grades, finishing with Tegramin-20, Struers, Copenhagen, Denmark). After polishing, an etching step was performed by briefly submerging the polished surface into a 5 vol.% Nital solution (5 vol.% nitric to 95 vol.% methanol); it was found that each sample needed marginally different etching times, so this was optimised for each one.

With the aim of explaining the results the surface roughness of the DED fabricated samples in relation to the operating parameters, the cooling rates of the DED processed specimen were estimated following Equation [125]:

$$\lambda_2 = B\left(\frac{dT}{dt}\right)^{-n}$$

Equation 5.3 Cooling rates calculation [125].

where λ_2 refers to the secondary dendrite arm spacing (SDAS, in μm), $\frac{dT}{dt}$ is the cooling rate (in K/s), and B and n represent empirically determined constants; their values are 42.1 μm.s.K^{-1} and 1/3, respectively [126]. The SDAS values were obtained from digitised SEM images of the cross-sectional microstructures of the DED fabricated samples, using the public domain ImageJ software (National Institutes of Health, Kensington, MD, USA); 5 measurements were conducted for each sample, while each measurement involved determining the average spacing along 10 to 15 secondary dendrites. The SEM microstructural images used for SDAS measurements were obtained using the same SEM outlined previously, operating with V_{acc} and I_e values of 15 kV and 15 μA, respectively.

In terms of the overhanging thin walls, the CLSM was used to measure the incline angles, while the thin walls were normalized in order to measure the angle in the X-Y plane (normal to the CLSM beam axis). The images for the thin-wall samples were captured

using a 10x magnification objective lens; they were subsequently analysed using the *Keyence Multifile Analyzer software*. The thin-walled samples, with design angles of 70° and 80°, used between 12 and 14 stitched images (2 columns, and 6 or 7 rows), while the overhanging walls with a 60° design angle required 18 stitched images (3 columns and 6 rows). For all samples, the angles between the horizontal line (the substrate surface), and the outer and inner wall surfaces were measured twice (from both sides), then averaged to get the mean value. With respect to the surface roughness of the inclined walls, only the outer surface was examined, following the same procedures that were used for determining the surface roughness of the DED processed rectangular specimens. However, the DED processed tilted wall samples were installed in a mounting vice, allowing them to be rotated, for the purpose of aligning the inclined surface perpendicular to the axis of the CLSM laser beam. Finally, the results of the measurements of the sample dimensional accuracy, surface roughness, and overhanging angles were statistically assessed using (Minitab®, State College, PA, USA). While a significance 'main effects plot' and contour plot was generated using the ANOVA software feature. The contour plots were used to evaluate the effect of both powder feed rate and laser scanning speed upon dimensional accuracy and surface roughness of the rectangular DED processed parts. Whereas, the main effects plots were used to demonstrate the impact of laser power, powder feed rate and laser scanning speed on the angle discrepancy and surface roughness of the overhanging DED processed thin walls. In main effects plots, for each power, speed and feed value, a mean value of the assessed measurement (surface roughness or angle discrepancy) is indicated by the software (the points demonstrated on each plot). The way in which the points are connected determines the trend of the process parameters. For instance, if the

there is no trend for the effect of a parameter on the selected measurement, the points will be connected by horizontal lines. While the connection of the points with incline lines demonstrates that there is a significant effect of that parameter. The main effect of the parameter is proportionally related to the slope of the line. Finally, the overall mean value is presented as dotted line on each main effects graph.

5.3 Results & Discussion

5.3.1 Characterisation of Raw Materials

The chemical compositions of the AISI D2 feedstock powder and substrates used in this work, which were obtained using ICP-OES analysis, are presented in Table 5.3. In both cases, the compositions were found to be within the normal range expected for D2 tool steel[87,119]. In addition, Table 5.4 outlines the measured D2 feedstock powder characteristics (i.e., particle size, flow behaviour, and density). It is apparent that the measured particle size is close to the manufacturer specification (i.e., a D_{50} of ~75 μm), which corresponds to the recommended particle size specified by the manufacturer of the DED system used in the current work. Figure 5.3(a) demonstrates the complete particle size distribution for the D2 feedstock powder, highlighting that it is monomodal in character. A representative SEM image of the feedstock powder is presented in Figure 5.3(b). It is apparent that the morphology of the powder is generally spherical, as would be anticipated from the gas atomisation process that was used. However, several attached micro-satellites and some irregular-shaped particles can also be observed, which may impact the powder flow response during DED processing.

Table 5.3. AISI D2 tool steel substrates and powder chemical compositions obtained by ICP-OES analysis.

Material Type	**Composition (wt.%)**									
	Fe	**C**	**Si**	**Mn**	**Cr**	**Mo**	**V**	**Co**	**Cu**	**Ni**
AISI D2 Powder	Bal.	1.55	0.41	0.33	11.27	0.64	0.79	0.01	0.01	0.06
AISI D2 Substrate	Bal.	1.50	0.3	0.3	12	0.75	0.9	-	-	-

Table 5.4. AISI D2 tool steel feed stock powder properties.

Properties (units)		**Value**
Particle Size	**D_{10} (µm)**	51.5
	D_{50} (µm)	73.6
	D_{80} (µm)	93.9
	D_{90} (µm)	106
Flowability (g/s)		3.2 ± 0.06
Density (g/cm^3)		4.20 ± 0.016

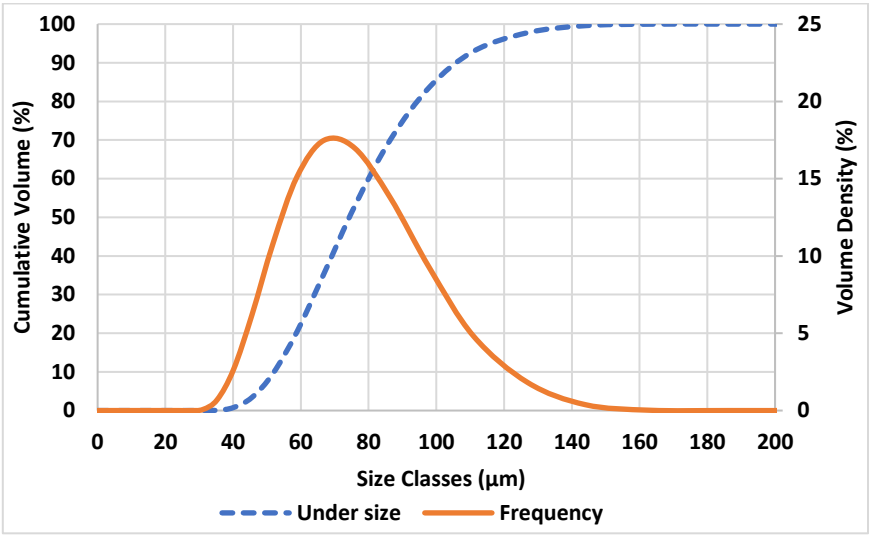

(a)

(b)

Figure 5.3. (a) Representative particle size distribution for the as-received D2 powder. (b) A typical SEM image of the as-received D2 tool steel powder, highlighting a generally spherical morphology with isolated satellite particles.

5.3.2 Geometrical Characteristics of the DED Processed Samples

- *Single-Track Clads*

In order to examine the dimensional accuracy of the DED processed specimens, it was crucial to assess the dependence of single-track clad observations upon the operating process conditions, since the examination of single-track dimensions can provide some indications about the accuracy of the overall manufactured samples, in particular whether they will be under- or oversized [163]. As mentioned previously, single-track layers were deposited using various different process parameters (i.e., laser scanning speed and powder feed rates), with CLSM used to determine the primary dimensions of the deposited single layer. The measured heights and widths of the deposited single-track beads are illustrated in Figure 5.4(a) and (b), respectively. In addition, a 'contour map' of the effects of scanning speed and powder feed rates on the single-track clad heights and widths are presented in Figure 5.5(a) and (b), respectively.

With respect to the influence of laser scanning speed on the overall deposited bead size, it can be concluded that the use of higher laser scanning speeds decreases both the clad height and width. These observations can be attributed to the significant effect of scanning speed variation upon the powder feed density and energy density. As an increase in laser scanning speed leads to a reduction in both the laser beam energy and powder feed rate per unit length this, in turn, decreases the time allowable for interaction between the laser beam and the deposited powder. As a consequence, there is a reduction in the melt pool size, and thereby the overall size of the clads (i.e., clad height and width) decreases [164–166].

In contrast, although the use of higher powder feed rates means that more powder is delivered to the laser beam interaction zone, there was no obvious monotonic trend that

could be seen in terms of the effects of powder feed rate on either the single-track heights or widths. This arose because the influence of powder feed rate on the size of the single clad was found to be significantly dependent upon the laser scanning speed. This can be explained by the fact that, as mentioned previously, the variation in laser scanning speed dominates the amount of powder deposited per unit length, in addition to the available time over which the deposited powder is subjected to the laser beam. For example, in the case when powder is feed at high rates, if either the energy input or the interaction time between the laser beam and the deposited powder is insufficient to melt the powder particles, it will cause a smaller track clad and melt pool size [167].

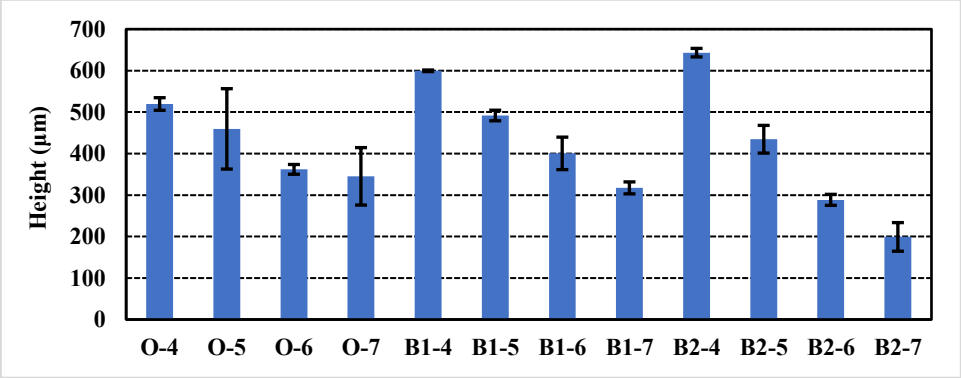

(a)

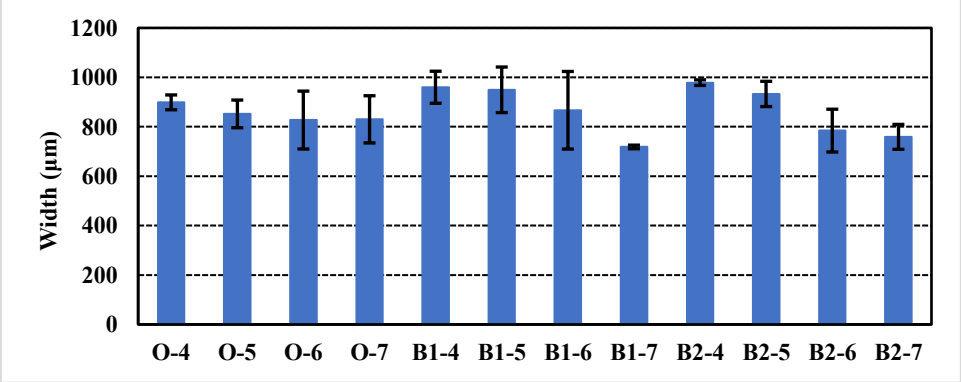

(b)

Figure 5.4. The effects of DED process parameters on the single-track layer dimensions: (a) height, and (b) width.

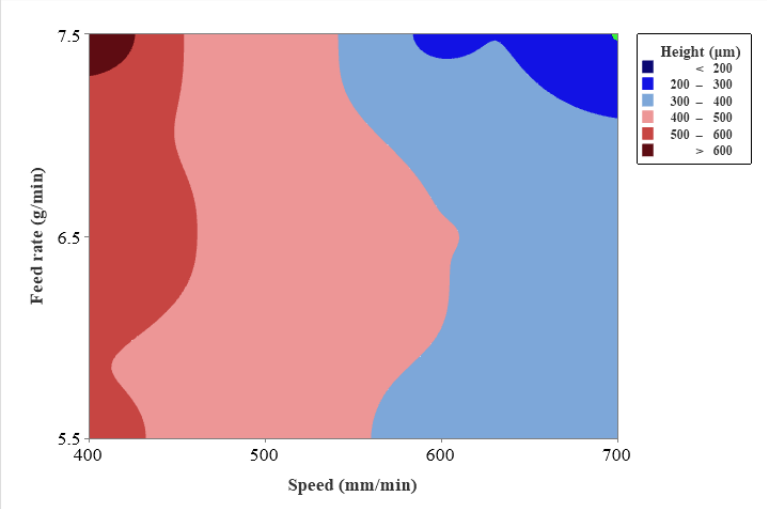

(a)

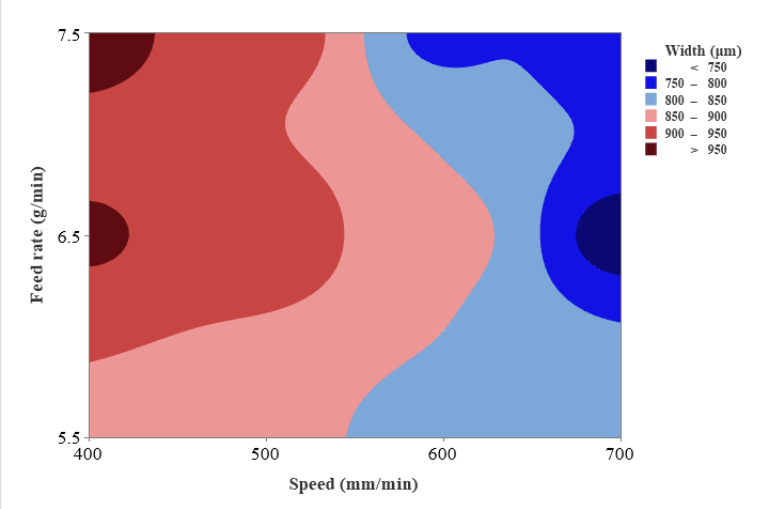

(b)

Figure 5.5 Contour maps showing the influence of scanning speed and feed rate on the single-track layer dimensions: (a) height, and (b) width.

- *Deposited rectangular parts*

Figure 5.6 demonstrates the relationship of the dimensional discrepancy of the rectangular DED samples, in terms of the sample height, to both the laser scanning speed and powder feed rate. The dimensional discrepancy is defined as the difference between the actual sample deposition height and the initially planned heights. It is worth noting that the differences in width and length between the various deposited specimens were minimal. As a consequence, only the errors in height were examined for the current work. In general, it is apparent that all of the samples were overbuilt, with sample heights ranging from 12.34 mm (± 0.04), at a scanning speed of 700 mm/min and powder feed rate of 5.5 g/min, to 13.06 mm (± 0.03), at a scanning speed of 400 mm/min and powder feed rate of 6.5 g/min; in this instance the initially planned height for the build was 10 mm.

In terms of the influence of scanning speed upon dimensional accuracy, it was found that the use of higher scanning speeds results in a lower extent of overbuilding of the specimens (i.e., a lower height error); this observation is consistent with that for the single clads heights. This result can be attributed to the lower amount of powder that is deposited per unit length at the higher scanning speeds. Consequently, lower sample height results as the scanning speed is decreased, which leads to less overbuilding in the current case [168].

With respect to the influence of the powder feed rate, no apparent trend was concluded, since the impact of powder feed rate on the height of the deposited specimens is noticed to be significantly sensitive to the variation in laser scanning speed. This effect arose because the selected value for the laser scanning speed dominates the power density which, in turn, impacts the level of powder taken into the melt pool and hence consolidated in the final

build. As a direct consequence, this affects the degree of under-/over-building for the DED processed samples [169,170].

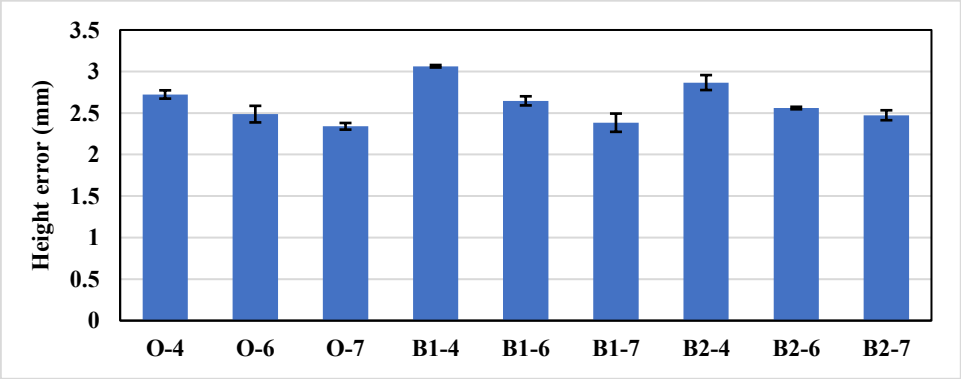

(a)

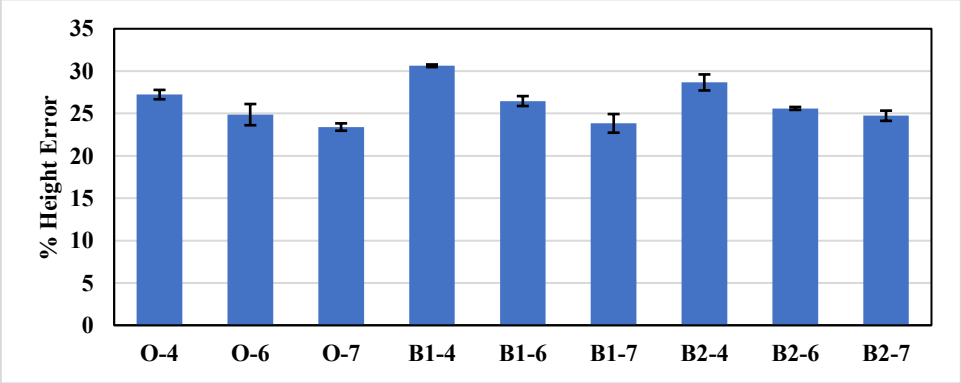

(b)

Figure 5.6. The effects of scanning speed and powder feed rate upon the measured errors in build height as a (a) Value and (b) percentage.

5.3.3 Surface Roughness

Figure 5.7(a-c) demonstrates the shape and surface finish of a typical DED processed sample (in this instance A2), with representative photographs and SEM graphs. It is apparent that the top surface has a lower surface roughness than those of the sides. This arose because there are isolated powder particles that are stuck to the side surfaces during the DED process. The surface roughness of the different samples was determined using

CLSM, as shown in Figure 5.7(d) and (e), which highlights typical CLSM scans that form the basis of subsequent quantitative roughness analysis.

(a)

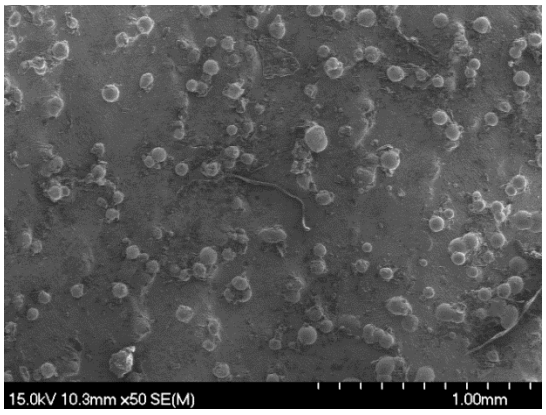

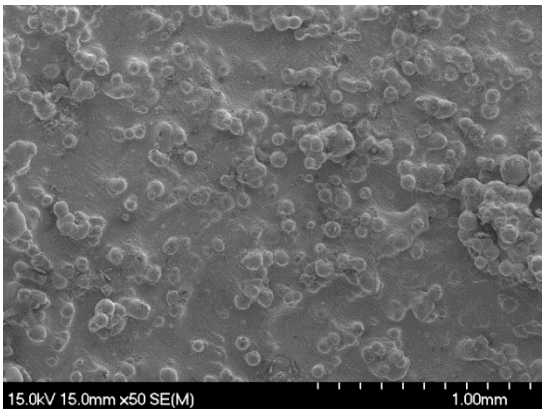

(b) (c)

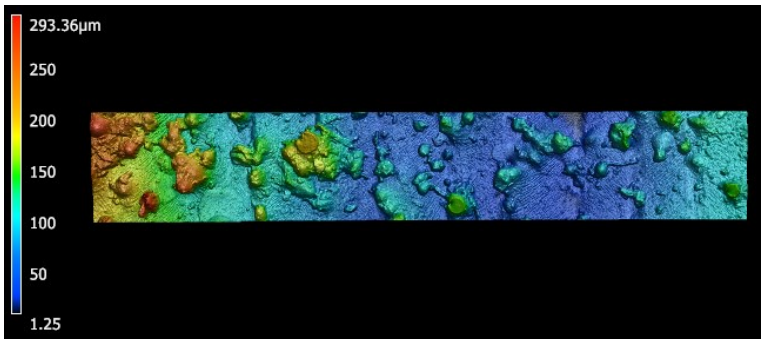

(d)

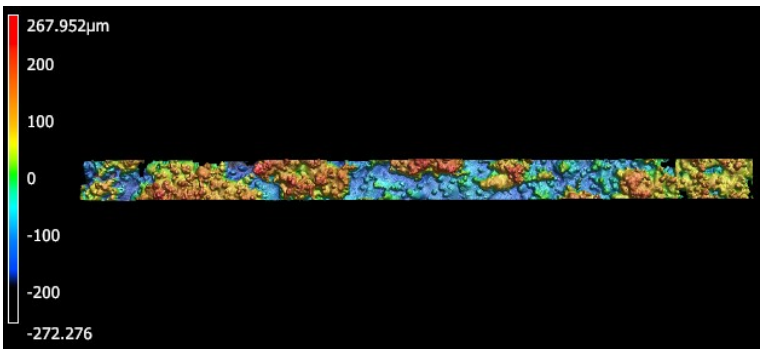

(e)

Figure 5.7. An example of the surface roughness for the DED printed samples, in this instance prepared under DED process conditions B2-6: (a) Macro-photograph, (b) representative SEM image of the top surface, (c) representative SEM of the side surface, (d) representative CLSM image of the top surface, and (e) representative CLSM image of the side surface.

The measured top and side surface roughness values are illustrated in Figures 5.8(a) and 5.9(a), respectively. It was demonstrated that the relation between surface roughness and scanning speed is highly dependent upon the powder feed rate, and vice versa.

In terms of the influence of the scanning speed and powder feed rate on the top surface roughness, it can be observed that the use of lower scanning speeds often leads to lower surface roughness. This response has resulted from the greater time available for heat absorption by the deposited powder at lower scanning speeds, which led to increased energy density. As a consequence, more effective melting of the powder occurs, with less adhesion of isolated particles to the surfaces. In other words, the melted area is increased and stays molten slightly longer such that the deposition nozzle has passed by before solidification arises, hence there are very few particles stuck to the surface. In terms of the effect of powder feed rate, it was observed that the use of lower powder feed rate improves the top surface roughness. This arises because, at the lower powder feed rates, less powder is available to be delivered into the melt pool, which results in more appropriate melting

conditions which, in turn, leads to less partially melted powder particles [165]. As a consequence, the minimum top surface roughness was recorded at a scanning speed and powder feed rate of 400 mm/min and 5.5 g/min, respectively, as demonstrated in Figure 5.8(a) and (b).

When examining the effects of scanning speed and powder feed rate on the side surface roughness, there was no obvious trend for either parameter, as demonstrated in Figure 5.9(a) and (b). This may be attributed to the fact that the side surface roughness is dramatically influenced by the heating-cooling cycles, through the whole DED processing cycle, which impacts the amount of partially melted powder that becomes adhered to the side surfaces. In contrast, the top surface roughness represents the deposition conditions of the last printed layer.

With respect to the scanning speed, it is believed that there are two contradictory effects of the scanning speed upon the heating-cooling cycles conditions, which impacts the side surface roughness. The first of these is that the use of lower scanning speed results in greater interaction time between the laser beam and the deposited powder. That, in turn, leads to higher energy density. As a consequence, lower temperature gradients arise (i.e., low cooling rates), which leads to lower surface roughness due to the reduced number of attached, un-melted powder particles [165]. However, in contrast, it should also be noted that a lower scanning speed leads to higher temperature gradients (high cooling rates) due to the increase in available time for the scanned point to cool down before being reheated, during the deposition of the subsequent pass. Hence, the rate of temperature build-up decreases, which causes higher temperature gradients and cooling rates. That leads to a

reduced degree of melting of the powder particles, which leads to higher surface roughness [170].

Consequently, in the present work, the results of the side surface roughness were evaluated by indicating the cooling rate (using Equation 5.3) as a function of scanning speed and powder feed rate, after measuring SDAS values from SEM micrographs of the cross-sections of the DED processed samples, as illustrated in Figure 5.10. The estimated cooling rates for the DED processed specimens are demonstrated in Figure 5.11. Comparison of the calculated side surface roughness, in Figure 5.9, with the calculated cooling rates, in Figure 5.11, reveals a broad trend consistency between the two. The lowest surface roughness was observed at scanning speed of 600 mm/min, which is consistent with the lowest estimated cooling rate for the DED processed samples. Moreover, it was found that the influences of powder feed rate on the side surface roughness strongly relies on the scanning speed, for the previously mentioned reasons. Finally, in terms of optimising the side surface roughness for the present DED processing variables, the lowest surface roughness was recorded at a scanning speed and powder feed rate of 400 mm/min and 6.5g/min, respectively.

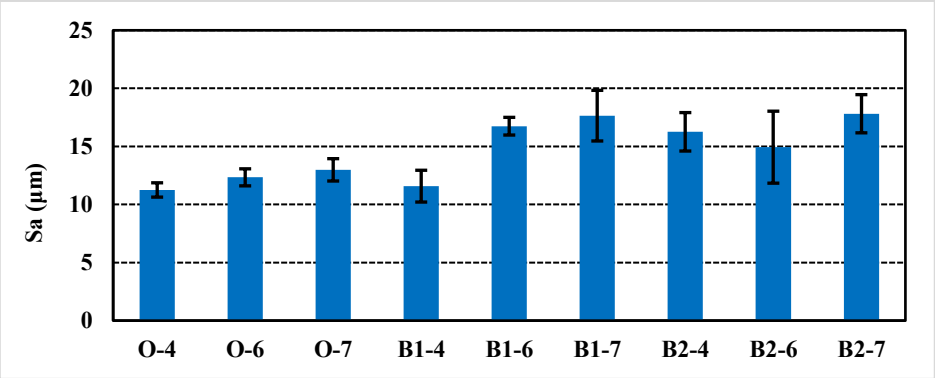

(a)

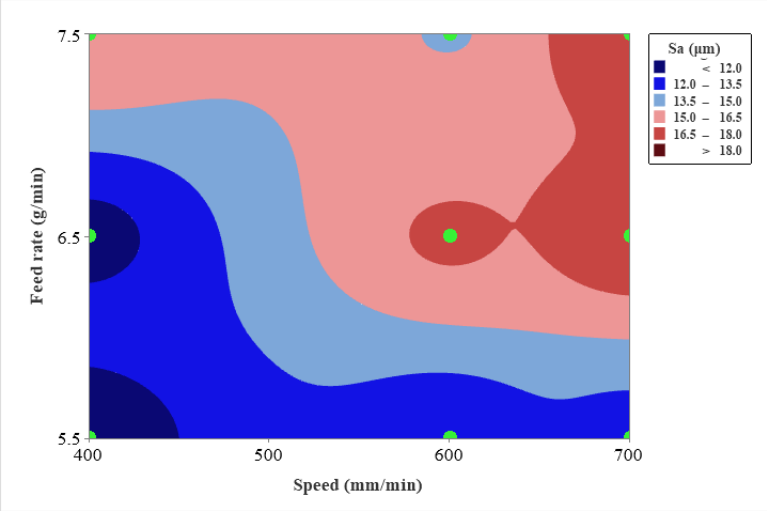

(b)

Figure 5.8. (a) The effects of scanning speed and powder feed rate on the CLSM measured top surface roughness values. (b) The contour map for the top surface roughness as a function of scanning speed and powder feed rate.

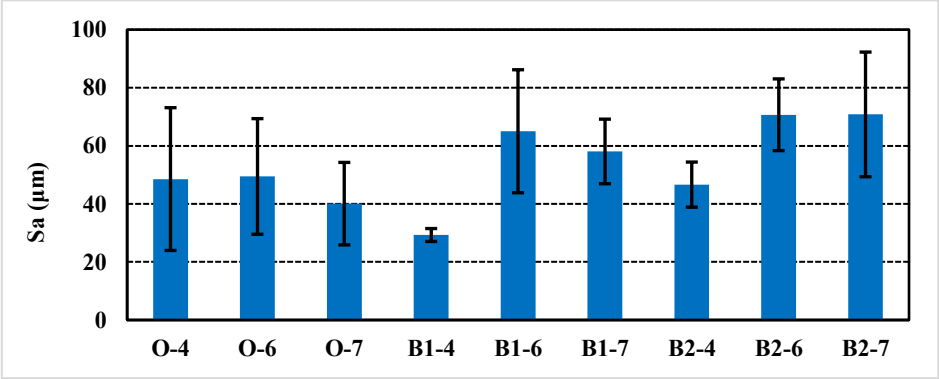

(a)

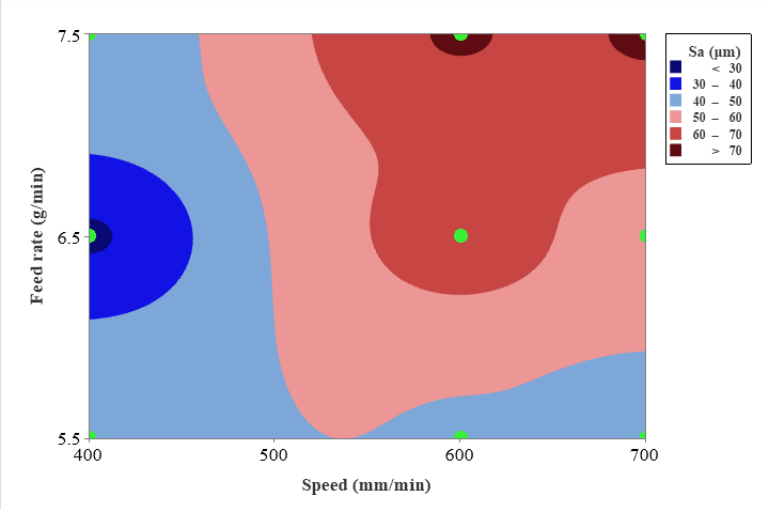

(b)

Figure 5.9. (a) The effects of scanning speed and powder feed rate on the CLSM measured side surface roughness values. (b) The contour map for the side surface roughness as a function of scanning speed and powder feed rate.

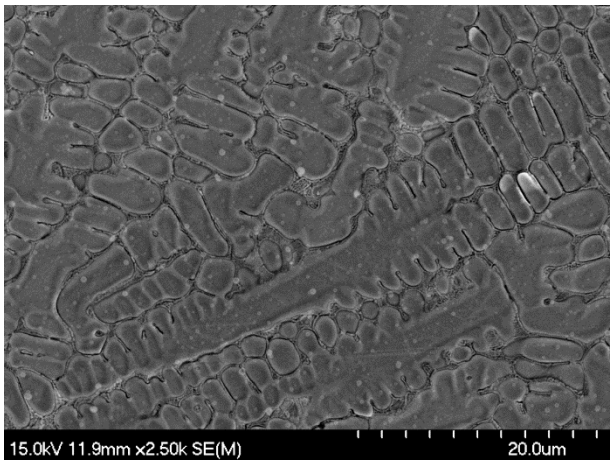

Figure 5.10. Representative SEM image of the middle region of the DED specimen processed following the conditions B2-6. The sample was etched with 5 vol.% Nital solution after polishing to reveal the dendrite development and grain structure.

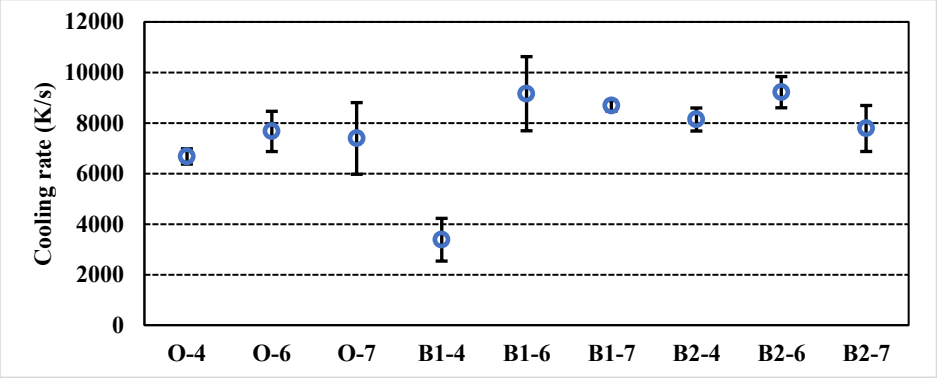

Figure 5.11. The calculated cooling rates for selected 'as-deposited' specimens using Equation 5.3.

5.3.4 Development of Overhanging Structures

In order to examine the ability for deposition of inclined D2 tool steel structures using the DED process, a series of overhanging thin-walled samples was fabricated at three different tilt angles relative to the substrate top surface (80°, 70°, 60°). These samples were deposited under a selection of DED process parameters, as outlined previously in Section 2.2 (Table 5.2). Figure 5.12 demonstrates representative CLSM images of the DED printed, inclined thin wall samples. It was observed that, at a deposition angle of 60°, there was some residual melted powder attached to the inner face of the wall. Therefore, it was essential to examine the minimum angle of deposition for which the overhanging clads could be deposited without failure, which was found to be at an initial design angle of 60°; this effect can be seen from Figure 5.2(a) and (b). In this work, sample failure could be defined as a sample that was not built to its full length and shape. In Figure 5.2(a), it is apparent that all of the printed inclined thin walls were successfully built, with the exception of sample O-7, with an incline angle of 60°. Similarly, as presented in Figure 5.2(b), when utilising the (O-6) DED operating conditions, neither of the samples deposited with designed angles of 58° nor 55° was successfully printed. It is notable that, for the

other operating conditions, none of the samples (pointed as validation of Equation 5.2 with 60°), was perfectly manufactured. It is worth noting that the modified design angles (θ_m) of those samples were determined using Equation 5.2. All of the modified design angles (θ_m) for these samples were lower than the actual design angles (θ_d), which have the value of 60°.

The success or failure in depositing the overhanging clads can be explained with respect the various 'force' conditions operating during the deposition process, as demonstrated in Figure 5.13. It was observed that there are two main categories of force that act on the deposited layer. The first is beneficial, and includes the supporting force (F_N), in which the previously deposited layer supports the newly added material, in addition to the surface tension force (F_s), which is controlled by the material properties and the molten pool temperature. Offsetting this, in the other category, which each has a negative effect on the build material, are the molten pool gravity (G) and the gas and powder stream impulsion force (N). Therefore, the balance between these forces dominates the probability of success or failure in depositing inclined specimens. Collapse of the molten pool occurs when the component forces of impulsion and gravity in the direction of (F_1) are higher than the surface tension force. This can arise in two situations. The first occurs at lower overhang angles (i.e., higher gravity and impulsion force components) [118], which explains why the minimum design angle was recorded at a value of 60°. While the second scenario is that, at lower molten pool temperatures, lower surface tension forces result. As a consequence, sample O-7 has collapsed at design angle of 60°, since the scanning speed was too high. This led to a lower interaction time between the laser beam and the deposited

powder, resulting in a lower molten pool temperature which, in turn, reduces the surface tension force [171].

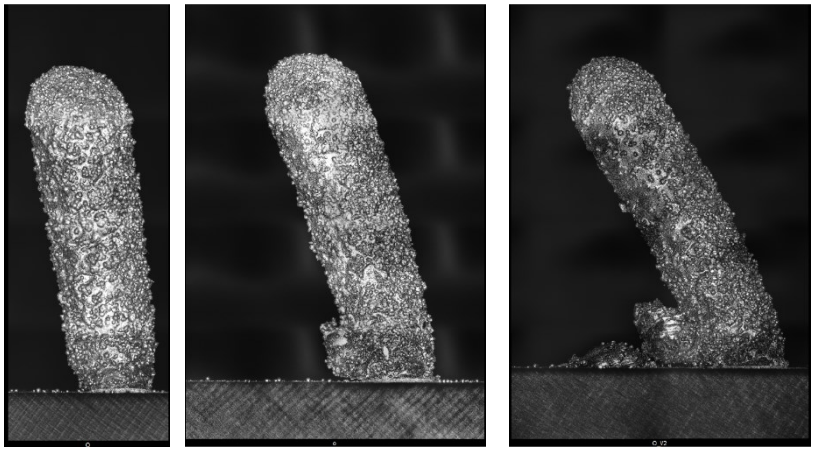

(a) **(b)** **(c)**

Figure 5.12**.** Representative CLSM images for the DED processed inclined thin walls built following the operating conditions (O-6) with deposition angles of: (a) 80°, (b) 70°, and (c) 60°.

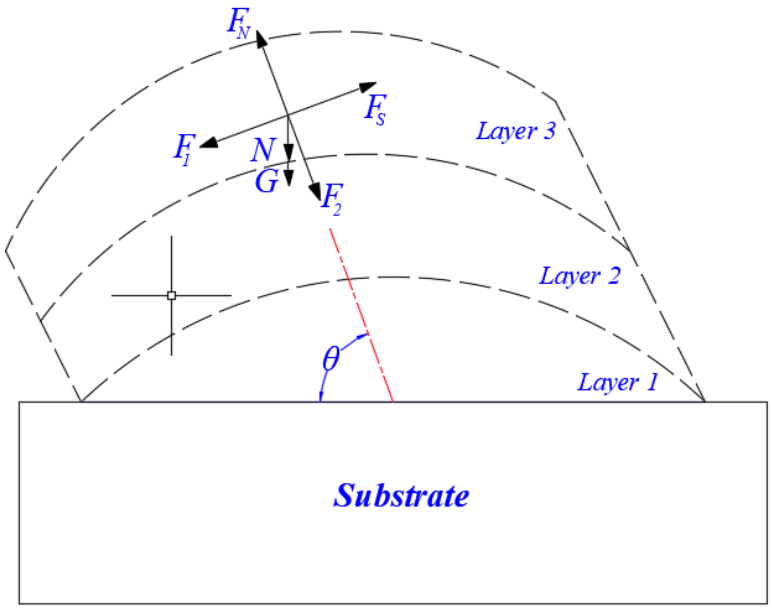

Figure 5.13. The force balance conditions during the deposition of the inclined thin walls (adapted from [118]).

With regards to the differences between the actual measured angles after DED processing and the initially designed angles, it is apparent from Figure 5.12 that the width of wall increases with increasing height of the build. This results in a discrepancy between the angles of the inner and outer surfaces of the wall in relation to the substrate. That difference in angles was highly dependent upon the width of the samples. This, in turn, was impacted by the process parameters, such as laser power, scanning speed, and powder feed rate. Figure 5.14(a) presents the effects of the DED process parameters on the deviation in both the printed face angles and the height of the DED processed inclined angles, where the 'error bars' actually represent the difference between the inner and outer wall angles. Similarly, Figure 5.14(b) illustrates the 'main effects plot' (as demonstrated in section 2.3) of average error of the overhanging angles.

It was observed that the relative discrepancy in angles was increased by increasing the laser power and decreasing the scanning speed. This can be explained with respect to the fact that use of either higher laser power or lower scanning speed results in a higher energy density. This leads to melting of a greater number of powder particles, leading to a higher level of overbuilding of the deposited walls, as demonstrated in Figure 5.14(c). The consequence of this is a higher positive error in the overhang angle, as also noted in a prior study on a Fe-Cr steel [118]. In terms of the effects of powder feed rate, it was observed that, at a higher feed rate, the overhang angle discrepancy was increased. This could clearly be attributed to the deposition of a greater amount of powder at higher powder feed rates, which also resulted in a larger height error in the DED processed clads, as presented in Figure 5.14(c). Therefore, the discrepancy in the inclining angles increases by increasing powder feed rate, confirming prior work [118]. Finally, it was noted that the highest error

in build angles was generated by using a high laser power of 600 W. Furthermore, the printed walls under the (O-6) set of DED parameters showed the lowest error in build angles and height.

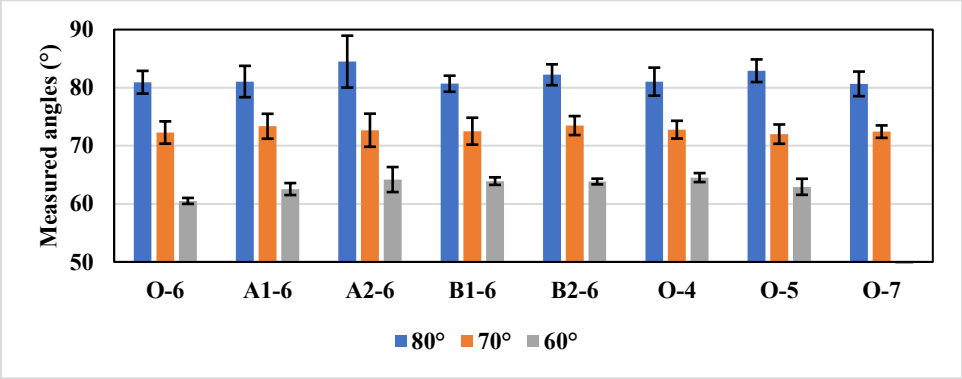

(a)

(b)

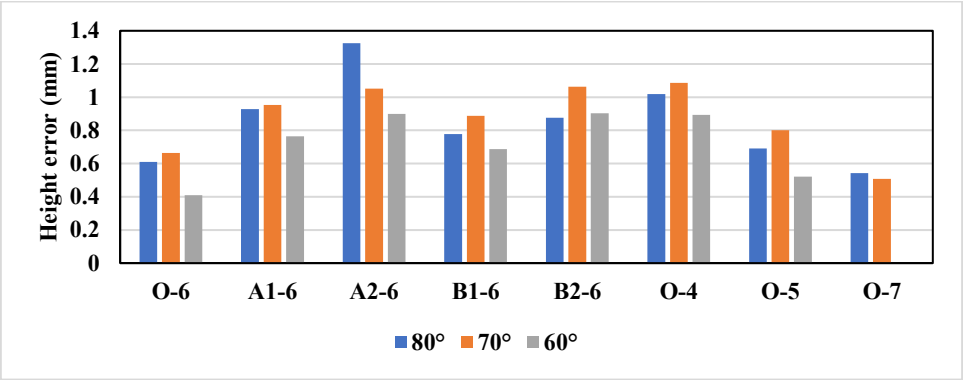

(c)

Figure 5.14. (a) The effects of process parameters on the DED build angles for inclined samples. (b) The main effects plot for the average error of the overhanging angles. (c) The effects of DED process parameters on the measured height error.

In order to minimise the discrepancy in the angles of the overhanging walls, the impact of the DED process parameters upon the ratio between the design angle (θ_d) and the actual measured angle (θ_a) was examined, as demonstrated in Figure 5.15(a). The process parameters were represented using the term ($P.f/v$), where P is the laser power (in W), f is the powder feed rate (in kg/s), and v is the scanning speed (in m/s). The developed relationship, presented in Equation 5.2, was found to have a correlation coefficient of R = 0.993 (i.e., R^2= 0.9877) which indicates a good correlation, as presented in Figure 5.15(a). Consequently, the minimum error in angles could be obtained when ($\tan(\theta_d)/\tan(\theta_a)$) is equal to 1. In other words, that could occur when the actual measured angle has the same value as the design angle. Therefore, the presented relationship in Figure 5.15(a) should be modified by substitution of the parameter θ_a with the value of θ_d. In addition, the term (θ_d), in Figure 5.15(a), should be replaced with the modified design angle (θ_m). In conclusion, Equation 5.2 could therefore be used to predict the modified design angle (θ_m) in relation to the the design angle (θ_d). Furthermore, Equation 5.2 was subsequently validated by

depositing eight different DED samples. These samples were processed using four of the overall DED parameter sets (i.e., O-4, O-6, A1-6, and B1-6) and at two different angles (namely 60° and 70°). Figure 5.15(b) demonstrates a comparison between the discrepancy in the measured angles for the samples deposited with the modified design angle, using Equation 5.2, and the specimens that were built without any modification to the design angle. It can be observed that fabricating the samples using the modified angle approach reduces the discrepancy between the required angle and the one that is actually printed and measured using CLSM.

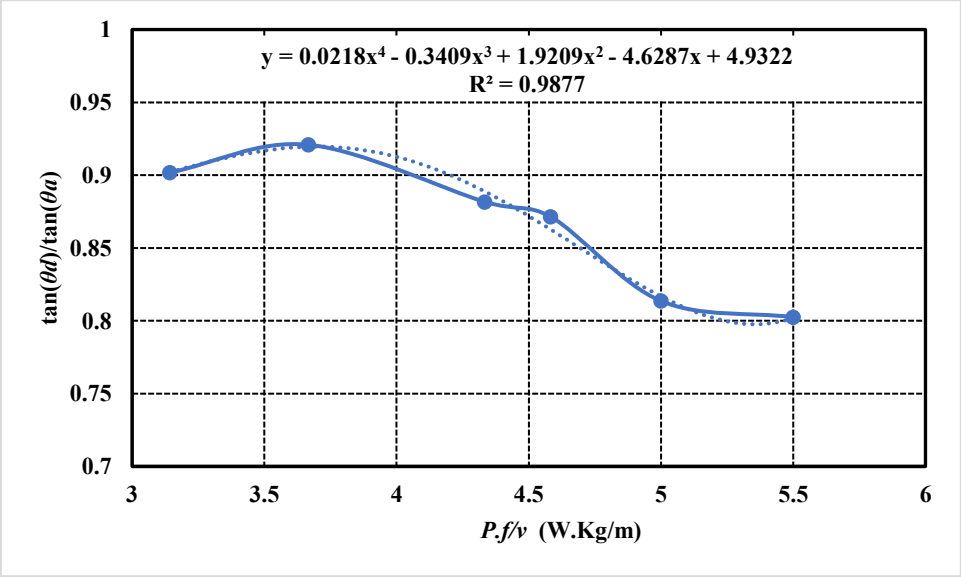

(a)

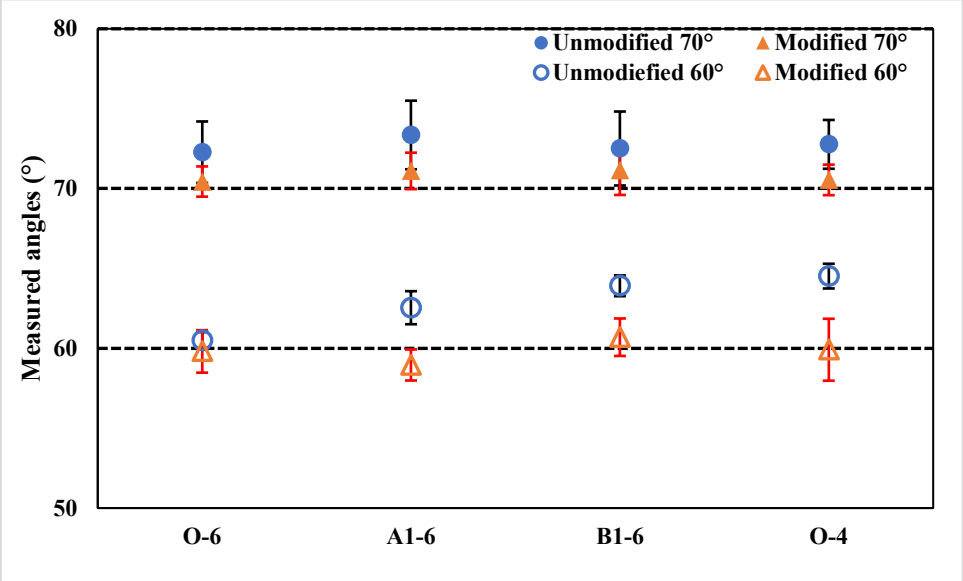

(b)

Figure 5.15. (a) The relationship between the ratio of the tangent of the design angle (θ_d) to the tangent of the actual measured angle (θ_a), and the term of ($P.f/v$). (b) The measured incline angles using Equation 5.2 in comparison to the unmodified samples.

Following a similar approach as that previously outlined in Section 3.3, the side surface roughness of the DED processed overhanging clads was also determined using CLSM. In this work, the surface roughness of the outer surface of the sample was examined. The effects of the operating conditions and the inclination angle on the side surface roughness of the DED processed samples, together with the main effects plot (as demonstrated in section 2.3) of the average side surface roughness, are presented in Figure 5.16(a) and (b), respectively. In terms of the influence of the overhang angle on the side surface roughness, there was no obvious trend for the impact of changing the angle. This arose because of the fact that the alteration of the inclination angle does not have a significant effect on the

heating-cooling cycles during deposition, which would dramatically impact the side surface roughness.

In terms of the influence of the process parameters, the results were observed to be consistent with those outlined in the previous section. It was noted earlier that prior studies of the influence of various process parameters on the side surface roughness has provided some conflicting observations and depends significantly upon the deposition conditions. It was observed in the current work that an increase in laser power from 400 W to 500 W improves the side surface roughness. This is because the use of higher energy density results in better melting conditions for the blown powder, so that the particles melt and effectively 'disperse' on the side surface instead of being minimally melted and adhering in this near original spherical form [172]. However, the further increase of laser power from 500 W to 600 W resulted in higher surface roughness, as the use of higher laser power leads to greater overbuilding in the deposited specimen. In addition, if the energy density is extremely high, this causes more adhesion of the powder particles, which in turn causes higher surface roughness.

Regarding the effects of laser scanning speed, as mentioned previously, there are two opposing effects for scanning speed upon the heating-cooling cycle during deposition. As a consequence of this balance of effects, there was a peak in surface roughness was observed at a laser scanning speed of 600 mm/min. At lower scanning speeds than 600 mm/min, a higher energy density results which improves the side surface by melting any adhered powder particles more fully, as noted previously [165]. In contrast, at scanning speeds higher than 600 mm/min, there is less available time for the deposited material to cool down before being effectively reheated by the laser beam while depositing the

subsequent layer. This leads to higher rate of temperature build-up in the sample, and hence to lower temperature gradients (i.e., lower cooling rates). The consequence of this is more complete melting of the powder and a better surface finish [170]. For the effects of powder feed rate, it was noticed that the surface roughness could be lowered by decreasing the powder feed rate. This arises because, at lower powder feed rates, the powder is more effectively melted due to the lower cooling rates and slower solidification, ultimately lowering the side surface roughness [165].

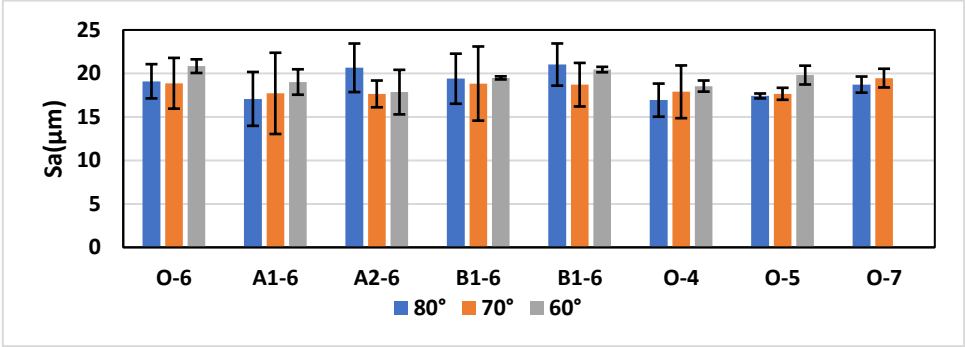

(a)

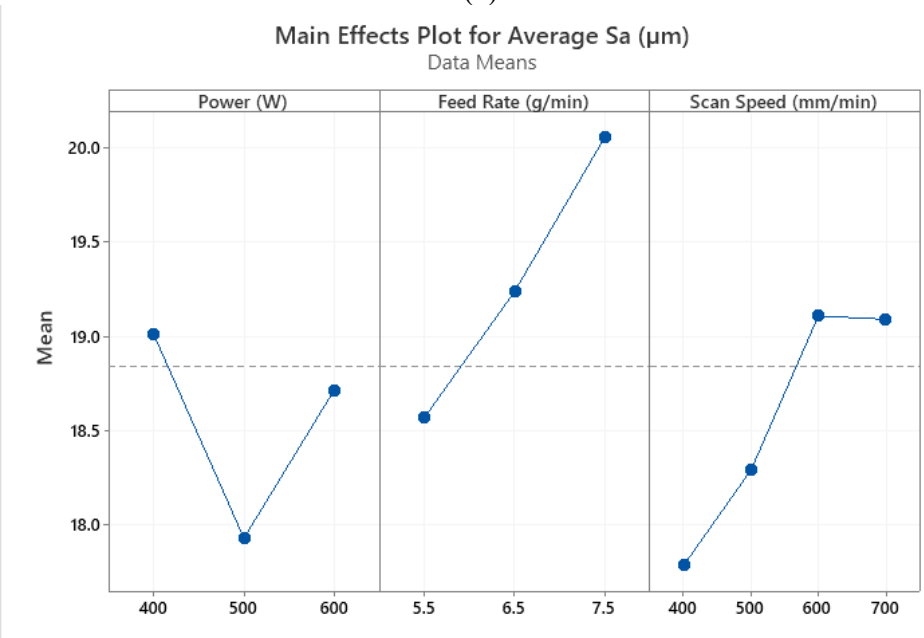

(b)

Figure 5.16 (a) The effects of process parameters and build angle on the side surface roughness of the outer surface of the inclined thin walls. (b) The main effects plot for the average side surface roughness of the inclined thin walls.

5.4 Conclusions

The current work has concentrated upon the effects of laser scanning speed and powder feed rate on the geometrical characteristics and surface roughness of DED processed D2 tool steel samples. This has included the single-track clads bead sizes and dimensional errors for multi-layer samples. The capability of printing overhanging, thin wall structures using DED was also examined, where various process parameters were again used to assess their influence on the angle accuracy and surface roughness. A simple model was developed to allow predict and correct build errors that might arise for DED printing of inclined walls.

It was concluded from the study that:

- In terms of the effects of scanning speed upon the geometrical characteristics, it was observed that the size of single clads, (i.e., clad height and width) has a inverse relationship with the scan speed. The same trend was also observed for the effects of scanning speed upon the degree of overbuilding, since an increase in laser scanning speed results in less available time for heat transfer from the laser beam to the substrate/deposited powder layer, while at the same time a lower amount of powder is delivered to melt pool. As a consequence, an increase of the laser scanning speed decreases the single-track clad size and the degree of positive error in height (over building).
- For the effects of powder feed rate on the geometrical characteristics, it was observed that the variation in laser scanning speed dramatically impacts the relationship between powder feed rate and the geometrical characteristics. This

could be attributed to the fact that both the quantity of powder deposited per unit length and laser-powder interaction time are dominated by the laser scanning speed. As a consequence, in the present study there was no obvious trend in terms of the powder feed rate upon single-track bead size and the level of over/under building of the rectangular DED processed samples.

- With respect to surface roughness, the top surface roughness (i.e., the face perpendicular to the laser axis) was found to be lower than that measured for the sides. This could be attributed to adhesion of isolated powder particles to the side surfaces.

- The top surface roughness was found to be improved by decreasing the laser scan speed and powder feed rate. This arose because, at lower scanning speeds, a higher energy density results, which leads to more complete melting of the particles and therefore a reduction in isolated, un-melted particles adhering to surfaces. A similar explanation can be concluded for the trend relating to the powder feed rate, as less powder is conveyed to the melt pool, resulting in more suitable melting conditions. As a consequence, the minimum top surface roughness was recorded at a scan speed and powder feed rate of 400 mm/min and 5.5 g/min, respectively.

- For the side surface roughness, the effects of laser scanning speed and powder feed rate were found to be dependent upon the heating-cooling cycles (i.e., temperature gradients and cooling rates) that occur during the DED process. A broad consistency was observed between the side surface roughness and the calculated cooling rates (from SDAS analysis). This resulted from slower solidification taking

place at the lower cooling rates, which, in turn, leads to more complete melting of any partially melted particles adhered to the surface. The lowest side surface roughness arose at a scan speed and powder feed rate of 400 mm/min and 6.5g/min, respectively; this corresponded to the minimum calculated cooling rate.

- In terms of DED printing of inclined thin walls, it was observed that the overhang structures can be successfully deposited using DED, up to a maximum overhang angle. Above this, the surface tension force is lower than the combined components of the gravity force of the deposited powder and the impulsion force of gas and powder stream, and the build cannot be sustained. In this study, this angle was found to be a design angle of 60° to the substrate.

- Significant discrepancy was demonstrated between the actual measured angles after DED and the initial design angle. This error was found to be reduced at lower laser power, lower powder feed rate, and/or higher scanning speed. This can be attributed to the reduced height error under these DED conditions, as a result of a lower degree of over-building; at lower laser power and higher scanning speed, a lower energy density resulted, so a smaller melt pool is developed. Similarly, at lower powder feed rates, a reduced amount of powder is delivered into the melt pool. As a consequence of this, an empirical model was developed in order to minimise the angle discrepancy, by predicting a modified design angle with respect to the process parameters of the DED processed sample.

- In terms of the side surface of roughness of the DED printed inclined thin walls, there was no obvious trend for the impact of either laser power, laser scanning

speed, powder feed rate, or the inclination angle. This arises because the side surface roughness is highly dependent upon the heating and cooling cycles.

Acknowledgements

The authors would also like to thank the technical assistance of Mr. Randy Cooke, Dr. Greg Sweet and Dr. Addison Rayner (Dalhousie University) with DED printing of the samples. Ms. Patricia Scallion is also gratefully acknowledged for support with SEM analyses. This work was financially supported through the NSERC Strategic Project Network Grant *Holistic Innovation in Additive Manufacturing* (HI-AM) through Grant No. NETGP 494158-16.

CHAPTER 6 The Effect of Layer Thickness on the Material and Geometrical Properties of Direct Energy Deposited AISI D2 Tool Steel

Status: ***Submitted***: The International Journal of Advanced Manufacturing Technology

Abstract

This research focuses on the influences upon the material characteristics, dimensional accuracy and surface roughness of directed energy deposition (DED) processed AISI D2 tool steel through alteration of the layer thickness while keeping the remaining system operating parameters at constant values. The DED process involved laser deposition of AISI D2 tool steel powder on an annealed AISI D2 substrate, in order to build multi-layered, rectangular samples. After deposition, the DED-manufactured specimens were assessed without any further machining processes. The dimensional accuracy (i.e., the actual height of the deposited specimen in comparison to the designed height) was evaluated using both a manual approach, using callipers, and a computational method, using confocal laser scanning microscopy (CLSM). It was observed that an increase in the layer thickness decreases the degree of overbuilding. Moreover, CLSM was used to examine the top and side surface roughness of the DED-processed specimens. It was found that the use of lower layer thickness improves the top surface roughness. However, there was not a monotonic effect for layer thickness upon the side surface roughness of the DED processed samples. In addition, the microstructures of the DED samples were investigated using scanning electron microscopy (SEM), energy dispersive X-ray spectroscopy (EDS), and X-ray diffraction (XRD), in addition to studying indentation hardness. The results

demonstrated a dendritic morphology with columnar grains was observed for the DED processed samples. In addition, the primary crystalline phase of the dendritic structure was found to be austenite. Furthermore, the hardness values of the DED fabricated parts were found to be higher at thinner layer thickness.

Keywords: tool steels; laser direct energy deposition; surface roughness; dimensional accuracy; microstructure development; layer thickness; hardness

6.1 Introduction

Direct energy deposition (DED) is one of the powder-based additive manufacturing (AM) technologies in which a powder delivery system is employed to coaxially convey a powder stream to an energetic heat source (i.e., laser beam) with the purpose of creating a molten pool on a metallic substrate. To form a single 2-D layer, an attached computer numerical control (CNC) system is utilised to move the laser beam in accordance with the desired route pattern. A fully dense three-dimensional structure can be produced by adding layers subsequently onto one another (i.e., layer-by-layer) [10,30–33]. DED is also referred to as laser consolidation [39], laser coating [37,38], solid free-form fabrication [44], rapid prototyping [43], laser powder deposition [41,42], or laser direct casting [40].

DED technique has several benefits over other AM technologies. Firstly, DED can be utilised to build components with hidden channels, thin walls, or deep cavities, since there are basically no restrictions for the geometry of the fabricated parts [16]. Additionally, DED is beneficial for repairing the corroding surfaces of high-value tools, which, in turn, conserves the cost of replacement [47].

However, one of the principal drawbacks of DED is that the quality of the fabricated part is highly sensitive to any trivial disturbance or variation in the process parameter, (e.g., layer thickness, scanning speed, powder feed rate, laser power, etc.). That, in turn, results in limited reproducibility for the manufactured parts [51]. Another disadvantage is that that the rapid heating-cooling cycles lead to residual stresses, which can often result in cracking or failure of the fabricated component [173]. Several studies were conducted on the impact of process parameters, especially layer thickness, on the quality of the DED processed parts for numerous range of materials

In the DED process, since the characteristics of the fabricated part (e.g., hardness, tensile strength, toughness, etc.) are significantly affected by the formed microstructure, several studies involved the microstructure evolution through the DED process. It was generally noticed that the microstructures of the DED processed structures have three-grain morphologies: equiaxed, columnar, and a mixture of equiaxed and columnar [133]. Park et al. [134] studied the microstructure of DED-processed D2 and H13 tool steel samples, deposited on substrates of D2 and H13, respectively. It was found that the microstructure of the D2 DED processed samples showed dendritic morphology. While a mix of equiaxed and dendritic morphologies was observed in H13 DED processed samples. In another study, the microstructure of the DED-manufactured parts showed fine cellular dendrites that involved fine carbides [136]. Additionally, Mazumder et al. [121] studied the effect of layer thickness on the cooling rates of the DED-processed samples. It was reported that lower cooling rates were determined when using higher layer thicknesses. The microstructure of DED-processed parts was also investigated. Three different regions were found to form the morphology of the DED-processed samples. Firstly, in the interface

region, reheating or remelting of the substrate or the previously deposited layers take place. Hence, there is available time for grain growth. Above the interface region, the grains are more columnar. That could be attributed to the high and directional cooling rates. Beyond the columnar region, equiaxed grains were noticed because of the similarity in temperature gradient after reaching a steady state. In addition, it was observed that the hardness increases gradually from the bottom of the deposited part toward the top surface. That arose because of the reheating effect of the formerly printed layers, which, in turn, leads to the annealing of the previously deposited material. Additionally, Baek *et al.* [138] reported that the fluctuation in laser power and irregular powder flow could result in a small range of variation in hardness along the height of the deposited part. In another study [137], a comparison was conducted between the hardness of DED-processed D2 tool steel to wrought material. Lower hardness was observed in as-printed D2 tool steel in comparison to the D2 substrate material. That arose due to the presence of a eutectoid structure in the microstructure of the as-printed samples, dissimilar to wrought D2, which contains M_7C_3 phases, and austenite, in addition to dendritic austenite.

Furthermore, the build time, dimensional accuracy and surface finish are influenced by layer height. Since faster build time could be achieved by using higher layer thickness. However, the fabricated part could be under-built. That arose because the rate of raising the nozzle is faster than the consolidated material. On the other hand, the set of thin layer heights results in overbuilt parts due to the deposition of more consolidated material [53]. Craig et al. [163] demonstrated that overbuilding of the proposed height was observed using a finer layer thickness; while using a coarser layer thickness can lead to underbuilding. In addition, Choi and Hua [155] observed that the use of lower layer

thickness decreases the side surface roughness. However, there was no significant influence of layer thickness on the top surface roughness. Furthermore, Mazumder et al. [121] reported that the increase in layer thickness resulted in a rougher wall surface. This was attributed to the defocusing of the beam diameter. While for thicker layer thickness, there was a long distance for the beam diameter to diverge. Hence, the cladding width was found to be larger at the bottom of the layer, compared to the top of the deposited layers.

The present work has involved DED of specimens of AISI D2 tool steel powder, deposited onto a substrate of the same material, where four different sets of targeted layer thickness' i.e., the increment that the laser beam focal point is shifted in the z direction to print the subsequent layer, were used. The effect of layer thickness was investigated while fixing the values of the other parameters. The DED fabricated parts were assessed in terms of their dimensional accuracy, top and side surface roughness, microstructure, and indentation hardness.

6.2 Experimental Procedures

6.2.1 Raw Materials

In the current DED study, the AISI D2 tool steel substrates were obtained as 101.6 x 101.6 x 6.35 mm (4 x 4 x 0.25 inches) plates from Hudson Toll Steel (Dover, NH, USA). Before DED processing, the substrate was sandblasted for the purpose of minimising laser reflection during the DED process. In terms of feedstock material, the utilised powder was provided from TLS Technik Spezialpulver (Bitterfeld-Wolfen, Germany), as gas atomized powder with a size range of 45 to 90 μm, as specified by the manufacturer.

6.2.2 Laser DED Processing

An Optomec MTS-CA equipment (Albuquerque, NM, USA) system, with a fiber laser of 1 kW and a 0.6 mm spot diameter was used for the DED processing stage. This DED system includes a five-axis machine transition control. Furthermore, the powder delivery system is provided with a coaxial powder nozzle with the option of four separate powder hoppers. Additionally, Ar was employed as the carrying gas for the added powder in addition to being utilised as a shielding environment inside the deposition chamber to prevent oxidation of the fabricated structure.

Table 6.1 demonstrates the selected DED process parameters. Four cubic samples with dimensions of 10 x 10 x 10 mm were built using four different layer thicknesses with values of 0.125, 0.25, 0.375, and 0.5mm. while other DED process parameters such as laser scanning speed, powder feed rate, laser power, and hatch spacing were kept at constant values of 600 mm/min, 6.5 g/min, 400 W, and 0.381 mm, respectively. It is worth mentioning that the assessed ranges for DED process parameters were concluded based on previous studies from the open literature and the equipment capabilities/design. The strategy of sample identification is presented in Table 6.2. Figure 6.1 shows a representative instance of the as-DED processed samples.

Table 6.1. A summary of the main DED processing parameters was examined in the present work.

Parameter	**Value**
Scanning speed (mm/min)	600
Powder feed rate (g/min)	6.5
Laser power (W)	400
Hatch spacing (mm)	0.381
Layer thickness (mm)	0.125-0.5

Table 6.2. Samples identification method.

Sample ID		Layer thickness (mm)			
		0.125	0.25	0.375	0.5
Speed (mm/min)	600	T1	T2	T3	T4
Feed rate (g/min)	6.5				
Power (W)	400				

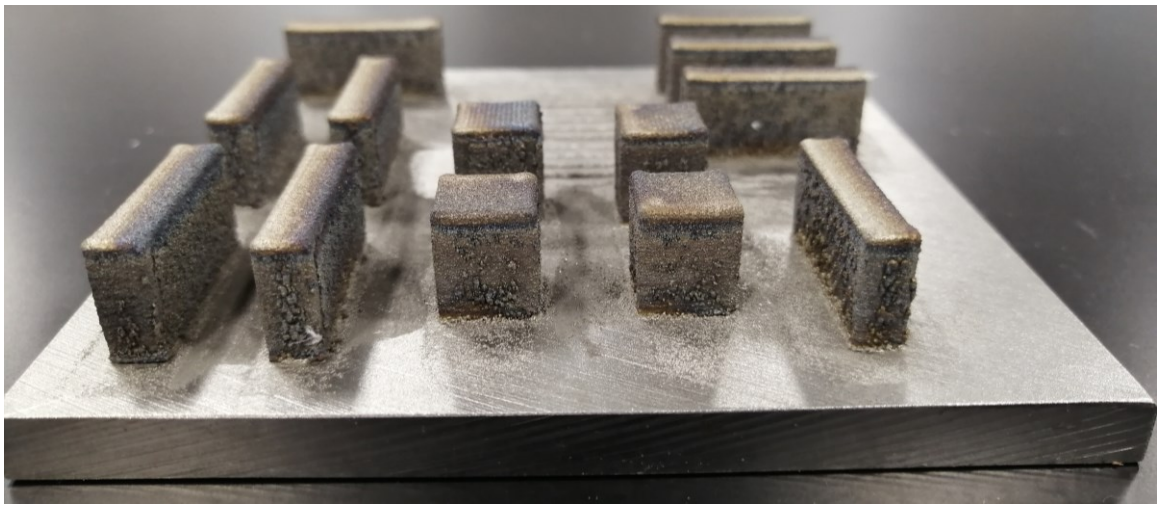

Figure 6.1. Direct energy deposited samples (the considered samples for this work are the cubic ones).

6.2.3 Materials Characterisation Procedures

- *Characterisation of Raw Materials*

In order to determine the chemical compositions of the used AISI D2 tool steel substrates and the feedstock powder, inductively coupled plasma optical emission spectroscopy (ICP-OES) analysis was conducted, with the aid of a Varian Vista-PRO system (Varian Inc., Palo Alto, CA, USA). Before analysis, an acid digestion step was conducted on the material being assessed (either feedstock powder or shavings from the substrate plates). A Hitachi S4700 field emission gun scanning electron microscope (SEM; Hitachi High Technologies

Inc., Tokyo, Japan) was used to examine the powder morphology and the microstructures of the D2 raw powder. The SEM was working under operating conditions of an accelerating voltage (V_{acc}) and beam current (I_e) of 3 kV and 15 μA, respectively, with the aim of minimising charging artifacts during powder morphology analysis. Furthermore, the particle size distribution of the D2 feedstock powder was evaluated using a Mastersizer 3000 system (Malvern Panalytical, Malvern, UK), where three measurements were conducted on different samples from the feedstock powder to assess the 'intra-batch' variability. Additionally, ASTM standard *B213-20: Standard Test Methods for Flow Rate of Metal Powders Using the Hall Flowmeter Funnel* was followed to assess the originally supplied powder flowability. As, the average of three different measurements was taken on 50-gram batches of the original powder, in which the time needed for the amount of powder to pass through the hall flowmeter orifice was recorded. ASTM standard *B703-17: Standard Test Method for Apparent Density of Metal Powders and Related Compounds Using the Arnold Meter* was also followed to measure the apparent density of the originally supplied powder, where three separate measurements were conducted and then averaged.

- *Characterisation of the DED Processed Materials*

Regarding the DED-processed materials, the microstructure of DED-processed samples was assessed using the same aforementioned SEM machine. The SEM was operated with an accelerating voltage (V_{acc}) of 15 kV and an accelerating voltage of 15 μA. The workpieces, which were assessed by SEM, were mounted in PolyFast (using Citopress-1, Struers, Copenhagen, Denmark). Such samples were ground and polished to a 1 μm finish (using successively finer SiC paper grades, finishing with Tegramin-20, Struers, Copenhagen, Denmark). The polished samples were then etched, by briefly immersing the

polished surface into 5 vol% Nital solution (5 vol% nitric to 95 vol% methanol). Furthermore, the SEM system also included an energy dispersive X-ray spectroscopy (EDS) system (Inca X-Max 80, Oxford Instruments, Abingdon, UK) which was utilised for chemical mapping of the DED deposited samples. The SEM operating conditions, for EDS analysis, were set at V_{acc} and I_e values of 5 kV and 20 μA, respectively. It is worth noting that SEM beam contamination has a profound impact on the accuracy of detecting carbon using EDS. However, EDS was only utilised, in the current work to determine chromium and carbide precipitate locations.

Additionally, X-ray diffraction (XRD; D8 Advance, Bruker Corp., Billerica, MA, USA) was employed to examine the phase formation in the DED-processed samples. The XRD system was operated, with a Co radiation source, operating at a voltage of 35 kV and current of 27 mA with Co-Kα radiation (Kα = 1.78897 Å) and a Fe filter. A range of 20-130° for 2θ was used with a step size of 0.02° and a time per step of 0.5 per second.

The indentation hardness of the DED processed D2 samples were evaluated using a Rockwell hardness tester (Wilson-2000, Instron, Norwood, MA, USA), where the Rockwell C scale was used, with a Rockwell spheroconical diamond indenter, with a preload and final applied load of 10 kgf and 150 kgf, respectively. The Rockwell C indentation hardness value was determined as a mean of six separate indentation measurements.

In addition, the dimensional accuracy of the as-printed DED parts was evaluated manually using a vernier calliper. Each dimension/sample was determined by performing five different measurements, then the mean value was obtained. A confocal laser scanning microscope (CLSM; model VK-X1100, Keyence Corp., Osaka, Japan) was used to assess

the as-deposited surface roughness of the DED manufactured samples, where a 20x magnification objective lens (with 535.7 nm theoretical resolution) was used. The arithmetical mean height (Sa) was used as an indicator for surface roughness evaluation, which was determined using the *Keyence Multifile Analyzer software*. For assessment purposes, Sa measurements were an average of five separate measurements for each surface, in each measurement an area slice was selected to determine the average Sa for the selected area slice. In addition, the evaluated area was selected that, qualitatively, demonstrated the most amount of partially melted powder particles stuck to the surface (the worst case). Measurements along the side surface were determined in the vertical direction, in consistency with what was observed by Mazumder et al. [121] that the higher side surface roughness was observed in the vertical direction than the horizontal one. In addition, the side surface was adjusted to be parallel to the CLSM lens. While no adjustment was needed for the top surface since it is naturally normal to the CLSM laser beam (i.e., parallel to the CLSM lens). Furthermore, two robust Gaussian filters were applied in order to isolate the surface roughness, as required by ISO standard 16610-21:2011: *Geometrical Product Specifications (GPS) – Filtration – Linear Profile Filters: Gaussian Filters* and ISO standard *11562:1996: Geometrical Product Specifications (GPS) - Surface Texture: Profile Method - Metrological Characteristics of Phase Correct Filters* [122,162]. Firstly, the small-scale measurement noise was eliminated by applying a shortcut filter (S-filter) with a cut-off scale of 2.5 μm [123]. Then, undulations and further lateral components were removed, using a long-pass filter (L-filter) with a cut-off scale of five times the profile length (in mm)) [124]. Finally, the surface roughness/morphology

was also evaluated using the aforementioned SEM with operating parameters (V_{acc} of 15 kV and I_e of 15 μA).

Further investigation on the as-printed DED samples included the estimation of the cooling rates with aim of justifying the relation between the DED operating parameters and the hardness and surface roughness of the DED fabricated specimens. The cooling rates were determined following Equation:

$$\lambda_2 = B\left(\frac{dT}{dt}\right)^{-n}$$

Equation 6.1 Cooling rates calculation [125].

where λ_2 represents the secondary dendrite arm spacing (SDAS, in μm), $\frac{dT}{dt}$ refers to the cooling rate (in K/s), and B and n are empirically determined constants with values of 42.1 μm.s.K^{-1} and 1/3, respectively [126]. The SDAS values were measured from digitised SEM images of the cross-sectional microstructures of the DED-processed samples. The public domain ImageJ software (National Institutes of Health, Kensington, MD, USA) was used, in which 5 measurements were conducted for each sample, while the average spacing along 10 to 15 secondary dendrites was recorded for each measurement.

6.3 Results & Discussion

6.3.1 Characterisation of Raw Materials

The chemical compositions of the AISI D2 feedstock powder and substrates used in this work, which was obtained using ICP-OES analysis, are presented in Table 6.3. In both cases, the compositions were found to be within the normal range expected for D2 tool steel [40,41]. In addition, Table 6.4 outlines the measured D2 feedstock powder

characteristics (i.e., particle size, flow behaviour, and density). It is apparent that the measured particle size is close to the manufacturer specification (i.e., a D_{50} of ~75 μm), which corresponds to the recommended particle size specified by the manufacturer of the DED system used in the current work. Figure 6.2(a) demonstrates the complete particle size distribution for the D2 feedstock powder, highlighting that it is monomodal in character. A representative SEM image of the feedstock powder is presented in Figure 6.2(b). It is apparent that the morphology of the powder is generally spherical, as would be anticipated from the gas atomisation process that was used. However, several attached micro-satellites and some irregular-shaped particles can also be observed, which may impact the powder flow response during DED processing.

Table 6.3. AISI D2 tool steel substrates and powder chemical compositions obtained by ICP-OES analysis.

Material Type	**Composition (wt.%)**									
	Fe	**C**	**Si**	**Mn**	**Cr**	**Mo**	**V**	**Co**	**Cu**	**Ni**
AISI D2 Powder	Bal.	1.55	0.41	0.33	11.27	0.64	0.79	0.01	0.01	0.06
AISI D2 Substrate	Bal.	1.50	0.3	0.3	12	0.75	0.9	-	-	-

Table 6.4. AISI D2 tool steel feedstock powder properties.

Properties (units)		**Value**
Particle Size	**D_{10} (μm)**	51.5
	D_{50} (μm)	73.6
	D_{80} (μm)	93.9
	D_{90} (μm)	106
Flowability (g/s)		3.2 ± 0.06
Density (g/cm^3)		4.20 ± 0.016

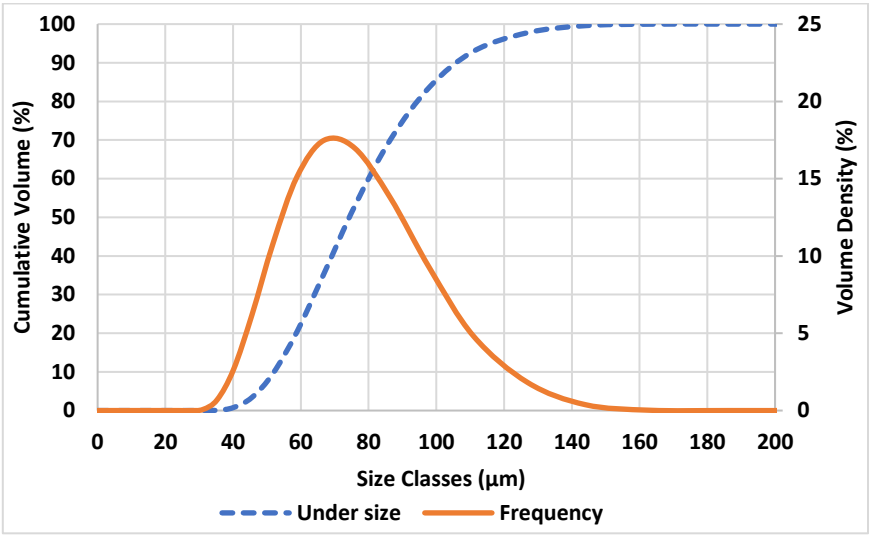

(a)

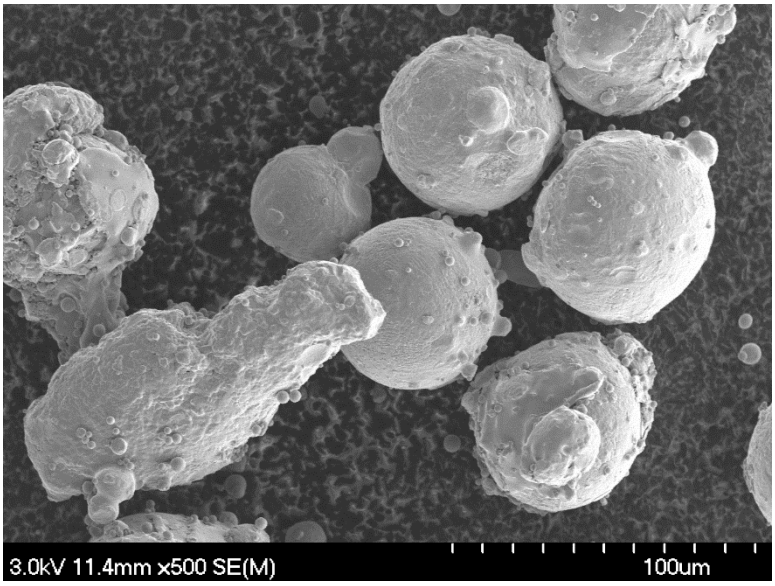

(b)

Figure 6.2. (a) Representative particle size distribution for the as-received D2 powder. (b) A typical SEM image of the as-received D2 tool steel powder, highlighting a generally spherical morphology with isolated satellite particles.

6.3.2 Microstructural Analysis

The microstructures of the DED-manufactured samples were subsequently evaluated using SEM. The comparison between Figures 6.3 and 6.4 demonstrates that the upper half of the DED processed parts shows more dendritic morphology with columnar grains. That could be attributed to 'constitutional supercooling'. Since, in DED, the dissipation of heat occurs through the liquid, (i.e., positive temperature gradient (G_r) in the liquid adjacent to the solid/liquid interface). Consequently, small protrusions are formed at the solid/liquid interface, thus leading to instability in the planar interface. Because there is a difference in growth rate between the bulk material and protrusions, the formation of dendritic morphology is promoted [51]. While it was found that the lower half of the DED processed samples shows equiaxed grains. That could be attributed to reheating the firstly deposited layers while printing newer ones, which, in turn, leads to the tempering of such layers, which results in homogenisation [139]. In other words, the formation of dendritic or cellular morphology is controlled by the degree of supercooling. For instance, a planar growth condition is observed at the high-temperature gradient and slow solidification rates (U_s) because constitutional supercooling is less probable in such cases. That explains why cellular structures are more favorable near the interface between the substrate and the deposited material [56].

Regarding the effect of layer thickness on the microstructure of the DED processed samples, it was found that there was no obvious effect of layer thickness upon the morphology of the DED processed samples. By the comparison of Figures 6.3(a) and 6.4(a) to Figures 6.3(b) and 6.4(b), Both samples demonstrate equiaxed morphology at the lower half and dendritic morphology at the upper half. However, cooling rates for the as-printed

DED components were determined by measuring the SDAS, as illustrated in Figure 6.5. It was observed that the cooling rate decreases by increasing the layer thickness. The same outcomes were reported by Mazumder et al. [121]. This could be attributed to that at higher layer thickness, the cooling rate is relatively low, due to the lower temperature in the regions adjacent to the deposited material and the lower thermal conductivity of the powder (i.e., more powder is delivered in case of thicker layer heights), which results in higher temperature gradients. In contrast, for the thinner layers' height, the thermal conductivity is higher as a result of the solidification of the previously deposited layers into a dense, solid state, which, in turn, leads to an increase in the cooling rates [145].

The EDS mapping of sample T1 is presented in Figure 6.6. It was observed that chromium carbides are primarily precipitated along the grain boundaries, consistent with previous observations for D2 [140]. Furthermore, the outer layers of the dendritic structure were found to involve eutectic coring, as presented in Figure 6.6. That could be attributed to the 'off-eutectic' composition of carbon in D2 tool steel (i.e., 1.5 wt.% C), which is more than the peritectic composition (0.5 wt.% C) but less than the eutectic composition (4.3 wt.% C). Therefore, as demonstrated in Figure 6.6, at the liquidus temperature for 1.5 wt.% C, solidification usually starts, which results in the formation of the primary γ dendrites. Then, the increase in the thickness of the dendrite leads to the rejection of the solute (carbon in this case) in to the remaining liquid, until the composition of 4.33 wt.% C is reached, at which point solidification of the eutectic occurs [56].

Regarding the formation of crystalline phases following the DED process, Figure 6.7 illustrates a comparison between the XRD pattern of the laser DED processed D2 tool samples T1 and T4. It was found that austenite was the primary (dendritic) structure for

the DED-processed samples. This could be attributed to that, despite the high cooling rates in the DED process, the high Cr and C content in D2 tool steel results in the formation of a metallic matrix that is primarily austenite and contains an excess of dissolved carbon. Therefore, the martensitic formation temperature is depressed [140].

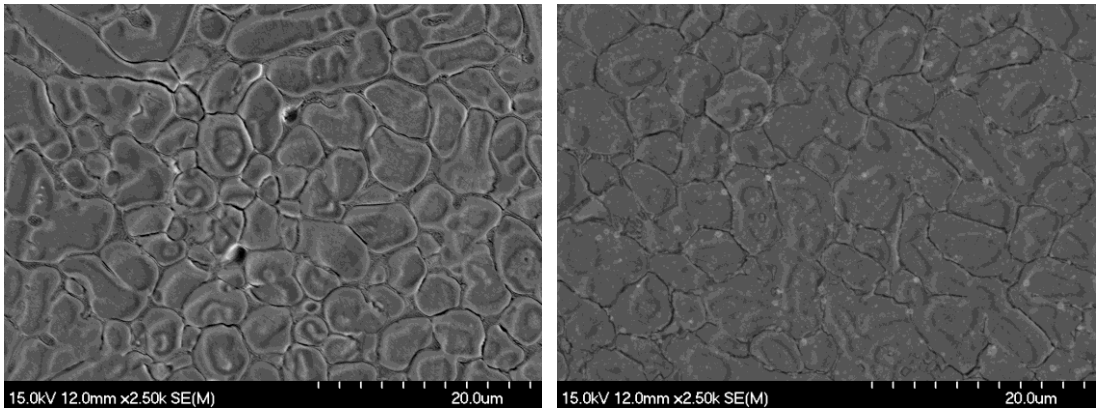

(a) (b)

Figure 6.3. SEM images of the lower half of DED processed samples (a) T1 and (b) T4. Samples were etched with 5 vol% Nital solution.

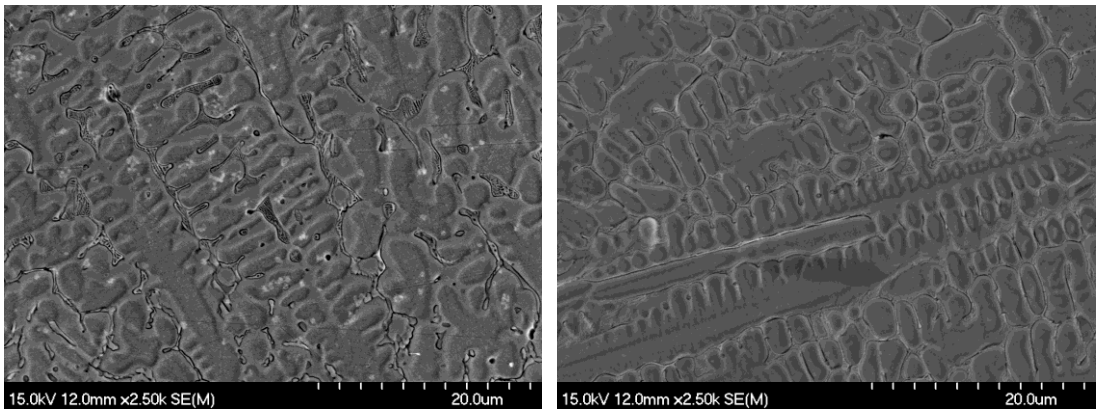

(a) (b)

Figure 6.4. SEM images of the upper half of DED processed samples (a) T1 and (b) T4. Samples were etched with 5 vol% Nital solution.

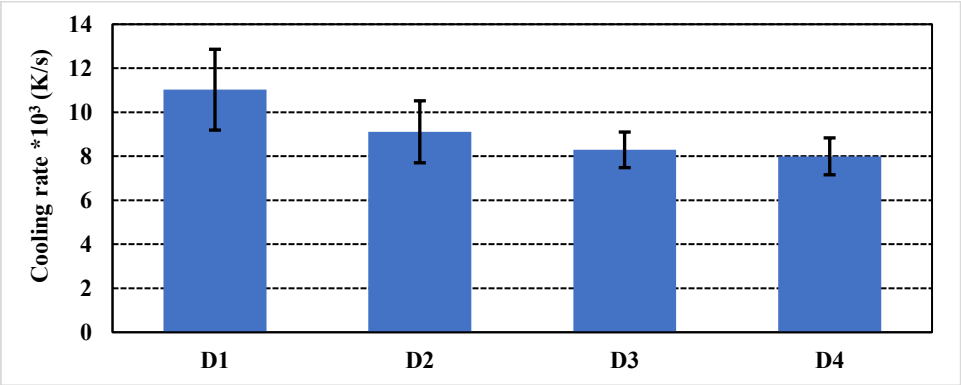

Figure 6.5. The calculated cooling rate of selected 'as-printed' samples using Equation 6.1.

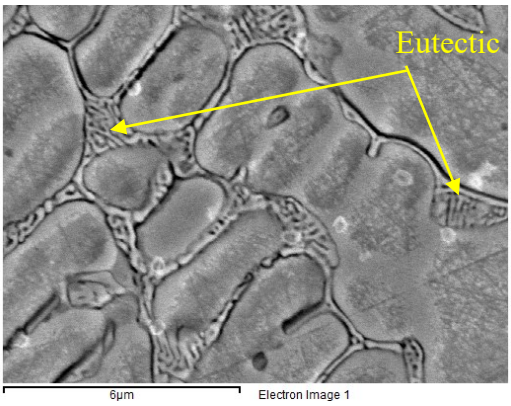

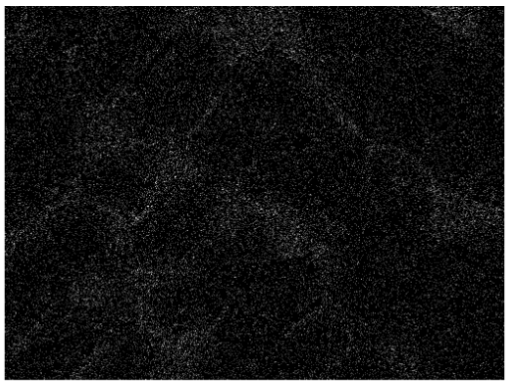
C Ka1_2

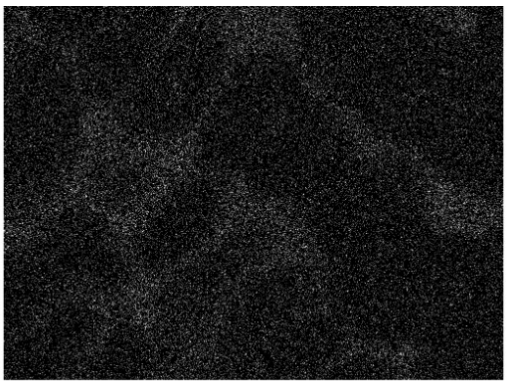
V Ka1

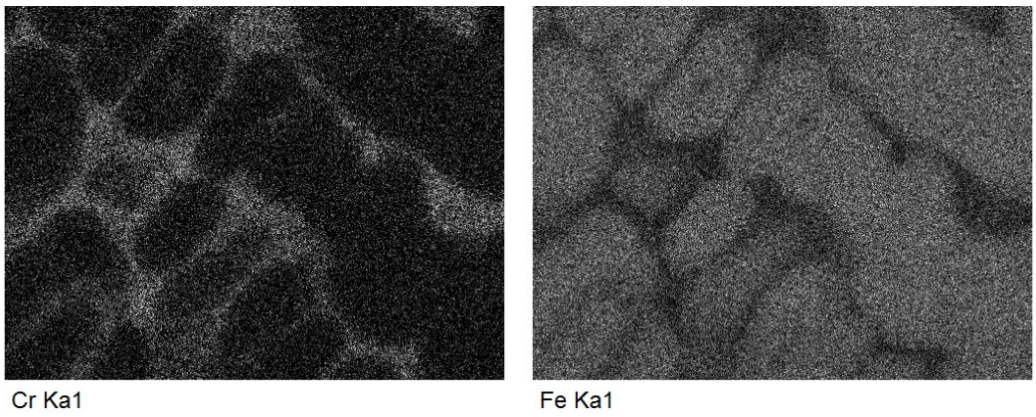

Figure 6.6. SEM image and the associated EDS mapping for the middle section of the DED processed sample T1.

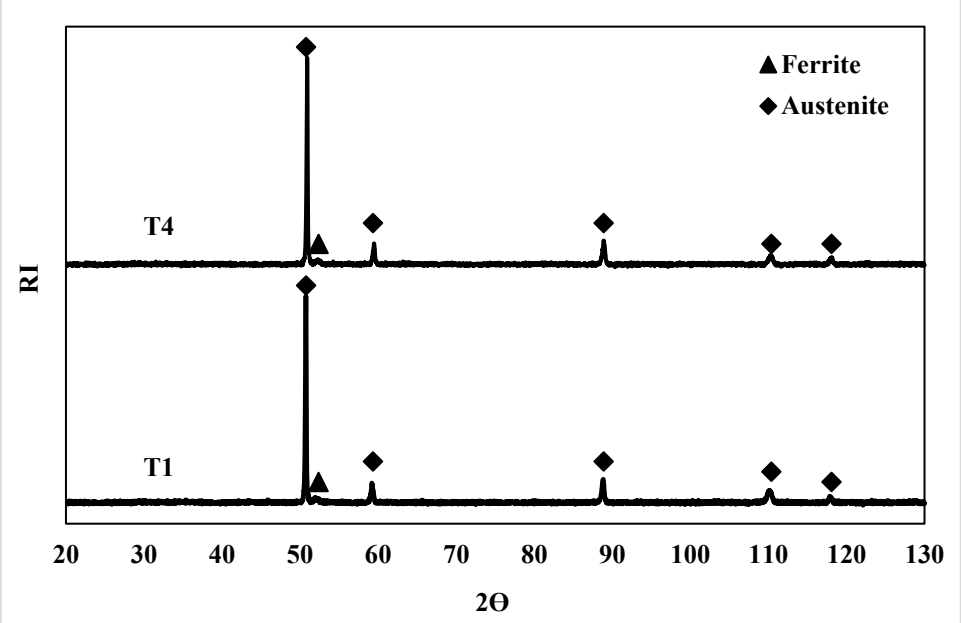

Figure 6.7. Comparison of the XRD patterns recorded for the DED processed D2 samples as printed (T1 and T4).

6.3.3 Indentation Hardness Evaluation

The Rockwell C scale hardness test was used to determine the indentation hardness values for the DED as-processed samples. Figure 6.8 illustrates the dependency of the Rockwell

hardness on the targeted layer thickness, for samples spatially positioned at the bottom, middle and top regions of the as-processes DED samples.

Generally, lower hardness could be readily observed at the bottom of the sample, near the interface between the substrate and deposited material than measured in either the middle or top regions of the DED as-printed samples. This could be attributed to the Hall-Petch effect. Since, at later stages of the deposition process, the initially deposited layers are reheated during the deposition of the top layers. That resulted in grain growth which, in turn, leads to a reduction in hardness. However, at the top layers, due to the high cooling rates, which were explained by observing the dendritic morphology (Figure 6.4), that results in higher hardness [143,144].

In terms of the effect of the designed layer height, as illustrated in Figure 6.8, it is apparent that there is some significant variation in the mean hardness between the various samples. It was observed that the use of thicker layer height leads to a reduction in the mean hardness. The results of the indentation hardness were compared to the estimated cooling rates (Figure 6.5). The comparison demonstrates that there is significant consistency between the trends for mean hardness and the cooling rates [174]. The highest measured mean Rockwell hardness was observed at the lowest thickness, with the highest cooling rate. That arose because, at small layer thickness, the cooling rates are higher as a result of the higher thermal conductivity, due to the solidification of the previously deposited layers into a dense, solid state, which results in higher hardness. While, for thicker targeted layer height, the thermal conductivity is lower due to the poor thermal conductivity of the powder and the lower temperature in the regions surrounding the deposited material (i.e.,

low melting pool temperature due to the more excess powder). That results in lower cooling rates which, in turn, leads to lower hardness [145].

Finally, regarding the optimised properties, the highest mean hardness, in the middle of the sample, was found at a targeted layer thickness of 0.125 mm for the present materials in the DED as-processed state (sample T1).

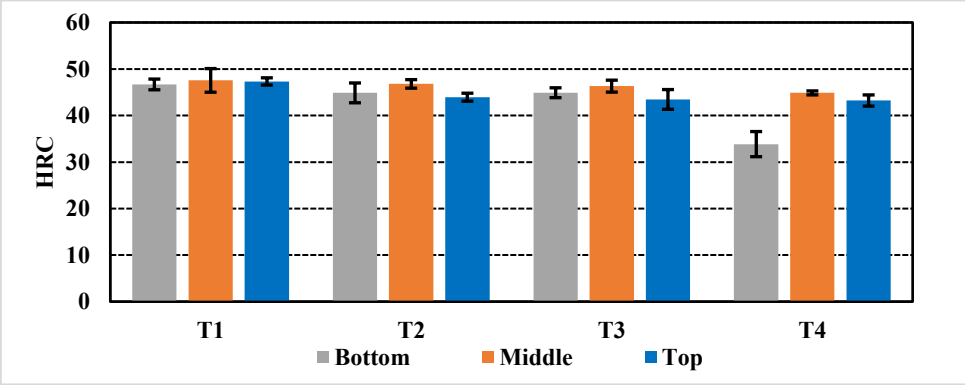

Figure 6.8. Measured Rockwell C indentation hardness of 'as-printed' samples as a function of location.

6.3.4 Geometrical Characteristics

The relationship between the dimensional accuracy of the as-printed DED samples, regarding the sample height, to the targeted layer thickness is demonstrated in Figure 6.9. The dimensional accuracy is described as the difference between the initially designed heights and the actual height of the as-deposited sample. The dimensional discrepancy in width and length directions was found to be minimal. Therefore, the current work only involves the discrepancy in height. In general, it is obvious that all of the samples were overbuilt, with sample heights ranging from 12.25 mm (± 0.06), at a layer thickness of 0.5

mm to 13.17 mm (± 0.2), at a layer thickness of 0.125 mm; in this case, the initially planned height for the DED processed part was 10 mm.

In terms of the effect of layer thickness upon dimensional discrepancy, it was observed that the use of lower layer thickness leads to a higher extent of overbuilding of the DED processed parts (i.e., a higher height discrepancy). That arose because, at lower layer height, more layers are deposited to build the DED part, resulting in higher height error [163].

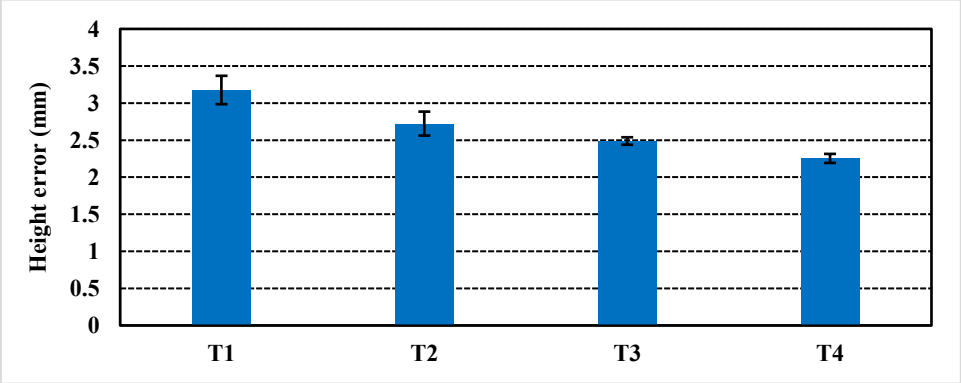

(a)

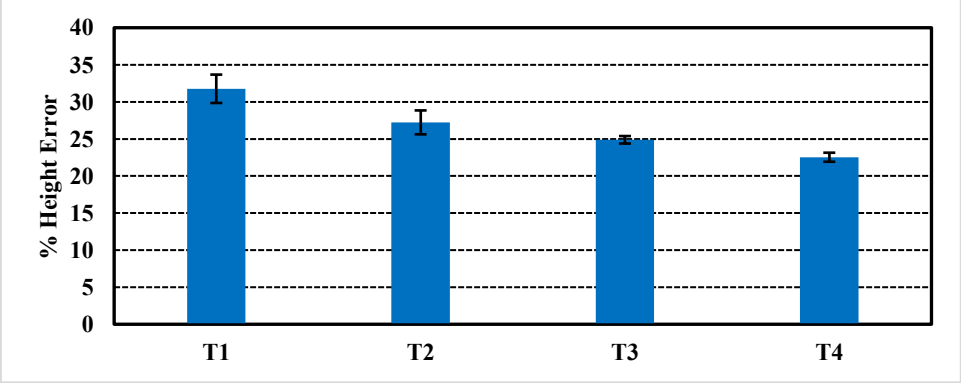

(b)

Figure 6.9. The effects of layer thickness upon the measured errors in build height as: (a) the measurement value, and (b) as a percentage of the originally specified height.

6.3.5 Surface Roughness

Figure 6.10 (a-c) illustrates the surface finish and shape of a typical DED processed sample (in this example T2), with representative photographs and SEM graphs. It could be significantly observed that the side surfaces are rougher than the top surface. That could be attributed to the partially melted powder particle, sticking to the side surface during the DED process. In addition, Figure 6.10 (d, e) demonstrates representative CLSM images for the top and side surfaces for sample T2, which form the basis of the following roughness analysis.

(a)

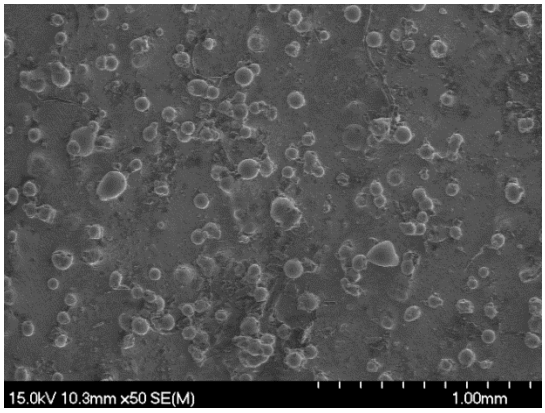

(b)

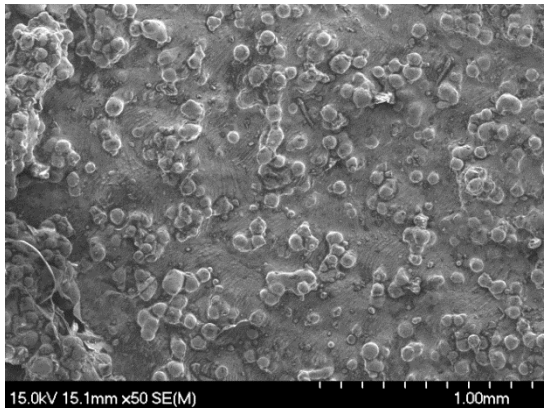

(c)

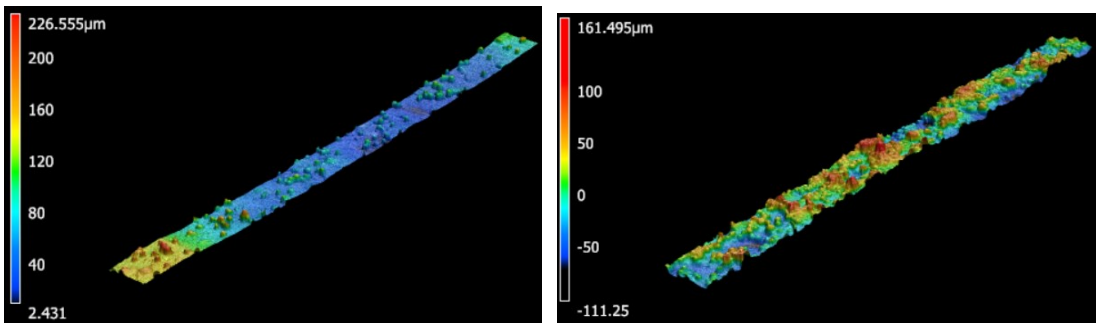

(d) (e)

Figure 6.10. An example of the surface roughness for the DED printed samples, in this instance prepared under DED process conditions T2: (a) Macro-photograph, (b) representative SEM image of the top surface, (c) representative SEM of the side surface, (d) representative CLSM image of the top surface, and (e) representative CLSM image of the side surface.

Figure 6.11 demonstrates the values of the measured top and side surface roughness. As previously mentioned, it could be generally noticed that the surface roughness of top surfaces is lower than the side surface ones.

Regarding the impact of the layer thickness on the top surface roughness, it could be observed that the use of thinner layer heights results in lower surface roughness. That could be attributed to that, at lower layer thickness, less amount of powder is deposited into the melt pool, which leads to more proper melting conditions. Therefore, less partially melted powder adheres to the top surface of the DED fabricated sample [165]. Hence, the minimum top surface roughness was observed at a layer height of 0.125 mm (the thinnest), as presented in Figure 6.11.

As shown in Figure 6.11, it was found that the trend for the influence of the layer thickness upon the side surface roughness is opposite to what was found for the top surface roughness. That could be attributed to that the top surface roughness is highly affected by the amount of the partly melted powder particles which adhered to the side surfaces, which, in turn, is dramatically affected by heating-cooling cycles, during the DED process. However, the top surface roughness is only affected by the process conditions of the last deposited layer. In consequence, the evaluation of the side surface roughness was accomplished by comparing the measured side surface roughness trend to the calculated cooling rate (Figure 6.5). That comparison reveals that there was no monotonic effect for varying layer thickness on the side surface roughness of the DED processed samples.

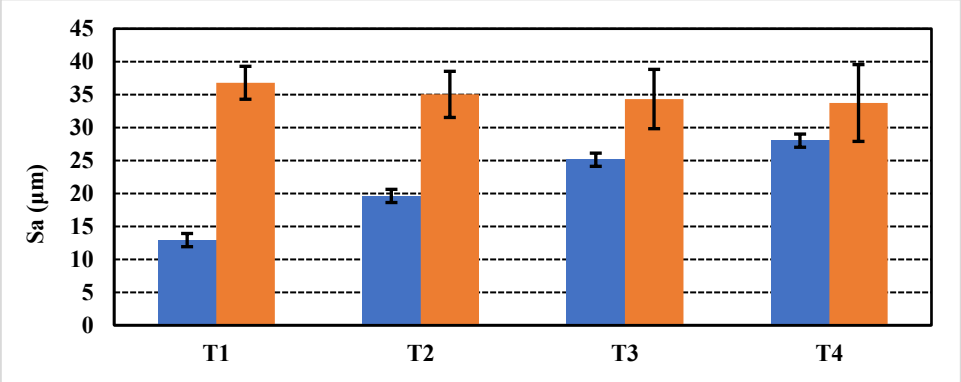

Figure 6.11 The effect of layer thickness on the CLSM measured the top and side surface roughness values.

6.4 Conclusions

The present work has focused on the influence of layer thickness upon the formed morphology, hardness, geometrical characteristics and surface roughness of DED processed samples on the layer thickness, after deposition of D2 tool steed powder onto a substrate of the same material. The following conclusions were obtained from this initial study:

- Regarding the morphology of the DED processed samples, a dendritic morphology, with the presence of columnar grains, was observed in the upper half of the DED samples. That arose because of the constitutional cooling due to the rapid cooling of the DED processed samples. While the lower half of the DED processed samples showed a more equiaxed morphology.
- Concerning the formation of crystalline phases following the DED process, it was found that austenite was the primary (dendritic) structure for the DED-processed samples. This could be attributed to that, despite the high cooling rates in the DED process, the high chromium and carbon content in D2 tool steel results in the formation of a metallic matrix that is primarily austenite and contains an excess of dissolved carbon. Therefore, the martensitic formation temperature is depressed.
- For the indentation hardness, lower hardness could be readily observed at the bottom of the sample, near the interface between the substrate and deposited material than measured in either the middle or top regions of the DED as-printed samples. This could be attributed to the Hall-Petch effect. Since, at later stages of the deposition process, the initially deposited layers are reheated during the

deposition of the top layers. That resulted in grain growth which, in turn, leads to a reduction in hardness.

- Regarding the effect of layer thickness on the hardness, it was observed that the use of thicker layer height leads to a reduction in the mean hardness. That was found to be consistent with the cooling rate trend. In other words, the highest measured mean Rockwell hardness was observed at the lowest thickness, with the highest cooling rate.
- Concerning the influence of layer thickness upon the geometrical characteristics, it was observed that the use of lower layer thickness leads to a higher extent of overbuilding of the DED processed parts (i.e., a higher height discrepancy). That arose because, at lower layer height, more layers are deposited to build the DED part, resulting in higher height error.
- In terms of surface roughness, the side surface roughness (i.e., the face parallel to the laser axis) was found to be higher than that measured for the top surface. That arose because of the adhesion of isolated powder particles to the side surfaces.
- The top surface roughness was found to be enhanced by decreasing the layer thickness. That could be attributed to that, at lower layer thickness, less amount of powder is deposited into the melt pool, which leads to more proper melting conditions. Therefore, less partially melted powder is adhered to the top surface of the DED fabricated sample.

- For the side surface roughness, the influence of layer thickness was found to be profoundly impacted by the heating-cooling cycles (i.e., cooling rates and temperature gradients) that occur during the DED process. A distinct consistency was noticed between the side surface roughness and the estimated cooling rates (from SDAS analysis). That could be attributed to that, at lower cooling rates, slower solidification occurs. Thus, leading to fewer partially melted powder particles adhering to the surface. The lowest side surface roughness was observed at a layer thickness of 0.5 mm; this agreed with the minimum estimated cooling rates.

Acknowledgements

The authors would also like to thank the technical assistance of Mr. Randy Cooke and Dr. Greg Sweet (Dalhousie University) with the DED printing of the samples. Ms. Patricia Scallion is also gratefully acknowledged for her support with SEM analyses. This work was financially supported through the NSERC Strategic Project Network Grant *Holistic Innovation in Additive Manufacturing* (HI-AM) through Grant No. NETGP 494158-16.

CHAPTER 7 Impacts of Heat Treatment upon Wear Resistance of Wrought and Directly Energy Deposited AISI D2 Tool Steel

Abstract

The wear resistance of laser directed energy deposited (DED) parts were examined to assess the cladding of AISI D2 tool steel feedstock onto annealed AISI D2 substrates. The wear behaviour was evaluated by measuring the specific wear rate, following the ball-on-flat reciprocating sliding wear ASTM standard test procedure, for various test durations. The specific wear rates were assessed by measuring the wear track volume using confocal laser scanning microscopy. The wear rate of the as-printed material was then compared to wrought, heat-treated D2. The microstructural and compositional characteristics of the wear tracks for both the 'as-printed' and heat-treated D2 samples were investigated using scanning electron microscopy, with associated energy dispersive X-ray spectroscopy for compositional analysis. It was demonstrated that the specific wear rate decreased with increased test duration, highlighting a change in the wear mechanism over time. Furthermore, the wear rates for the DED fabricated parts were found to be lower than an annealed wrought D2, but higher than the air-cooled D2 variant.

Keywords: tool steels; additive manufacturing; laser direct energy deposition; wear; tempering; heat-treatment.

7.1 Introduction

The additive manufacturing (AM) approach in which a fine powder stream is (coaxially) conveyed to an energetic heat source (i.e., laser beam) to create a molten pool on a metallic substrate is referred to as direct energy deposition (DED) [10,30–33]. With DED, in order to initially build a single layer, an associated computer numerical control (CNC) system is utilised to scan the laser beam over a desired path. Then, the subsequent deposition of layers on top of one another (i.e., layer by layer) generates a 3D object [36]. DED is also known as laser powder deposition [41,43], laser direct casting [128], laser consolidation [39], solid free-form fabrication [44], laser coating [37,38], etc.

The DED technique has several potential benefits over other AM technologies. For instance, the critical contacting surfaces for high-value tools could be repaired using DED, instead of replacing the whole part [46,47], when wear or corrosion degradation arise. Furthermore, thanks to the absence of restrictions on the geometry of the manufactured part, DED is an excellent candidate for generating parts with thin walls, deep cavities, or hidden channels [16,25]. However, on the other hand, poor reproducibility in the quality of the DED fabricated part is one of the main drawbacks of this process, which can be attributed to the dramatic sensitivity of the clad quality to disturbances in the process (i.e., minor variations in the operating parameters (laser power, scanning speed, powder feed rate, etc.) [51]. In addition, residual stresses or cracking can be present in DED fabricated parts, due to the high thermal gradients that arise through the DED process which, in turn, could result in failure of the fabricated component [48–50].

The wear resistance of the DED processed parts, when compared to conventionally fabricated ones, is one of the main questions that researchers still largely have to answer,

in order to more fully characterise the DED process. For instance, Wang et al. [175] reported that the wear resistance of as-DED processed material depends on the microstructure and the shape, size, distribution, and proportion of the secondary carbides that can be formed. Since the DED process creates a 'wavy', as-printed surface, the peaks and valleys from the AM process showed that the wear was higher in the valleys than on the peaks and the distance between peaks matched the hatch spacing of the process parameters. The valleys were associated with the as-printed clad deposit and the peaks with the re-heated zone. However, there was not a significant difference in the wear rates between these areas. Post-deposition heat treating will improve the number of carbides slightly and potentially their morphology, which can improve the wear resistance but, due to the tempering effect, will be expected to lower the hardness and scratch resistance. Testing conditions can also influence the wear resistance, with slower sliding speeds showing that laser clad samples preformed similarly to the cast equivalent, although once the sliding speed increased the laser cladded sample had a lower wear rate than the cast sample [176].

The limited studies conducted to-date, have resulted in a conflicting consensus on whether the as-printed condition is better than the wrought equivalent. Rahman et al. [177] observed that laser cladding samples had better wear resistance, arising from the refined microstructure, at room temperature and resisted three-body abrasion when compared to the wrought material. However, at elevated temperatures, the wrought material had better wear resistance than the clad material, due to the homogenous oxide layer; it appears that the anisotropic structure formed with DED also leads to inhomogeneous oxidation during elevated testing. Xue et al. showed that in the as-printed state, their DED processed H13

material had better wear resistance than the wrought equivalent, with even the counter-surface exhibiting less wear [178]. The improved wear resistance of the DED consolidated material was attributed to the finer microstructure and higher hardness than the wrought equivalent. When the DED H13 was heat treated, it still performed better in a tribological scenario than the wrought variant, even though there was a slight decrease in hardness. A separate study by Shim et al. [179], showed that the wear resistance of both as-printed and heat treated, DED processed M4 tool steel samples was better than wrought, heat treated D2. It appears that heat treating can help with peeling issues for DED-based fabrication processes, especially going straight to a tempering heat treatment, instead of quenching and then tempering. A further study, by Tuominen and colleagues [74], examined several tool steel grades and all of the clad samples outperformed the equivalent wrought reference material. Navas et al. [180] noted that deposited M2 exhibited only slightly better unlubricated sliding behavior and wear resistance than quenched, wrought M2. This was reported to be due to the greater amount of retained austenite in the matrix, which transforms into martensite during testing. In an assessment of DED processed D2 tool steel, Yu et al. [181] concluded that the clad material had significantly higher wear resistance than the heat treated, wrought D2 equivalent. In contrast, Rahman et al. [177] concluded that heat treatment is unlikely to improve the wear resistance of HSS. However, Chen et al. [182] observed that heat treated H13 did see an improvement in the wear resistance, with the greatest amount of volume loss occurring for samples heat treated at 550°C for two hours, which was then sharply reduced for samples heat treated at either 600°C and 650°C. Overall, it can be seen that applying a heat treatment is highly recommended, however it was also noted that selection of the correct heat treatment must be done

carefully, because if the tempering temperature is too high it could be detrimental to the substrate [183].

The present work has involved DED of specimens of AISI D2 tool steel powder, deposited onto a substrate of the same material. After the DED stage, samples were subjected to post-heat-treatments. The as-printed and post heat-treated DED processed, as well as the equivalent wrought D2 samples, were then subjected to ball-on-flat wear testing, for three different test durations. The wear tracks were subsequently evaluated in terms of their volume (to determine the specific wear rate), microstructure, and chemical composition (in terms of any tribolayer that might be generated). In addition, the alumina (Al_2O_3) counter face surfaces were also analysed, to evaluate the rate of subtracted volume from the spheres used in the wear test.

7.2 Experimental procedures

7.2.1 Raw Materials

All of the wrought D2 tool steel, used for baseline performance analysis, was obtained from Hudson Tool Steel (Dover, NH, USA). For the heat-treatment evaluation, circular rods of wrought D2 tool steel were provided with a diameter and length of 19.05 mm and 900 mm, respectively. Subsequently, the rods were sectioned into disc-shaped samples with the same original diameter (19.05 mm) and a thickness of 5 mm. For DED, wrought D2 plates with dimensions of 101.6 x 101.6 x 6.35 mm (4 x 4 x 0.25 inches) were supplied to be used as substrates. Before DED processing, the top surface of the substrate was sandblasted with the aim of eliminating any potential laser reflection effects within the DED system. In terms of the D2 feedstock powder utilised for the DED processing, this was supplied as a

gas atomized powder from TLS Technik Spezialpulver (Bitterfeld-Wolfen, Germany), with a nominal particle size range of 45 to 90 μm, as specified by the manufacturer. The chemical compositions of both the AISI D2 substrates and the gas atomised feedstock powder has been reported in a prior study [174].

7.2.2 Laser DED Sample Fabrication

A 1-kW fiber laser, with a 600 μm spot diameter, was utilised for conducting the DED processing stage (MTS-CA system, Optomec, Albuquerque, NM, USA). The DED system is provided with five-axis machine movement control. The powder supply system of the DED equipment consists of a coaxial powder nozzle, with four separate powder delivery hoppers. The injected powder is then delivered to the molten pool region using Ar as a carrier gas. In addition, the DED chamber is operated in Ar as a shielding atmosphere, in order to minimise potential for oxidation of the workpiece. All the process parameters were kept constant, based upon our prior work [REF], with the selected values presented in Table 7.1. A representative example of the actual printed samples is shown in Figure 7.1.

Table 7.1. A summary of the main DED processing parameters

Parameter	**Value**
Sample dimensions, L x W x H (mm)	10 x 10 x 5
Laser power (W)	400
Scanning speed (mm/min)	600
Powder feed rate (g/min)	5.5
Targeted layer thickness (mm)	0.251
Hatch spacing (mm)	0.381

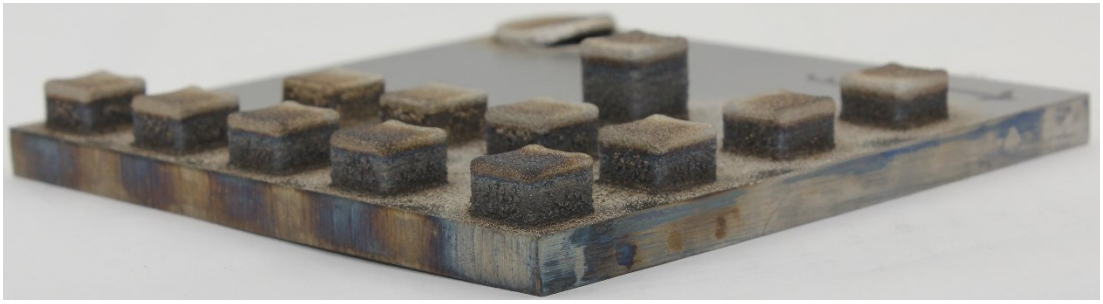

Figure 7.1. Typical examples of the DED processed D2 tool steel samples.

7.2.3 Heat-Treatment Cycles

In order to evaluate the effects of various tempering heat-treatment schedules on the wear resistance, the wrought D2 samples were subjected to heat-treatment under different scenarios. In the current work, all of the heat-treated specimens were firstly subjected to an austenising stage, in which the sample is held for a period of 30 minutes at 1,010 °C; a stabilisation stage was also employed (750 °C, for 30 minutes) during heating to the austenising temperature to ensure a uniform temperature distribution through the specimen. After austenitising, the heat-treated specimens were rapidly air-cooled down to room temperature in order to lock-in the austenitised structure.

A selection of tempering treatments were then conducted on the sample immediately after air-cooling. In the first, a single-step tempering treatment, the specimens were held for 120 minutes at various temperatures from 400-600 °C. A further batch of samples, referred to as double-tempered, was subjected to retempering stage after the first, single step treatment, in which the specimens were kept again in the furnace for 120 minutes, at the same tempering temperature. A summary of the respective heat-treatment scenarios and the associated sample codes used is presented in Table 7.2. A schematic representation of

the cycle used for a typical heat-treatment scenario, when double tempering at 500 °C (DT5) in this instance, is presented in Figure 7.2.

Table 7.2. Sample identification for the heat-treated D2 materials.

Sample ID		**Temperature (°C)**	
		Tempering	**Retempering**
No Heat-treatment	NHT	-	-
Single Tempered	T4	400	-
	T5	500	-
	T6	600	-
Double Tempered	DT3	300	300
	DT4	400	400
	DT5	500	500
	DT6	600	600
Air-cooled	Q	-	-
As DED Processed	DED	-	-

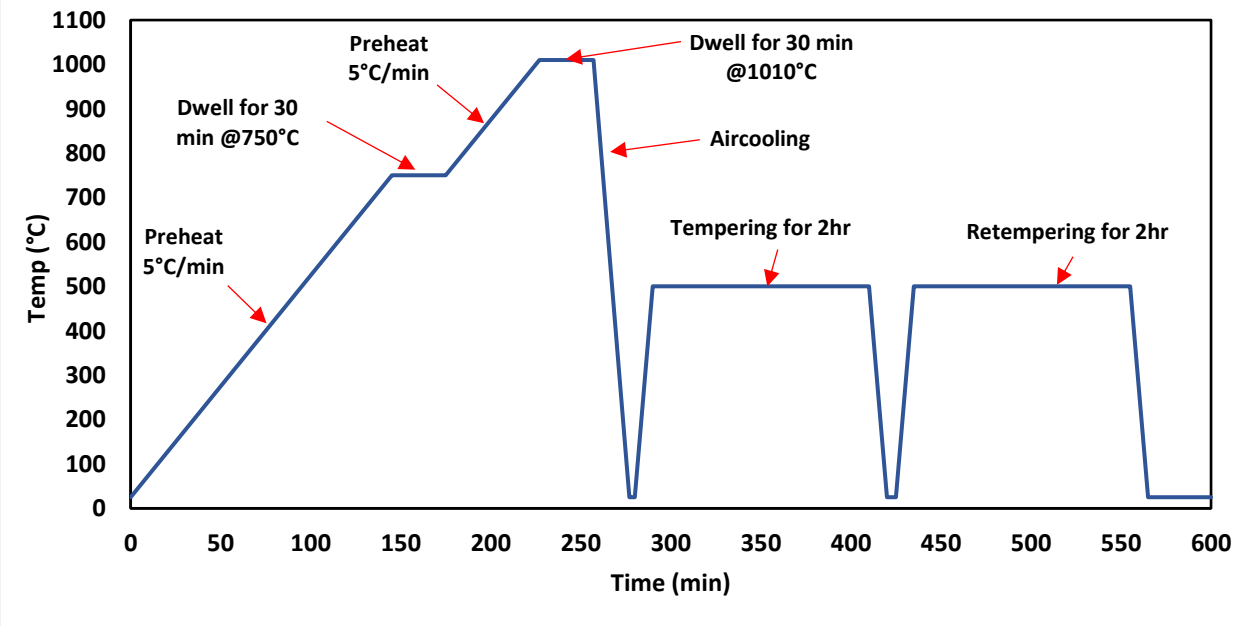

Figure 7.2**.** A schematic representation of the typical heat-treatment cycle that was applied for both the wrought and DED processed samples. In this example, a 'double-temper' treatment has been applied, with each step of the temper treatment conducted at 500 °C for 120 minutes.

7.2.4 Wear Resistance Evaluation

The wear resistance of the various D2 samples was determined following ASTM standard *G133-05*: *Standard Test Method for Linearly Reciprocating Ball-on-Flat Sliding Wear*. However, the parameters used were not in full compliance with the provisions of Test Method ASTM-G133 (Procedure A), as the normal force used in the present tests was 5 N, instead of 25 N as prescribed by the standard, while the stroke length used was 5.03 mm, instead of 10.0 mm as prescribed by the standard. The wear tracks on the wrought, heat-treated, and DED processed D2 tool steel samples were generated using a UMT-1 model universal micro tribometer system (CETR Corp., Campbell, CA, USA), at room temperature (20 ± 2 °C), in an air atmosphere. with Polycrystalline Al_2O_3 spheres (McMaster-Carr, Elmhurst, IL, USA) were used for these tests with diameter of 6.34 mm. All other provisions of Test Method G133 have been followed. The wear tests were conducted for three different test durations (500, 1000, and 2000 s), to assess wear response evolution. The surface of the wear samples was ground with SiC paper up to 2000 grit prior to testing, while the sample surfaces were cleaned with ethanol immediately before the tests. In addition, it is worth noting that the wear tracks applied on the top surface of DED deposited samples.

It is worth mentioning that the full effects of varying DED process parameters and post-heat treatment will be included in future work, since the wear tester broke down after completing the presented work in this thesis.

The specific wear rate was determined using Equation 7.1:

$$WR = \frac{V_{loss}}{2.t.L.f_o.F}$$

Equation 7.1 Wear rate calculation [127].

where WR is the wear rate in (mm^3/N.m), V_{loss} refers to the wear track volume in mm^3, t is the test time in seconds, L represents the length of the stroke in m, f_o is the oscillating frequency in Hz, and F is the applied load in N.

Three individual wear tracks were generated on each sample for each set of wear testing parameters, in order to obtain a mean value and an associated standard deviation error. The wear track volume losses were determined from 3D images generated using a confocal laser scanning microscope (CLSM; model VK-X1100, Keyence Corp., Osaka, Japan), with a 10x magnification objective lens. CLSM, with a 10x magnification objective lens. The CLSM wear track image data was evaluated using the Keyence Multifile Analyzer software, as illustrated in Figure 7.3(a). In addition, the removed volume from the counter surfaces of the Al_2O_3 spheres was assessed using CLSM, as presented in Figure 7.3(b). In this instance the surface curvature of the worn sphere was converted into a flat surface through comparison with a perfect (unused) sphere, using the option of flatten curvatures in Keyence Multifile Analyzer software, which allowed a more accurate determination of wear loss from the sphere surface (Figure 7.3(c)).

The wear tracks were also examined using a Hitachi S4700 field emission gun scanning electron microscope (SEM; Hitachi High Technologies Inc., Tokyo, Japan). The SEM was also equipped with an energy dispersive X-ray spectroscopy (EDS) system (Inca X-Max 80, Oxford Instruments, Abingdon, UK) for chemical mapping of the DED processed and heat-treated materials. For SEM and EDS mapping, accelerating voltage (V_{acc}) and beam current (I_e) values of 5 kV and 20 μA were used, respectively. Although EDS is highly affected by SEM beam contamination, which in turn, affects the accuracy of detecting

carbon, in the present work it was used to demonstrate the locations where chromium and carbides precipitate in addition to the amount of oxidation developed during the wear test.

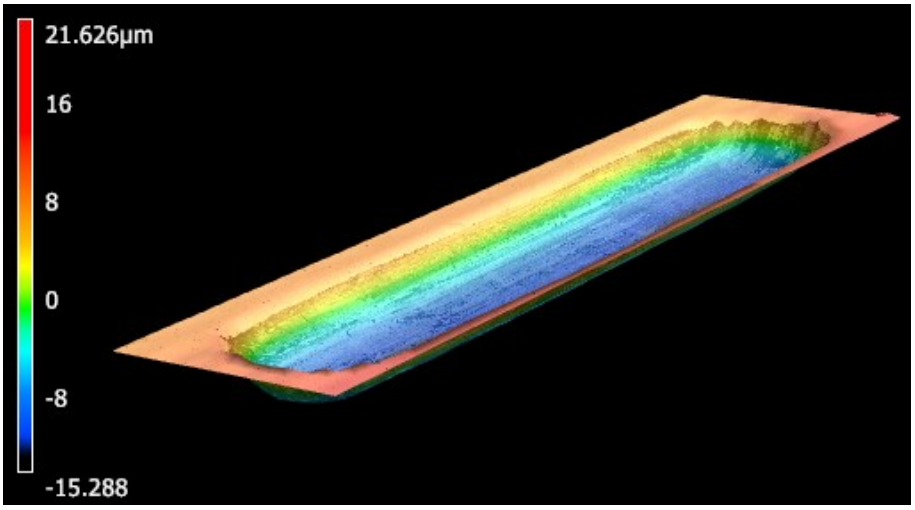

(a)

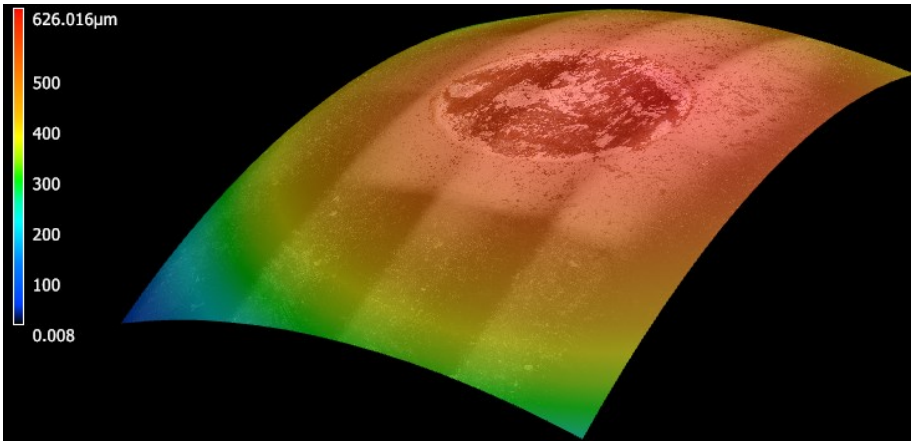

(b)

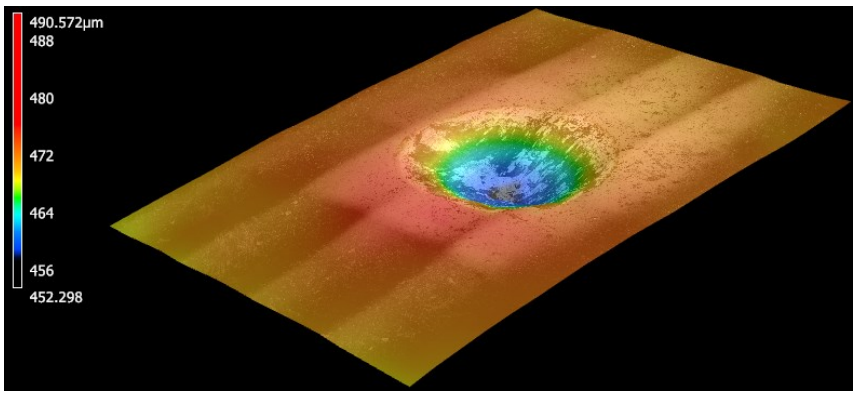

(c)

Figure 7.3. Representative CLSM images of: (a) an example wear track on a wrought D2 sample, and (b) the wear track on an Al_2O_3 counter face sphere. (c) A 'corrected' (i.e., flattened) CLSM image generated through comparison of a perfect (i.e., unworn) sphere and one after testing, to assess the wear track volume on the counter sphere.

7.3 Results and Discussion

7.3.1 Microstructure Evaluation of Laser DED samples

The topographies and EDS mapping of wear scars for the as-printed DED samples, evaluated for two wear test durations (500 and 2,000 seconds), are presented in Figures 7.4 and 7.5. In general, as shown in Figure 7.4 (a) and (c), it can be observed for both test durations that the wear mechanism appears to be a mixture of adhesive and abrasive wear. As would be expected, the width of the wear track increases with test duration. The impact of abrasive wear is shown in terms of deep ploughing grooves, which arose because the microstructure of the DED-processed samples shows fine carbide precipitates located at the grain boundaries, as outlined in our prior work [174]. These grooves are believed to be formed due to the abrasion effect of these fine carbide particles, effectively being pushed along the wear track, since the fine carbide particles are squeezed between the specimen and counter face surfaces. These observations help to explain the formation of the ploughing grooves in the wear tracks, as noted in a prior study [179]. Figure 7.5 (a) and (b)

illustrate that there are torn particles of carbides (especially chromium carbides) which were pushed to the edges. The amount of carbide particles transferred to the edges of the wear tracks was found to be greater after 2,000 s than at 500 s.

Regarding the transition from an abrasive to an adhesive wear mechanism, regions of adhesion are noted in Figure 7.4 (b) and (d). Formation of a tribofilm, or tribolayer, is also apparent in these images, which is the result of the wear debris being consistently refined in size due to the reciprocating action of the wear test. It was apparent that the fracture of the adhered material is clean, with little deformation and produces fewer wear particles, due to the increased brittleness of the as-DED processed sample [174]. When the material transfers from the workpiece surface to the counter surface, it is usually smaller than the wear debris but is significantly work hardened (and hence far less ductile), resulting in cracking from the high tensile stresses [66]. This can be seen by coarse grooves on the worn surface of the DED-processed sample. Furthermore, cracking is apparent within the wear scar for the tribolayer, cause by tensile stress generation associated with the edges of the contact point between the sphere and the direction of motion, which has been suggested to be propagated preferentially along the interface between the matrix and the carbides in prior work [184]. In addition, the tribolayer can be seen to include a high oxide content (observed as light contrast regions in SEM, due to lower average atomic mass), as confirmed by EDS mapping (Figure 7.5 (a) and (b)). These tribofilms readily form on ferrous materials, and can act as a solid lubricant (with a lower coefficient of friction), being reformed after occasional removal by spallation (due to their brittleness). When the oxide layer is damaged, a return to an adhesion wear mechanism is likely to occur [66].

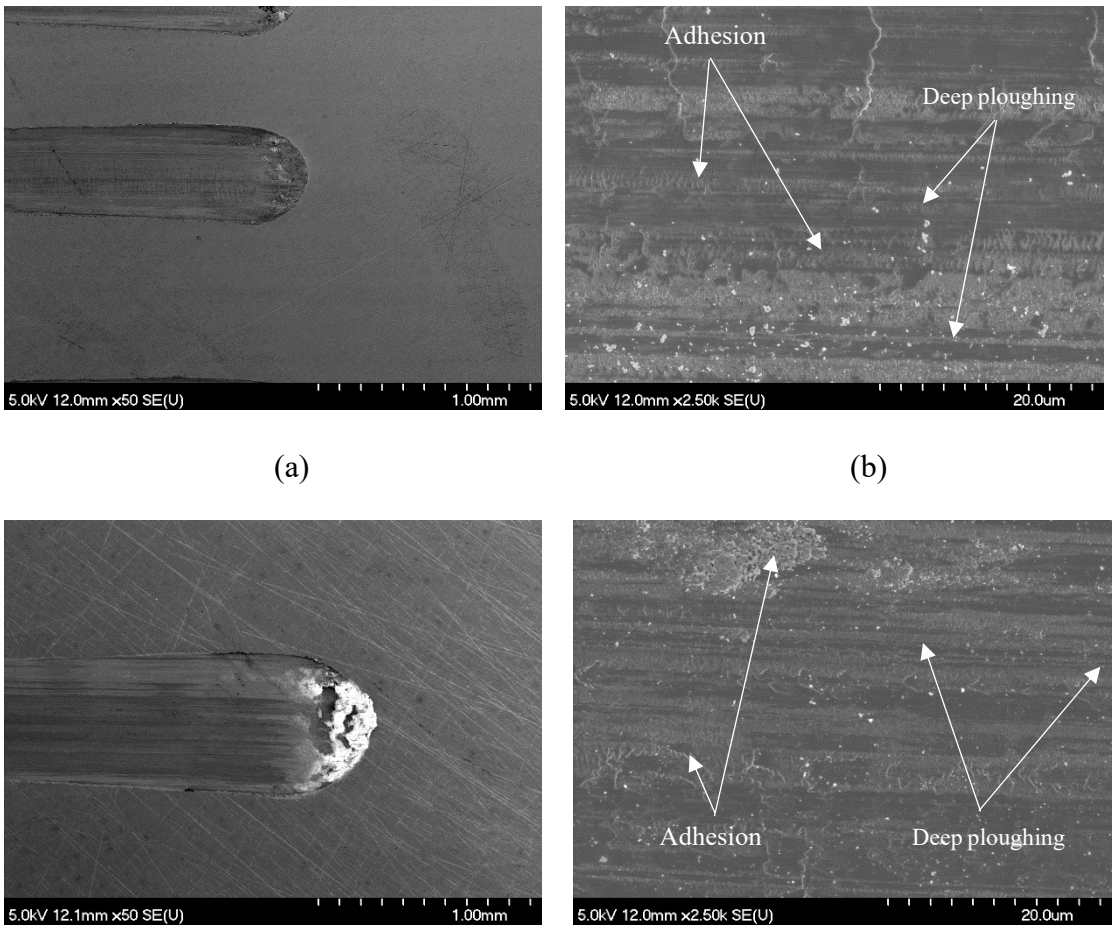

Figure 7.4. Representative SEM micrographs of the wear tracks formed on the DED samples for wear test times of: (a,b) 500 s, and (c,d) 2,000 s.

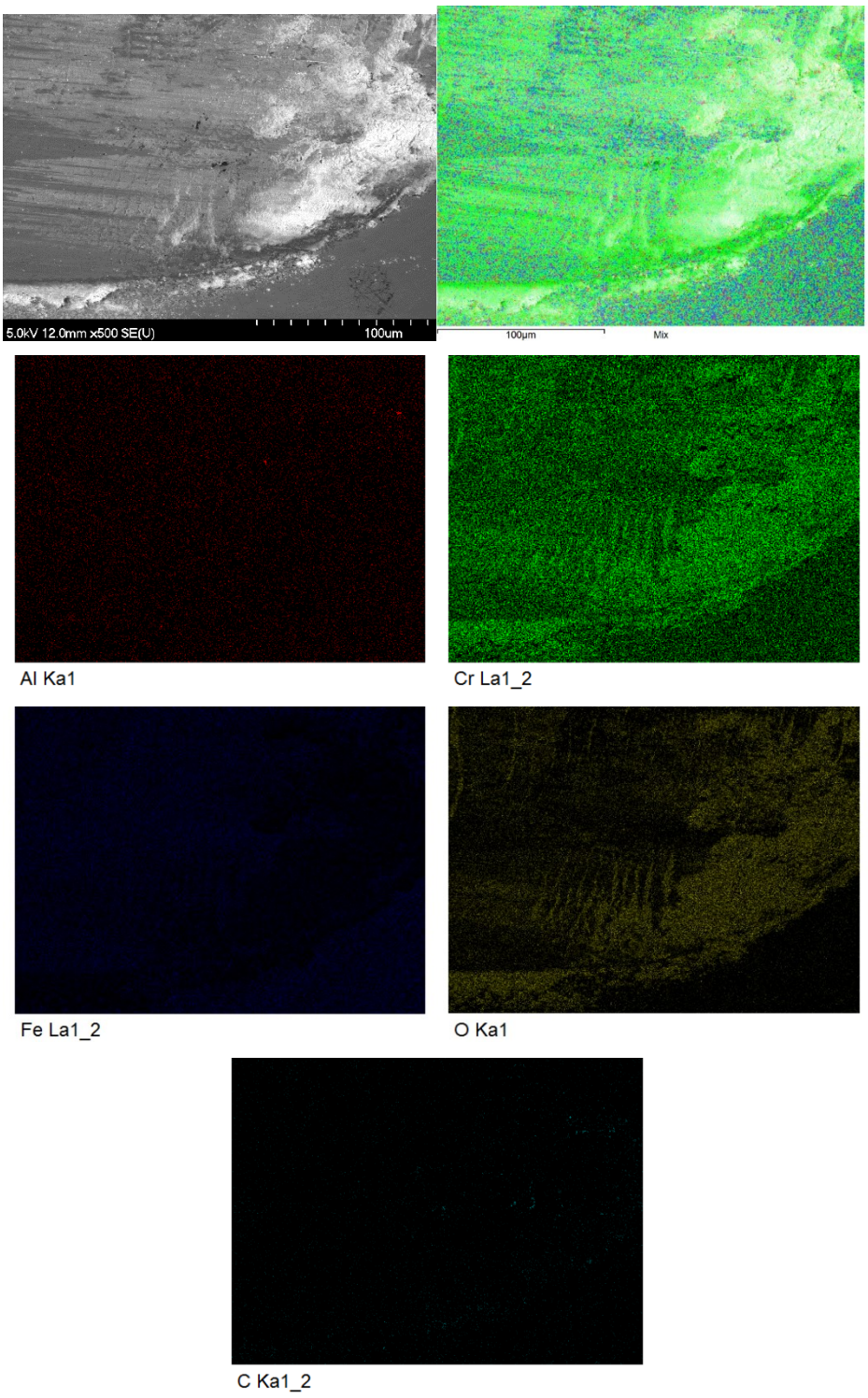
5.0kV 12.0mm x500 SE(U)
100um
100µm
Mix
Al Ka1
Cr La1_2
Fe La1_2
O Ka1
C Ka1_2

(a)

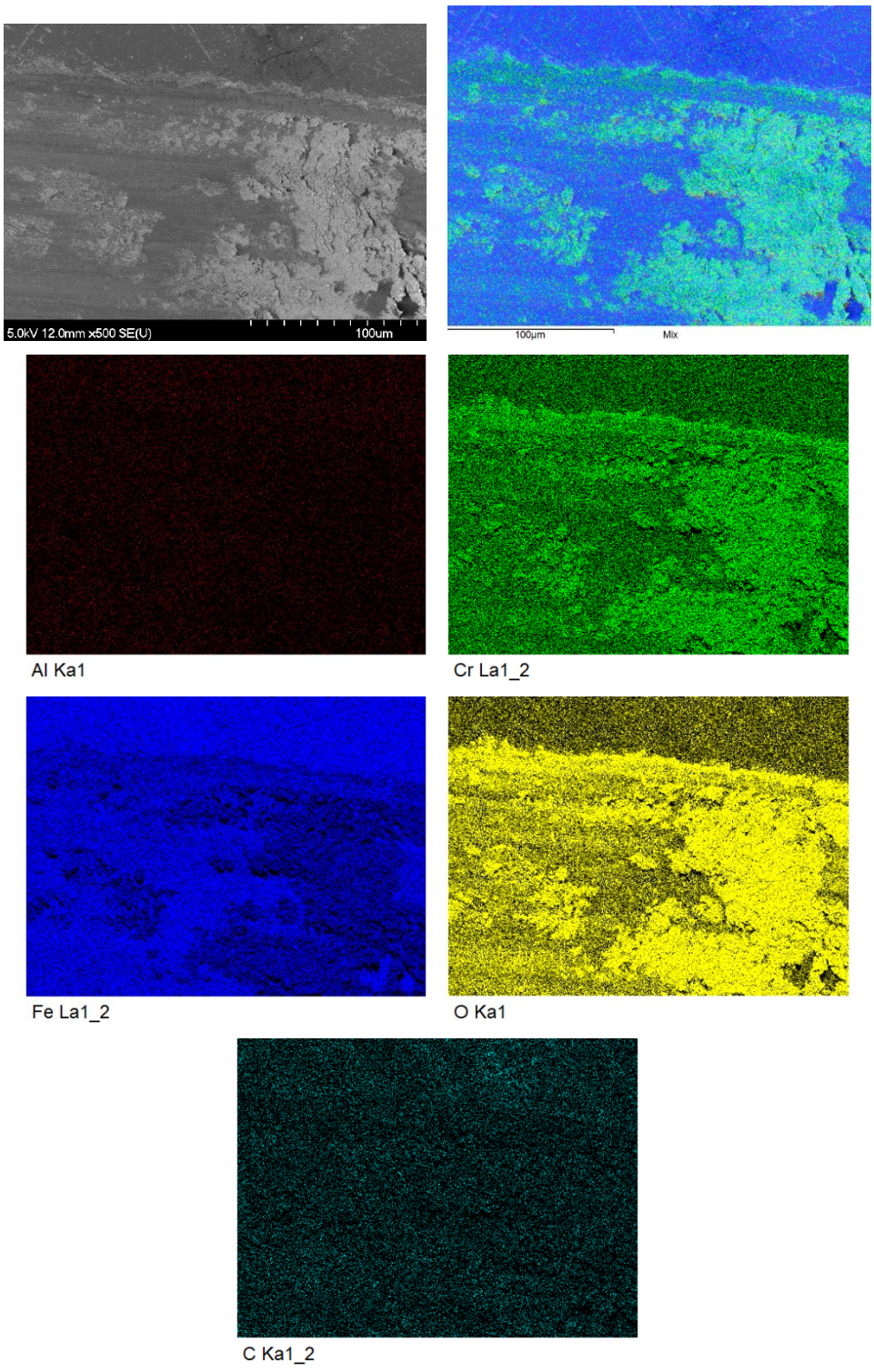

(b)

Figure 7.5. Representative SEM micrographs and associated EDS mapping of the ends of wear tracks generated on DED-processed samples for: (a) 500s, and (b) 2,000s test times.

7.3.2 Microstructure evaluation of Wrought heat treated D2 tool steel

Figures 7.6 and 7.7 show representative SEM micrographs, along with the associated EDS mapping analysis, for the wear tracks arising on a heat-treated wrought D2 tool steel sample. As reported in our previously published work [174], it was observed that the microstructure of the heat treated (i.e., tempered) D2 tool steel (sample NHT) involved coarse particles of M_7C_3 carbides, which were formed by precipitation during solidification [132]. In contrast, the microstructure of the air-cooled (after austenitising), wrought D2 tool includes primary and secondary carbides, in addition to retained austenite and martensitic laths in the matrix. The tempered samples showed variety in the size and quantity of primary and secondary carbides, depending on the tempering/re-tempering temperature applied [174].

In terms of analysis of the microstructure of the wear tracks for the as-received air-cooled, and double-tempered wrought D2 (in this instance sample DT5), evidence of an adhesive wear mechanism was observed for each sample. In addition, oxide tribofilms (again, the light contrast regions observed in the SEM) which form during the reciprocating wear tests through attrition of the wear debris, as a lubricant and reform after getting removed, as confirmed by EDS mapping (Figure 7.5 (a) and (b)). As noted earlier, if the the oxide layer is damaged, the potential for further adhesion wear occurs [66]. It is also worth noting that the extent of adhesive wear was more obvious in the as-received sample when compared to the double tempered sample, which in-turn exhibited greater wear than in the air-cooled sample. This can be attributed to the martensitic structure developed in the air-cooled, which is more brittle than the double tempered sample, and hence results in the production of fewer wear particle as a result of the clean break of the adhered material with less

deformation in the air-cooled sample than the doubled tempered one [66]. Furthermore, abrasive wear in the shape of deep ploughing grooves was presented in the wear tracks of both the air-cooled and double tempered (DT5) samples. As noted in the previous section, the deep ploughing grooves were most likely formed as a result of the fine carbide particles being torn from the surface and acting as fine abrasive particles between the two rubbing materials (i.e., the specimen and the counter face Al_2O_3 sphere). Therefore, the carbide particles are squeezed forwards in the sliding direction, forming a flow line within the wear scars [179]. As demonstrated in the EDS maps, the torn carbide particles are gradually displaced from the wear track and are then gathered around the edges of the tracks (Figure 7.7 (b) and (c)); this is evidenced by the increased high Cr concentration is significantly observed around the edges. Furthermore, islands of Cr-rich oxides were found to be attached to the wear track of the air-cooled and double tempered sample which demonstrates that a tribolayer was again formed as a result of the occurence of three-body abrasion [185].

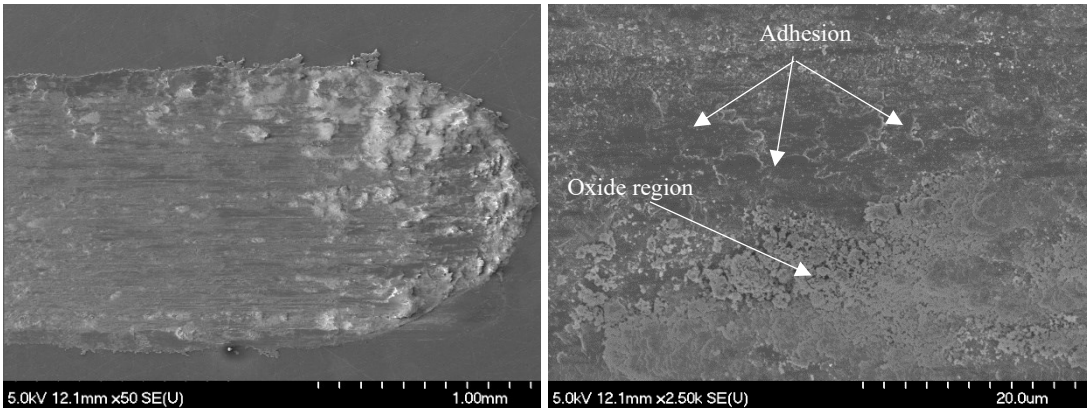

(a) (b)

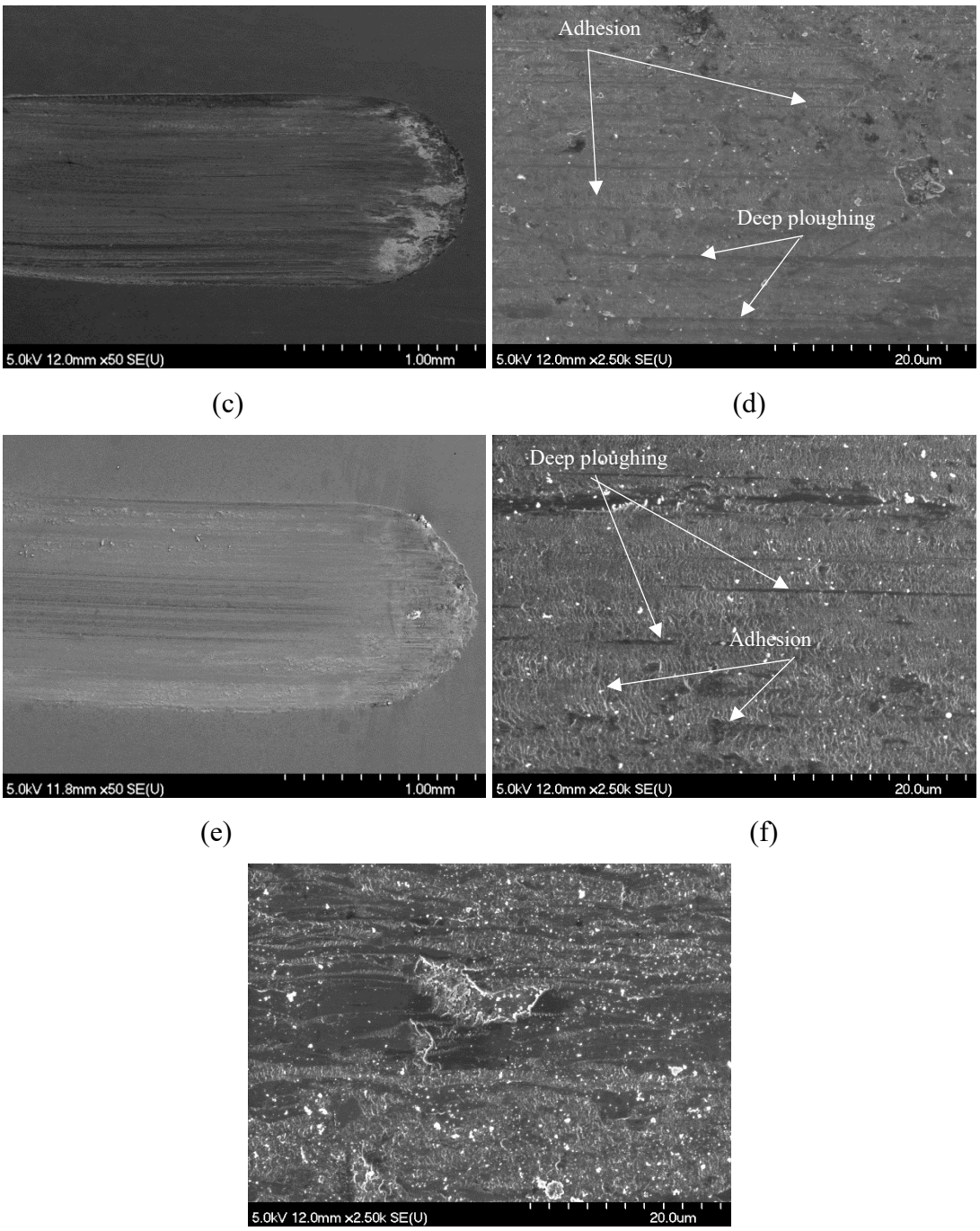

Figure 7.6. Typical SEM micrographs of the wear tracks for the wrought D2 samples after testing for 2,000 s: (a,b) as-received, (c,d) air-cooled, and (e-g) double tempered (sample DT5).

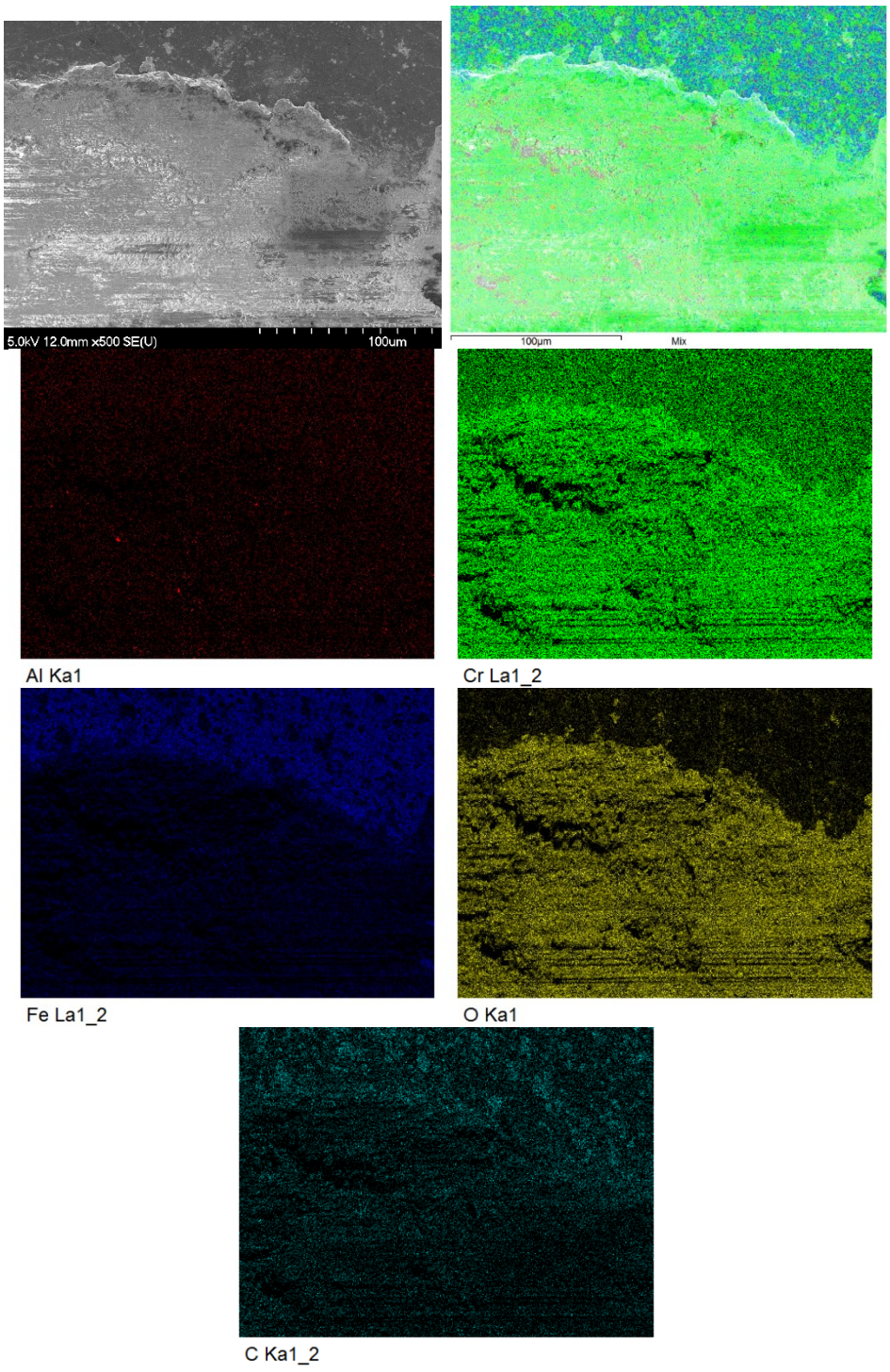
5.0kV 12.0mm x500 SE(U)
100um
100µm
Mix
Al Ka1
Cr La1_2
Fe La1_2
O Ka1
C Ka1_2

(a)

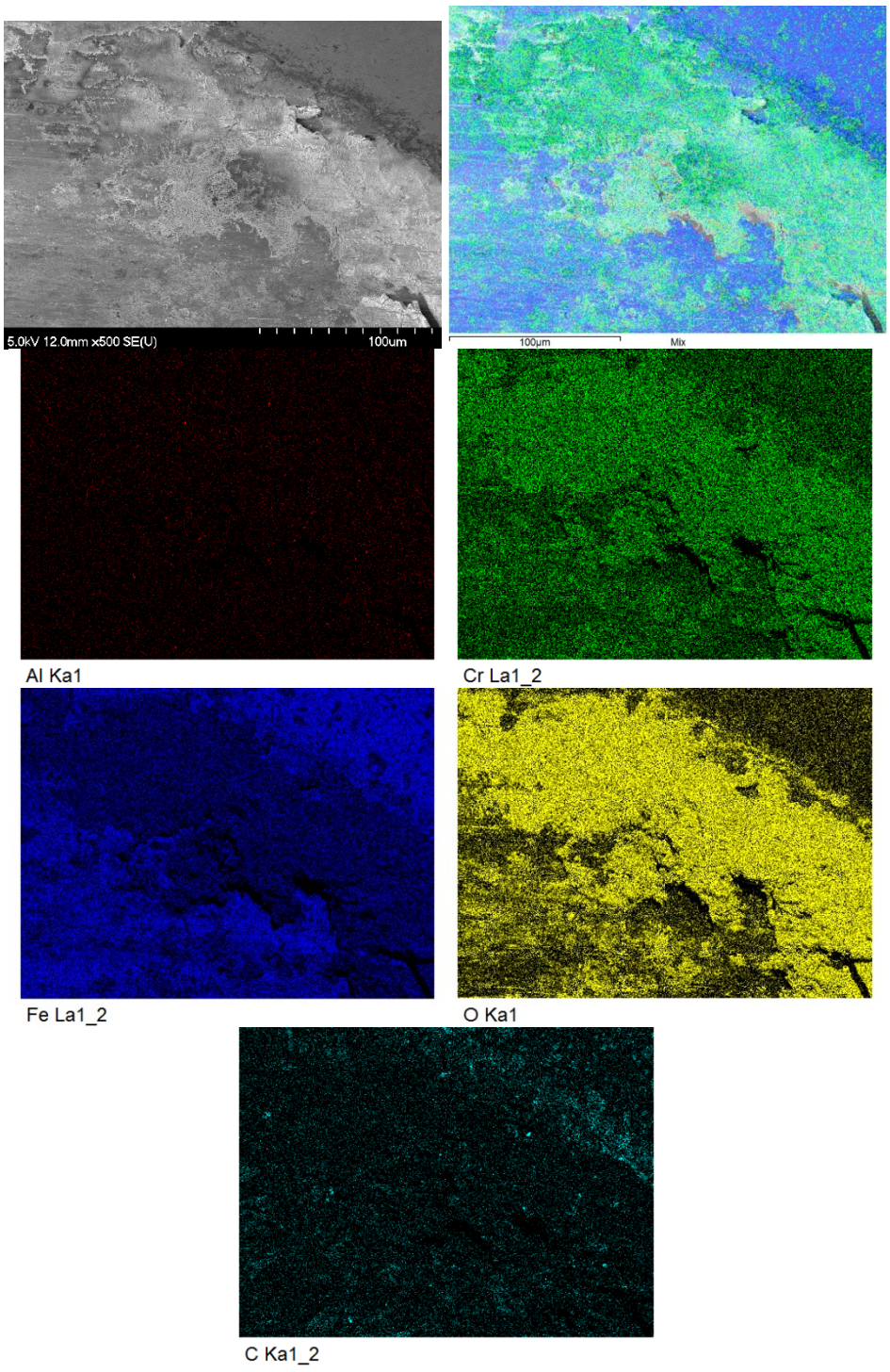
5.0kV 12.0mm x500 SE(U)
100um
100µm
Mix
Al Ka1
Cr La1_2
Fe La1_2
O Ka1
C Ka1_2

(b)

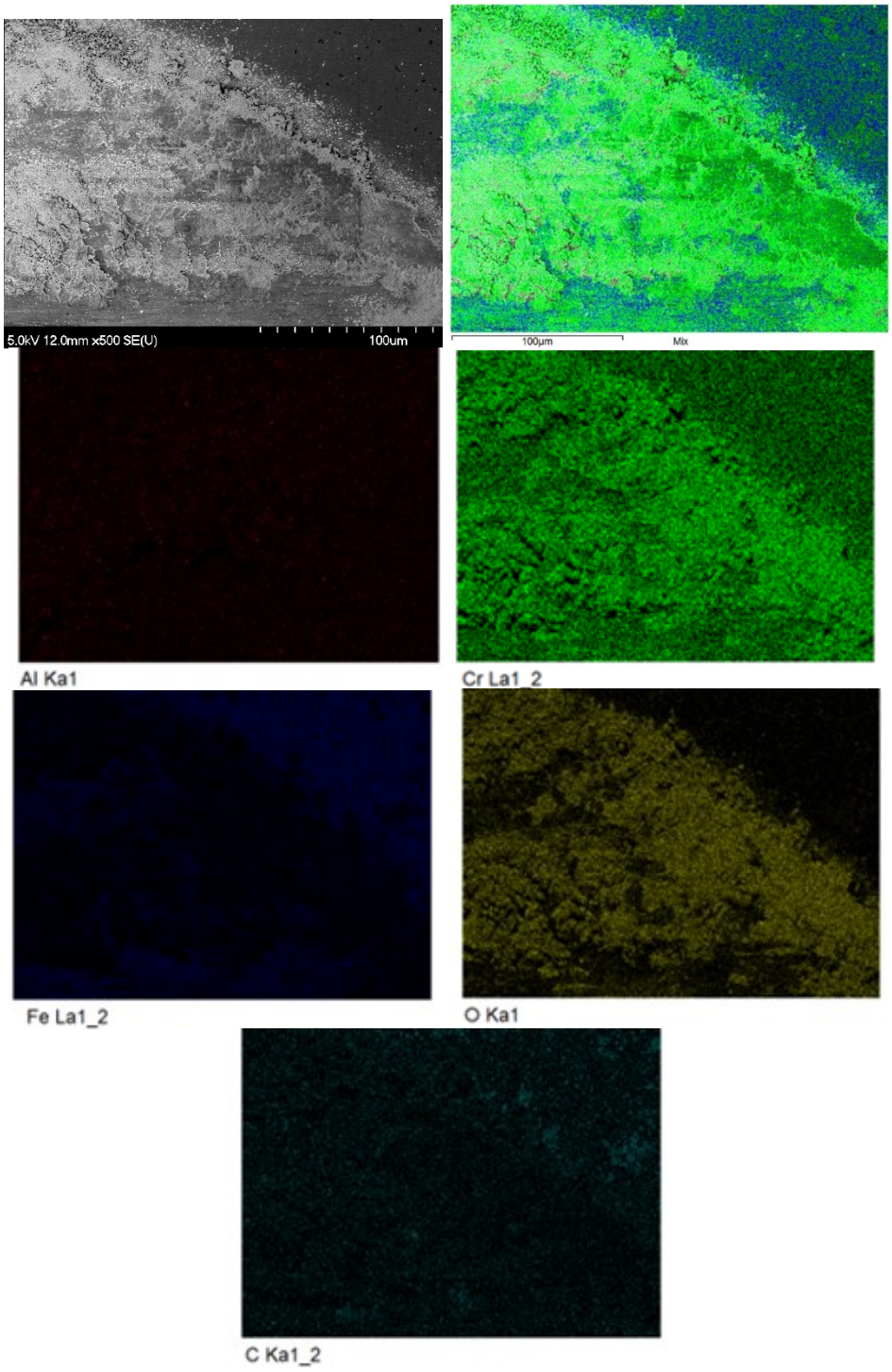

(c)

Figure 7.7. Representative SEM micrographs along with the associated EDS maps obtained at the ends of wear tracks for samples tested for 2,000 s: (a) as-received, (b) air-cooled , and (c) double tempered (sample DT5).

7.3.3 Wear Rate Assessment

Figure 7.8(a) demonstrates a comparison of the mean specific wear rates of the as-printed DED samples to both the as-received and heat-treated D2 tool steel samples, for the three examined wear test durations (i.e., 500, 1,000, 2,000 seconds). In general, it was observed for all samples that the specific wear rate decreases with increasing test duration. This can be attributed to the transition from the initial two-body abrasive wear through to the formation of a three-body wear mechanism, at longer durations, with the concurrent formation of an oxide tribolayers which lowers friction and thus acts in a semi-protective manner.

In terms of a comparison of mean specific wear rates recorded for the various samples, it was reported in literature that the wear rate is profoundly affected by the microstructure, hardness, chemical composition, and potential phase transformations [69,186,187]. Additionally, and especially in tool steels, the primary and secondary carbides play a vital role in controlling tribological characteristics [188]. Furthermore, in steels wear, more generally, hardness has been stated to have the most important influence on wear resistance, since the higher the hardness, the better the wear resistance characteristics [119]. As a consequence, a comparison between Figure 7.8 (a) and (b) demonstrates an obvious consistency between the results of hardness discussed in our prior work [174] and the present measured specific wear rates.

In terms of the wrought D2 tool steel, it was observed that the air-cooled sample has the lowest wear rate, while the highest wear rate was determined for the as-received samples. This significant improvement in wear resistance can be expected to result from the formation of high hardness (and wear resistant) martensite in the air-cooled D2 tool steel

[132,187]. Regarding the heat-treated samples, it was apparent that the specific wear rates were higher than those for the air-cooled condition, due to the decomposition of martensite (previously developed in the air-cooling step) into carbide and ferrite phases [146]. Furthermore, it was found that the single or double tempering temperature influences the measured wear rate. That could be attributed to the formation of finer alloy carbides in preference to coarse cementite, which is described as the 'secondary hardening phenomenon' [147]. Due to the high content of chromium in the D2 tool steel composition, chromium carbides preferentially are formed at the expense of cementite (formed during tempering in preference to retained austenite). However, the formation of chromium carbides requires high temperatures for initiating the substitutional diffusion of chromium into the cementite matrix [141]. The critical temperature for carbide formation was previously determined to be around 500 °C [141], which matches well with present findings in terms of the wear response. Above this temperature, coarsening of the carbides can eventually be expected, which will likely increase the wear damage arising from carbide particle gouging. At single or double tempering temperatures higher than 500 °C, a noticable increase in wear rate was apparent. That arose because of coarsening of carbides, which results in lower hardness and higher wear rates [141]. Consequently, there is a plateau in the wear rate values around this critical 500 °C point.

In terms of the wear resistance of the DED processed samples, it was observed that they showed higher wear rates in comparison to air-cooled or tempered wrought D2 samples (except for the wrought material single/double tempered at 600°C). These results could be attributed to crystalline phases which formed in the as-DED processed samples. As demonstrated in [174], the primary structure of the as-printed samples was found to be

austenite. This can be attributed to the fact that there is a high Cr and C content in D2 tool steel which, despite a rapid cooling rate during the DED build process, supresses the martensitic start temperature. This subsequently results in the formation of a metallic matrix with a primary austenitic structure, comprising of an excess of dissolved carbon [140]. As a result of the presence of retained austenite in the matrix of the DED processed samples, lower hardness and wear resistance arise, in comparison to the case with martensite in the air-cooled samples [189–192].

Finally, it was found that the volume removed from the alumina sphere surface (counter surface) is inversely related to the wear rate, since the largest amount of removed material was found for Al_2O_3 spheres sliding against the air-cooled samples, which has the lowest wear rate.

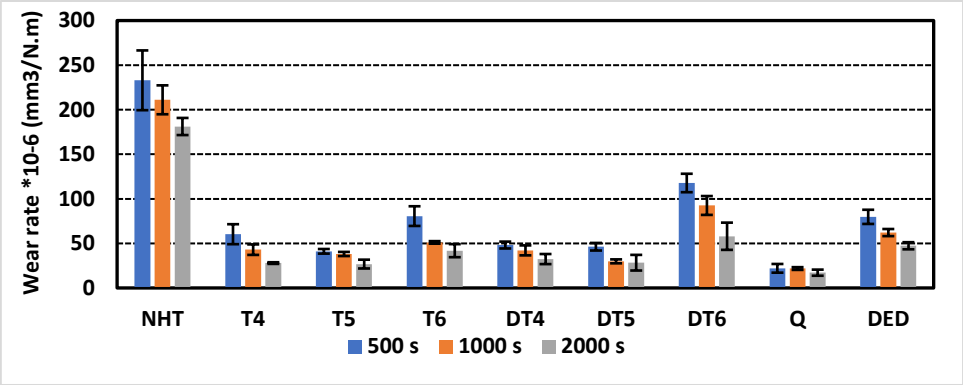

(a)

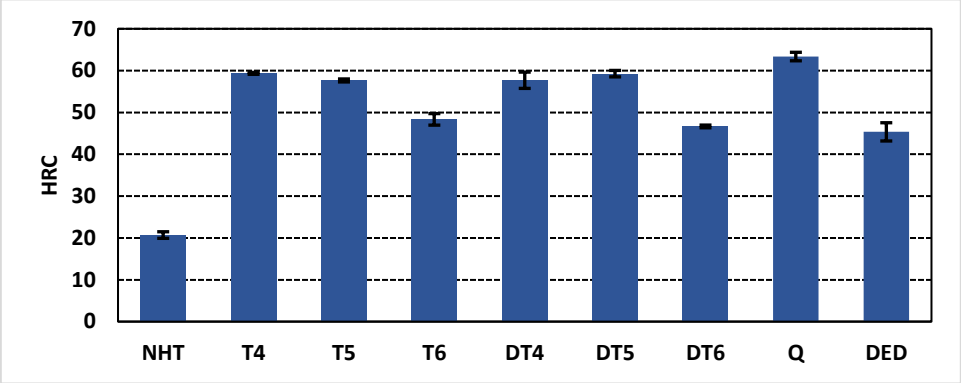

(b)

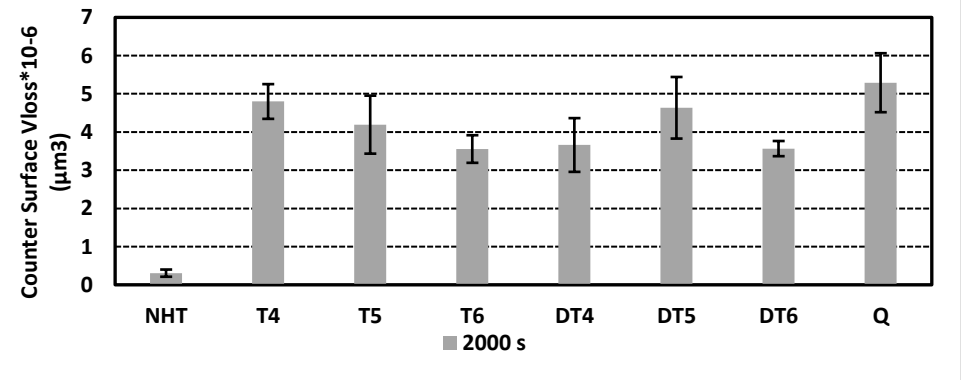

(c)

Figure 7.8. The effects of different tempering heat treatment schedules upon the wear response of the wrought D2 tool steel substrates and Al_2O_3 counter face spheres for: (a) the specific wear rate, (b) the Rockwell C hardness, and (c) volume removed from the sphere counter surface**.**

7.4 Conclusions

The present work examined the influences of different heat-treatment schedules for wrought D2 tool stool on wear characteristics, in comparison to DED processed D2 tool steel.

The following conclusions were obtained from the present study:

- In terms of the microstructures of the wear tracks for the DED processed specimens, it was apparent that the wear mechanism shows a transition from, initially, two-body abrasive wear, through to a combination of three-body abrasive wear and adhesive wear (with generation of an associated tribofilm). The abrasive wear was present in the form of ploughing grooves, which are believed to be formed due to the abrasion effect of fine carbide particles pulled out or fractured from the ferrous matrix. The fine carbides are then pushed along between the test specimen and the counter face sphere. In addition, carbide particles and their fragments (especially chromium carbides) were preferentially found at the wear track edges, having been displaced there by the back-and-forth counter face movement. Unsurprisingly, the amount of carbides deposited at the edges of the wear tracks increased with increasing time.
- In terms of the adhesive wear mechanism, it was apparent that fracture of the adhered material was clean with little deformation, and produced fewer wear particles when compared to the brittleness of the DED processed sample. In addition, the oxide tribofilm act as a lubricant and continually reform after occasional partial failure through spallation. When the oxide layer is damaged, adhesion can occur.
- In terms of the microstructure of the wear tracks for the wrought D2 tool steel, adhesive wear was observed on the air-cooled and double-tempered samples. Adhesive wear was more obvious in the double tempered samples than in the air-cooled condition. This could be attributed to the air-cooled sample being more brittle, which results in the production of fewer wear particles as a result of the clean fracture of the adhered material with less deformation in air-cooled sample than the doubled tempered one. Furthermore, islands of Cr-rich oxides were found to be attached to the wear track of

the air-cooled and double tempered sample which demonstrates that tribolayer was formed as a result of presence of three-body abrasion and adhesive wear.

- Evidence of abrasive wear, in the shape of deep ploughing grooves, was also present in the wear tracks of the air-cooled and double tempered samples. The deep ploughing grooves were believed to form as a result of the fine carbides, which are torn from the surface and act as third-body abrasive particles between the specimens and the testing spheres. The freed carbide particles are squeezed in the sliding direction, forming a flow line within the wear tracks. In addition, the EDS mapping demonstrated that fractured carbide particles accumulated around the edges of the wear tracks.

- For the wrought D2 tool steel, it was observed that the air-cooled sample has the lowest wear rate, while the highest wear rate occurred in the as-received (annealed) specimen. This significant improvement in wear resistance results from the formation of high hardness and wear resistance martensite in the air-cooled D2 tool steel. The wear rates for the heat-treated specimens were higher than those for air-cooled , due to the decomposition of martensite (developed in the air-cooling step) into carbide and ferrite phases during tempering.

- The single or double tempering temperature also influences the wear rate. That could be attributed to the formation of finer alloy carbides, in preference to coarse cementite. Due to the high content of chromium in the D2 tool steel composition, chromium carbides are formed at the expense of cementite (formed during tempering in preference to retained austenite). However, the formation of chromium carbides requires high temperatures for initiating the substitutional diffusion of chromium into the cementite

matrix; a critical temperature for forming carbides was determined to be ~500 °C. Consequently, there is a plateau in the wear rate values.

- The wear rates of as-printed DED samples were found to be higher in comparison to either the air-cooled or single/double tempered wrought D2 samples. This was attributed to the primary structure of the as-printed samples being austenite. This arises because of the high Cr and C content in D2 tool steel which, in spite of the extremely rapid cooling rate during DED processing, supresses the martensitic start temperature, resulting in the formation of a metallic matrix with a primary austenitic structure with an excess of dissolved carbon. As a result of the presence of retained austenite in the matrix of the as-deposited laser DED samples, this leads to lower hardness and wear resistance, in comparison to the highly martensitic structure in air-cooled samples.
- In terms of the effects of test duration on the specific wear rate, it was observed that the wear rate decreases with increasing test duration. This can be attributed to the transition to three-body/adhesive wear at longer durations, with the formation of oxide tribolayer lowering friction and resulting in a more protective surface structure.

Acknowledgments

The authors would also like to thank the technical assistance of Dr. Addison Rayner (Dalhousie University) with DED printing of the samples. Ms. Patricia Scallion is also gratefully acknowledged for support with SEM analyses. This work was financially supported through the NSERC Strategic Project Network Grant *Holistic Innovation in Additive Manufacturing* (HI-AM), through Grant No. NETGP 494158-16.

CHAPTER 8 Conclusions and Suggestions for Future Work

8.1 Research Significance

The main objectives of the current thesis were to identify the best DED process parameters to produce D2 tool steel parts with good mechanical and geometrical properties, and to determine the optimum post-heat treatment schedule to improve the mechanical properties of the as-printed DED parts.. This overall evaluation included, firstly, generating and characterising additively manufactured structures of D2 tool steel on 'like' substrates (i.e., wrought D2) using DED. To determine starting printing parameters, characterization of pure DED D2 was evaluated, beginning with:

- Microstructural characterization of DED D2 in the as-printed and heat-treated condition when the scanning speed and powder feed rates are varied (Section 4.3.2), as well as varying layer thickness (Section 6.3.2), to obtain AM parts with desirable mechanical properties and surface integrity.
- Measurement of the hardness characteristics of DED D2 in the as-printed and heat-treated conditions, when altering the scanning speed and powder feed rate (Section 4.3.3 and 4.3.4), and also when changing the deposited layer thickness (Section 6.3.3). Furthermore, the wear resistance was also investigated for as-printed and heat-treated conditions (Section 7.3.3).
- The geometrical and surface characterization of as-printed D2, when the scanning speed and powder feed rates were varied (sections 5.3.2 and 5.3.3), in addition to investigating the effect of layer thickness (sections 6.3.4 and 6.3.5). The purpose for this is exploring the feasibility of reducing the number of post-deposition processes

needed to obtain AM parts with desirable surface finish and dimensional accuracy, through optimization of the process parameters.

- Assessment of design strategies and simple test components with overhung structures, which were produced by minimizing the discrepancy between designed and actual deposited components (Section 5.4.3). This study again leads to a decrease in the post-processes needed to produce structures with inner holes or fill inner cracks.

The findings from these studies contributed to the scientific knowledge of DED of AISI D2 tool steel by determining the optimum window for the process parameters, and simultaneously reducing the post-processes to obtain a high wear resistance, better component dimensional accuracy, and improved surface roughness.

8.2 Conclusions

8.2.1 Microstructural Analysis of As-Printed and Heat-Treated DED Samples

A range of scanning speeds, powder feed rates and layer heights were examined to determine the microstructure of DED processed samples. Such evaluation was followed by heat-treatment of selected samples, in which the microstructures of the post heat-treated samples were compared to the microstructure of the as DED-processed and, furthermore, wrought heat-treated D2 tool steel.

The following conclusions were obtained from these microstructural studies:

- In terms of the sample microstructures after DED processing, the middle zone of the DED processed samples showed a dendritic morphology, with the presence of columnar grains, which was attributed to the constitutional cooling as a result of rapid

cooling of the DED processed samples. A more equiaxed morphology was observed at the lower half of the DED processed samples.

- After tempering heat-treatments, the dendritic morphology transforms into a significantly more equiaxed microstructure through homogenisation. Additionally, fine secondary carbides were precipitated in the matrix due to substitutional diffusion of chromium into the matrix to form chromium carbides at the expense of cementite. In contrast, chromium carbides were only formed at the grain boundaries for the as-processed DED samples.
- Austenite was the primary (dendritic) structure for the DED processed sample, despite the rapid cooling rate during the DED process; the high chromium and carbon content in D2 steel leads to the formation of a metallic matrix which is primarily austenite and includes excess dissolved carbon. In turn, this suppresses the martensitic formation temperature.
- After heat-treatment, the austenite in the dendritic structure was transformed into tempered martensite. At the austenitizing temperature, diffusion of excess carbon in the austenite occurs into the eutectoid structure, forming chromium carbides. Consequently, the carbon content in the austenite decreases, increasing the martensitic transformation temperature.

8.2.2 Hardness Evaluation of As-Printed and Heat-Treated DED Samples

As with the approach taken for microstructural analysis, various scanning speeds, powder feed rates, and layer heights were investigated to determine the hardness response of the DED processed samples. In addition, the effect of using various tempering scenarios on

the Rockwell indentation and scratch hardness of the DED-processed and wrought D2 tool steel were examined. The following conclusions were obtained from the hardness studies:

- In terms of the indentation and scratch hardness of the 'as-deposited' DED-processed parts, the hardness of the initially deposited layers (i.e., adjacent to the substrate) were much lower than the vlaues measured in either the middle or upper regions after laser deposition. This is observation was attributed to the reheating effects that occur for the initially deposited layers, which in turn leads to grain growth and consequently a reduced hardness of the deposited material through the Hall-Petch effect.
- Applying tempering heat-treatments to the DED processed samples, it was observed that the heat-treatments significantly improve the hardness, to essentially the level of the air-cooled D2 tool steel. This can be explained in terms of the transition from austenite in the dendritic regions of the DED clads, to a tempered martensite during the heat treatment in combination with the formation fine secondary carbides.
- Regarding the effects of the deposited layer thickness upon the hardness, it was observed that the use of a larger layer height leads to a reduction in the mean hardness. This was found to be consistent with the cooling rate trends. In other words, the highest measured mean Rockwell hardness was observed for the lowest deposited thickness, which is associated with the highest cooling rates.

8.2.3 Wear Resistance of As Printed and Heat-Treated DED Samples

The influences of different heat-treatment schedules applied to wrought D2 tool stool on the material's wear characteristics, in comparison to as-DED processed D2 tool steel, were investigated in this portion of the research.

The following conclusions were obtained from these heat-treatment studies:

- In terms of the wear track microstructures for the as-DED processed specimens under different wear test durations, it was observed that the wear mechanism is a combination of adhesive and abrasive wear, with the width of the wears track increases by increasing test duration. The observations for abrasive wear were shown in terms of the shape of deep ploughing grooves. These grooves are believed to be formed due to the abrasion effects of fine carbides, since these carbides are effectively squeezed between the specimens and counter surface. This helps to explain the formation of the ploughing grooves in the wear track. In particular, evidence of fragmented carbide particles (especially chromium carbides) was found to be noticeably greater for 2000 s tests than for 500 s. Furthermore, in terms of the adhesive wear mechanism, it was noticed that failure of the adhered material arises, which was clean with little deformation, and produced fewer wear particles for the heat-treated D2 compared due to the brittleness of the as-DED processed sample. In addition, it was apparent that oxide films act as a lubricant and can then reform after getting removed through a passivation-based mechanism. When the oxide layer is damaged, adhesion occurs.
- Regarding the microstructure of the wear tracks of the wrought D2 tool steel, an adhesive wear mechanism was observed on both the air-cooled and double-tempered samples. Adhesive wear was more obvious in the as-received (annealed) versus the double tempered sample, which in turn was more obvious than the air-cooled samples. This observation could be attributed to the fact that the air-cooled samples are more brittle than the double tempered ones, which results in the production of fewer wear particles as a result of the clean fracture of the adhered material with less deformation

in the air-cooled sample than the doubled tempered one. Furthermore, abrasive wear in the shape of deep ploughing grooves was presented in the wear tracks of the air-cooled and double tempered (DT5) samples. It is believed that the deep ploughing grooves were formed as a result of the fine carbides, which are torn from the surface, and act as abrasive particles between the two rubbing materials (the specimens and the testing spheres); this results in a transition from two-body to three-body wear. Therefore, the carbides are squeezed in the sliding direction, forming a flow line in the wear scars. In addition, the EDS mapping demonstrated fragmented carbide particles, preferentially located around the edges of the wear tracks. Islands of Cr-rich oxides were found to be formed within the wear track of the air-cooled and double tempered sample, which demonstrates that a chemical tribolayer was formed as a result of presence of two-body/three-body abrasion.

- For comparative purposes, in terms of wear rate of the wrought D2 tool steel, it was observed that the air-cooled sample has the lowest wear rate, while the highest wear rate was observed for the as-received (annealed) specimens. This significant improvement in wear resistance could result from the formation of high hardness and wear resistance martensite in the air-cooled D2 tool steel. Regarding the heat-treated samples, it was noticed that the wear rate values for the heat-treated specimens were higher than those for the air-cooled samples, due to the decomposition of martensite (developed in the air-cooled step) into carbide and ferrite phases. Furthermore, it was found that the single or double tempering temperature influences the wear rate. This can be attributed to the formation of finer alloy carbides in preference to coarse cementite, which is described as the secondary hardening phenomenon. Due to the high

content of chromium in D2 tool steel composition, chromium carbides are formed at the expense of cementite (formed during tempering in preference to retained austenite). However, the formation of chromium carbides requires high temperatures for initiating the substitutional diffusion of chromium into the cementite matrix. A critical temperature for forming carbides was previously determined to be approximately 500 °C, which matches well with the present findings. Consequently, there is a plateau in the wear rate values at Double tempering at 500 °C.

- The wear rate of as-printed DED samples was found to be higher in comparison to air-cooled or single/double tempered wrought D2 samples, which could be attributed to the observation that the primary structure of the as-printed samples was found to be austenite. This arose because of the high Cr and C content in D2 tool steel which, in spite of the rapid cooling rate during the DED process, depresses the martensitic formation temperature. This results in the formation of a metallic matrix with a primary austenitic structure and comprises an excess of dissolved carbon. As a result of the presence of retained austenite in the matrix of the as-DED processed samples, this leads to lower hardness and wear resistance, in comparison to martensite in the air-cooled sample.
- In terms of the effects of wear test duration on the wear rate, it was observed that the wear rate decreases by increasing the test duration. This could be attributed to the formation of three body wear mechanism at longer duration time and, because of this, the formation of semi-protective oxide layers in the form of a tribolayer.

8.2.4 Geometrical Characteristics and Surface Roughness

The effects of laser scanning speed and powder feed rate were assessed in terms of the geometrical characteristics and surface roughness of DED processed D2 tool steel samples. This portion of the study has included assessing the single-track clads bead sizes and dimensional errors for multi-layer samples.

It was concluded that:

- In terms of the effects of scanning speed upon the geometrical characteristics, it was observed that the size of single clads, (i.e., clad height and width) has an inverse relationship to the scan speed. The same trend was also observed for the effects of scanning speed upon the degree of overbuilding, since an increase in laser scanning speed results in less available time for heat transfer from the laser beam to the substrate/deposited powder layer, while at the same time a lower amount of powder is delivered to the melt pool. As a consequence, an increase of the laser scanning speed decreases the single-track clad size and the degree of positive error in height (i.e., the extent of over building).
- For the effects of powder feed rate on the geometrical characteristics, it was observed that the variation in laser scanning speed dramatically impacts the relationship between powder feed rate and the geometrical characteristics. This could be attributed to the fact that both the quantity of powder deposited per unit length and laser-powder interaction time are dominated by the laser scanning speed. As a consequence, in the present study, there was no obvious trend in terms of the powder feed rate upon single-track bead size and the level of over/under building of the rectangular DED processed

samples. In terms of the influence of layer thickness upon the geometrical characteristics, it was observed that the use of lower layer thickness leads to a higher extent of overbuilding of the DED processed parts (i.e., a higher height discrepancy). This arose because, at lower layer heights, more layers are deposited to build the DED part, resulting in higher height error.

- With respect to surface roughness characteristics, the top surface roughness (i.e., the face perpendicular to the laser axis) was found to be lower than that measured for the sides. This could be attributed to adhesion of isolated powder particles to the side surfaces, which does not appear to arise significantly for the top surface.
- Furthermore, the top surface roughness was found to be improved by decreasing the laser scan speed and powder feed rate. This observation arose because, at lower scanning speeds, a higher energy density results, which leads to more complete melting of the particles and therefore a reduction in isolated, un-melted particles adhering to surfaces. A similar explanation can be concluded for the trend relating to the powder feed rate, as less powder is conveyed to the melt pool, resulting in more suitable melting conditions. As a consequence, the minimum top surface roughness was recorded at a scan speed and powder feed rate of 400 mm/min and 5.5 g/min, respectively. In addition, the top surface roughness was found to be enhanced by decreasing the layer thickness. This can be attributed to the fact that, at lower layer thickness, a lesser amount of powder is deposited into the melt pool, which leads to more suitable melting conditions. Therefore, less partially melted powder is adhered to the top surface of the DED fabricated sample

- For the side surface roughness, the effects of laser scanning speed and powder feed rate were found to be dependent upon the heating-cooling cycles (i.e., temperature gradients and cooling rates) that occur during the DED process. A broad consistency was observed between the side surface roughness and the calculated cooling rates (from SDAS analysis). This resulted from slower solidification taking place at the lower cooling rates, which, in turn, leads to more complete melting of any partially melted particles adhered to the surface. The lowest side surface roughness arose at a scan speed of 400 mm/min and powder feed rate of 6.5g/min; this corresponded to the minimum calculated cooling rate at same process conditions. Furthermore, for the side surface roughness, the influence of layer thickness was found to be profoundly impacted by the heating-cooling cycles (i.e., cooling rates and temperature gradients) that occur during the DED process. A distinct consistency was noticed between the side surface roughness and the estimated cooling rates (from SDAS analysis), which could be attributed to the slower solidification that occurs at lower cooling rates. Consequently, this leads to fewer partially melted powder particles adhering to the surface. The lowest side surface roughness was observed at a layer thickness of 0.5 mm; this agreed with the minimum estimated cooling rates.

8.2.5 Overhanging Structures

The capability for printing overhanging, thin wall structures using DED was also examined, where various process parameters were again used to assess their influence on the angle accuracy and surface roughness. A simple model was developed to allow the prediction and correction of build errors that might arise for DED printing of inclined walls.

It was observed that the overhang structures can be successfully deposited using DED, up to a maximum overhang angle. Above this, the surface tension force is lower than the combined components of the gravity force of the deposited powder and the impulsion force of gas and powder stream, and the build cannot be sustained. In this study, this angle was found to be a design angle of 60° to the substrate.

In addition, significant discrepancy was demonstrated between the actual measured angles after DED and the initial design angle. This error was found to be reduced at lower laser power, lower powder feed rate, and/or higher scanning speed. This can be attributed to the reduced height error under these DED conditions, as a result of a lower degree of over-building; at lower laser power and higher scanning speed, a lower energy density resulted, so a smaller melt pool is developed. Similarly, at lower powder feed rates, a reduced amount of powder is delivered into the melt pool. As a consequence of this, an empirical model was developed in order to minimise the angle discrepancy, by predicting a modified design angle with respect to the process parameters of the DED processed sample.

In terms of the side surface of roughness for the DED printed inclined thin walls, there was no obvious trend for the impact of either laser power, laser scanning speed, powder feed rate, or the inclination angle. This arises because the side surface roughness is highly dependent upon the heating and cooling cycles.

8.3 Suggestions for Future Work

The current study included optimisation of the DED process parameters to manufacture parts of D2 tool steel with good mechanical and geometrical properties. The effects of post-DED heat treatments on the possible enhancement of the mechanical properties was also investigated. However, additional future steps are suggested to increase the manufacturing capabilities and quality of D2 tool steel DED parts as follows:

- Investigating the effects of varying the DED process parameters and post-heat treatment schedules on the wear resistance of the DED processed samples. In order to continue the work which was stopped due to the wear tester breaking down. It is expected that varying process parameters will affect the wear resistance of the as-printed samples. Furthermore, it is predicted that the wear resistance could be enhanced by applying post-DED heat treatments.

- Exploring the response from preheating the feedstock powder and/or substrate should be investigated. That could involve preheating to a constant temperature for a specific time or applying a number of laser scans on the substrate prior to depositing the powder. This would be combined with mechanical testing and microstructural analysis of the DED printed samples. It is expected that the preheating of the substrate will result in less steep temperature gradients which leads to decrease in residual stress and distortion.

- Examining the effects of varying process parameters during DED process on the quality and integrity of the deposited part. For example, one of the findings of this research is that there is a significant difference between the properties at the lower half and upper

half of DED processed parts. Therefore, functionally varying the process parameters could result in more homogeneous properties of the DED deposited part. This would be combined with mechanical testing (i.e., wear testing, indentation hardness, scratch hardness, etc.) and microstructural analysis of the DED printed samples.

- Investigating the possibility of functionally graded printing of D2-Cu parts. The key challenge will be to control the interface development due to the miscibility gap of tool steel and Cu. Therefore, that research topic could include optimising the system printing parameters. Furthermore, it could involve depositing D2-Cu parts onto D2 tool steel or Cu substrates. In addition, as a solution for the miscibility gap of tool steel and Cu compounded, a buffer layer of soluble material in D2 and Cu (e.g., Ni-based alloys) could be added. Initial residual stresses should be examined due to the significant difference in thermal conductivity and expansion coefficient of D2 and Cu, which is expected to be less severe by adding a buffer layer. Furthermore, thermal conductivity testing at varying elevated temperatures should be conducted due to the difference in heat dissipation rate between D2-Cu, D2-Ni-Cu and pure-D2 DED processed components. This would be combined with mechanical testing (i.e., wear testing, indentation hardness, scratch hardness, etc.) and microstructural analysis of the DED printed samples. In addition, developing a finite element model for predicting residual stresses and distortion under various process parameters, would be extremely useful for pure D2, D2-Cu, and D2-Ni-Cu.

BIBLIOGRAPHY

[1] Wohlers T. Wohlers report 2021. 2021.

[2] Cherdo L. The Best Metal 3D Printers in 2020 [Internet]. 2021. Available from: https://www.aniwaa.com/best-of/3d-printers/best-metal-3dprinter/

[3] Vafadar A, Guzzomi F, Rassau A, Hayward K. Advances in metal additive manufacturing: A review of common processes, industrial applications, and current challenges. Appl Sci. 2021;11(3):1–33.

[4] Kok Y, Tan XP, Wang P, Nai MLS, Loh NH, Liu E, et al. Anisotropy and heterogeneity of microstructure and mechanical properties in metal additive manufacturing: A critical review. Mater Des. 2018;139:565–86.

[5] Ding D, Pan Z, Cuiuri D, Li H. Wire-feed additive manufacturing of metal components: technologies, developments and future interests. Int J Adv Manuf Technol. 2015;81(1):465–81.

[6] Anandan Kumar H, Kumaraguru S. Distortion in metal additive manufactured parts. In: 3D Printing and Additive Manufacturing Technologies. Springer; 2019. p. 281–95.

[7] Santos JA. Cost Estimation Model for the Directed Energy Deposition Process Adopting an Activity-Based Approach. Instituto Superior de Engenharia do Porto; 2018.

[8] Algarni M. Mechanical properties and microstructure characterization of AISI "D2" and "O1" cold work tool steels. Metals (Basel). 2019;9(11):1169.

[9] bin Abdul Rahim MAS, bin Minhat M, Hussein NISB, bin Salleh MS. A comprehensive review on cold work of AISI D2 tool steel. Metall Res Technol. 2018;115(1):104.

[10] ASTM Standard. F2792-12a - Standard Terminology for Additive Manufacturing Technologies. West Conshohocken, PA: ASTM International; 2012.

[11] Huang SH, Liu P, Mokasdar A, Hou L. Additive manufacturing and its societal impact: A literature review. Int J Adv Manuf Technol. 2013;67(5–8):1191–203.

[12] Kruth JP, Leu MC, Nakagawa T. Progress in additive manufacturing and rapid prototyping. CIRP Ann - Manuf Technol. 1998;47(2):525–40.

[13] Wong K V., Hernandez A. A Review of Additive Manufacturing. ISRN Mech Eng. 2012;2012:1–10.

[14] Horn TJ, Harrysson OLA. Overview of current additive manufacturing technologies and selected applications. Sci Prog. 2012;95(3):255–82.

[15] Chu C, Graf G, Rosen DW. Design for additive manufacturing of cellular structures. Comput Aided Des Appl. 2008;5(5):686–96.

[16] Grimm T. User's guide to rapid prototyping. Dearborn, MI: Society of Manufacturing Engineers; 2004.

[17] Wohlers T, Grimm T. Is CNC Machining Really Better Than RP ? Gardner Publ. 2003;20:2012.

[18] Stein A. Disadvantages of 3D printers. eHow TECH. 2012.

[19] Kruth JP. Material Incress Manufacturing by Rapid Prototyping Techniques. CIRP Ann - Manuf Technol. 1991;40(2):603–14.

[20] Frazier WE. Metal additive manufacturing: A review. J Mater Eng Perform. 2014;23(6):1917–28.

[21] Cooper KG. Rapid Prototyping Technology: Selection and Application. New York: Marcel Dekker Inc; 2005.

[22] Krauss H, Zeugner T, Zaeh MF. Layerwise monitoring of the selective laser melting process by thermography. Phys Procedia. 2014;56:64–71.

[23] Fayazfar H, Salarian M, Rogalsky A, Sarker D, Russo P, Paserin V, et al. A Critical Review of Powder-Based Additive Manufacturing of Ferrous Alloys: Process Parameters, Microstructure and Mechanical Properties. Mater Des. 2018;144:98–128.

[24] Gong X, Anderson T, Chou K. Review on Powder-Based Electron Beam Additive Manufacturing Technology. In: International Symposium on Flexible Automation. American Society of Mechanical Engineers; 2012. p. 507–15.

[25] Gibson I, Rosen D, Stucker B. Additive Manufacturing Technologies. 2nd ed. Additive Manufacturing Technologies: 3D Printing, Rapid Prototyping, and Direct Digital Manufacturing, Second Edition. Springer; 2015. 1–498 p.

[26] Cormier D, Harrysson O, West H. Characterization of H13 Steel Produced Via Electron Beam Melting. Rapid Prototyp J. 2004;

[27] Bai Y, Wagner G, Williams CB. Effect of bimodal powder mixture on powder packing density and sintered density in binder jetting of metals. In: 2015 Annual International Solid Freeform Fabrication Symposium. 2015. p. 758–71.

[28] Basalah A, Shanjani Y, Esmaeili S, Toyserkani E. Characterizations of additive manufactured porous titanium implants. J Biomed Mater Res Part B Appl Biomater. 2012;100(7):1970–9.

[29] Sheikh MA. Modelling & simulation of laser material processing: predicting melt pool geometry and temperature distribution. In: Proceeding of International Conference, India. 2007. p. 5–9.

[30] Mazumder J, Dutta D, Kikuchi N, Ghosh A. Closed loop direct metal deposition: art to part. Opt Lasers Eng. 2000;34(4–6):397–414.

[31] Mazumder J, Choi J, Nagarathnam K, Koch J, Hetzner D. The direct metal deposition of H13 tool steel for 3-D components. Jom. 1997;49(5):55–60.

[32] Hua Y, Choi J. Feedback control effects on dimensions and defects of H13 tool steel by DMD process. In: International Congress on Applications of Lasers & Electro-Optics. Laser Institute of America; 2003. p. 1308.

[33] Choi J, Hua Y. Adaptive laser aided DMD (direct metal deposition) process control. In: International Congress on Applications of Lasers & Electro-Optics. Laser Institute of America; 2001. p. 730–9.

[34] Shamsaei N, Yadollahi A, Bian L, Thompson SM. An overview of Direct Laser Deposition for additive manufacturing; Part II: Mechanical behavior, process parameter optimization and control. Addit Manuf [Internet]. 2015;8:12–35. Available from: http://dx.doi.org/10.1016/j.addma.2015.07.002

[35] Mehta PP, Otten RR, Cooper Jr EB. Method and apparatus for repairing metal in an article. Google Patents; 1988.

[36] Vrancken B, Thijs L, Kruth JP, Van Humbeeck J. Heat treatment of Ti6Al4V produced by Selective Laser Melting: Microstructure and mechanical properties. J Alloys Compd [Internet]. 2012;541:177–85. Available from: http://dx.doi.org/10.1016/j.jallcom.2012.07.022

[37] Jianglong L, Peidao D, Gongqi S. A scanning electron microscopy study of laser coating microstructures. Mater Charact. 1994;33(4):387–91.

[38] Ritter U, Kahrmann W, Küpfer R, Glardon R. Laser coating proven in practice. Tech Rundschau Sulzer;(Switzerland). 1991;73(3).

[39] Xue L, Purcell CJ, Theriault A, Islam MU. Laser consolidation for the manufacturing of complex flextensional transducer shells. In: International Congress on Applications of Lasers & Electro-Optics. Laser Institute of America; 2001. p. 702–11.

[40] McLean M. Laser direct casting high nickel alloy components. Adv Powder Metall Part Mater. 1997;3:21.

[41] Xu XY, Liu WJ, Zhong ML, Sun HQ. Synthesis and fabrication of WC particulate

reinforced Ni 3 Al intermetallic matrix composite coating by laser powder deposition. J Mater Sci Lett. 2003;22(19):1369–72.

[42] Toyserkani E, Corbin S, Khajepour A. Iron aluminide coating of mild steel using laser assisted powder deposition. In: Proceeding of International Symposium on Processing and Fabrication of Advanced Materials Processing XI, TS Srivatsan and RA Varin, Eds. 2002. p. 244–57.

[43] Pinkerton AJ, Li L, Lau WS. Effects of powder geometry and composition in coaxial laser deposition of 316L steel for rapid prototyping. CIRP Ann. 2003;52(1):181–4.

[44] Chang YC, Pinilla JM, Kao JH, Dong J, Ramaswami K, Prinz FB. Automated layer decomposition for additive/subtractive solid freeform fabrication. In: 1999 International Solid Freeform Fabrication Symposium. University of Texas at Austin, TX; 1999. p. 111–2.

[45] Laser Metal Deposition and Fluid Particles [Internet]. Available from: https://www.flow3d.com/laser-melting-deposition-fluid-particles/

[46] Islam MU, Xue L, McGregor G. Process for manufacturing or repairing turbine engine or compressor components. Google Patents; 2001.

[47] Gaumann M, Rusterholz H, Baumann R, Wagnière JD, Kurz W. Single crystal turbine components repaired by epitaxial laser metal forming. Mater Adv Powder Eng. 1998;1479:1–6.

[48] Hollander D, Wirtz T, Walter M, Linker R, Schultheis A, Paar O. Development of Individual Three-Dimensional Bone Substitutes Using “Selective Laser Melting.” Eur J Trauma. 2003;29(4):228–34.

[49] Thijs L, Verhaeghe F, Craeghs T, Humbeeck J Van, Kruth JP. A study of the microstructural evolution during selective laser melting of Ti-6Al-4V. Acta Mater [Internet]. 2010;58(9):3303–12. Available from: http://dx.doi.org/10.1016/j.actamat.2010.02.004

[50] Yasa E, Kruth JP. Microstructural investigation of Selective Laser Melting 316L stainless steel parts exposed to laser re-melting. Vol. 19, Procedia Engineering. 2011. p. 389–95.

[51] Toyserkani E, Khajepour A, Corbin S. Laser Cladding. Vol. 11. New York: CRC Press; 2005. 221 p.

[52] Taimisto L. Process parameters in laser sintering process. Lappeenranta University of Technology; 2009.

[53] Miedzinski M. Materials for additive manufacturing by direct energy deposition. Chalmers University of Technology; 2017.

[54] Telasang G, Majumdar JD, Padmanabham G, Tak M, Manna I. Effect of laser parameters on microstructure and hardness of laser clad and tempered AISI H13 tool steel. Surf Coatings Technol. 2014;258:1108–18.

[55] ASTM F3187. Standard Guide for Directed Energy Deposition of Metals. ASTM International; 2016.

[56] Porter DA, Easterling KE, Sherif MY. Phase Transformations in Metals and Alloys. 3rd edition. CRC Press; 2009.

[57] Policelli M. Development of a new method to fabricate titanium metal matrix composites via LENS with improved material properties. Penn State University; 2014.

[58] Lee H, Lim CHJ, Low MJ, Tham N, Murukeshan VM, Kim YJ. Lasers in additive manufacturing: A review. Int J Precis Eng Manuf Technol. 2017;4(3):307–22.

[59] Hu Y, Cong W. A review on laser deposition-additive manufacturing of ceramics and ceramic reinforced metal matrix composites. Ceram Int. 2018;44(17):20599–612.

[60] Pinkerton AJ, Li L. Multiple-layer laser deposition of steel components using gas- and water-atomised powders: the differences and the mechanisms leading to them. Appl Surf Sci. 2005;247(1–4):175–81.

[61] Leyens C, Beyer E. Innovations in laser cladding and direct laser metal deposition. In: Laser Surface Engineering. Elsevier; 2015. p. 181–92.

[62] Shim DS, Baek GY, Lee EM. Effect of substrate preheating by induction heater on direct energy deposition of AISI M4 powder. Mater Sci Eng A [Internet]. 2017;682(August 2016):550–62. Available from: http://dx.doi.org/10.1016/j.msea.2016.11.029

[63] Gu D. Laser additive manufacturing (AM): classification, processing philosophy, and metallurgical mechanisms. In: Laser additive manufacturing of high-performance materials. Springer; 2015. p. 15–71.

[64] Chandler H. Introduction to hardness testing. Hardness testing USA ASM Int. 1999;1–13.

[65] Callister WD. Fundamentals of materials science and engineering. Vol. 471660817. Wiley London; 2000.

[66] Stachowiak GW, Batchelor AW. Engineering Tribology. 3rd ed. Oxford: Elsevier; 2006. 832 p.

[67] Bhushan B. Principles and Applications of Tribology. Second Edi. Chichester: Wiley; 2013. 962 p.

[68] ASM International. ASM Handbook, Vol. 5 - Surface Engineering. 1995. 2535 p.

[69] Goto H, Amamoto Y. Effect of varying load on wear resistance of carbon steel under unlubricated conditions. Wear. 2003;254(12):1256–66.

[70] Hutchings I, Shipway P. Tribology: Friction and wear of engineering materials: Second Edition. Tribology: Friction and Wear of Engineering Materials: Second Edition. 2017. 1–388 p.

[71] Khruschov MM. Principles of abrasive wear. Wear. 1974;28(1):69–88.

[72] Rendón J, Olsson M. Abrasive wear resistance of some commercial abrasion resistant steels evaluated by laboratory test methods. Wear. 2009;267(11):2055–61.

[73] Kenneth C, Layo Ajayi. Chapter 9, "Wear." In: Friction, Wear, Lubrication : A Textbook in Tribology, Second Edition. 2nd ed. CRC Press; 2020. p. 151–80.

[74] Tuominen J, Näkki J, Pajukoski H, Hyvärinen L, Vuoristo P. Microstructural and abrasion wear characteristics of laser-clad tool steel coatings. Surf Eng. 2016;32(12):923–33.

[75] Hardell J, Hernandez S, Mozgovoy S, Pelcastre L, Courbon C, Prakash B. Effect of oxide layers and near surface transformations on friction and wear during tool steel and boron steel interaction at high temperatures. Wear. 2015;330–331:223–9.

[76] Ramalho A, Miranda JC. The relationship between wear and dissipated energy in sliding systems. Wear. 2006;260(4–5):361–7.

[77] Jian-Min T, Yi-Zhong Z, Tian-Yi S, Hai-Jin D. The influence of retained austenite in high chromium cast iron on impact-abrasive wear. Wear. 1990;135(2):217–26.

[78] Pereloma E, Edmonds D, editors. Phase Transformation in Steels. 1st ed. Woodhead Publishing; 2012. 680 p.

[79] Chintha AR. Metallurgical aspects of steels designed to resist abrasion, and impact-abrasion wear. Mater Sci Technol (United Kingdom). 2019;35(10):1133–48.

[80] Ninham A. The effect of mechanical properties on erosion. Wear. 1988;121(3):307–24.

[81] Xu L, Wei S, Xiao F, Zhou H, Zhang G, Li J. Effects of carbides on abrasive wear properties and failure behaviours of high speed steels with different alloy element content. Wear. 2017;376–377:968–74.

[82] Kashcheev VN. Some aspects of improving abrasive resistance. Wear. 1983;89(3):265–72.

[83] Guo ZH, Xiao FR, Lu SL, Li HY, Liao B. Effects of heat-treatment on the microstructure and wear resistance of a high-chromium cast iron for rolls. Adv Mater Sci Eng. 2016;2016:1–8.

[84] Edmonds D V., He K, Rizzo FC, De Cooman BC, Matlock DK, Speer JG. Quenching and partitioning martensite-A novel steel heat treatment. Mater Sci Eng A. 2006;438–440(SPEC. ISS.):25–34.

[85] Wang L, Speer JG. Quenching and Partitioning Steel Heat Treatment. Metallogr Microstruct Anal. 2013;2(4):268–81.

[86] Masoumi M, Echeverri EAA, Tschiptschin AP, Goldenstein H. Improvement of wear resistance in a pearlitic rail steel via quenching and partitioning processing. Sci Rep. 2019;9(1):1–12.

[87] ASM. Vol 1: Properties and Selection: Irons, Steels, and High-Performance Alloys. ASM Handbook. ASM International; 1990. 1063 p.

[88] Mumtaz K, Hopkinson N. Top surface and side roughness of Inconel 625 parts processed using selective laser melting. Rapid Prototyp J. 2009;

[89] Gu D, Dai D, Chen W, Chen H. Selective laser melting additive manufacturing of hard-to-process tungsten-based alloy parts with novel crystalline growth morphology and enhanced performance. J Manuf Sci Eng. 2016;138(8).

[90] Charles A, Elkaseer A, Thijs L, Hagenmeyer V, Scholz S. Effect of process parameters on the generated surface roughness of down-facing surfaces in selective laser melting. Appl Sci. 2019;9(6):1256.

[91] Masuo H, Tanaka Y, Morokoshi S, Yagura H, Uchida T, Yamamoto Y, et al. Influence of defects, surface roughness and HIP on the fatigue strength of Ti-6Al-4V manufactured by additive manufacturing. Int J Fatigue. 2018;117:163–79.

[92] Bayoumi MR, Abdellatif AK. Effect of surface finish on fatigue strength. Eng Fract Mech. 1995;51(5):861–70.

[93] Kang N, Li Y, Lin X, Feng E, Huang W. Microstructure and tensile properties of Ti-Mo alloys manufactured via using laser powder bed fusion. J Alloys Compd. 2019;771:877–84.

[94] Zhang Y, Wu L, Guo X, Kane S, Deng Y, Jung YG, et al. Additive manufacturing of metallic materials: a review. J Mater Eng Perform. 2018;27(1):1–13.

[95] Irrinki H, Harper T, Badwe S, Stitzel J, Gulsoy O, Gupta G, et al. Effects of powder characteristics and processing conditions on the corrosion performance of 17-4 PH stainless steel fabricated by laser-powder bed fusion. Prog Addit Manuf. 2018;3(1):39–49.

[96] Han X, Zhu H, Nie X, Wang G, Zeng X. Investigation on selective laser melting AlSi10Mg cellular lattice strut: Molten pool morphology, surface roughness and dimensional accuracy. Materials (Basel). 2018;11(3):392.

[97] Lu J. Prestress engineering of structural material: a global design approach to the residual stress problem. Handbook of Residual Stress Formation and Distorsion of Steel. ASM International; 2002.

[98] Szost BA, Terzi S, Martina F, Boisselier D, Prytuliak A, Pirling T, et al. A comparative study of additive manufacturing techniques: Residual stress and microstructural analysis of CLAD and WAAM printed Ti–6Al–4V components. Mater Des. 2016;89:559–67.

[99] Carpenter K, Tabei A. On residual stress development, prevention, and compensation in metal additive manufacturing. Materials (Basel). 2020;13(2):255.

[100] Lu X, Lin X, Chiumenti M, Cervera M, Hu Y, Ji X, et al. Residual stress and distortion of rectangular and S-shaped Ti-6Al-4V parts by Directed Energy Deposition: Modelling and experimental calibration. Addit Manuf. 2019;26:166–79.

[101] LeBrun T, Nakamoto T, Horikawa K, Kobayashi H. Effect of retained austenite on subsequent thermal processing and resultant mechanical properties of selective laser melted 17–4 PH stainless steel. Mater Des. 2015;81:44–53.

[102] DebRoy T, Wei HL, Zuback JS, Mukherjee T, Elmer JW, Milewski JO, et al. Additive Manufacturing of Metallic Components – Process, Structure and Properties. Prog Mater Sci. 2018;92:112–224.

[103] Chattopadhyay R. Green tribology, green surface engineering, and global warming. ASM international; 2014.

[104] Alimardani M, Toyserkani E, Huissoon JP, Paul CP. On the delamination and crack formation in a thin wall fabricated using laser solid freeform fabrication process: An experimental–numerical investigation. Opt Lasers Eng. 2009;47(11):1160–8.

[105] Rossinia NS, Dassistia M, Benyounisc KY, Olabib AG. Review of Methods for Measuring Residual Stresses in Components.

[106] Withers PJ, Bhadeshia H, Withers PJ, Bhadeshia H. Residual stress. Part 1–Measurement techniques Residual stress Part 1–Measurement techniques. vol; 2016.

[107] Gauthier J, Krause TW, Atherton DL. Measurement of residual stress in steel using the magnetic Barkhausen noise technique. Ndt E Int. 1998;31(1):23–31.

[108] Pokharel R, Patra A, Brown DW, Clausen B, Vogel SC, Gray III GT. An analysis of phase stresses in additively manufactured 304L stainless steel using neutron diffraction measurements and crystal plasticity finite element simulations. Int J Plast. 2019;121:201–17.

[109] Corbin DJ, Nassar AR, Reutzel EW, Beese AM, Michaleris P. Effect of Substrate thickness and preheating on the distortion of laser deposited Ti–6Al–4V. J Manuf Sci Eng. 2018;140(6).

[110] Svetlizky D, Das M, Zheng B, Vyatskikh AL, Bose S, Bandyopadhyay A, et al. Directed energy deposition (DED) additive manufacturing: Physical characteristics, defects, challenges and applications. Mater Today. 2021;49:271–95.

[111] Denlinger ER, Heigel JC, Michaleris P, Palmer TA. Effect of inter-layer dwell time on distortion and residual stress in additive manufacturing of titanium and nickel alloys. J Mater Process Technol. 2015;215:123–31.

[112] Yamaguchi H, Fergani O, Wu PY. Modification using magnetic field-assisted finishing of the surface roughness and residual stress of additively manufactured components. CIRP Ann. 2017;66(1):305–8.

[113] Smith WF. Structure and Properties of Engineering Alloys. 1st ed. Julienne V. Brown JWM, editor. New York: McGraw-Hill Inc.; 1981. 512 p.

[114] Hudok D. Properties and selection: irons, steels, and high-performance alloys. Met Handb. 1990;1:200–11.

[115] Ballentine K. Examples of Iron-Iron Carbide Transformations [Internet]. 1996. Available from: http://sv.rkriz.net/classes/MSE2094_NoteBook/96ClassProj/examples/kimttt.html

[116] Zener C. Elasticity and Aelasticity of Metals. University of Chicago press; 1948.

[117] Walker J, Middendorf JR, Lesko CCC, Gockel J. Multi-material laser powder bed fusion additive manufacturing in 3-dimensions. Manuf Lett. 2022;31:74–7.

[118] Wang X, Deng D, Hu Y, Ning F, Wang H, Cong W, et al. Overhang structure and accuracy in laser engineered net shaping of Fe-Cr steel. Opt Laser Technol. 2018;106:357–65.

[119] Totten GE. Steel heat treatment: metallurgy and technologies. 2nd ed. Boca Raton, FL: CRC press; 2006.

[120] Gaier M, Todorova TZ, Russell Z, Farhat ZN, Zwanziger JW, Plucknett KP. The influence of intermetallic ordering on wear and indentation properties of TiC-Ni3Al cermets. Wear. 2019;426:390–400.

[121] Mazumder J, Schifferer A, Choi J. Direct materials deposition: designed macro and microstructure. Mater Res Soc Symp - Proc. 1999;542:51–63.

[122] Itamiya H, Kubo MO, Sugita R, Sugai T. New method of structural analysis and measurement of V-shaped percussion cracks in quartz sands surface by confocal laser scanning microscope (CLSM). Micron. 2022;153:103174.

[123] Keynce corporation. JIS B 0601 Surface (Line) Roughness Terminology [Internet]. Available from: https://www.keyence.com/ss/products/microscope/roughness/line/cutoff-values.jsp

[124] Keyence corporation. Evaluation Processing And Filtering [Internet]. Available from: https://www.keyence.com/ss/products/microscope/roughness/surface/evaluation_process.jsp

[125] Delshad Khatibi P, Phillion AB, Henein H. Microstructural investigation of D2 tool steel during rapid solidification. Powder Metall. 2014;57(1):70–8.

[126] Boccalini M, Goldenstein H. Solidification of high speed steels. Int Mater Rev. 2001;46(2):92–115.

[127] ASTM G. 133 Standard Test Method for Linearly Reciprocating Ball-on-Flat Sliding Wear. ASTM Int West Conshohocken, PA, USA. 2016;

[128] Das S. Physical aspects of process control in selective laser sintering of metals. Adv Eng Mater. 2003;5(10):701–11.

[129] Thompson SM, Bian L, Shamsaei N, Yadollahi A. An Overview of Direct Laser Deposition for Additive Manufacturing; Part I: Transport Phenomena, modeling and Diagnostics. Addit Manuf [Internet]. 2015;8:36–62. Available from: http://dx.doi.org/10.1016/j.addma.2015.07.001

[130] PP M, RR O, EB CJ. Method and Apparatus for Repairing Metal in an Article. United States; US 4743733, 1988.

[131] Sarma DS. Cold Work and Hot work Tool Steels. 1994;

[132] Roberts G, Krauss G, Kennedy R. Tool Steels. 5th ed. Krauss, George; Kennedy R, editor. Materials Park, OH: ASM International; 1998.

[133] Fayazfar H, Salarian M, Rogalsky A, Sarker D, Russo P, Paserin V, et al. A critical review of powder-based additive manufacturing of ferrous alloys: Process parameters, microstructure and mechanical properties. Mater Des. 2018 Apr 15;144:98–128.

[134] Park JS, Park JH, Lee MG, Sung JH, Cha KJ, Kim DH. Effect of Energy Input on the Characteristic of AISI H13 and D2 Tool Steels Deposited by a Directed Energy Deposition Process. Metall Mater Trans A Phys Metall Mater Sci. 2016 May 1;47(5):2529–35.

[135] Baek GY, Shin GY, Lee EM, Shim DS, Lee KY, Yoon HS, et al. Mechanical characteristics of a tool steel layer deposited by using direct energy deposition. Met Mater Int. 2017 Jul 1;23(4):770–7.

[136] Baek GY, Shin GY, Lee EM, Shim DS, Lee KY, Yoon HS, et al. Mechanical characteristics of a tool steel layer deposited by using direct energy deposition. Met Mater Int. 2017;23(4):770–7.

[137] Park JS, Lee MG, Cho YJ, Sung JH, Jeong MS, Lee SK, et al. Effect of heat treatment on the characteristics of tool steel deposited by the directed energy deposition process. Met Mater Int. 2016;22(1):143–7.

[138] Baek GY, Shin GY, Lee KY, Shim DS. Mechanical properties of tool steels with high wear resistance via directed energy deposition. Metals (Basel). 2019;9(3).

[139] Kou S. Welding metallurgy. 2nd ed. New Jersey: Wiley; 2003.

[140] Uhlenhaut DI, Kradolfer J, Püttgen W, Löffler JF, Uggowitzer PJ. Structure and properties of a hypoeutectic chromium steel processed in the semi-solid state. Acta Mater. 2006;54(10):2727–34.

[141] Bhadeshia HKDH, Honeycombe RWK. Steels: Microstructure and Properties. 4th ed. Oxford: Butterworth-Heinemann; 2017. 461 p.

[142] Maalekian M. The effects of alloying elements on steels (I). 2007;

[143] Arrizubieta JI, Cortina M, Mendioroz A, Salazar A, Lamikiz A. Thermal diffusivity measurement of laser-deposited AISI H13 tool steel and impact on cooling performance of hot stamping tools. Metals (Basel). 2020;10(1).

[144] Zhang K, Liu W, Shang X. Research on the processing experiments of laser metal deposition shaping. Opt Laser Technol. 2007;39(3):549–57.

[145] Chen Z, Guo X, Shi J. Hardness prediction and verification based on key temperature features during the directed energy deposition process. Int J Precis Eng Manuf Technol. 2021;8(2):453–69.

[146] Singh K, Khatirkar RK, Sapate SG. Microstructure evolution and abrasive wear behavior of D2 steel. Wear. 2015;328:206–16.

[147] Bain EC, Paxton HW. Alloying elements in steel. 1966, 291 P Am Soc Met Met Park OHIO. 1966;

[148] Laird G, Gundlach RB, Röhrig KK. Abrasion-resistant cast iron handbook. American Foundry Society; 2000.

[149] Lee EM, Shin GY, Yoon HS, Shim DS. Study of the effects of process parameters on deposited single track of M4 powder based direct energy deposition. J Mech Sci Technol. 2017;31(7):3411–8.

[150] Ravi GA, Hao XJ, Wain N, Wu X, Attallah MM. Direct laser fabrication of three dimensional components using SC420 stainless steel. Mater Des. 2013;47:731–6.

[151] Shim DS, Baek GY, Seo JS, Shin GY, Kim KP, Lee KY. Effect of layer thickness setting on deposition characteristics in direct energy deposition (DED) process. Opt Laser Technol [Internet]. 2016;86:69–78. Available from: http://dx.doi.org/10.1016/j.optlastec.2016.07.001

[152] Fathi A, Toyserkani E, Khajepour A, Durali M. Prediction of melt pool depth and dilution in laser powder deposition. J Phys D Appl Phys. 2006;39(12):2613–23.

[153] Sreekanth S, Ghassemali E, Hurtig K, Joshi S, Andersson J. Effect of direct energy deposition process parameters on single-track deposits of alloy 718. Metals (Basel). 2020 Jan 1;10(1).

[154] Bi G, Gasser A, Wissenbach K, Drenker A, Poprawe R. Characterization of the process control for the direct laser metallic powder deposition. Surf Coatings Technol [Internet]. 2006;201(6):2676–83. Available from: http://dx.doi.org/10.1016/j.surfcoat.2006.05.006

[155] Choi J, Hua Y. Dimensional and material characteristics of direct deposited tool steel by CO2 laser. J Laser Appl. 2004;16(4):245.

[156] Ma M, Wang Z, Wang D, Zeng X. Control of shape and performance for direct laser fabrication of precision large-scale metal parts with 316L Stainless Steel. Opt Laser Technol [Internet]. 2013;45(1):209–16. Available from: http://dx.doi.org/10.1016/j.optlastec.2012.07.002

[157] Panchagnula JS, Simhambhatla S. Additive manufacturing of complex shapes through weld-deposition and feature based slicing. In: ASME International Mechanical Engineering Congress and Exposition. American Society of Mechanical Engineers; 2015. p. V02AT02A004.

[158] Liou F, Slattery K, Kinsella M, Newkirk J, Chou H, Landers R. Applications of a hybrid manufacturing process for fabrication of metallic structures. Rapid Prototyp J. 2007;

[159] Nassar AR, Reutzel EW. Beyond layer-by-layer additive manufacturing–Voxel-Wise directed energy deposition. In: Solid Freeform Fabr Symp Proc. 2015. p. 273–83.

[160] Bullen J, Keicher D. Greater angle and overhanging materials deposition. United States; US 0003095A1, 2006.

[161] Hensinger DM, Ames AL, Kuhlmann JL. Motion planning for a direct metal deposition rapid prototyping system. In: Proceedings 2000 ICRA Millennium Conference IEEE International Conference on Robotics and Automation Symposia Proceedings (Cat No 00CH37065). IEEE; 2000. p. 3095–100.

[162] Keynce corporation. Introduction to Surface Roughness Measurement [Internet]. 2012. Available from: https://www.keyence.eu/landing/lp_micro_surface_download.jsp

[163] Craig O, Bois-Brochu A, Plucknett K. Geometry and surface characteristics of H13 hot-work tool steel manufactured using laser-directed energy deposition. Int J Adv Manuf Technol. 2021;116:699–718.

[164] Jang JH, Joo BD, Mun SM, Sung MY, Moon YH. Application of direct laser melting to restore damaged steel dies. Met Mater Int. 2011;17(1):167–74.

[165] Mahamood RM, Akinlabi ET. Scanning speed and powder flow rate influence on the properties of laser metal deposition of titanium alloy. Int J Adv Manuf Technol. 2017;91(5):2419–26.

[166] Caiazzo F, Alfieri V, Argenio P, Sergi V. Additive manufacturing by means of laser-aided directed metal deposition of 2024 aluminium powder: Investigation and optimization. Adv Mech Eng. 2017;9(8):1–12.

[167] Mahamood RM, Akinlabi ET. Effect of Powder Flow Rate on Surface Finish in Laser Additive Manufacturing Process. In: IOP Conference Series: Materials Science and Engineering. IOP Publishing; 2018. p. 12005.

[168] Kobryn PA, Moore EH, Semiatin SL. The effect of laser power and traverse speed on microstructure, porosity, and build height in laser-deposited Ti-6Al-4V. Scr Mater. 2000;43(4):299–305.

[169] Park JS, Park JH, Lee MG, Sung JH, Cha KJ, Kim DH. Effect of energy input on the characteristic of AISI H13 and D2 tool steels deposited by a directed energy deposition process. Metall Mater Trans A. 2016;47(5):2529–35.

[170] Peyre P, Gharbi M, Gorny C, Carin M, Morville S, Carron D, et al. Surface finish issues after direct metal deposition. In: Materials Science Forum. Trans Tech Publ; 2012. p. 228–33.

[171] Wei PS, Chung FK. Unsteady Marangoni flow in a molten pool when welding dissimilar metals. Metall Mater Trans B. 2000;31(6):1387–403.

[172] Gharbi M, Peyre P, Gorny C, Carin M, Morville S, Le Masson P, et al. Influence of various process conditions on surface finishes induced by the direct metal deposition laser technique on a Ti-6Al-4V alloy. J Mater Process Technol [Internet]. 2013;213(5):791–800. Available from: http://dx.doi.org/10.1016/j.jmatprotec.2012.11.015

[173] Thijs L, Verhaeghe F, Craeghs T, Humbeeck J Van, Kruth JP. A study of the microstructural evolution during selective laser melting of Ti–6Al–4V. Acta Mater. 2010;58(9):3303–12.

[174] Omar SMT, Plucknett KP. The influence of DED process parameters and heat-treatment cycle on the microstructure and hardness of AISI D2 tool steel. J Manuf Process. 2022;81:655–71.

[175] Wang SH, Chen JY, Xue L. A study of the abrasive wear behaviour of laser-clad tool steel coatings. Surf Coatings Technol. 2006;200(11):3446–58.

[176] Hashemi N, Mertens A, Montrieux HM, Tchuindjang JT, Dedry O, Carrus R, et al. Oxidative wear behaviour of laser clad High Speed Steel thick deposits: Influence of sliding speed, carbide type and morphology. Surf Coatings Technol. 2017;315:519–29.

[177] Ur Rahman N, de Rooij MB, Matthews DTA, Walmag G, Sinnaeve M, Römer GRBE. Wear characterization of multilayer laser cladded high speed steels. Tribol Int. 2019;130(August 2018):52–62.

[178] Xue L, Chen J, Wang SH. Freeform Laser Consolidated H13 and CPM 9V Tool Steels. Metallogr Microstruct Anal. 2013;2(2):67–78.

[179] Shim DS, Baek GY, Lee SB, Yu JH, Choi YS, Park SH. Influence of heat treatment on wear behavior and impact toughness of AISI M4 coated by laser melting deposition. Surf Coatings Technol. 2017;328:219–30.

[180] Navas C, Conde A, Fernández BJ, Zubiri F, de Damborenea J. Laser coatings to improve wear resistance of mould steel. Surf Coatings Technol. 2005;194(1):136–42.

[181] Yu Z, Cherng TC, Yuan X, Zeng X. Wear and impact resistance of laser cladding steel for die cutting application. Laser Inst Am Proc. 1997;83(2).

[182] Chen C, Yan K, Qin L, Zhang M, Wang X, Zou T, et al. Effect of Heat Treatment on Microstructure and Mechanical Properties of Laser Additively Manufactured AISI H13 Tool Steel. J Mater Eng Perform. 2017;26(11):5577–89.

[183] Leunda J, Soriano C, Sanz C, Navas VG. Laser cladding of vanadium-carbide tool steels for die repair. Phys Procedia. 2011;12:345–52.

[184] Okonkwo PC, Kelly G, Rolfe BF, Pereira MP. The effect of temperature on sliding wear of steel-tool steel pairs. Wear [Internet]. 2012;282–283:22–30. Available from: http://dx.doi.org/10.1016/j.wear.2012.01.017

[185] Iakovakis E, Avcu E, Roy MJ, Gee M, Matthews A. Dry sliding wear behaviour of additive manufactured CrC-rich WC-Co cemented carbides. Wear. 2021;486:204127.

[186] Ueda M, Uchino K, Kobayashi A. Effects of carbon content on wear property in pearlitic steels. Wear. 2002;253(1–2):107–13.

[187] Lin YC, Wang SW, Chen TM. A study on the wear behavior of hardened medium carbon steel. J Mater Process Technol. 2002;120(1–3):126–32.

[188] Steven G, Catlin JP. A controlled dry wear test for high-hardness tool steels. J MATER. 1966;1(2).

[189] Podgornik B, Brunˇ M. Retained Austenite Content and Kinetically. Metals (Basel). 2020;10(5):672.

[190] Stepankin IN, Pazdniakou EP. Effect of Retained Austenite on the Wear Resistance of C80W1 and 90CrSi5 Tool Steels. J Frict Wear. 2021;42(4):239–45.

[191] Wang Y, Song R, Huang L. The effect of retained austenite on the wear mechanism of bainitic ductile iron under impact load. J Mater Res Technol. 2021;11:1665–71.

[192] Fábián ER, Tóth L, Huszák C. Examination of Heat Treatment on the Microstructure and Wear of Tool Steels. Acta Mater Transylvanica. 2019;2(2):87–92.

APPENDIX A RESEARCH DISSEMINATION

The NSERC HI-AM network required semi-annual internal progress reports that included the completion of goals and examples of findings. Published material from these studies is listed below. All the data collection, sample preparation, material characterization, manuscripts preparation of journal articles and this thesis was completed by the author, unless otherwise stated, with the guidance of the PhD supervisor Dr Kevin Paul Plucknett.:

- Omar SMT, Plucknett KP, "Wear Properties of Wrought and Directly Deposited AISI D2 Tool Steel", *The 6th NSERC HI-AM Conference*, Halifax, Jun 2023.
- Omar SMT, Plucknett KP, "The Influence of DED Process Parameters and Heat-Treatment Cycle on the Microstructure and Hardness of AISI D2 Tool Steel", *Journal of Manufacturing Processes,* 81 (2022), P. 655-671.
- Omar SMT, Plucknett KP, "Influence of Layer Thickness Upon the Dimensional Accuracy and Surface Roughness of AISI D2 Tool Steel Manufactured Using Directed Energy Deposition", *The 61st Conference of Metallurgists*, Montreal, Aug 2022.
- Omar SMT, Plucknett KP, "Influence of Layer Thickness Upon Material Characteristics of AISI D2 Tool Steel Manufactured Using Directed Energy Deposition", *The 5th NSERC HI-AM Conference*, Montreal, Jun 2022.
- Craig O, Omar S, Plucknett KP, "Material Characterization Comparison of D2 and H13 Tool Steels Manufactured Using Directed Energy Deposition", *The 60th Conference of Metallurgists*, Virtual, Aug 2021.
- Omar S, Plucknett KP, "Influence of Heat Treatment on Microstructure and Hardness of Directed Energy Deposition (DED) Processed AISI D2 Tool Steel", *The 4th NSERC HI-AM Conference*, Virtual, Jun 2021.
- Omar S, Plucknett KP, "Effects of Process Parameters on Material Characteristics During Direct Energy Deposition of AISI D2 Tool Steel", *The 3rd NSERC HI-AM Conference*, Virtual, Jun 2020.

APPENDIX B COPYRIGHT PERMISSION LETTER

February 6th, 2023

Dear chair of Journal of Manufacturing Processes,

I am preparing my PhD thesis for submission to the Faculty of Graduate Studies at Dalhousie University, Halifax, Nova Scotia, Canada. I am seeking your permission to include a manuscript version of the following paper(s) as a chapter in the thesis:

Omar SMT, Plucknett KP, "The Influence of DED Process Parameters and Heat-Treatment Cycle on the Microstructure and Hardness of AISI D2 Tool Steel", *Journal of Manufacturing Processes,* 81 (2022), P. 655-671.

Canadian graduate theses are reproduced by the Library and Archives of Canada (formerly National Library of Canada) through a non-exclusive, world-wide license to reproduce, loan, distribute, or sell theses. I am also seeking your permission for the material described above to be reproduced and distributed by the LAC(NLC). Further details about the LAC(NLC) thesis program are available on the LAC(NLC) website (www.nlc-bnc.ca).

Full publication details and a copy of this permission letter will be included in the thesis.

Yours sincerely,

Samer Omar

Permission is granted for:

a) the inclusion of the material described above in your thesis.

b) for the material described above to be included in the copy of your thesis that is sent to the Library and Archives of Canada (formerly National Library of Canada) for reproduction and distribution.

Name: _____ Title: _____

Signature: _____ Date: _____

The influence of DED process parameters and heat-treatment cycle on the microstructure and hardness of AISI D2 tool steel

Author: S.M.T. Omar,K.P. Plucknett

Publication: Journal of Manufacturing Processes

Publisher: Elsevier

Date: September 2022